

# Study of impurity ion transport using charge exchange spectroscopy on TCV

Présentée le 14 octobre 2022

Faculté des sciences de base  
SPC - Physique du Tokamak TCV  
Programme doctoral en physique

pour l'obtention du grade de Docteur ès Sciences

par

**Filippo BAGNATO**

Acceptée sur proposition du jury

Prof. R. Houdré, président du jury  
Dr B. Duval, directeur de thèse  
Prof. E. Viezzer, rapporteuse  
Dr J. Rice, rapporteur  
Dr A. Merle, rapporteur



Ma noi non faremo l'errore,  
Come fanno le altre persone, di  
Fare sempre la scelta più giusta  
Invece di quella migliore  
Siamo giovani come la notte  
E urliamo quel nostro timore  
Che questo vedere più chiare le cose  
Andrà via con la notte accecato dal sole  
— Massimo Pericolo

It's all just a game people...and I play the game.  
The game is how comfortable can you  
become with your own insanity.  
— Daniel Woods

*A mia madre...*





# Abstract

One of the main objectives of plasma physics research is the development of controlled thermonuclear fusion as a reliable method for large scale energy production. The Swiss Plasma Center (SPC), located at the Polytechnic School of Lausanne, Switzerland, is one of the active members of this undertaking with its largest experimental installation, the *Tokamak à configuration variable* (TCV). In a tokamak, one of the leading candidates for a practical fusion reactor, high temperature plasmas are confined in a toroidal shape by means of toroidal and poloidal magnetic fields. TCV is a medium size research fusion reactor, with the distinguishing feature of having a highly elongated vacuum vessel. Its 16 poloidal magnetic field coils allow for unique and extreme shaping capabilities, exploited to study the effects of plasma shape on stability and performances of the reactor. Plasma energy and particle confinement, that are essential for a net energy production, are limited by collisional and turbulent transport mechanisms, that naturally arise from the gradients that develop between the hot and dense plasma core and the cold and rarefied plasma edge.

In this work, impurity transport in the TCV tokamak was studied by means of a Charge Exchange Recombination diagnostic, a spectroscopic system that exploits the charge exchange reaction between externally injected neutral particles and impurity ions, usually C, naturally present in TCV due to its graphite-tiled walls, to perform temporal and spatial resolved measurements of ion temperature, density and velocity. TCV's CXRS employs a non-perturbative diagnostic neutral beam injector (DNBI) as a source of neutral particles for the CX reaction with plasma ions. The DNBI is a low power beam, optimised, in terms of energy of injected particles, for the observation of a C emission line at 529.1 nm. Its injection geometry was designed to maximise the beam penetration whilst minimising the injected toroidal momentum. As a non-perturbative beam, it provides an optimal environment for the investigation of low-torque scenarios and intrinsic rotation studies.

During this work, two CXRS systems, that exploit the CX reaction between the C ions and the neutrals injected by TCV's two heating beams, were developed and successfully operated. For the first time, reliable ion temperature measurements were performed during ELMy H-modes, where the DNBI-CXRS systems' background signals are often too strongly perturbed, inevitably compromising the measurements. These NBI-systems, due to the higher injected neutral density, provide a stronger active signal compared to the DNBI-systems. Therefore, they were employed, again for the first time, to perform measurements of impurity ions other

than C, opening to the possibilities of tracking multiple impurities (C, B, N, O) simultaneously.

A large portion of this thesis focused on the investigation of the correlation between the linear to saturated ohmic confinement (LOC/SOC) transition and toroidal rotation reversal, two phenomena often observed around a plasma density threshold that, in some specific cases, appears to coincide. As most studies were reported from D majority plasmas only, a set of experiments was designed to extend previous investigations in D plasmas to discharges of majority hydrogen and helium. The results presented in this thesis show a clear separation of the two phenomena in D and He, whilst no rotation reversal was observed in H, despite the evident LOC/SOC transition. A strong correlation between the toroidal rotation gradient and the plasma density gradient was observed, in agreement with theoretical models [6] [89]. Strong variations of turbulence are necessary to explain the changes of local density gradients that, in turn, favor variations in rotation profiles. Therefore, the stabilisation (or destabilisation) of turbulent modes appears to play a major role in understanding rotation reversal. As the maximum growth rate of trapped electron modes (TEM), the dominant instability in low density plasmas, increases with decreasing ion mass [190] [163], it is likely that the stabilisation of TEMs by collisional detrapping, often observed during D density ramps, is less effective in H, thus reducing any effect on density profiles, explaining the absence of rotation reversal in H. To further probe the effect of density peaking, X2 ECRH was employed in a H discharge, also replicated in D, to successfully trigger a rotation reversal, showing, again, a strong correlation between  $\nabla n_e$  and  $\nabla v_{tor}$ .

Recent experiments performed in JET and Alcator C-mod [148] [133] [132] [48], however, showed a rotation reversal in H plasmas, as well as co- and counter rotation profiles with identical density profiles. These results, in contrast with TCV's, are addressed during this thesis and a possible explanation to the controversy is given in chapter 4.

TCV's extreme flexible shaping capabilities were exploited to extend impurity transport studies to negative triangularity. Light impurity transport is deemed to be mainly driven by turbulence [2]. The turbulent flux is described by a combination of diffusive and convective terms and evolves according to the interplay of ion temperature, rotation and density gradients that mutually affect each-other. A practical way of studying turbulent transport is to investigate the correlations between these impurity ion gradients that, in this study, highlighted significant differences between positive and negative  $\delta$  plasmas.  $\delta$  scans ( $-0.6 < \delta < +0.6$ ) were performed in limited and diverted configuration, showing no correlation between C temperature, rotation and density gradients in positive triangularity. This stiff response at  $\delta > 0$  appears to be relieved in negative triangularity, where a linear correlation between  $\nabla T_i$  and  $\nabla n_C$ , and  $\nabla v_{tor}$  and  $\nabla n_C$ , was observed over a range of negative  $\delta$ , suggesting that transport in NT is mainly driven by temperature and toroidal velocity gradients. A possible explanation to this phenomenon could be linked to turbulence suppression and stabilisation of TEM often observed for  $\delta < 0$  [125] [65]. Furthermore, this may also explain why no rotation reversal was observed at  $\delta < 0$  where, conversely to its positive  $\delta$  counterpart, TEMs stabilisation is accompanied by an increase of ion dilution with density. Consequently, ITGs are maintained

stable and TEMs remain the dominant instability, reducing the effects on density profiles that appear to induce the strong changes in toroidal velocity observed in discharges at positive triangularity.



## Sinossi

La realizzazione della fusione termonucleare controllata è uno dei principali obiettivi della ricerca nella fisica del plasma avente, come scopo ultimo, lo sviluppo di reattori affidabili per la produzione di energia su larga scala. L'SPC (Swiss Plasma Center), centro di ricerca affiliato alla Scuola Politecnica Federale di Losanna, con il suo reattore a fusione sperimentale *Tokamak à configuration variable* (TCV), è uno dei membri attivi della ricerca sperimentale e teorica nel campo della fisica dei plasmi fusionistici. Il Tokamak è uno dei candidati più promettenti per lo sviluppo di un reattore a fusione. All'interno del Tokamak, un plasma ad altissima temperatura viene confinato sotto forma di toro grazie alla combinazione di campi magnetici toroidali e poloidali. La principale caratteristica di TCV sta nella forma della camera a vuoto che ospita il plasma, la cui altezza è tre volte maggiore della larghezza. Questo, grazie all'uso di 16 bobine per la produzione di campi magnetici poloidali, permette un'estrema flessibilità nella definizione della forma del plasma, caratteristica unica tra i Tokamak attualmente operativi. Lo studio degli effetti della forma del plasma sulla stabilità e le prestazioni del reattore, tra cui il confinamento dell'energia, è tra i principali obiettivi di TCV. Il confinamento dell'energia e delle particelle all'interno del plasma è, infatti, essenziale per ottenere un bilancio netto di energia prodotta nei futuri reattori. Tuttavia, fenomeni di trasporto indotti dalle collisioni tra le particelle e da fenomeni turbolenti, presenti naturalmente nel plasma a causa dei gradienti di temperatura che si sviluppano tra il plasma caldo e denso del nucleo e quello più freddo e rarefatto al bordo, riducono inevitabilmente il confinamento.

Questo lavoro presenta un ampio studio del trasporto di impurezze nel tokamak TCV, realizzato attraverso i sistemi di spettroscopia CXRS (Charge eXchange Recombination Spectroscopy). La diagnostica CXRS utilizza la reazione di scambio di carica tra gli ioni carbonio, naturalmente presenti in TCV date le pareti interne ricoperte di grafite, e le particelle neutre immesse dall'esterno attraverso un iniettore diagnostico di fasci neutri a bassa potenza (DNBI). Il DNBI, a differenza degli iniettori normalmente utilizzati per il riscaldamento del plasma, è stato sviluppato con il solo scopo di fornire neutri per la reazione di scambio di carica. Di conseguenza, la sua geometria, così come la potenza immessa, sono state ottimizzate in modo da minimizzare le perturbazioni indotte nel plasma mantenendo, allo stesso tempo, un'alta penetrazione del fascio, al fine di avere un numero sufficiente di reazioni di scambio di carica anche nella regione più interna del tokamak. Le particelle neutre vengono immesse con un'energia tale da massimizzare la probabilità di osservare la linea di emissione del C a 529.1 nm. Il DNBI, essendo un fascio non perturbativo, fornisce un ambiente ottimale per lo

studio della rotazione intrinseca del plasma, ovvero non indotta dall'esterno.

Due sistemi CXRS addizionali sono stati sviluppati e utilizzati con successo nelle operazioni sperimentali durante questa tesi. Questi spettrometri sfruttano la reazione di scambio di carica tra gli ioni C del plasma e le particelle neutre immesse dai due iniettori ad alta potenza di TCV, regolarmente utilizzati per il riscaldamento del plasma. Per la prima volta in TCV, misure affidabili della temperatura ionica sono state effettuate in plasmi ad alta potenza (H-mode) in presenza di ELM, dove normalmente il segnale passivo dei sistemi installati sul DNBI è eccessivamente perturbato, compromettendo irrimediabilmente le misure. L'alta densità dei fasci NBI permette di ottenere un segnale di CXRS attivo molto più alto rispetto ai sistemi DNBI. Di conseguenza, tali spettrometri sono stati utilizzati, ancora per la prima volta, per realizzare misure di impurezze diverse dal carbonio, aprendo alla possibilità di misurare contemporaneamente impurezze multiple (C, B, N, O).

Un'ampia parte di questa tesi è stata dedicata allo studio delle correlazioni tra la transizione da confinamento ohmico lineare a confinamento omico saturo (LOC-SOC) e l'inversione della rotazione toroidale, due fenomeni che spesso avvengono a una densità critica che, in casi specifici, sembra essere la stessa. Dato che larga parte degli studi pubblicati in passato è stata effettuata su plasmi a maggioranza di deuterio, una serie di esperimenti è stata sviluppata per ampliare gli scenari precedentemente studiati a plasmi a maggioranza di idrogeno ed elio. I risultati presentati in questa tesi mostrano una chiara separazione tra i due fenomeni nei plasmi di D e di He. Curiosamente, l'inversione della rotazione toroidale non è stata osservata nei plasmi di H, nonostante una chiara transizione LOC-SOC.

Durante questi esperimenti, una forte correlazione tra i gradienti di rotazione toroidale e quelli di densità è stata evidenziata, in accordo con numerosi modelli teorici precedentemente pubblicati [6] [89]. Forti variazioni nella turbolenza del plasma sono necessarie per spiegare i cambiamenti di densità osservati che, a loro volta, tendono a indurre variazioni nella rotazione toroidale. La stabilizzazione (o destabilizzazione) dei modi turbolenti sembra giocare un ruolo fondamentale per la spiegazione dell'inversione di rotazione. La frequenza di accrescimento dei TEM (Trapped Electron Modes), instabilità dominante nei plasmi a bassa densità, aumenta in modo inversamente proporzionale alla massa degli ioni [190] [163]. Di conseguenza, è plausibile che la stabilizzazione dei TEM attraverso il cosiddetto "detrapping" collisionale, spesso osservata durante le rampe di densità, sia meno efficace nei plasmi di H, riducendo l'effetto perturbativo sui profili di densità e, possibilmente, spiegando l'assenza dell'inversione di rotazione. Per investigare ulteriormente l'effetto dei gradienti di densità, un fascio di microonde (ECRH) è stato iniettato in un plasma di H, successivamente replicato in D, per indurre con successo l'inversione di rotazione toroidale. Questo ha mostrato, ancora una volta, la forte correlazione tra i gradienti di densità e quelli di rotazione.

L'estrema flessibilità di TCV nel realizzare le più disparate forme di plasma è stata sfruttata per studiare il trasporto di impurezze in plasmi a triangularità negativa. Il trasporto delle impurezze leggere, come il carbonio, sembra essere dominato da fenomeni turbolenti. Il

flusso turbolento viene descritto da una combinazione di termini di convezione e diffusione [2] ed evolve secondo l'interazione tra i gradienti di temperatura, densità e velocità dei ioni. Un metodo pratico per studiare il trasporto turbolento sta nel ricercare le possibili correlazioni tra questi gradienti le quali, in questa tesi, hanno evidenziato differenze sostanziali tra triangolarità positiva e negativa. Numerose scariche di plasma sono state effettuate all'interno di un ampio intervallo di  $\delta$  ( $-0.6 < \delta < +0.6$ ), senza mostrare alcuna correlazione tra i gradienti dei profili ionici a triangolarità positiva. I plasmi a triangolarità negativa, invece, hanno evidenziato una relazione lineare tra  $\nabla T_i$  e  $\nabla n_C$ , e  $\nabla v_{tor}$  e  $\nabla n_C$ , suggerendo che il trasporto a  $\delta < 0$  è dominato dai gradienti di temperatura e velocità toroidale. Una possibile spiegazione di questo fenomeno può essere legata alla riduzione della turbolenza e alla stabilizzazione dei TEM a triangolarità negativa [125] [65]. Inoltre, questo potrebbe anche spiegare per quale motivo l'inversione di rotazione non è stata osservata a  $\delta < 0$  dove, contrariamente a quanto accade a triangolarità positiva, la stabilizzazione dei TEM è accompagnata da un aumento della diluzione degli ioni principali con la densità. Conseguentemente, gli ITG (Ion Temperature Gradients) vengono stabilizzati e i TEM restano i modi turbolenti dominanti, riducendo così gli effetti sui profili di densità che sembrano indurre le variazioni di rotazione osservate a triangolarità positiva.





# Résumé

La réalisation de la fusion nucléaire contrôlée est l'un des objectifs principaux, dans la recherche de la physique du plasma dans le but ultime de développer des réacteurs fiables pour la production d'énergie à grande échelle. Le SPC (Swiss Plasma Center), centre de recherche affilié à l'école Polytechnique Fédérale de Lausanne, avec son réacteur à fusion expérimental *Tokamak à configuration variable* (TCV), est l'un des membres actifs de la recherche expérimentale et théorique dans le domaine de la physique des plasmas fusionnistiques. Le Tokamak est l'un des candidats les plus prometteurs pour le développement d'un réacteur à fusion. À l'intérieur du Tokamak, un plasma à très haute température est confiné sous forme de tore grâce à une combinaison de champs magnétiques toroïdaux et poloïdaux. La principale caractéristique de TCV est la forme de sa chambre à vide, dont la hauteur est trois fois supérieure à sa largeur. Ceci, grâce à l'utilisation de 16 bobines pour la production des champs magnétiques poloïdaux, permet une extrême flexibilité dans la définition de la forme du plasma, une caractéristique unique parmi les Tokamaks actuellement actifs. L'étude des effets de la forme du plasma sur la stabilité et les performances du réacteur, y compris le confinement de l'énergie, est l'un des principaux objectifs de TCV. Le confinement de l'énergie et des particules dans le plasma est, en effet, essentiel pour obtenir un bilan positif d'énergie produite dans les futurs réacteurs. Toutefois, les phénomènes de transport induits par les collisions entre les particules et la turbulence, naturellement présents dans le plasma à cause des gradients de température qui se développent entre le plasma chaud et dense du noyau et celui plus froid et raréfié du bord, réduisent inévitablement le confinement.

Cette thèse présente une étude du transport des impuretés dans le Tokamak TCV, réalisé à l'aide de systèmes de spectroscopie CXRS (Charge eXchange Recombination Spectroscopy). Le diagnostic CXRS utilise la réaction d'échange de charge entre les ions de carbone, naturellement présents dans TCV en raison de ses parois internes recouvertes de graphite, et les particules neutres injectées de l'extérieur par un injecteur diagnostique de faisceau neutre à basse puissance (DNBI). Le DNBI, contrairement aux injecteurs normalement utilisés pour chauffer le plasma, a été développé dans le seul but de fournir des particules neutres pour la réaction d'échange de charge. Par conséquent, sa géométrie, ainsi que la puissance qu'il injecte, ont été optimisées pour minimiser les perturbations induites dans le plasma tout en maintenant une pénétration élevée du faisceau afin d'avoir un nombre suffisant de réactions d'échange de charge même dans la région la plus interne du Tokamak. Les particules neutres sont injectées à une énergie qui maximise la probabilité d'observer la ligne d'émission du C

à 529.1 nm. Le DNBI, étant un faisceau non perturbatif, fournit un environnement optimal pour étudier la rotation intrinsèque du plasma, c'est-à-dire la rotation qui n'est pas induite de l'extérieur.

Deux systèmes CXRS additionnels ont été développés et implémentés avec succès dans les opérations expérimentales au cours de cette thèse. Ces spectromètres exploitent la réaction d'échange de charge entre les ions C du plasma et les particules neutres introduites par les deux injecteurs à haute puissance de TCV, qui sont régulièrement utilisés pour le chauffage du plasma. Pour la première fois dans TCV, des mesures fiables de température ionique ont été réalisées dans des plasmas à haute puissance (H-modes) en présence d'ELM, où normalement les signaux passives des systèmes CXRS installés sur le DNBI sont excessivement perturbés, compromettant irrémédiablement les mesures. La haute densité des faisceaux NBI permet d'obtenir un signal CXRS actif bien plus élevé comparé aux systèmes installés sur le DNBI. Par conséquent, ces spectromètres ont été utilisés, toujours pour la première fois, pour effectuer des mesures d'impuretés autres que le carbone, permettant ainsi de mesurer simultanément plusieurs impuretés (C, B, N, O).

Une grande partie de cette thèse a été consacrée à l'étude des corrélations entre la transition LOC-SOC (confinement ohmique linéaire à confinement ohmique saturé) et l'inversion de la rotation toroïdale du plasma, deux phénomènes souvent observés à une densité critique qui, dans des cas spécifiques, semble être la même. Vu qu'une grande partie des études publiées ont été réalisées sur des plasmas à majorité de deutérium, une série d'expériences a été développée pour étendre les scénarios précédemment étudiés à des plasmas en H et He. Les résultats présentés dans cette thèse montrent une séparation évidente entre les deux phénomènes dans les plasmas D et He. Curieusement, l'inversion de la rotation toroïdale n'a pas été observée dans des plasmas en H, malgré une évidente transition LOC-SOC.

Une forte corrélation entre les gradients de la rotation toroïdale et les gradients de la densité a été mise en évidence au cours de ces expériences, en accord avec ses nombreux modèles théoriques précédemment publiés [6] [89]. Des fortes variations dans la turbulence du plasma sont nécessaires pour expliquer les changements de densité observés qui, à leur tour, tendent à induire des variations dans la rotation toroïdale. La stabilisation (ou déstabilisation) des modes turbulents semble jouer un rôle fondamental dans l'explication de l'inversion de la rotation toroïdale. La fréquence de croissance des TEM (Trapped Electron Modes), une instabilité dominante dans les plasmas à faible densité, augmente de façon inversement proportionnelle à la masse des ions [190] [163]. Par conséquent, il est plausible que la stabilisation des TEM à travers le soi-disant "detrapping" collisionnel, souvent observé lors des rampes de densité, soit moins efficace dans les plasmas en H, ce qui réduit l'effet des perturbations sur les profils et explique peut-être l'absence de l'inversion de la rotation. Pour examiner plus en détail l'effet des gradients de densité, un faisceau de microondes (ECRH) a été injecté dans un plasma en H, ensuite reproduit en D, afin d'induire avec succès l'inversion de la rotation toroïdale. Cela a montré, une fois de plus, la forte corrélation entre les gradients de densité et les gradients de rotation.

L'extrême flexibilité de TCV dans la réalisation de formes de plasma les plus variées a été exploitée pour étudier le transport d'impuretés dans des plasmas à triangularité négative. Le transport des impuretés légères, telles que le carbone, semble être dominé par des phénomènes turbulents. Le flux turbulent est décrit par une combinaison de termes de convection et diffusion [2] et évolue en fonction de l'interaction entre les gradients de température, densité et vitesse des ions. Une méthode pratique pour étudier le transport turbulent consiste à rechercher les corrélations entre ces gradients qui, dans cette thèse, ont montré des différences importantes entre triangularité positive et négative. Des nombreuses décharges de plasma ont été effectuées dans une large gamme de  $\delta$  ( $-0.6 < \delta < +0.6$ ), ne montrant aucune corrélation entre les gradients des profils ioniques à triangularité positive. Les plasmas à triangularité négative, en revanche, ont montré une relation linéaire entre  $\nabla T_i$  et  $\nabla n_C$ , et  $\nabla v_{tor}$  et  $\nabla n_C$ , suggérant que le transport à  $\delta < 0$  est dominé par les gradients de température et vitesse toroïdale. Une explication plausible de ce phénomène peut être liée à la réduction de turbulence et à la stabilisation des TEM à triangularité négative [125] [65]. En outre, cela pourrait également expliquer pourquoi l'inversion de la rotation n'a pas été observé à  $\delta < 0$  où, contrairement à ce qui se produit à triangularité positive, la stabilisation des TEM s'accompagne d'une augmentation de la dilution des ions principaux avec la densité. Par conséquent, les ITG (Ion Temperature Gradients) sont stabilisés et les TEM restent les modes turbulents dominants, réduisant ainsi les effets sur les profils de densité qui semblent induire les variations de rotation observées à triangularité positive.



# Contents

<b>Abstract</b>	<b>i</b>
<b>1 Introduction</b>	<b>1</b>
1.1 The ignition problem . . . . .	5
1.2 The Tokamak concept . . . . .	7
1.2.1 Machine design . . . . .	7
1.2.2 Plasma heating . . . . .	10
1.3 The Tokamak à Configuration Variable . . . . .	11
1.3.1 TCV heating systems . . . . .	16
1.3.2 TCV diagnostics . . . . .	19
1.4 Thesis objectives and outline . . . . .	21
<b>2 CXRS diagnostic</b>	<b>25</b>
2.1 Measurement principle . . . . .	25
2.1.1 Density measurements . . . . .	27
2.1.2 Temperature measurements . . . . .	28
2.1.3 Velocity measurements . . . . .	29
2.1.4 Main ions and impurities comparison . . . . .	29
2.2 Hardware . . . . .	30
2.2.1 Input Optical System . . . . .	31
2.2.2 CCD cameras . . . . .	33
2.3 EDGE system . . . . .	38
2.4 Calibration . . . . .	38
2.4.1 Wavelength calibration and tracks alignment . . . . .	38
2.4.2 Absolute calibration and spatial alignment . . . . .	40
2.5 DNBI . . . . .	44
2.6 Passive signal subtraction - DNBI systems . . . . .	48
2.7 NBI-systems . . . . .	50
2.7.1 Main heating beam . . . . .	50
2.7.2 NBI-1 CXRS . . . . .	51
2.7.3 Second neutral beam injector . . . . .	53
2.7.4 NBI-2 CXRS . . . . .	54
2.7.5 Commissioning discharges . . . . .	54

## Contents

---

2.7.6	Passive signal subtraction for NBI systems . . . . .	57
2.8	Impurity content tracking . . . . .	65
2.8.1	C, B, and O tracking during NBI-2 injection . . . . .	65
2.8.2	N tracking in detachment studies . . . . .	69
2.9	ELMy H-modes: comparison between DNBI and NBI-CXRS systems . . . . .	71
2.10	Conclusions . . . . .	75
<b>3</b>	<b>Rotation and particle transport: phenomenology and theoretical background</b>	<b>77</b>
3.1	Plasma rotation and momentum balance equation . . . . .	77
3.1.1	Rotation decomposition . . . . .	79
3.1.2	Momentum transport . . . . .	82
3.2	Radial electric field . . . . .	83
3.3	Sawteeth instability and rotation . . . . .	84
3.3.1	Overview of previous results . . . . .	85
3.4	Light impurity transport . . . . .	88
3.4.1	Classical and Neoclassical transport . . . . .	88
3.4.2	Turbulent flux, ITG and TEM microinstabilities . . . . .	90
3.5	Conclusion . . . . .	92
<b>4</b>	<b>Isotope effect on rotation and confinement</b>	<b>95</b>
4.1	LOC-SOC transition . . . . .	95
4.1.1	TEM-ITG bifurcation . . . . .	96
4.1.2	Isotope effect on the LOC-SOC transition . . . . .	97
4.2	Intrinsic rotation reversal . . . . .	100
4.2.1	Rotation reversal in deuterium plasmas . . . . .	101
4.2.2	Rotation reversal in hydrogen plasmas . . . . .	104
4.2.3	Rotation reversal in helium plasmas . . . . .	104
4.3	Effect of Sawteeth activity on rotation . . . . .	108
4.3.1	q-threshold for rotation reversal . . . . .	109
4.4	Effect of density peaking . . . . .	113
4.4.1	Density peaking in D plasma . . . . .	114
4.4.2	Density peaking in He plasma . . . . .	116
4.4.3	Density peaking in H plasma . . . . .	116
4.5	Diverted configuration . . . . .	129
4.6	Linear gyrokinetic simulations . . . . .	132
4.7	Discussion and conclusions . . . . .	134
<b>5</b>	<b>Impurity transport in negative triangularity</b>	<b>141</b>
5.1	Negative triangularity . . . . .	142
5.1.1	Triangularity scan in limited configuration . . . . .	143
5.1.2	External torque injection through Neutral Beam . . . . .	148
5.1.3	Triangularity scan in diverted configurations . . . . .	156
5.1.4	LOC/SOC transition in negative triangularity . . . . .	157

5.2 Discussion and conclusions . . . . .	159
<b>6 Conclusions and outlook</b>	<b>169</b>
<b>Acknowledgements</b>	<b>173</b>
<b>Bibliography</b>	<b>175</b>
<b>Bibliography</b>	<b>191</b>





# 1 Introduction

The fast, global increase of population, followed by the raising standards of living, led to a continually growing demand for energy over the past century. Most of our available energy sources are finite and give rise to pollution, making it necessary to find other solutions with lower impact on the environment. Controlled nuclear fusion aims to deliver clean and efficient energy. Fuel resources are accessible all over the planet, the production process can be made inherently safe and it does not give rise to long duration nuclear waste, as is the case for fission plants.

Starting from the experiments of Ernest Rutherford on nuclei, Mark Oliphant obtained the first intentional fusion reaction between two heavy hydrogen isotopes in 1932. During those years, Hans Bethe studied the phases of the nuclear reactions taking place in stars, but it was only after World War II, approximately in 1950, that thermonuclear fusion became the main topic of research programs. The first reactors that could approach fusion conditions, called tokamaks, were built during the 1960s. The word tokamak is a Russian acronym meaning "toroidal chamber with magnetic coils". Its aim is to confine an ionised gas (a plasma) by means of electromagnetic fields [187]. The goal is to generate heat from the same reactions that occur inside stars and, nowadays, this research still continues to evolve, having achieved unpredicted and, to this author, optimistic results.

Two projects, ITER [95] and the National Ignition Facility [136], are currently working on providing the next steps for a reliable source of energy from fusion. After 60 years of research and technology development, their goal is to produce fusion energy by 2050. Other devices, like the ARC (Affordable, Robust, Compact) fusion reactor in the US [8] [45] or STEP (Spherical Tokamak for Energy Production) in the UK [167] [40] [189], have a more aggressive schedule, aiming at producing net electricity from fusion energy by 2030 and 2040, respectively. However, showing a working fusion reaction is not necessarily the same as providing stable and robust power to the electrical grid for large periods of time that, in the end, should be the ultimate goal of future fusion power plants.

In the '70s, the most advanced European laboratories that studied physics of fusion united, creating a collaboration to build JET (Joint European Torus [98]). From then, many other laboratories joined in the collaborations and other fusion research facilities were built. In 1999

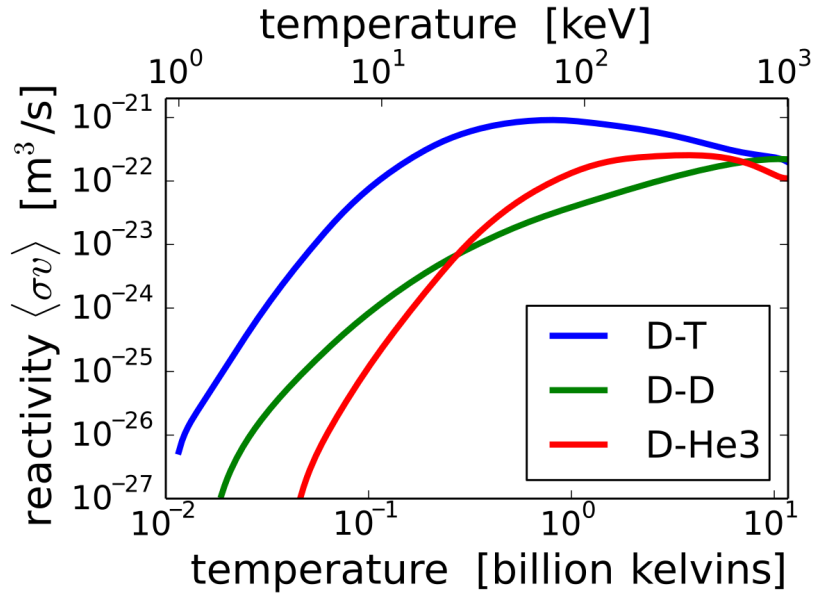


Figure 1.1 – Medium cross sections for the following reactions: deuterium-deuterium (D-D), deuterium-tritium (D-T), deuterium-helium-3 ( $\text{D-}^3\text{He}$ ).

the EFDA (European Fusion Development Agreement) was signed, in order to improve the collaboration. On 9 October 2014, the European commission officially developed the consortium EUROfusion, which has the task of handling fusion research for Euratom, the European Atomic Energy Community (also known as EAEC). Nowadays it collaborates with worldwide organisations to develop a fusion reactor, ITER, a project that involves Europe, China, South Korea, India, Japan, Russia and USA. Switzerland, with its Tokamak TCV (Tokamak à Configuration Variable), which began operations in 1992, is an active member of this undertaking and, as other participating countries, follows EUROfusion leadership and guidance to design its experiments.

Even though nuclear fusion is a demanding task on Earth, it is the only source of energy of the universe. In the Sun, as in the other stars, hydrogen nuclei fuse and release enormous quantities of energy. The Sun can be seen as a huge fusion reactor that holds the reacting plasma together by gravitational force. It fuses light nuclei into heavier elements and releases energy according to the formula  $E = mc^2$ , as the heavier fused atoms have less mass than the initial fuel.

The candidates to fuel fusion reactions on Earth are many. The reaction between hydrogen isotopes deuterium ( $^2\text{H}$  or D) and tritium ( $^3\text{H}$  or T) has the largest cross-section at the lowest temperature, as Figure 1.1 shows.

This makes the D-T process



the most accessible reaction.

In the pursuit of a sustainable energy producing system, the fusion fuel also has to be sufficiently abundant. Deuterium occurs in nature with a weight fraction of  $3.3 \times 10^{-5}$  in water, thus the fuel is abundant and accessible in the long term in the oceans. Tritium instead is a radioactive isotope of hydrogen, with a half-life of 12.3 years. It decays to  ${}^3\text{He}$  in the following way

$$T \rightarrow {}^3\text{He} + e^- + \bar{\nu}_e$$

Due to this lifetime, no significant amount of tritium exists in nature. Therefore, it has to be produced using nuclear reactions where the most self sustaining path will be to use neutrons from the D-T reaction and lithium:

$$n + {}^6\text{Li} \rightarrow {}^4\text{He} + T + 4.8 \text{ MeV}$$

$$n + {}^7\text{Li} + 2.5 \text{ MeV} \rightarrow {}^4\text{He} + T + n$$

Two colliding nuclei repel each other due to their same-sign charge. To fuse, this electrostatic potential must be overcome, until they are brought very close to each other, in a range of the order of  $10^{-15}$  m. At this distance, the attractive, and considerably stronger, nuclear force is sufficient to overcome the Coulomb repulsion. The gravitational field that keeps stars together also compresses their cores, where, consequently, enormous density is achieved. Here again, the nuclei are brought close together allowing for the fusion reactions to occur. Inside a Tokamak, fusion conditions are achieved thanks to a combination of high plasma temperature and density. Density is limited in tokamaks by a so-called "density limit", a critical value above which plasma heat and current are rapidly lost. Therefore, the fuel temperature must be extremely high (on the order of 100 million degrees, 10 times higher than the core of the Sun) to compensate for the limited density. It has to be mentioned that this is the specific case of tokamaks as, for instance, the previously mentioned NIF experiment aims at reaching similar fusion conditions by compressing a pellet of fuel to extremely high density, thus requiring lower temperatures compared to tokamaks. At these temperatures, the thermal collisions ionise the atoms since the chemical bond energy is overcome by the free collisional energy and a plasma is formed [38].

Ideally, in a Tokamak, the electron density  $n_e$  and the electron temperature  $T_e$  of fusion reactors plasmas are  $n_e \sim 10^{20} \text{ m}^{-3}$  and  $T_e \sim 10 \text{ keV}$ , depending on the machine size and power resources [66]. At such temperatures, thermal energy dominates over Coulomb energy

$$E_{\text{coul}} = \frac{e^2}{4\pi\epsilon_0} n_e^{\frac{1}{3}} \quad (1.1)$$

## Introduction

---

Electric fields are shielded by the displacement of other charges inside a plasma. Therefore, charge perturbations are relevant on spatial scales below the so-called Debye length

$$\lambda_D \simeq \sqrt{\frac{\epsilon_0 k T_e}{n_e q_e^2}} \quad (1.2)$$

The number of electrons in a sphere of radius  $\lambda_D$  is

$$N_D = \frac{4}{3} \pi n_e \lambda_D^3 \quad (1.3)$$

and in a plasma  $N_D \ll 1$ . The high mobility of electrons, and the consequent shielding of any electric field outside the Debye sphere, generate a condition of quasi-neutrality, expressed by

$$\frac{n_e - \sum_i Z_i n_i}{n_e} \ll 1 \quad (1.4)$$

which is usually attained within  $10^{-6}$ . The typical time response of electrons to perturbations is given by the plasma frequency

$$\omega_p = \sqrt{\frac{n_e e^2}{m_e \epsilon_0}} \quad (1.5)$$

Plasma oscillations are only observed if the system is studied over a time period longer than the plasma oscillation period  $\tau_p = \frac{1}{\omega_p}$ , which is the temporal equivalent of the Debye length. If external actions change the system faster than  $\omega_p$ , no plasma behaviour can be observed. In summary, the plasma state is defined by the following conditions:

$$\lambda_D \ll L \quad (1.6)$$

$$N_D \ll 1 \quad (1.7)$$

$$\omega_p \tau_n > 1 \quad (1.8)$$

where  $L$  is the plasma size and  $\tau_n$  the electron-neutral collision time.

The aim of fusion research is to create a burning plasma, that is a plasma in which most of the fusion energy and plasma heating comes from fusion reactions involving thermal ions. The final goal is to build a plasma driven power plant that produces more electrical power than it consumes, including the power necessary to heat and sustain the plasma. Ideally, a self-sustaining discharge would be the most efficient way to achieve this goal, as the rate of energy produced by fusion reactions is sufficiently high to heat the surrounding fuel rapidly enough to maintain the temperature against losses to the environment [118]. Until the time of writing, it has proven difficult to confine the plasma well enough to make fusion a reliable energy source. Research is then focused on plasma control and confinement, so that the reactor can ignite. Mastering control techniques, understanding the plasma behaviour, as well as its instabilities, and being able to suppress them is the great challenge of Tokamak physics.

The reward will be a clean and long term energy source.

## 1.1 The ignition problem

The reaction between deuterium and tritium has been identified as the most efficient for tokamak devices [95], as it has the largest cross-section that is peaked at a lower temperature compared to the other hydrogen isotopic reactions [187]. As shown in Figure 1.1, the reaction rate of the D-T reaction reaches its peak for temperatures of the order of 70keV, which would require a very low density, not attainable in present devices that need to operate at  $n_e \propto 10^{20} m^{-3}$  for heating purposes. However, other plasma parameters than temperature can be tuned and, through their optimisation, lower temperatures are sufficient to attain fusion.

Ignition is a self-sustained reaction that maintains plasma through its own fusion power. The Lawson criterion shows that such a threshold does not depend solely on temperature, but a combination of three major plasma parameters: temperature, density and confinement time. The Lawson criterion is a figure of merit employed to characterise the performance of a device. It is derived from a simple power balance equation and it is expressed by the "triple product" [104], which states that the product between density  $n$ , temperature  $T$  and confinement time  $\tau_E$  needs to surpass a value that depends on the reaction rate  $\langle \sigma v \rangle$  and the energy per reaction  $E_f$ :

$$n\tau_E T \geq \frac{12k_b}{E_f} \frac{T^2}{\langle \sigma v \rangle} \quad (1.9)$$

The confinement time is defined as the ratio between the plasma energy  $W$  and the injected power  $P_{heat}$ , *i.e.* the average duration that energy remains within the plasma. Considering that any tokamak has an upper operational limit for the pressure ( $p = nT$ ), the access to ignition is optimised when the quantity  $\frac{T^2}{\langle \sigma v \rangle}$  is minimised. For the D-T reaction this translates into  $n\tau_E T \geq 3 \cdot 10^{21} \frac{keVs}{m^3}$ .

At a density of  $10^{20} m^{-3}$  and a confinement time of 1 s, the temperature at which ignition would be attained is  $\sim 10$  keV.

However, these three quantities are coupled to each other: injecting gas to increase the density cools the plasma. At the same time, raising the temperature often results in confinement degradation, particularly when auxiliary heating, often required to increase the plasma temperature above 1 keV, is employed. An exception to this systemic degradation is given by magnetically confined plasmas self-reorganising and transiting to a high confinement mode (H-mode), where confinement improves for a given injected power threshold by around a factor of two with respect to the pre H-mode, low confinement mode (L-mode). H-mode operation is, however, often characterised by quasi-periodic disruptive relaxations occurring at the plasma edge (where most of the improved confinement's effects occur), the so-called edge localised modes (ELM). These represent a major threat for the device integrity, since the relaxation is short lived but powerful, such that the heat flux can damage the machine vessel. Moreover, H-mode is often accompanied by impurity accumulation [181] [105], increasing the ion dilution, with detrimental effects for plasma stability [2].

An improved confinement regime, I-mode, could possibly solve the issues raised for H-mode. I-mode discharges feature H-mode like confinement levels in an ELM-free plasma [183]. The edge energy transport barrier that forms during I-mode is not accompanied by a density barrier [188]. Therefore, similar to L-mode, particle confinement is reduced, avoiding core impurity accumulation [108].

Other ELM-free regimes include a "stationary ELM-free H-mode" studied at AUG [173] that, similar to the "quiescent H-mode" and "edge harmonic oscillation" found in the DIII-D tokamak [28], showed ELM-free H-mode operation with good density control. ELM-suppression techniques, achieved by pellet injection, were developed to obtain ELM-free scenarios [179]. H-mode regimes with small ELMs were also explored (*e.g.* in JET [70]), showing high thermal confinement and low core impurity accumulation. More recently, negative triangularity appeared to offer H-mode like confinement without the formation of an edge barrier and, thus, no ELMs [42] [113]. This scenario is further described in chapter 5. Only the future will know whether other self-forming transport barriers that improve confinement, and the triple product, will appear. It is to be noted that the gradients, collisionality, connection lengths and, above all, alpha particle dominated plasma heating of reactor development experiments such as ITER remain, at this date, to be explored.

The ratio  $Q$  between the produced fusion power and the power needed for steady operation is called fusion energy gain factor:

$$Q = \frac{P_{fus}}{P_{heat}} \quad (1.10)$$

Ignition is not strictly necessary for a reactor to operate. The condition  $Q = 1$  is called breakeven and it is the threshold at which a reactor starts producing more energy than that required to maintain the plasma (often called "scientific breakeven"). This value, realistically, must be higher still to compensate for inefficiencies in the reactor performance (power supplies, etc.), for which an "engineering  $Q$ " can be defined.

As of 2021, the record for the highest  $Q$  is held by the National Ignition Facility in the US, at scientific  $Q = (1.35 \text{ MW}) / (1.9 \text{ MW}) \sim 0.70$ , first attained in August 2021 [41]. The highest value of scientific  $Q$  in a tokamak device, instead, was reached by the JET (Joint European Tokamak [145] [102]) device ( $Q = 0.65$ ) in 1998.

The challenge of future devices is to reach and surpass breakeven, which is expected to be achieved mainly by improving confinement time, by increasing machine size and magnetic field. This is why the design of next-generation machines concentrates on bigger, but more costly devices, such as ITER (International Thermonuclear Experimental Reactor [93]), currently in construction at Cadarache in France. Operation in H-mode is also envisioned, with the strict requirement that ELMs must be mitigated or, better still, suppressed.

Other devices, such as SPARC (as Soon as Possible ARC) [8], aim at reaching breakeven with compact, and thus less costly, machines. SPARC will exploit YBCO (yttrium barium copper oxide) high temperature superconducting magnets, that can retain superconductivity at temperatures as high as 77 K. This device is expected to yield a  $Q \geq 2$ , but it is projected to reach  $Q$

~ 11 [45].

However, although these results are promising, breakeven (scientific and then engineering) will still remain to be translated into a working, closed cycle reactor.

## 1.2 The Tokamak concept

A *Tokamak* (from the russian "TOroidal'naya KAmera s MAgnitnymi Katushkami - toroidal chamber with magnetic coils") is a device that uses strong magnetic fields to confine hot plasma into a toroidal shape [187].

The Tokamak is one of several types of magnetic confinement devices developed to house the hot plasma needed to produce thermonuclear reactions and fusion power. It employs external coils, but crucially, fields generated internally through high currents within the plasma to confine the plasma. Today, it is the leading candidate for a practical fusion reactor, followed by the *Stellarator* configuration, which confines plasma in a shape similar to a Moebius strip using external fields alone. Magnetic fields are used, since no existing material can withstand the extremely high temperature that can be attained through contact with a plasma. Charged particles, in the absence of other forces, will follow the imposed magnetic field lines that are organised so as to not intercept the surrounding machine vessel.

The world's largest Tokamak project is ITER (International Thermonuclear Experimental Reactor), currently under construction in Saint-Paul-lès-Durance, in southern France. Scheduled to begin operation in 2025, ITER is expected to produce an output power of 500 MW and approach ignition by 2035, when D-T operations will start, demonstrating, for the first time, majority plasma self-heating.

### 1.2.1 Machine design

Generally, a mixture of gaseous deuterium and tritium is used to produce plasma. When this mixture reaches the plasma state, it is completely ionised and so it is fully confined by external electromagnetic fields from the Lorentz force. Magnetic fields are generally divided into three groups: a toroidal one, externally induced, and a poloidal one, generated by inducing a current in the plasma itself (Figure 1.2). Finally, a vertical field, also generated via external magnetic coils, allows for control of plasma position inside the torus. It is employed to compensate vertical drifts and prevent the plasma from interacting with the machine vessel.

The toroidal field is generated by toroidal coils, creating a magnetic field which runs around the torus axis of symmetry, albeit with a stronger field where the coils are close (internal, High Field Side). Therefore, charged particles can flow freely, and hypothetically endlessly, around the machine. The principle is simple. Electrons and ions, being charged particles, follow a certain helicoidal trajectory defined by Larmor's law, which defines its radius too:

$$\rho_L = \frac{mv_{\perp}}{ZeB} \quad (1.11)$$

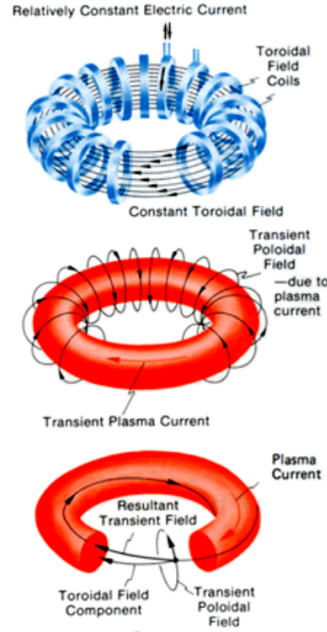


Figure 1.2 – Tokamak magnetic fields and current.

where  $v_{\perp}$  is the particle velocity perpendicular to the magnetic field,  $m$  is its mass,  $B$  the magnetic field intensity and  $Ze$  the ion charge. Since a charged particle can not drift away more than  $\rho$  from the field line, a magnetic field is sufficient to confine a plasma. This is formalised by Alfvén theorem. In this frame, the toroidal field constrains moving particles into ring shaped lines.

However, this simple field is not sufficient to optimally confine the plasma. In fact, field gradients created by different intensity or curvature lead to drift motions with respect to the field lines. Magnetic drift is of the order

$$\frac{v_{grad}}{v_{\perp}} \simeq \frac{\rho}{R} \quad (1.12)$$

where  $R$  is the major torus radius.

Even if  $\rho$  is small, particles velocity, due to the very high temperature reached during fusion experiments ( $T = 1 \text{ keV}$ ), can be really high (order  $10^2 \frac{\text{km}}{\text{s}}$ ). Charged particles make a large number of turns around the torus during a plasma discharge and will drift to the vessel walls. The solution is to introduce another component of the magnetic field, perpendicular to the toroidal field, in order to rotate the field lines to obtain a helicoidal magnetic field shape [84]. This is a poloidal field. Now, this drift velocity points alternatively to the inner and on the outer side of the surface, and averages to zero.

In a tokamak, this poloidal field is produced by a current flowing in the hot plasma that, initially, also serves to heat the plasma through plasma electrical resistivity. In fact, if we regard plasma as formed by many current carrying wires, the current flowing into them undergoes an attractive Lorentz force. One confinement strategy, called the Z-pinch, used this strategy in



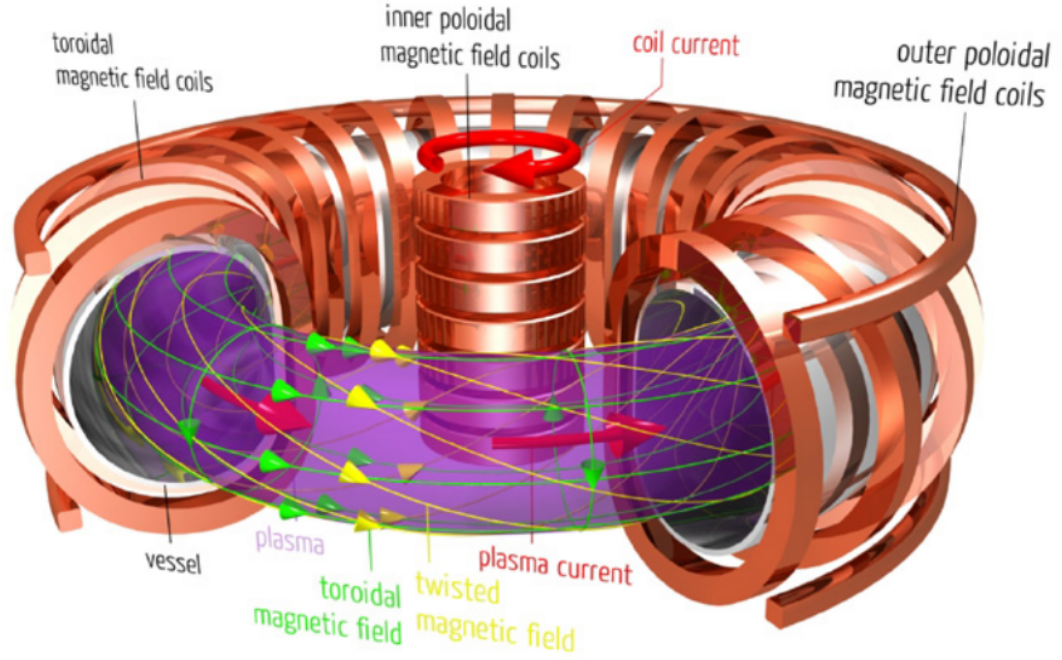


Figure 1.3 – Tokamak scheme, with currents, fields shape, coils and magnets.

early confinement schemes. In present-day Tokamaks the poloidal field is a combination of Z-pinch and  $\phi$ -pinch.

In a Z-pinch,  $J_\phi = B_z = 0$ . In this configuration the equilibrium equation for pressure is

$$\frac{dP}{dr} = -\frac{1}{4\pi} \frac{B_\phi}{r} \frac{\partial(rB_\phi)}{\partial r} \quad (1.13)$$

Note that, integrating it and considering that  $B_\phi = \frac{2}{c} \frac{I}{r}$ , we obtain

$$F_P = \int_0^a 2\pi r P(r) dr = \frac{1}{c^2} J^2(a) \quad (1.14)$$

where  $a$  is the border of the torus surrounding the plasma. This shows that equilibrium is achieved by the current flowing in the cylinder: the higher it is, the higher the confinement.

In  $\phi$ -pinch  $J_z = B_\phi = 0$ . Here the equation is

$$\frac{dP}{dr} = -\frac{1}{4\pi} B_z \frac{\partial B_z}{\partial r} = \frac{dP_z^{(m)}}{dr} \quad (1.15)$$

The last term is called magnetic pressure. This equation can be written in the following way, taking into account that  $B_z$  is zero at  $r = 0$  (by symmetry) and  $P(r) = 0$  both at the origin and at the edge ( $r = a$ ),

$$P(r) + \frac{1}{8\pi} B_z^2(r) = \frac{1}{8\pi} B_z^2(a) \quad (1.16)$$

## Introduction

---

This means that the equilibrium, in  $\phi$ -pinch, is achieved by the axial (vertical) field, particularly by its border value.

The combination of these two can be summarised by the equilibrium equation for pressure

$$\frac{\partial P}{\partial r} = -\frac{1}{4\pi} B_z \frac{\partial B_z}{\partial r} - \frac{1}{4\pi} \frac{B_\phi}{r} \frac{\partial(r B_\phi)}{\partial r} \quad (1.17)$$

where the first term on the right is the  $\phi$ -pinch equilibrium equation and the last term the Z-pinch.

It can be integrated, as before, from  $r = 0$  to  $r = a$  obtaining

$$\langle P \rangle = \frac{F_P}{\pi a^2} = \frac{1}{8\pi} [B_z^2(a) + B_\phi^2(a) - \langle B_z^2 \rangle] \quad (1.18)$$

Note that  $B_\phi$  represents a free parameter to control equilibrium, since  $B_\phi$  appears just with its edge value and is set by changing the current flowing in the field coils.

The concept of plasma pressure will be recalled in chapter 3, where plasma toroidal and poloidal rotation components in a Tokamak will be derived from a force balance equation.

### 1.2.2 Plasma heating

In an operating fusion reactor, part of the energy generated is needed to maintain plasma temperature by compensating the exhausted fluxes. During plasma initiation, plasma must be heated in order to reach a working temperature greater than 10 keV (over  $10 \times 10^7$  °C). This starts by the ohmic heating, when a current passes through the plasma, and then by so called additional methods, that are neutral beam injection, magnetic compression and radio frequency absorption. Note, however, that modern Tokamaks still do not produce sufficient energy to maintain operating temperatures, so all these methods are still being considered and researched to obtain, and possibly maintain, the working conditions on ITER.

#### Ohmic heating

The induced toroidal current not only provides the tokamak poloidal field but also heats the plasma that retains finite resistivity. An electromagnetic winding is linked with the torus, so the plasma gets heated by slowly increasing the current flowing within it. This is, by nature, a pulsed process, because there is a limit to the current flowing in the external coil. This current has to increase to provide the magnetic flux change driving the resistive plasma current and instabilities can arise for high current densities within the plasma. Moreover, plasma resistance decreases as temperature rises ( $\rho \sim T^{-\frac{3}{2}}$ ) so, above a certain temperature, ohmic heating becomes too inefficient for plasma heating and must be supported by other methods, although a plasma current must be maintained to preserve the Tokamak's magnetic configuration. Usually, the maximum plasma temperature attainable by ohmic heating is  $T_e \leq 1$  keV, with some exceptions like C-Mod, where  $T_e \leq 3$  keV was reached [172] [68].

#### Neutral beam injection

Neutral beam injection consists in the injection of high energy neutral atoms into a pre-heated plasma. The fast neutrals are first generated as ions in an arc or RF chamber and are extracted into a high voltage accelerating grid set. The extracted fast ions then travel through a neutraliser section of the beamline where they are neutralised through charge exchange reactions without losing their kinetic energy gained from the ion acceleration. The remaining ions are deflected by magnetic fields, such that only neutral particles reach the vessel, since charge particles cannot penetrate the Tokamak's magnetic field structure. As these neutral atoms enter the Tokamak, they interact with plasma ions through collisions, ionise, and then form part of the plasma where they are then confined and can deposit more of their kinetic energy, further heating the plasma.

Deuterium is often the primary fuel for neutral beam heating but it should be noted that fusion reactions generated directly from these fast ions are not the primary source of fusion energy that is generated Thermo-Nuclearly, *i.e.* within the heated plasma bulk. Hydrogen, helium and tritium [99] are sometimes used for selected experiments.

#### Radio frequency heating

Oscillators, like gyrotrons or klystrons, are employed to generate high frequency electromagnetic waves that are directed towards the preheated (hot) plasma. If the waves have a certain frequency and polarisation, their energy can be transferred to the charged particles that gain kinetic energy and in turn collide with other plasma particles, thus heating the bulk plasma. There are many methods of radio frequency heating, like ECRH (Electron Cyclotron Resonance Heating), ICRH (Ion Cyclotron Resonance Heating) and LHCD (Lower Hybrid Current Drive), corresponding to resonances in the plasma due to the confinement magnetic field or internal plasma resonances. Figure 1.4 shows two types of antennas positioned on the inner vessel wall of Tore Supra Tokamak, used to direct high frequency electromagnetic waves to the plasma. It is of note that, by introducing some toroidal asymmetry in these power distributions, toroidal plasma current can be induced that supplements the Ohmic Current that can allow the plasma pulse to last longer (Current Drive).

### 1.3 The Tokamak à Configuration Variable

The experimental work presented in this thesis was developed and performed at the SPC (Swiss Plasma Center) on the TCV Tokamak (Tokamak à Configuration Variable).

TCV is a medium size tokamak designed to deliver a great flexibility in terms of plasma shaping [88]. The vacuum vessel is highly elongated (1.5 m height, 0.5 m width). Although TCV is capable of creating plasmas in diverted configuration, *i.e.* a magnetic field configuration in which the toroidally confined plasma region is separated from the wall by a separatrix (Figure 1.5), it is not equipped with a dedicated divertor chamber. The divertor targets are designed to withstand high heat loads. This peculiar configuration is achieved by generating one or more

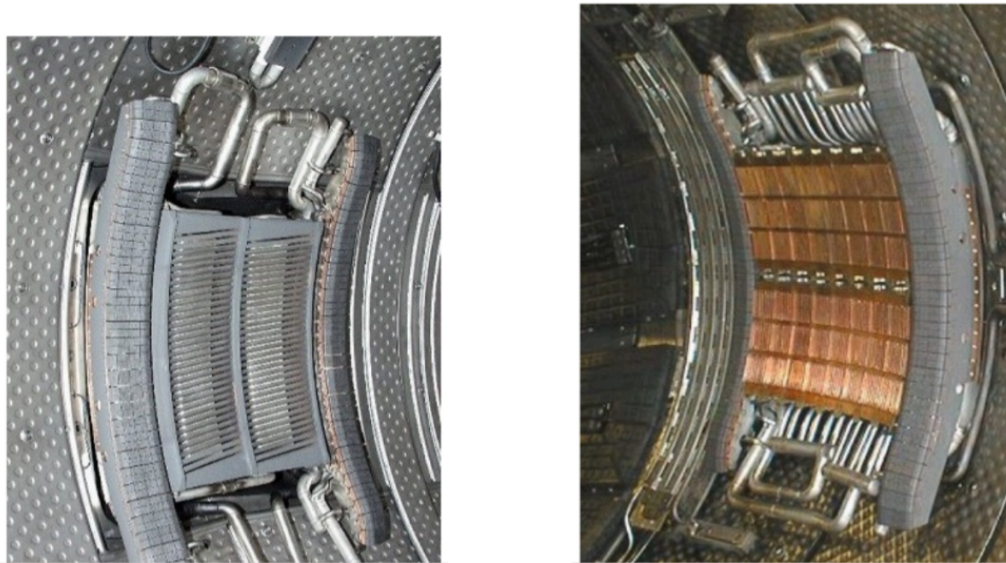


Figure 1.4 – Plasma heating antennas. On the left, Tore Supra ICRH antenna, Cadarache. On the right, Tore Supra LH antenna.

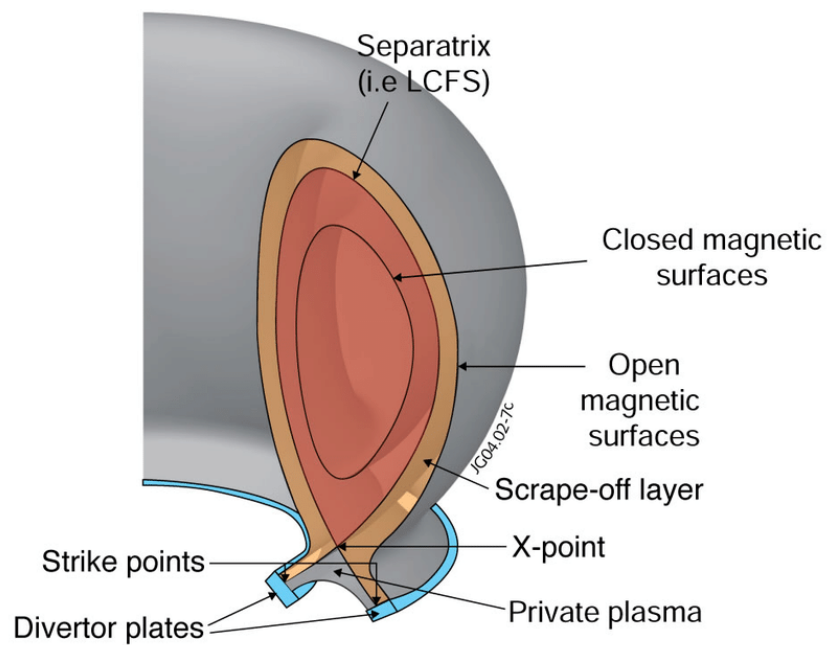


Figure 1.5 – Schematic view of a plasma diverted configuration [178].

### 1.3. The Tokamak à Configuration Variable

Table 1.1 – Main TCV technical specifications and plasma parameters.

Parameter	Symbol	Value
Major radius	$R_0$	0.88 m
Minor radius	$a$	0.255 m
Aspect ratio	$\frac{1}{\epsilon} = \frac{R_0}{a}$	$\leq 3.5$
Vessel height	$h$	1.54 m
Vessel elongation	$\kappa_{TCV}$	3
Vessel base vacuum	$\rho_{TCV}$	$10^{-7}$ mbar
Vessel time constant	$\tau_{TCV}$	6.7 ms
Toroidal field on axis	$B_0$	1.54 T
Loop voltage	$V_{loop}$	1-2 V
Plasma current	$I_p$	1 MA
Installed Power	$P_{TCV}$	200 MW
Ohmic Heating Power	$P_{OH}$	1 MW
NBH heating	$P_{NBH}$	1 MW
ECRH X2 heating	$P_{X2}$	2.8 MW
ECRH X3 heating	$P_{X3}$	1.4 MW
Plasma species	10 Mg	D (He, H)
Main impurities	10 Mg	C, B
Plasma elongation	$\kappa_a$	0.9-2.8
Plasma triangularity	$\delta_a$	-0.8 + 0.9
Electron density	$n_e$	$leq 2 \times 10^{20} \text{ m}^{-3}$
Electron temperature (OH)	$T_e$	$leq 2 \text{ keV}$
Electron temperature (ECRH)	$T_e$	$leq 15 \text{ keV}$
Ion temperature (OH - ECRH)	$T_i$	$leq 1 \text{ keV}$
Ion temperature (+NBH)	$T_i$	$leq 3.7 \text{ keV}$
Electron cyclotron frequency	$f_{ce}$	41 GHz
Plasma frequency	$f_{pe}$	30-120 GHz
Electron Larmor radius	$\rho_e$	30-50 $\mu\text{m}$
Ion Larmor radius	$\rho_{hi}$	2-7 mm

null magnetic field points (called X-points) that convey plasma that transits to the divertor targets. The first wall is carbon tiled and serves both as a limiter or as a divertor target. This allows for almost complete freedom on plasma positioning, as well as on X-point location, that is often fixed by design on other machines. The main impurity is C, which is released from the tiles by plasma erosion. Boron is also common in TCV, especially after boronisation, a procedure which reduces the presence of oxygen released from the walls (mostly due to water, held in the tile mass, dissociating during plasma operations) [29] [141].

With an open machine and a generous array of independently controlled poloidal field magnets around the machine, large part of experimental research conducted in TCV is dedicated to the effects of plasma shape on confinement, stability and transport.

Table 1.1 shows the main TCV specifications and plasma parameters. The toroidal Ohmic plasma current is induced by a transformer composed of 7 coils, (A) in figure 1.6. The toroidal

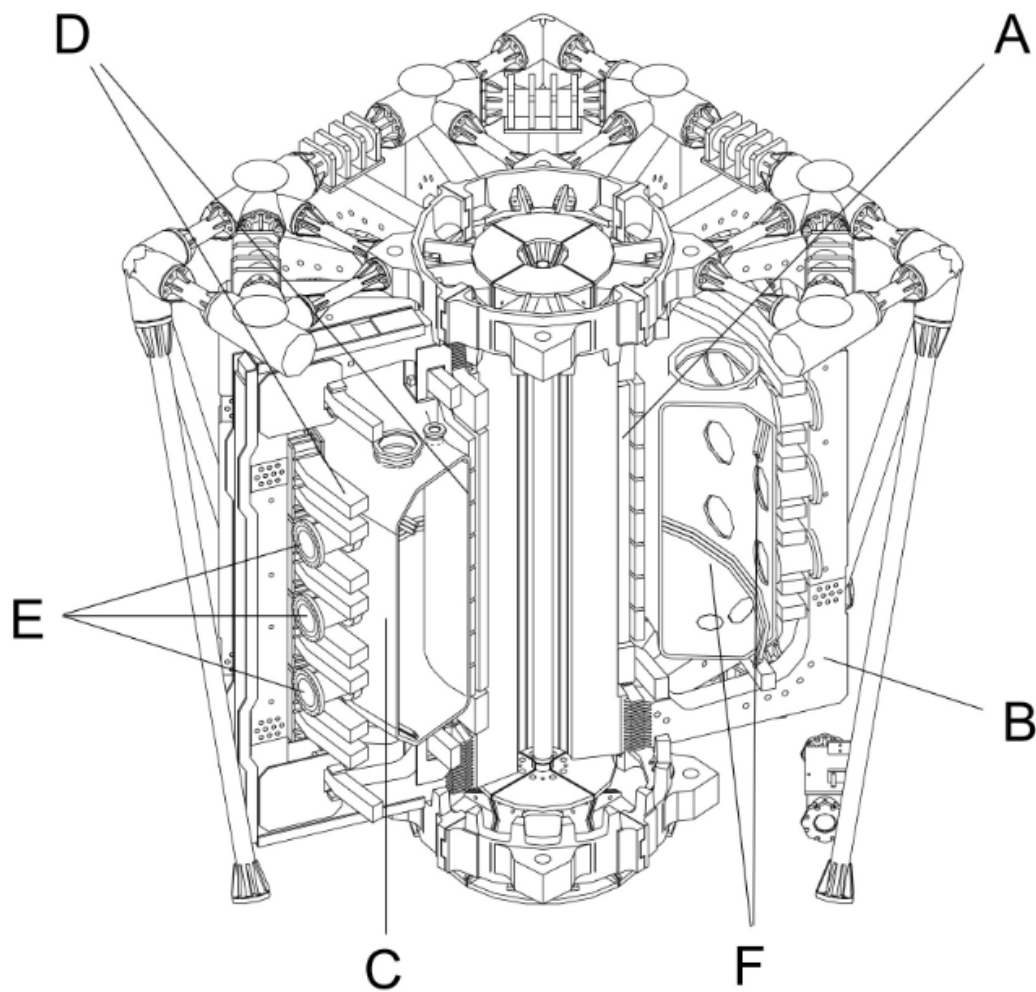


Figure 1.6 – Sketch of TCV. (A) central solenoid for inducing ohmic current, (B) toroidal field coils, (C) vacuum vessel, (D) shaping coils (poloidal field coils), (E) flanges (access windows) and (F) in vessel vertical (poloidal) field coils.

magnetic field is generated by a set of 16 Ohmic coils (B) connected in series and can reach a maximum value of 1.5 (normally 1.44) T on axis. A set of 16 poloidal field (PF) coils (D) is mounted on both sides outside of the TCV vessel (C). Each coil has a dedicated power supply to maximise the plasma shaping flexibility.

Vertical plasma stability is particularly challenging for highly elongated plasmas  $\kappa > 2$ ; in TCV, a feedback stabilisation is enhanced exploiting a set of two vertical field coils located inside the vacuum vessel (F), and is able to act upon the plasma within 0.1 ms. These coils, in conjunction with a high conductivity (stabilising) vacuum vessel and the PF coils, enabled TCV to reach a record plasma elongation of  $\kappa = 2.8$  [128].

Figure 1.7 shows some examples of TCV extremely flexible shaping capabilities [107].

### 1.3. The Tokamak à Configuration Variable

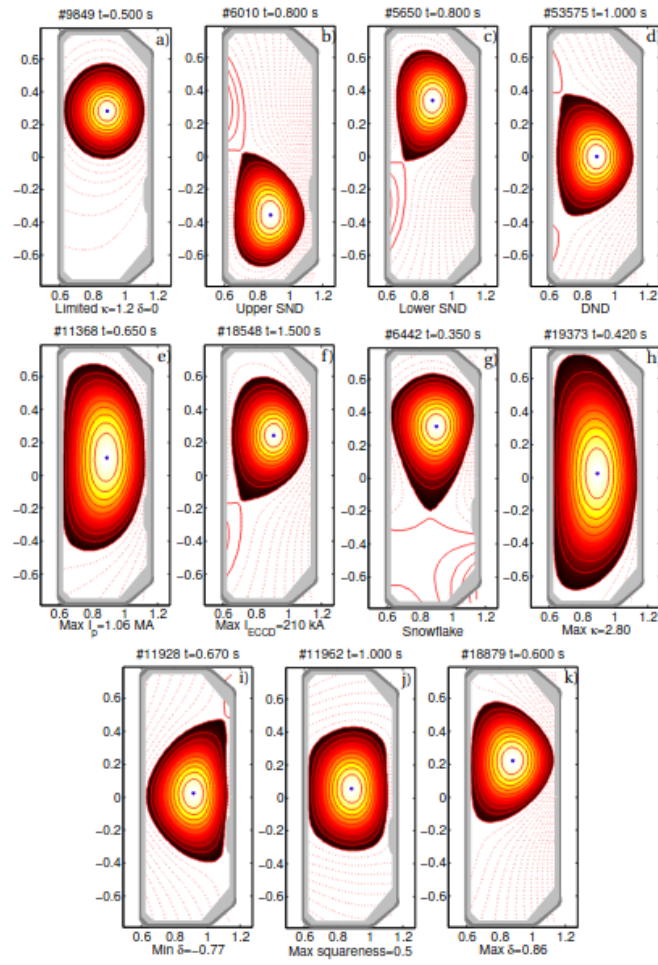


Figure 1.7 – Magnetic reconstruction (LIUQE) of some selected TCV discharges showing TCV plasma shape capabilities.

### 1.3.1 TCV heating systems

The induced Ohmic current provides the initial plasma heating with a temperature to  $T_e \leq 1\text{keV}$ .

Two auxiliary heating systems are employed to reach fusion-relevant conditions: The ECRH (Electron Cyclotron Resonant Heating), which targets electrons, and the NBH (or NBI, Neutral Beam injection Heating), which mainly heats the ions on TCV.

#### ECRH system

TCV's ECRH is currently composed by six microwave beam injector ports. The system exploits the resonant interaction between microwaves and the gyro-motion of the confined electrons. The resonance condition is achieved when the electromagnetic (EM) wave frequency is an integer multiple of the electron cyclotron frequency  $\Omega_c$ . As  $\Omega_c$  is proportional to the magnetic field  $|B|$  (and  $B \propto \frac{1}{R}$ ), it follows that ECRH resonance is localised on a vertical layer at fixed  $R$ , that can be adjusted through  $B_\phi$  variations.

The power coupling is optimised for EM wave polarised in the extraordinary mode (X-mode), *i.e.* when the EM field is orthogonal to the magnetic field. The EM wave can also drive current if injected with a component in the toroidal direction. This effect is called ECCD (Electron Cyclotron Current Drive).

Two gyrotrons are available at the second harmonic at 82.7 GHz (termed X2, 750kW/2s each) and two at 118 GHz (X3, 450kW/2s each), all of them with low-field side launch. Moreover, two dual-frequency gyrotrons are available at 84 GHz or 126 GHz (900kW/2s each) for X2-ECH/ECCD in low-field side launch or X3-ECH in top-launch [60].

EM waves can propagate in the plasma only when their frequency is above a cut-off frequency proportional to the square root of the electron density. Whilst X1 and X2 resonances are strong and the power is localised both toroidally and poloidally, X3 resonance is weaker. Therefore, vertical injection angles are specially chosen to increase the beam path length according to the resonance conditions and to obtain a reasonable absorption factor [90].

For X2, the corresponding cut-off density is  $4.25 \times 10^{19} \text{m}^{-3}$ . For the X3, the cut-off density is  $11.5 \times 10^{19} \text{m}^{-3}$ . It should further be noted that X2 absorption is very strong at relatively lower plasma temperatures whereas X3's absorption increases strongly with electron temperature. It is interesting to note that all plasma heating techniques have advantages and limits so present-day research is still seeking combinations of many technologies to achieve economical and reliable Fusion conditions for a reactor.

Figure 1.8 shows the EC lateral ports injection systems. As the plasma discharge evolves, a mirror can be displaced, under RT computer control, in each injector to modify the microwave absorption position.



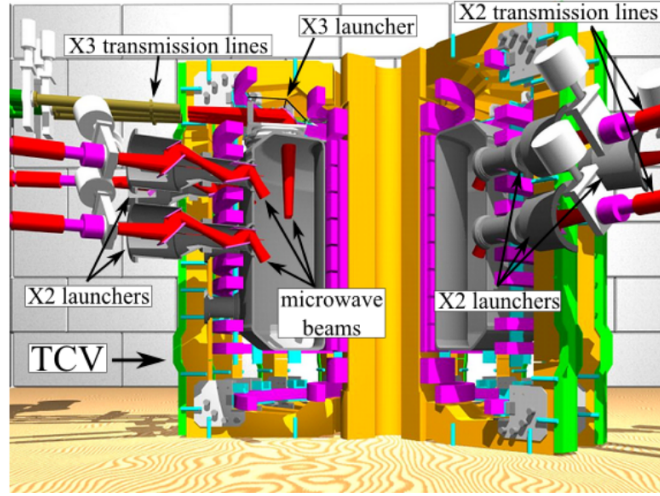


Figure 1.8 – Sketch of TCV ECRH launchers.

#### NBH systems

TCV is equipped with a neutral beam injector that can provide up to 1.3 MW of power [101] with an energy of injected particles of  $\sim 25 \frac{\text{keV}}{\text{amu}}$ . A second neutral beam injector was installed in 2021. TCV's NBI-2 can provide up to 1 MW of power with higher particles energy up to  $60 \frac{\text{keV}}{\text{amu}}$ . It injects neutral particles in the opposite toroidal direction of NBI-1.

For most TCV conditions, NBH power is coupled to the plasma ions, so the systems expands the working parameter space of TCV to regimes where  $\frac{T_e}{T_i} \sim 1$  (Ohmic heating is mostly to the lighter particles, *i.e.* electrons), opening the path to more relevant fusion conditions (where  $T_i$  is expected to exceed  $T_e$ ) as well as the study of fast ions physics. Moreover, due to the injection geometry, with both systems operating, external torque variations, including the balanced torque that is thought to correspond most to reactor conditions, can be investigated. The beam power facilitates the access to H-mode, changes the ELM and sawteeth characteristics and frequencies and provides significant current drive. Moreover, the NBI acts as an active source of torque, allowing for momentum transport studies that are no longer limited to intrinsic rotation scenarios. During maximum power injections, toroidal velocities up to  $200 \frac{\text{km}}{\text{s}}$  in the beam direction have been observed, whereas intrinsic torque values are often an order of magnitude lower.

Figure 1.9 shows the heating beam injection geometry (on the left). The installation of the two high-power neutral beams required new apertures to be machined into the original TCV machine vessel. As can be seen in Fig. 1.9, the size of these apertures was limited by the toroidal field coil assemblies, indicated in red. On the bottom right, the Diagnostic Neutral Beam Injector is depicted. This system, along with the two neutral beam heating systems, will be presented in detail in the next chapter as they were fundamental to this thesis work.

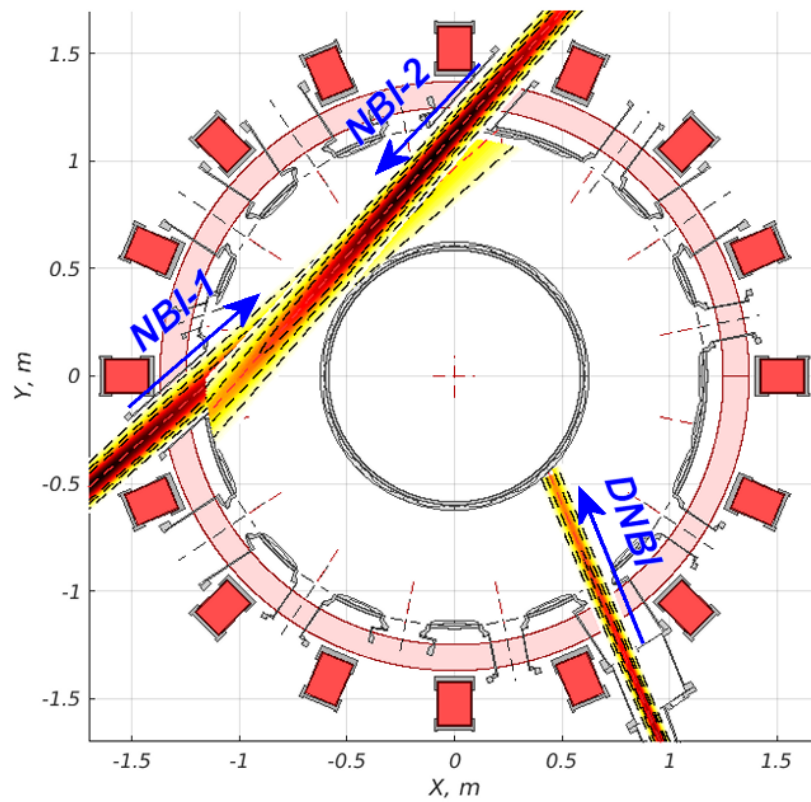


Figure 1.9 – Sketch of TCV neutral beam injectors geometry. On the left, the main heating beam (NBH or NBI-1). On the right, the second heating beam (NBI-2). On the bottom, the diagnostic Neutral Beam Injector (DNBI).

### 1.3.2 TCV diagnostics

An extensive number of diagnostics is installed on TCV to monitor relevant experimental parameters during plasma discharges.

A brief description of the main systems, of particular pertinence to this work, is given in the following paragraphs.

#### Magnetics

TCV's magnetic equilibrium is reconstructed by the LIUQE code, a Grad-Shafranov solver which exploits the measurements of the Mirnov coils installed between the vacuum vessel and the graphite tiles and other magnetic pickup coils installed around the TCV vessel. When requested, experimental temperature and density profiles are also employed to help determine the resulting magnetic field structure. The same probes are used to detect MHD activity, from plasma instabilities and resonant modes.

Four sets of poloidal probes arrays, of 38 probes each, measure the component of the poloidal field tangential to the vacuum vessel at fixed toroidal positions (equispaced by 90 degrees). Three pairs of toroidal arrays are positioned at different vertical positions:  $top_z = 35$  cm,  $middle_z = 0$  cm and  $bottom_z = -35$  cm. Each pair consists of a set of equispaced probes, 8 at the HFS and 16 at the LFS, with an additional probe in the LFS set (total of 17 probes) with the breaking of symmetry permitting the detection of modes with toroidal numbers up to  $n=16$ . Three (TOP, MIDDLE and BOTTOM) sets of saddle loop, 8 probes each, complete the MHD acquisition system. The maximum acquisition frequency is 1 MHz, although for standard operation an acquisition frequency of 250 kHz is used, which is satisfactory to measure MHD activity in most TCV plasmas and more than sufficient for plasma shape reconstruction. The poloidal Mirnov coil array of TCV are treated as a discrete approximation of a complete Rogowski coil and are used to estimate the plasma current  $I_p$ .

#### Thomson scattering

The Thomson scattering diagnostic provides local measurements of both electron density  $n_e$  and temperature  $T_e$ . Thomson scattering is the elastic scattering of electromagnetic radiation by free charged particles. The electron density is proportional to the intensity of the scattered light, whereas  $T_e$  can be calculated by spectral analysis of the scattered radiation. The wavelength of the scattered signal differs from the incident light due to Doppler broadening from the thermal movement of the electrons.

The incident electromagnetic wave is provided by three Nd-YAG lasers. Their wavelength is 1064 nm, with a repetition rate of 20 Hz and a maximum energy of 0.85 J each.

The lasers optical paths nearly overlap in TCV vessel but are, in fact, slightly separate, particularly in the lower divertor region. They can operate with a simultaneous or independent trigger. The former is employed to achieve higher signal to noise ratio, for instance, for low density plasmas. The latter, when possible, increases the time resolution of the system. In this

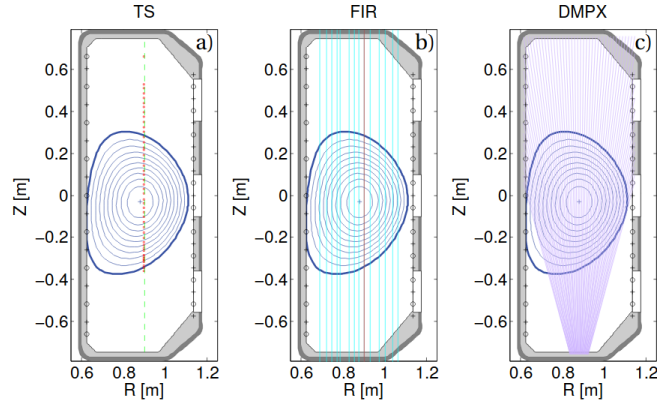


Figure 1.10 – Lines of sight of different diagnostics: Thomson, FIR and DMPX.

case, the system can acquire 3 profiles with a temporal inter-pulse resolution of down to 2 ms, which is the sensor sampling time (but only for up to three measurement bursts at a time). The laser beams traverse the plasma at mid-radius ( $R=0.9$  m).

The system is absolutely calibrated using Raman scattering of a N<sub>2</sub> gas filled TCV vessel, but can drift in both alignment of the laser beams and in the detection optics that affect the calibration consistency. The absolute, line-integrated FIR diagnostic density measurement (see next paragraph) is used as a reference to adjust the TS density profile integrals.

The Thomson system is an essential electron diagnostic in TCV, ordinarily required by many post-shot analysis routines and for the interpretation of most diagnostics results, including the CXRS system central to this work.

### FIR

The Far InfraRed interferometer (FIR) diagnostic is a Mach-Zender interferometer providing line integrated electron density measurements along 14 vertical paths across TCV minor radii. The plasma refractive index, that is near linear with plasma density, introduces a phase delay in each beam's transit through the plasma. The interferometer measures the phase difference of the laser beam and a reference external path that remains unaffected. The line integrated electron density is then proportional to the measured phase shifts. The standard temporal resolution is 20 kHz and the laser beam has a wavelength of  $184.3 \mu\text{m}$ .

FIR is another essential diagnostic for TCV operations. The measurement along the central chord ( $R=0.9$  m) is employed for real time control of plasma density by comparison with a reference trace and action on one or more of TCV's gas injection valves.

The density profiles can be reconstructed by tomographic inversion, albeit with a range of regularisations that can be probed from the Thomson Scattering profiles.

**CXRS**

The Charge Exchange Recombination Spectroscopy (CXRS) diagnostic provides local measurements of plasma impurity density, temperature and rotation velocity ( $n_i, T_i, v_i$ ). The original diagnostic system exploits the active charge exchange (CX) reaction between an impurity ion and a high energy neutral hydrogen atom of a diagnostic neutral beam injector (DNBI). The low power ( $\leq 80$  kW delivered into the vessel) of TCV DNBI allows for unperturbed rotation measurements, which are preferable for intrinsic rotation studies. 5 spectrometers measure the line radiation emitted by the recombined impurities which are excited after the CX reaction. The measured quantities are related to the first three moments of the impurity emission line. The main TCV intrinsic impurity is carbon, that is released from the wall, and it is routinely measured through the C VI line at 529.06 nm. The maintenance, development and upgrade of this diagnostic constituted part of this thesis work. The CXRS diagnostic is described in considerable detail in the next chapter.

**DMPX**

The duplex multiwire proportional X-ray counter (DMPX) is a soft X-ray (SXR) detector composed of 2 Krypton-CH<sub>4</sub> wire-chambers, that have a total of 64 LOS in the TCV poloidal section. The diagnostic is sensitive to X-rays in the energy range [1-30] keV. A fixed beryllium filter imposes the lower limit of 1 keV, but it can be increased to 15 keV by the insertion of additional filters. With a 200 kHz sampling rate and its high spatial resolution (8 mm at the midplane), DMPX is particularly useful for the study of fast events such as the sawteeth MHD instability.

**1.4 Thesis objectives and outline**

The initial objective of this thesis was to study light impurity transport in the TCV tokamak with the CXRS diagnostic. Accurate measurements of the ion kinetic profiles were required for this purpose. Whilst ion temperature and general ion motion velocity only depend on a wavelength calibration, which is routinely performed after plasma discharges, density measurements require an absolute calibration, which can be performed only during machine openings, when the TCV vessel is accessible. Density measurements also depend strongly upon the geometry of the CXRS system, with reference to the plasma and a model relating the measured intensity to the underlying ion density. An accurate alignment of the diagnostic is fundamental to know where the spectrometer lines of sight intersect the beam that provides neutrals for the charge exchange reactions. Furthermore, a precise model of the beam itself and its interaction with the plasma is needed in order to estimate the neutral density profile it provides and, through a collisional radiative model, the effective charge exchange emission coefficients needed to calculate the ion density (chapter 2).

TCV recently underwent a vessel configuration upgrade. Mechanical structures, called baffles, were installed in the machine to close or, more precisely, restrict the divertor region fluence [146]. Various sets of baffles were designed in different sizes and tested on TCV. Therefore,

frequent CXRS absolute calibrations were performed during the opening periods for baffle installations. Absolute calibration measurements, and the relative data analysis, took long periods of time but were essential to correct the misalignment in the carbon density profiles measured by different CXRS systems. Moreover, the accurate estimation of  $n_C$  helped improving the estimation of the  $Z_{eff}$  with the CXRS diagnostic.

A new CXRS system was designed and installed on the main heating beam (NBI-1) during this work, with the aim of exploiting its higher power (higher neutral density in the observation region compared to the DNBI), possibly providing a stronger active charge exchange signal. After the installation of a second high power neutral beam injector (NBI-2), a further spectrometer was installed with lines of sight intersecting its path. The main goal of these additional systems was to expand the diagnostic observation capabilities. The agreement between spectrometers with LOS installed on different beams and looking at different regions of the plasma was used to strengthen the experimental results and the reliability of the interpretive models. Moreover, the higher active signal of the NBH-systems provides, for the first time on TCV, reliable measurements during ELMy H-modes, where the DNBI-systems are usually catastrophically perturbed due to their lower active to passive signal ratio, adding a powerful tool to TCV's diagnostic capabilities.

As six spectrometers were available by the end of 2020, measurements of different light impurities (C, B, O, N) during the same discharge were envisaged. However, due to delays in the commissioning and in the modelling required for accurate estimations of ion density, the focus of this work shifted towards C transport in positive and negative triangularity confinement configurations [42].

A wide range of experimental scenarios was explored with particular focus on the effects of plasma shape and isotopes on ion (mainly carbon) kinetic profiles (temperature, density and velocity) and confinement.

TCV ushered the research on negative triangularity (NT) since its earliest phases of operations. In the late 90s, the enhanced confinement in  $\delta < 0$  was discovered and the properties of negative triangularity plasmas were explored and documented in the following years [42]. The main focus of those experiments was on plasma confinement and on the development of stable scenarios. A variety of limited and diverted NT shapes robustly stable with Ohmic heating was developed. Record performances for L-mode plasmas were reached through the application of auxiliary heating (ECRH and NBH), with  $\beta$  values reaching 2.8 transiently or 2 in steady state and with comparable  $T_e$  and  $T_i$  [42].

The international interest in the NT configuration grew in the past years, harnessing the sentiment that a solution free of edge localised modes (ELM) is needed for future reactors. In this frame, negative triangularity offers a level of confinement in an intrinsically ELM-free L-mode regime comparable to that of H-mode, making it a potential candidate for a nuclear fusion reactor [103]. This enthusiasm increased after recent results from DIII-D [11] [113] and AUG [174] that confirmed TCV's findings and reduced concerns around its technical feasibility. TCV underwent an experimental campaign to further explore the NT configuration in reactor scenarios. Specifically, a broad range of  $\frac{T_e}{T_i}$  was studied, including cases of  $T_i > T_e$  made

possible using NBH injection. In this regard, an extensive experimental study of light impurity transport (C in particular, due to its natural presence in TCV) in negative triangularity was performed.

A set of experiments included in TCV internal experimental campaign commenced in summer 2020 under the name of "Impurity transport in negative triangularity". The objective was to observe the effect of triangularity on C impurity ions transport. Scans in triangularity of L-mode plasmas were performed, both in limited and diverted configuration and employing external heating (NBH).

The study of impurity transport and impurity concentration measurements gained more interest in the past years, as shown by numerous recent publications [2]. Experimental and theoretical works focused on the investigation of turbulence, showing that diffusive and convective mechanisms play a non-negligible role in driving light impurities transport [3] [120] compared to neo-classical. Carried by the improvements in turbulence modelling and experimental measurement capabilities, light impurities of different nature have been studied on several tokamaks (especially ASDEX-U [120] and JET [21]). The shaping capability of TCV provides physical scenarios that are not obtainable on other machines. In particular, access to extreme positive and negative triangularity is currently exploited to investigate changes in the ion confinement compared to the strong changes in energy confinement and turbulence strengths already reported [64] [65] [63].

A second set of experiments, also included in TCV internal campaign, started in late 2020 under the name "Isotope effect on confinement". Here, the aim was to explore the changes in confinement and carbon transport during ohmic density ramps for different hydrogenic species.

Since the early 70s, it has been observed that the energy confinement time increases linearly with electron density in Tokamak plasmas until a certain value from where it saturates. This density threshold separates the discharge into two regimes, one named Linear Ohmic Confinement (LOC) and the other Saturated Ohmic Confinement (SOC).

The study of the LOC-SOC transition has gained more attention recently with recent improvements in turbulence studies, both with theoretical and experimental investigations. Moreover, the association of the curious rotation reversal phenomenon, which is described in the following chapters, led to an increased interest on its possible link to the LOC/SOC phenomena over the last decade.

The objective of the experiments was to explore whether these two phenomena occur in the same way for different hydrogenic species. Discharges were performed for a wide range of  $I_p$ ,  $B_T$  and  $q$  to explore the possible previously suggested effects of sawteeth instability crashes on rotation measurements.

This work is organised as follows. After an introduction to the TCV tokamak, its diagnostics and the available heating systems are presented. The Charge Exchange Recombination Spectroscopy (CXRS) diagnostic employed throughout the experiments is described in this work. Due to its major role, this is described in detail in a dedicated chapter, where both the

## Introduction

---

legacy systems and the recently installed NBI-systems are presented. A review of rotation and particle transport is presented in the following chapter, introducing relevant concepts that are going to be recalled in the discussion sections. A discussion on the experimental results obtained during this work follows, divided into two chapters concerning rotation reversal in ohmically heated plasmas and impurity transport in negative triangularity, respectively. A final chapter summarises and concludes the work.



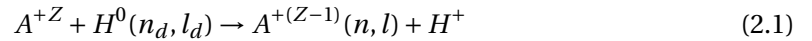
## 2 CXRS diagnostic

Charge Exchange Recombination Spectroscopy (CXRS) is a diagnostic commonly used in Tokamak experiments to measure localised impurity ions kinetic profiles (velocity, temperature and density).

Local measurements are performed acquiring active CX emission, where the measured light comes from the intersection between the CXRS LOS (Lines Of Sight) and a NBI (Neutral Beam Injector), which supplies high velocity donors for the reaction. Whilst, commonly, high power NBI is used for such measurements (the same beam that is employed for heating purposes), TCV has adopted another solution. Since a high power neutral beam would perturb the plasma, inducing non-negligible effects on the data, a DNBI (Diagnostic Neutral Beam Injector) is employed. This beam injects  $\approx 50\text{keV}$  H atoms in a near radial direction for a total power  $P_{TOT} \leq 80\text{kW}$ . With this configuration, the NBI perturbations to the plasma and the measurement itself are negligible and it is possible to measure directly ion kinetic parameters such as the intrinsic rotation, *i.e.* the rotation that spontaneously develops in momentum source-free Tokamaks.

### 2.1 Measurement principle

The charge exchange reaction consists in the transfer of a bound electron from a donor neutral atom to a plasma ion. Usually the donor atoms in a Tokamak are the same injected by the neutral beam, *i.e.*  $H^0$  or  $D^0$ . If we represent the ion as  $A^+$ , the reaction can be written as follows



The electron, after the reaction, has a finite probability of occupying an excited state in the target ion of principal quantum number  $n$  and orbital quantum number  $l$ . For fully stripped  $C^{6+}$  ions, like those normally measured in TCV, the highest probability is found at  $n_{max} = Z^{\frac{3}{4}}$ . Also the donor excitation level is very important, since CX cross section depends on energy and  $n_d$  as shown in Figure 2.1. The radiative de-excitation takes place within a few ns, which is much faster than the ionisation time, that is of the order of ms for the usual

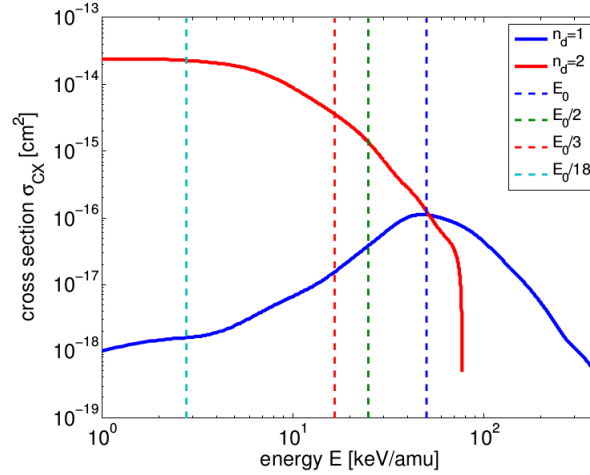


Figure 2.1 – Charge Exchange reaction cross section with respect to energy and  $n_d$ .

plasma parameters. The excited electron de-excites, eventually, to the ground level  $n = 1$  through a cascade  $(n, l) \rightarrow (n - 1, l - 1)$  before re-ionising (depending upon the initial angular momentum of the recombined excited electron). The emission lines of this process lie in the range from the X-ray to visible spectral regions. The latter is of particular interest for CXRS measurements due to the ready availability of high quantum efficiency sensors, optics and high resolution spectrometers. Fully stripped carbon is present with substantial density across the full plasma radius, and even in the edge region (SOL) where, due to the low  $T_e$ , it should not be created. This is due to radial transport from the hot plasma core, that dominates over recombination processes, such that  $C^{6+}$  is found also across the whole minor radius (see [25], ch 2.3 or [191] [111] for a precise derivation of the models).

The Carbon transition chosen in TCV for CXRS is the CVI( $n = 8 \rightarrow 7$ ) line, corresponding to a wavelength  $\lambda = 529.06$  nm. Carbon concentrations of few % are common in TCV as a result of plasma interaction with the C-tiled walls, whereas immediately after a boronisation procedure, the C density is significantly lower, due to the Boron coating on the graphite tiles reducing Carbon release. This wall conditioning typically lasts a few weeks (several tens of full power TCV discharges) and in this period a Boron CX emission line can alternatively be observed. The selected emission line for Boron is in the blue visible range, from the transition BV( $n = 7 \rightarrow 6$ ) centered at  $\lambda = 494.467$  nm. As the charge exchange cross section depends upon the energy of the neutrals, it is possible to choose a particular injection energy to target a specific emission spectral line, thus enhancing both the beam penetration and the spectral line intensity. This is done in TCV's Diagnostic Neutral Beam Injector (DNBI) that, with its injected energy  $E_{inj} \sim 50 \frac{keV}{amu}$ , targets the C emission line at 529.06 nm, whilst assuring high beam penetration, also thanks to the optimised beam injection geometry.

Thermalised impurities (as C ions in TCV) follow the Maxwell-Boltzmann distribution function

$$f_C(\mathbf{v}_C) = \frac{n_C}{(2\pi\sigma_C^2)^{\frac{3}{2}}} e^{-\frac{(\mathbf{u}_C - \mathbf{v}_C)^2}{2\sigma_C^2}} \quad (2.2)$$

with  $n_C$  [ $\text{m}^{-3}$ ] the carbon density,  $\mathbf{u}_C$  [ $\frac{\text{m}}{\text{s}}$ ] the carbon (bulk) velocity and  $\sigma_C$  the Gaussian standard deviation

$$\sigma_C^2 = \frac{eT_C}{m_C} \quad (2.3)$$

where  $e$  [C] is the elementary charge and  $m_C$  the C ion mass in kg.

The spectral emissivity  $\epsilon_\lambda$  [ $\text{ph/s/m}^3/\text{sr}/\text{\AA}$ ] of the active CXRS signal viewed by a LOS in direction  $\mathbf{e}_{LOS}$  can be described, to first approximation, by a Gaussian function:

$$\epsilon_\lambda = \frac{\epsilon_I}{(2\pi\sigma_\lambda^2)^{\frac{1}{2}}} e^{-\frac{(\lambda-\lambda_1)^2}{2\sigma_\lambda^2}} \quad (2.4)$$

where  $\epsilon_I$ ,  $\lambda_1$  and  $\sigma_\lambda$  are the first three moments of the emissivity, *i.e.* the line emissivity, the line central wavelength and the line spectral width. A detailed derivation of this formula can be found in [111].

The moments of the spectral emissivity are related to the moments of the Carbon distribution function in equation 2.2 in the following way:

$$\epsilon_I = \sum_b \sum_k \frac{1}{4\pi} n_C n_{d,k,b} q_k^{eff}(E_b, n_e, T_e) \quad (2.5)$$

$$\lambda_I = \lambda_0 \left(1 + \frac{\mathbf{u}_C \cdot \mathbf{e}_{LOS}}{c}\right) \quad (2.6)$$

$$\sigma_\lambda = \sqrt{\frac{eT_C}{m_C} \frac{\lambda_0}{c}} \quad (2.7)$$

where  $q_k^{eff}$  [ $\text{ph m}^3/\text{s}$ ] is the effective emission coefficient for the transition ( $n \rightarrow n'$ ) characterised by the rest wavelength  $\lambda_0$ . The term  $n_{d,k,b}$  represents the donor density at the excited level  $k$  and energy  $E_b$ .

The relation between these terms and the ion density, temperature and velocity are further detailed in the following paragraphs.

### 2.1.1 Density measurements

Impurity density measurements rely on the accurate alignment of the diagnostic lines of sight with the neutral beam and on the knowledge of the optical transmission between the plasma and the CCD sensor. Both the transmission measurements and the optical alignment, *i.e.* the absolute calibration, can be performed only when TCV vessel is accessible.

Ion density is measured through equation 2.8.

$$n_C = 4\pi \frac{Rad}{q_{eff}} \quad (2.8)$$

The term in the numerator is the ratio between the active signal measured by the diagnostic and the transmission measured from an absolutely calibrated source which, in our case, is a

LabSphere calibration lamp. The ratio is normalised over the integration time:

$$Rad = \frac{Active}{c_{trans} dt} \left[ \frac{ph}{sm^2 sr} \right]$$

$q_{eff}$ , instead, can be decomposed into two other terms:

$$q_{eff} = term_1 + term_2 = q_{eff,n_1} \frac{n_b}{R_{norm}} + q_{eff,n_2} \frac{n_b R_{21}}{R_{norm}} = \frac{n_b}{R_{norm}} (q_{eff,n_1} + q_{eff,n_2} R_{21})$$

As explained in more detail in a dedicated paragraph, the DNBI injects neutrals with an energy spectrum consisting of four main components. The term  $R_{21}$  is the ratio  $\frac{n_2}{n_1}$  of beam's energy components. This term is calculated using the nominal diagnostic beam energy.  $R_{norm}$  is a normalisation factor which sums all the R-terms:

$$R_{norm} = 1 + R_{21} + R_{31} + R_{41} + R_{51} + R_{61}$$

The  $q_{eff,n}$  terms are the effective emission coefficients for the requested CXRS transition and for the given plasma conditions (B field, electron temperature, etc.). Consequently, they do not depend upon the beam.

The term  $n_b$  is the beam density:

$$n_b = \frac{J_s}{e_{CH} v_b} \quad (2.9)$$

In the numerator there is the neutral current density integrated along the CXRS LOS

$$J_s = \int_{LOS} n_{d,k,b}(s) ds \quad (2.10)$$

Whereas in the denominator there are the electron charge  $e_{CH}$  and the neutral velocities

$$v_b = \sqrt{2E_b \times 10^3 \frac{e_{CH}}{m_{H1}}} \quad (2.11)$$

### 2.1.2 Temperature measurements

Carbon temperature can be calculated through equation 2.7

$$T_C [eV] = \frac{m_C c^2}{e} \frac{\sigma_\lambda^2}{\lambda_0^2} \quad (2.12)$$

which takes into account the effect of the Doppler broadening alone.

### 2.1.3 Velocity measurements

Ion velocity, projected on the LOS direction, is measured through the line emissivity 2.6

$$u_{LOS}[m/s] = \mathbf{u}_C \cdot \mathbf{e}_{LOS} = \frac{\lambda_I - \lambda_0}{\lambda_0} c \quad (2.13)$$

Equation 2.13 shows that a velocity resolution of 1 km/s requires a spectral wavelength resolution of less than 0.0018 Å for the main C transition employed herein.

### 2.1.4 Main ions and impurities comparison

The CXRS diagnostic measures impurities density  $n_\alpha$ , temperature  $T_\alpha$  and velocity  $v_\alpha$ . The relation between impurities and main ions is of great interest since it provides information about the corresponding main ions parameters ( $n_i$ ,  $T_i$ ,  $v_i$ ). Main ions and impurity ions have often been assumed to be well coupled, meaning that their temperature and velocity are assumed to be the same. Based on this assumption and the absence of direct main ion profiles measurements, their temperature is often assumed to be the same. However, as proven by recent publications [77], main and impurity ions temperature and velocity profiles can be severely different, particularly in strong gradients regions such as those found in the plasma edge, where transport and atomic physics mechanisms, as well as the interaction with cold ions, can strongly alter  $D^+$  and  $C^{6+}$  kinetic profiles in different ways.

From a comparison of the ion-electron equipartition time ( $\tau_{e-i} \sim 10 - 100$  ms for typical TCV plasmas) and ion-ion equipartition time ( $\tau_{i-i} \sim 0.1 - 1$  ms), it is estimated that impurities main ions are, to a good approximation, in thermal equilibrium ( $T_i \sim T_\alpha$ ), also confirmed by a comparison with CNPA measurements in [161].

Impurities, main ions and electron density can be gathered into a single figure from their charge contributions. by the definition of the plasma effective charge  $Z_{eff}$ :

$$Z_{eff} = \frac{\sum_l Z_l^2 n_l}{\sum_l Z_l n_l} \quad (2.14)$$

where  $l$  labels all the ions (both main and impurities). If we include also the charge neutrality  $\sum_l Z_l n_l = n_e$ , the relation between all the species is found.  $C^{6+}$  is usually considered to be the dominant impurity in TCV, hence  $Z_{eff}$  is often estimated by combining CXRS and TS data. The relation between impurities and main ion rotation is more complicated. The neoclassical theory, in fact, does not rule out differences in species velocities [86]. Moreover, features unexplained by neoclassic theory such as the spontaneous toroidal rotation reversal, also studied in this work, were found [56]. Poloidal rotation measurements are also subject of debate as experiments on different devices resulted in cases of adequate agreement [14] [23] as well as in cases of discrepancies [15] [165].

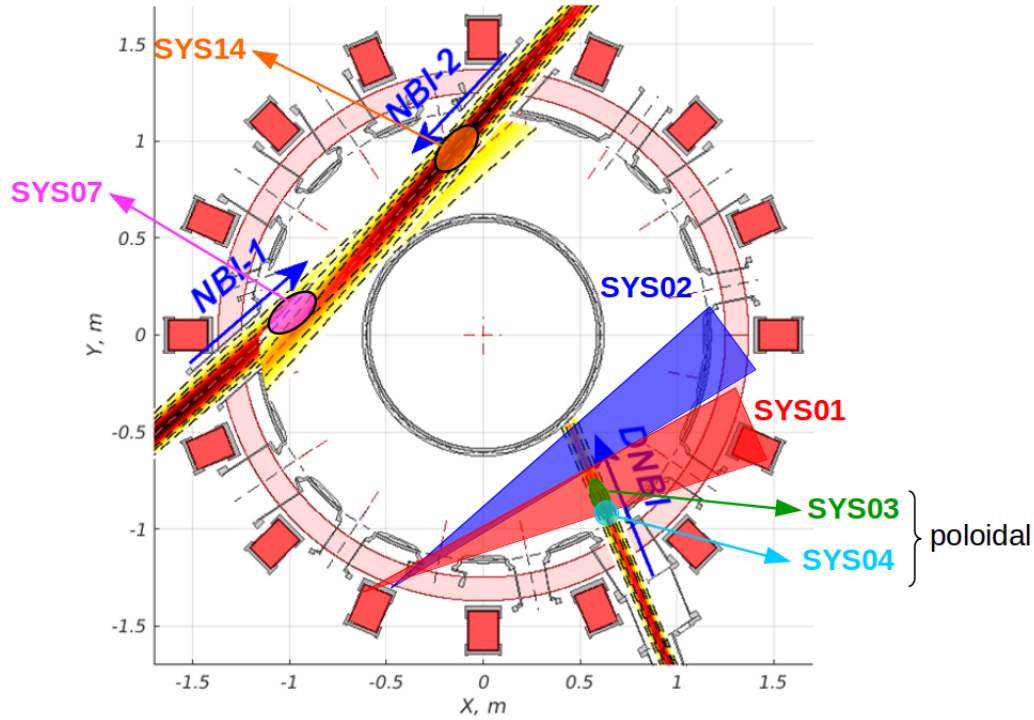


Figure 2.2 – Toroidal view of TCV with all CXRS systems' LOS.

## 2.2 Hardware

TCV's CXRS is composed of six systems:

- 1) LFS (Low Field Side, SYS1): toroidal measurements in the LFS;
- 2) HFS (High Field Side, SYS2): toroidal measurements in the HFS;
- 3) VERT (Vertical, SYS3): poloidal measurements;
- 4) EDGE (Edge, SYS4): poloidal measurements at the edge of the LFS;
- 5) NBI-1 (SYS7): poloidal measurements between  $R = [0.8 - 1.0]$  m. This system was installed at the start of 2020 and exploits the reaction between the C ions and the neutrals injected by the main heating beam;
- 6) NBI-2 (SYS14): poloidal measurements between  $R = [0.9 - 1.1]$  m. This system was developed in 2021 after the installation of the second, higher neutral energy, neutral beam injector. It exploits the reaction between the C ions and the neutrals injected by the second heating beam;

Figure 2.2 shows a toroidal section of TCV with all 6 CXRS systems' LOS intersecting the neutral beams. More details about the LOS geometry are given in dedicated sections.

All six systems, with their designs and geometries, are characterised by the following components (note the "missing" numbers eg: SYS8, correspond to DSS (Divertor Spectroscopy System) spectroscopic systems [116] [180] that employ much similar hardware and are controlled and acquired with the same software):

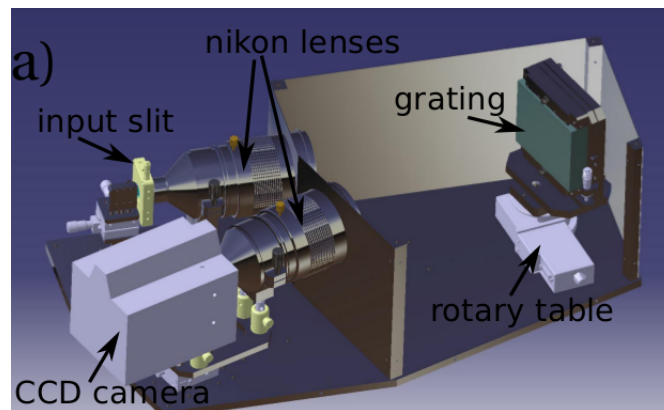


Figure 2.3 – Rendering of CXRS spectrometer design.

- 1) An input optical system, which collects the light emitted by the CX reaction and focuses it on optical fiber arrays, determining the geometry of the LOS;
- 2) An optical fiber bundle that carries the photons from the collection optics to the spectrometer;
- 3) A spectrometer that disperses the collected light allowing its spectral analysis;
- 4) A charge coupled device (CCD) detector, called CCD camera, that converts the photons from the spectra into digital counts.

A CAD (Computer-Aided Design) rendering image of a CXRS spectrometer is shown in Figure 2.3.

Next sections will present the Input Optical System, the CCD cameras and the DNBI. One paragraph is finally dedicated to the EDGE system and another on the recently installed NBI-systems.

### 2.2.1 Input Optical System

Each of the systems features 40 LOS arranged in pairs of 20 fibers per slit (thus 2 slits per system, except the EDGE system, which only has 1 slit and 20 LOS) at the spectrometer entrance. The spectra from the 2 slits overlap on the CCD sensor, since no narrowband chromatic filter is used. A total of 120 fused silica optical fibres is employed by the three legacy systems to transmit the light to the spectrometers. The core diameter is  $636\ \mu m$ , whilst the total diameter, including the cladding of each fibre, is  $1000\ \mu m$ , resulting in a fiber separation of  $\sim 800\ \mu m$  when arranged vertically on a slit. Figure 2.4 shows photos of the fibers arrangement. The fibers numerical aperture is  $NA = 0.12$ , which does not limit the throughput of the systems, that is limited by the spectrometers. The LOS of SYS1, SYS2 and SYS3 are shown in Figure 2.5 together with the DNBI orientation. The spatial resolution is  $\pm 1.5\ cm$  for the toroidal systems (SYS1 and SYS2) and  $\pm 0.7\ cm$  for SYS3.

The time resolution is limited by photon statistics and the requirement of accurate back-

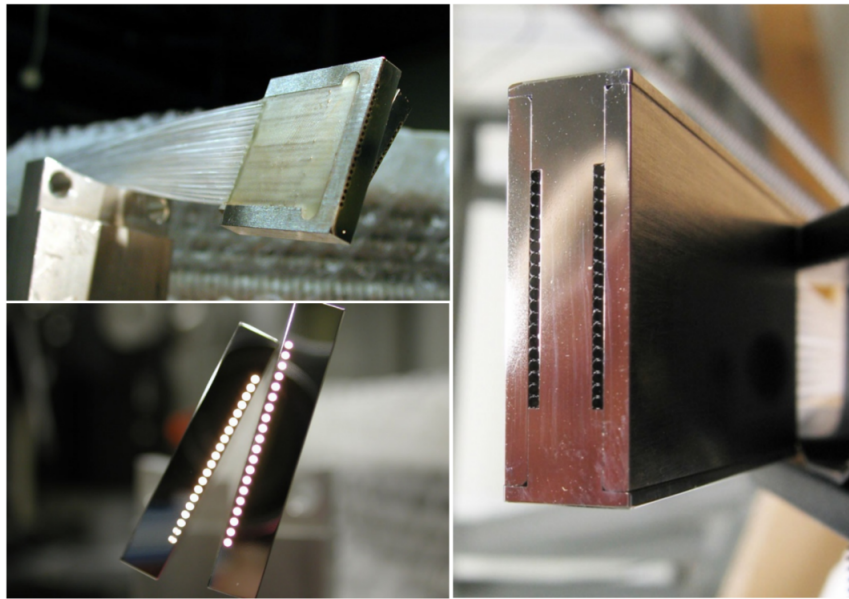


Figure 2.4 – Photos of CXRS fibers arrangement.

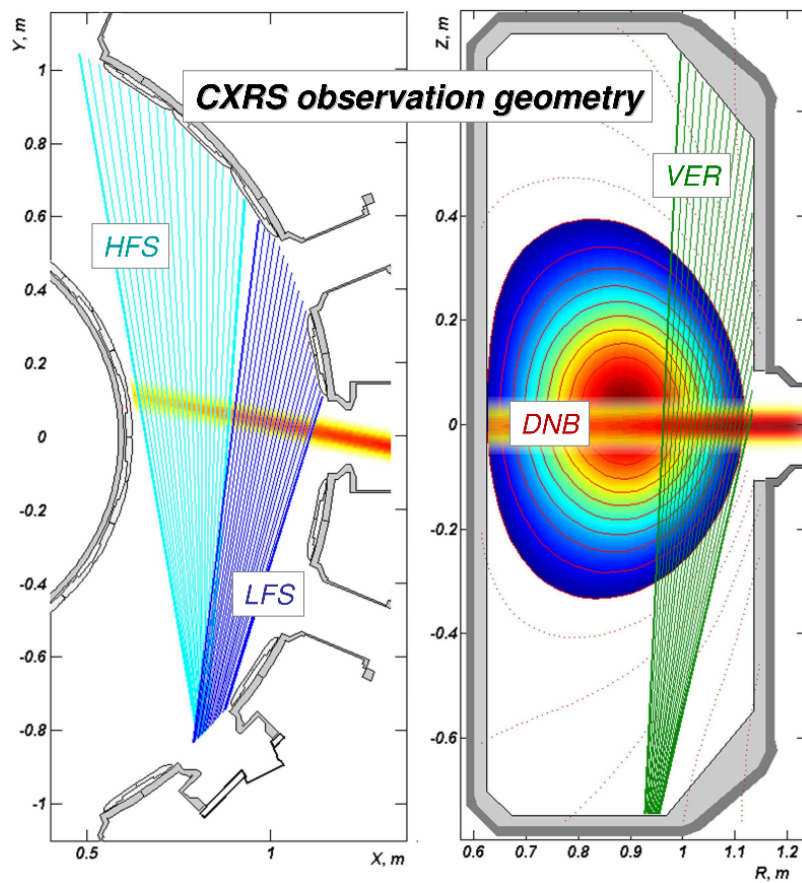


Figure 2.5 – Poloidal lines of sight of SYS1 and SYS2 (left) and toroidal SYS3 (right).



ground subtraction. An integration time of 2 ms or more is available for all the systems. SYS1 and SYS2 are equipped with the same Czerny-Turner spectrometer model, the SPEX750Mi, with 0.75 m focal length and f-number f/7.5. The image at the spectrometer output is demagnified of a factor 0.58 with lenses to fit simultaneously all the 20 fibres onto the CCD detector. The VERT and EDGE spectrometers comprise two SPC designed and manufactured f/2, 200 mm focal length lens spectrometers. Although chromatic and achromatic lenses have been employed, it should be noted that CXRS observes one wavelength at a time such that chromatic effects entail spectrometer refocussing rather than additional instrumental width. The optical reducer for this system is placed at the spectrometer input to avoid increasing of the reciprocal dispersion. All systems are equipped with 2400 l/mm holographic gratings, for an effective reciprocal dispersion of 8 Å/mm in SYS1 and SYS2 and 18 Å/mm for VERT and EDGE. The corresponding spectral ranges are 66 Å and 148 Å respectively. The detectors for both toroidal systems are Andor iXon X3 EM+ DU897D-CSO-BV cameras, that feature a readout frequency of 10 MHz, whereas the VERT system employs the iXon Ultra EM+DU897U-CSO-BV model, the same as the EDGE system, that can reach a 17 MHz readout rate. A detailed description of the CCD camera working principles and performance and the DNBI description are given in next sections.

### 2.2.2 CCD cameras

The charge coupled device (CCD) camera is the sensor used in all TCV CXRS systems to convert the photons exiting the spectrometer into digital counts. The sensor features a 2-D array of silicon MOS capacitors, termed pixels (pix), that absorb the incoming photons, producing an electron-hole pair by the photoelectric effect. Photons in the range 1.14 - 4 eV produce a single electron-hole pair, resulting in a linear response of the sensor. Lower energy photons are not detected, as their energy is lower than the detector's band gap, whilst higher energy photons can produce multiple pairs, generating a non-linear response. The quantum efficiency of the photon-pair conversion (ratio of incoming photons over produced pairs) reaches values higher than 90% in the spectral range of interest for TCV CXRS, as shown in Figure 2.6-a. The TCV CXRS cameras have a 512×512 pixel chips, each pixel of size 16×16 μm. The chip is positioned in the image plane of the spectrometer, where the convention is to name horizontal direction that of spectral dispersion. Each (pair of) fibers is therefore imaged at a different vertical position (direction perpendicular to the spectral direction).

The photo-electrons accumulate in each pixel's potential well during the acquisition period, *i.e.* integration time (IT). The pixels are composed of 3 conductive structures (gates) that can be placed at different potentials, controlled by clocking circuits. The shift of electrons in a vertical column of the chip is achieved by changing the gates potential sequentially (Figure 2.6-b). This process has an efficiency extremely close to 100%, quantified by the charge transfer efficiency (CTE). All rows are shifted simultaneously by one pixel in the vertical direction. The shift is completed in either [0.3 0.5 0.9 1.7 3.3] μs, depending on the selected vertical shift speed (VSS). The shift speed influences the frame transfer time (*i.e.* optical smearing) and CTE. The optimal VSS for these cameras is 0.5 μs [111].

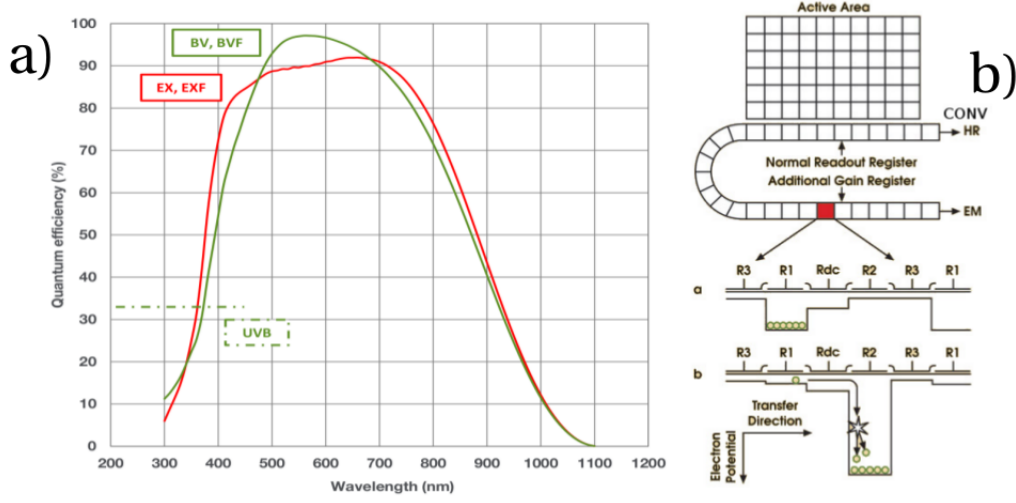


Figure 2.6 – (a) quantum efficiency of the CCD camera chip used in the CXRS system (BV-BVF curve). (b) sketch of the CCD-EM working principle. The photo-electrons are collected in each pixel during the acquisition time and then shifted to the readout register. The shift is achieved by changing the capacitor's potential (b-a). In the EM-register the potential applied for the shift is higher than the one needed for charge transfer (b-b), resulting in the production of secondary electrons by impact ionisation. The signal is hence amplified before the readout, reducing the impact of the read-out amplification noise [109].

The Andor cameras are frame transfer devices. The charges collected during an integration time period are shifted into a copy of the unexposed sensor, which is later decoupled from the light sensitive region and used in the readout register. After this frame transfer, a new integration time period begins, allowing for a "continuous" acquisition chain. The collected charge is then transferred to the analog-to-digital converter, where the charge of each pixel is converted into a digital number (analog-to-digital unit (ADU), commonly called count). Camera performance is strongly influenced by the speed of the readout process (horizontal shift speed-HSS), as shown in Figure 2.7. An output amplifier, characterised by a gain  $G_{r-o}[\frac{e}{ADU}]$ , that is the number of electrons necessary to produce 1 ADU, amplifies the signal during the readout phase. The resulting counts  $N_{ADU}$  are then obtained by the ratio between the number of electrons at the output of the readout register and the gain:

$$N_{ADU} = \frac{N_{e-out}}{G_{r-o}} \quad (2.15)$$

The charge of multiple vertical pixels can be summed into the readout register before readout. This technique is called *binning*. It is employed to reduce the readout time and to increase the S/N ratio, at the expense of reduced vertical resolution. The standard CXRS acquisition is performed by binning the pixels receiving light from an optical fibre pair in the vertical direction, which results in 20 regions of interest (ROI) or tracks. These tracks are defined during the wavelength calibration procedure, as described in the following paragraphs.

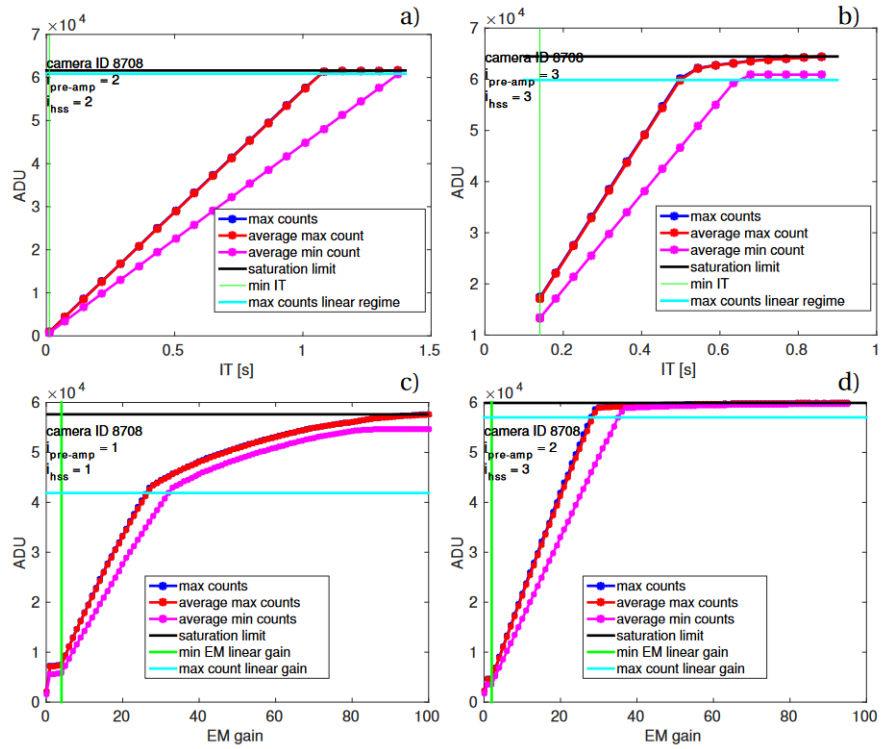


Figure 2.7 – Camera linearity test. Counts VS IT with different pre-amplifier and horizontal shift speed settings (a and b). The response is linear for almost the entire dynamic range. The linearity of the ADU VS EM gain relation (c and d) is strongly influenced by the readout setup.

Two readout registers are available: a conventional register, which works as described above, and an electron multiplier (EM) register, where the photo-electrons are multiplied by an EMCCD process [109] before readout. The process is depicted in Figure 2.6-b. Secondary electrons are produced during the readout phase, when the potential applied in the EM register is above the threshold for impact ionisation. A large number of multiplying elements assures a total gain in the range  $G_{em} = 2 - 300$ . Therefore, the number of photo-electrons needs to be multiplied by this gain factor to obtain the number of electrons at the output of the EM register:

$$N_{e^{-}out} = N_{pe}G_{em} \quad (2.16)$$

Combining equations 2.15 and  $N_{e^{-}out}$ , the relation between the counts and the photo-electrons is found:

$$N_{ADU} = \frac{N_{pe}G_{em}}{G_{ro}} \quad (2.17)$$

which remains valid in the conventional register when  $G_{em} = 1$ . Tests on the camera indicate a strong dependence of the ADU-EM gain relation upon amplifier and HSS setup (see Figure 2.7-c and -d). Knowing the saturation limit is important to prevent "blooming", that consists on the spreading of photo-electrons from one pixel to the neighbours when its well capacity is exceeded. This can result in erroneous counts also in the non saturated pixels. This phenomenon, though similar, should not be confused with optical "smearing", that is caused by the light falling on pixels during the frame transfer, resulting in the attribution of photo-electrons to an erroneous pixel. Optical smearing can be prevented by using physical shutters. When the transfer time is a non-negligible fraction of the IT, optical smearing must be corrected. In TCV, an algorithm for smearing correction was developed (see [111]) and is employed by default in data analysis.

Andor's CCD 2-D sensor allows for operating the device with different binning patterns, often referred to as *Readout Modes* (Figure 2.8):

- Full vertical binning;
- Single-Track;
- Multi-Track;
- Random-Track;
- Image;
- Cropped;

Full Vertical Binning (FVB) is the simplest mode of operation. The charge from each column of pixels is vertically binned into the shift register, resulting in a net single charge per column.

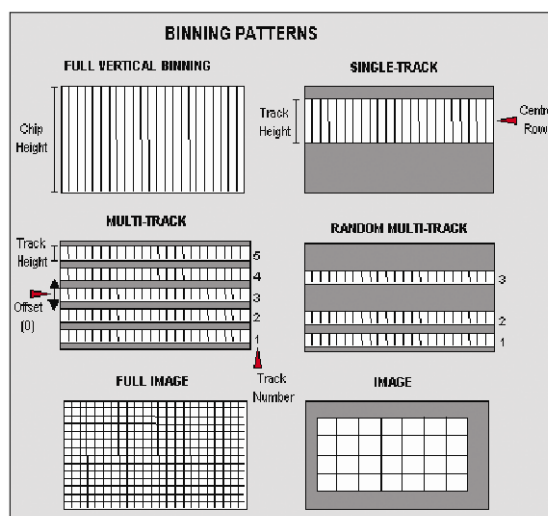


Figure 2.8 – Andor's sensor binning patterns [109].

Therefore, for TCV's CXRS systems, an acquisition in FVB results in 512 data points.

Single-Track (ST) allows for the specification of the height (in pixels) of the area to be acquired and its vertical position on the CCD sensor. Similarly to the FVB, ST also results in 512 data points. To ensure the best possible signal to noise ratio, all the rows within the specified area are binned together into the shift register of the CCD sensor and then digitised. ST is particularly useful in low level light applications, as it is possible to specify only the area of the CCD sensor illuminated by light, thus minimising the contribution of dark current.

With the Multi-Track (MT) mode it is possible to create one or more track, each behaving like the ST previously described. The number of tracks, as well as their height, can be specified and the driver internally sets the actual position of each track, so that they are evenly spaced across the sensor. The tracks can be vertically shifted by specifying a positive or negative offset in the central position. This mode is useful when simultaneously acquiring multiple spectra, typically delivered by optical fiber bundles.

In Random-Track (RT) mode, the position and height of each track is specified by the user.

In Image mode, the CCD is operated as a camera. In this mode, a value is measured for each pixel on the CCD, effectively "taking a picture" of the light pattern falling on the pixel matrix of the sensor. To avoid smearing, light must be prevented from falling onto the CCD sensor whilst the pixel charges are being binned into the shift register prior to the readout process. This is done by the shutter control, which can be set to automatically open and close according to the acquisition parameters, or can be set by the operator in a custom mode. To reduce the file size and the readout speed, it is also possible to specify a sub-area of the sensor to be acquired. Pixels can also be binned together horizontally and vertically to create "super-pixels" (see the bottom right image on Figure 2.8).

Finally, in Cropped mode, the sensor size is virtually reduced (Figure 2.9) and the readout process is performed continuously at a much faster frame rate. The spectral time resolution is dictated by the time taken to read the smaller defined section of the sensor.

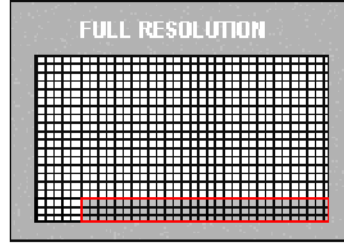


Figure 2.9 – Schematic picture of the Andor's sensor in *Cropped* mode.

## 2.3 EDGE system

CXRS SYS04, also called EDGE system, was designed to improve the spatial resolution in the TCV plasma edge and across the LCFS. It can resolve small scale spatial features ( $< 3$  mm) of the kinetic profiles.

A retractable periscope is installed on the lower lateral TCV port below the DNBI duct (Figure 2.10). It consists of a movable cylindrical aluminium pipe of external diameter 44.5 mm, which houses the input optic lens and mirror. The periscope aperture is centered with the DNBI path when fully inserted. To prevent damage during the glow cleaning plasma between TCV discharges, the periscope is automatically retracted when not operating. Moreover, an automatic safety check was implemented to predict whether the programmed plasma shape is safe and compatible with the periscope inserted location, inhibiting operation if considered too risky [111].

## 2.4 Calibration

CXRS spectra analysis and data interpretation require frequent, accurate, calibrations. Whilst temperature and velocity measurements rely only on a wavelength calibration, which can be performed rapidly by collecting the spectrum of a known emitting source (such as a Ne lamp), the absolute calibration can be a demanding task, since it requires access to the vessel. The following sections describe the two calibration methods, as well as the spectrometer alignment technique, essential for the final data quality.

### 2.4.1 Wavelength calibration and tracks alignment

The correct interpretation of the data requires a highly precise wavelength calibration. A mismatch of  $\Delta\lambda = 0.018 \text{ \AA}$  (corresponding to a fraction of a pixel, 0.06 pix) leads to an erroneous velocity estimation of  $\approx 1 \text{ km/s}$ . Also a change in barometric pressure of only 2 %, mechanical drifts or temperature excursions can influence the calibration reference value, so it is necessary to perform regular calibrations to correct them.

SYS01, SYS02 and SYS03 are equipped with a remotely controlled pneumatic system that can place a calibration lamp in the LOS path filling the acceptance cone of the observing optical

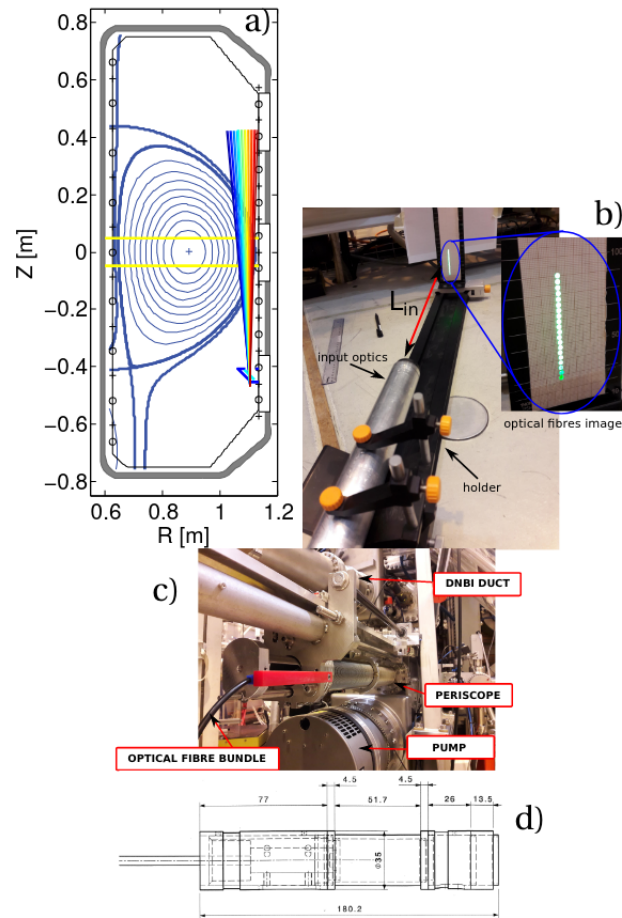


Figure 2.10 – (a) TCV poloidal cross section showing the 20 EDGE LOS. (b) alignment of the EDGE input optics for a focal plane at Li n=483 mm. (c) picture of the EDGE periscope installed on TCV on sector 14, below the DNBI. (d) input optics schematics. Courtesy of C. Marini.

fibers. This is used for wavelength calibration automatically after each plasma discharge. The calibration of the EDGE system, due to the periscopic view lines, requires access to the TCV hall so is, consequently, performed manually and thus more sparsely.

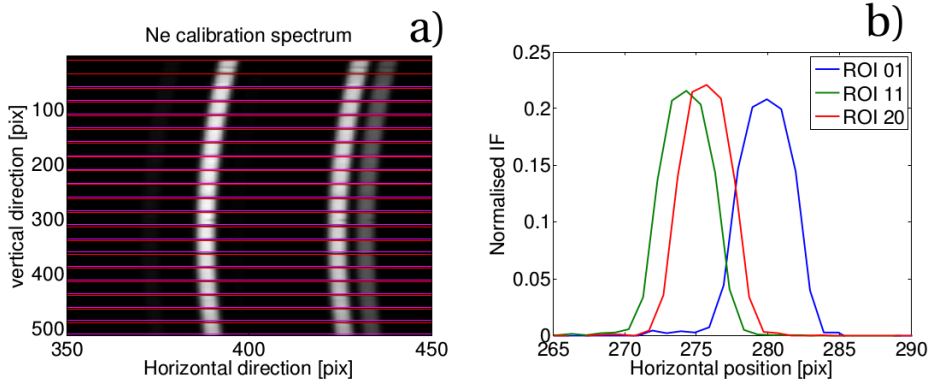


Figure 2.11 – (a) Zoom of a full frame Ne spectrum for SYS4 wavelength calibration. Horizontal lines delimit the tracks definition. Geometrical curvature and channels imperfections are visible. (b) Corresponding measured normalised instrumental functions for a subset of channels. The geometrical curvature causes the visible displacement in the average position.

The calibration procedure employs a full frame image of the spectrum of a Pen-Ray Neon lamp, averaged over multiple acquisitions, for a total integration time  $\geq 10$  s. Figure 2.11 shows an example of such an image, where a sub-section of the frame shows the three brightest lines (NeI 5330.78 Å, NeI 5341.09 Å and NeI 5343.28 Å) in the wavelength range of a spectrometer prepared for the CVI measurements. The full frame image is also used to verify the tracks alignment, which is represented in the figure by horizontal lines. The curvature in the detector plane of the straight entrance slit image (a) is a consequence of the dependence of the dispersion on the vertical tilt angle for non axial rays. It is approximately parabolic and influences the wavelength-pixel relation and the spectrometer instrumental function since spectra at different heights on the detector belonging to a ROI (Region Of Interest) are summed by the binning operation. This, when strong geometrical curvature is present in the acquired slit image, can result in an asymmetric instrumental function (IF). Other factors that influence the IF are imperfections of the entrance slit and of the optical fibres, misalignments, dust, etc. Since it is difficult to account for all these effects within an analytic function (usually a combination of Lorentzian and Gaussian functions) we use directly the experimental IF in the calibration fitting procedure, which removes any ambiguity in the wavelength definition. Consequently, the uncertainty in the absolute wavelength position for a measured line is determined by the uncertainty in the reference Ne line position, which is  $< 10^{-3}$  Å.

#### 2.4.2 Absolute calibration and spatial alignment

Since the vacuum window mounted on TCV remains in series with the optic, the absolute calibration and the spatial alignment of the lines of sight (LOS) can only be performed when



TCV's vessel is accessible, which necessarily correspond to periods when the machine is not operational and vented. Therefore, the frequency of these operations is often unpredictable and temporally limited.

A proper spatial alignment is essential to localise the measurements and obtain accurate profiles, particularly when mapped to the Tokamak's reconstructed magnetic structure. This is performed by introducing a target covered with a millimetre paper inside the vacuum vessel along the DNBI path. The optical fibres are back-illuminated by a lamp (white light). The positions of the fibre images through the observation optics are adjusted and, when considered adequately aligned to the DNBI, recorded as a digital picture, an example of which is shown in Figure 2.12. The digital pictures are then analysed using an in-house software to

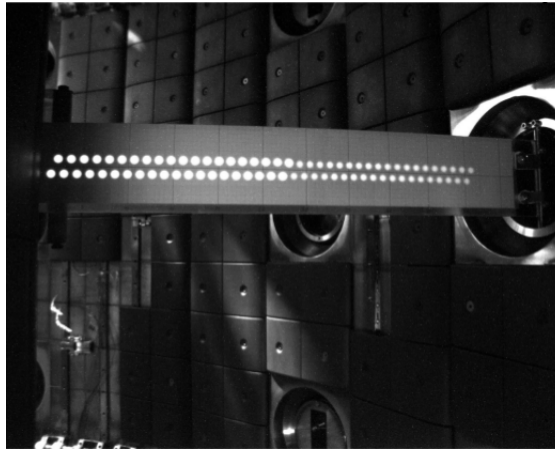


Figure 2.12 – LOS alignment (toroidal LFS and HFS).

obtain the diagnostic chord description (DCD). The estimated final uncertainty in the absolute position is  $< 5$  mm (often much less), which is smaller than the sampling size of the legacy systems [111]. A proper alignment is essential to improve the accuracy of the experimental measurements that, eventually, result in matching kinetic profiles.

Moreover, as discussed in the previous paragraphs, knowledge of the LOS and beam geometry is fundamental to correctly align the measured profiles. An example of good alignment of  $T_i$  profiles measured by 4 different systems (toroidal LFS and HFS, poloidal LFS and EDGE LFS) is given in Figure 2.13.

The absolute calibration is necessary for density calculation but also to detect transmission problems, such as component displacements or degradation of optical elements. Whilst the spectrometers are less prone to degradation, the closer plasma components such as windows and mirrors are more exposed to possible detrimental effects. Figure 2.14 shows CXRS toroidal systems mirrors degradation seen after the 2021 campaign. The absolute calibration performed after the opening revealed that this damage caused a loss of  $\sim 30\%$  in SYS01 and SYS02 transmission, underlining the need for frequent measurements and correction factors.

To include the entire optical chain between the vessel window and the CCD sensor, a source of known radiance is placed at the vessel entrance at the CXRS input optics mount position. The

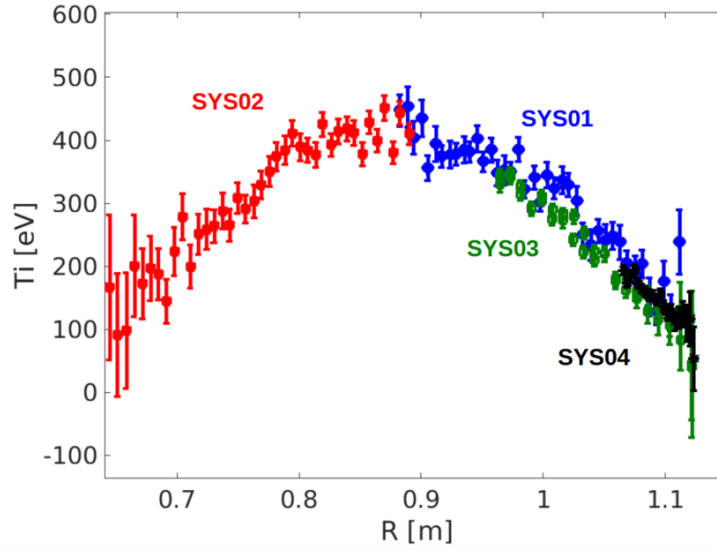


Figure 2.13 – Good alignment of  $T_i$  profiles measured by 4 different CXRS systems.

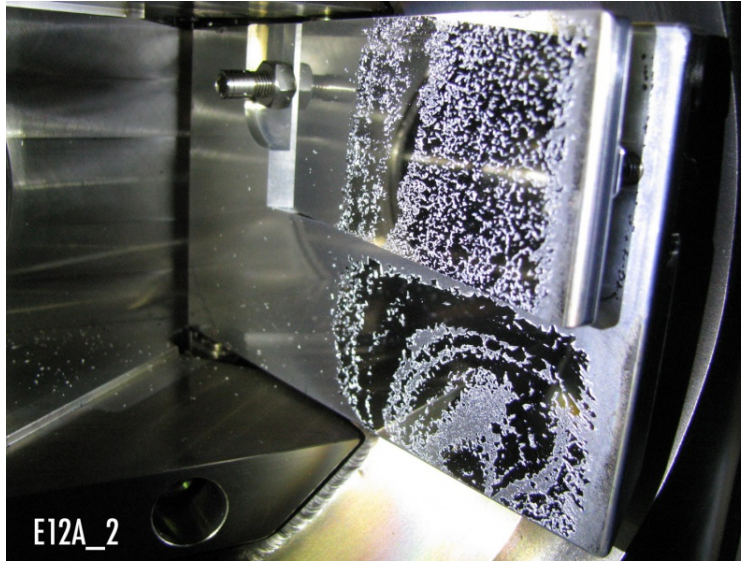


Figure 2.14 – CXRS mirrors degradation after 2021 campaign.

source is a commercial Ulbricht sphere Labsphere, model US-060-SF, which is considered an ideal Lambertian source, *i.e.* a source of constant radiance independent of the viewing angle and sampled area.

The aim is to work out the relation between the photon counting rate ( $R_s$ ) on the CCD sensor of a certain wavelength range and the radiance in the emission zone of the source ( $L_{emi}$ ).

Radiance can be expressed as

$$L_{emi} = \frac{\partial^2 \Phi_e}{\partial S \cos(\Theta_s) \partial \Omega_s} \quad (2.18)$$

where, with reference to Figure 2.15,  $\Phi_e$  is the radiant flux (photons emitted per second),  $S \cos(\Theta_s)$  is the projected area and  $\Omega_s$  is the solid angle. Two relations can be used to bond the

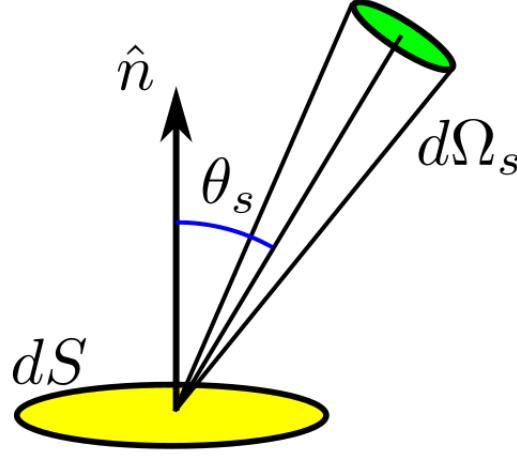


Figure 2.15 – Sketch showing a light beam crossing a surface  $dS$  at an angle  $\Theta_s$  and confined in a solid angle  $d\Omega_s$ .

counting rate and the radiance:

$$R_s = L_{emi} G_{in} T \quad (2.19)$$

and

$$T = \frac{R_{s,cal}}{L_{cal} G_{in}} \quad (2.20)$$

$G_{in}$  is the throughput of the input optics of the acquisition system and  $T$  is the total transmission, which is a function of the spectrometer parameters. Putting everything together we get

$$L_{emi} = \frac{R_s}{R_{s,cal}} L_{cal} = k_{ABS} R_s \quad (2.21)$$

where  $k_{ABS}$  is the absolute calibration coefficient. This equation shows the importance of the absolute calibration. As long as the calibration is performed in the same conditions as the experiments, *i.e.* the same geometry and optical elements, knowledge of  $G_{in}$  is not necessary for the determination of  $L_{emi}$ . Nevertheless, deterioration of optical components over time must be taken into account and frequent absolute calibration remain necessary.

It is always useful to analyse the properties of the input optics to assess the improved system performances and to evaluate the optical transmission. The throughput of an optical fiber of core radius  $r$  and numerical aperture  $NA$  is defined as

$$G = \pi NA^2 \pi r^2 \quad (2.22)$$

and can be used as the system input  $G_{in}$ , assuming no vignetting in the input optics [111]. One of the objectives of this work was to improve the quality of C density measurements for impurities transport studies. Therefore, absolute calibrations and alignments were frequently

performed during machine openings. Recently, the mirror + input optics block was extracted from the vessel entrance and it was possible to measure the transmission of the optical chain without venting the machine (Figure 2.16). This technique allows for a quick transmission measurement for adjustments as well as for frequent monitoring of mirrors state.

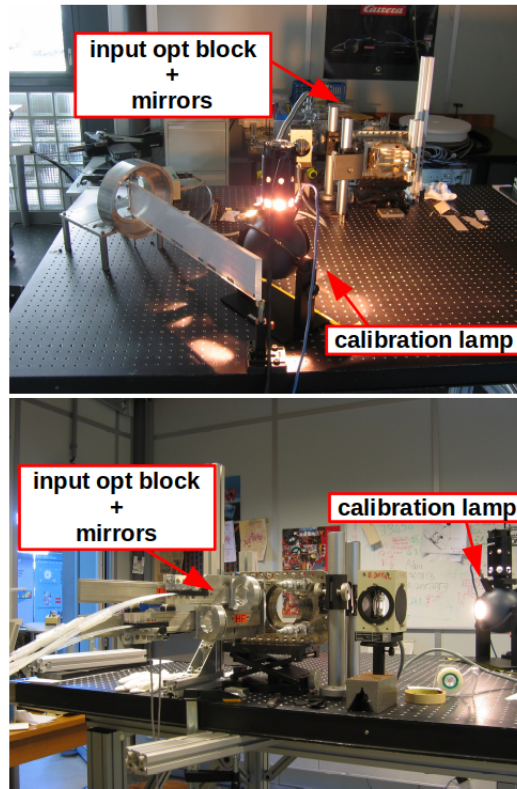


Figure 2.16 – Pictures taken during a test of CXRS SYS01 and SYS02 mirrors transimission. The input optics block was extracted from the vessel entrance and installed in the optical lab to measure the transmission of the optical chain. This technique allows for a quick transmission measurement for adjustments or frequent monitoring of mirrors state without necessarily accessing the vented vessel.

An example of C density profiles measured by different CXRS systems is shown in Figure 2.17. The top plot is an example of profiles that were not corrected with most recent absolute calibration, whilst the bottom plot shows matching  $n_C$  after the correction.

## 2.5 DNBI

The diagnostic neutral beam injector in TCV was manufactured by the Budker Institute of Nuclear Physics, Novosibirsk, Russian Federation and installed on TCV in 2000. The scope of the DNBI is to provide neutral donor for the charge exchange reaction while minimising the perturbations to the plasma. The beam consists of:

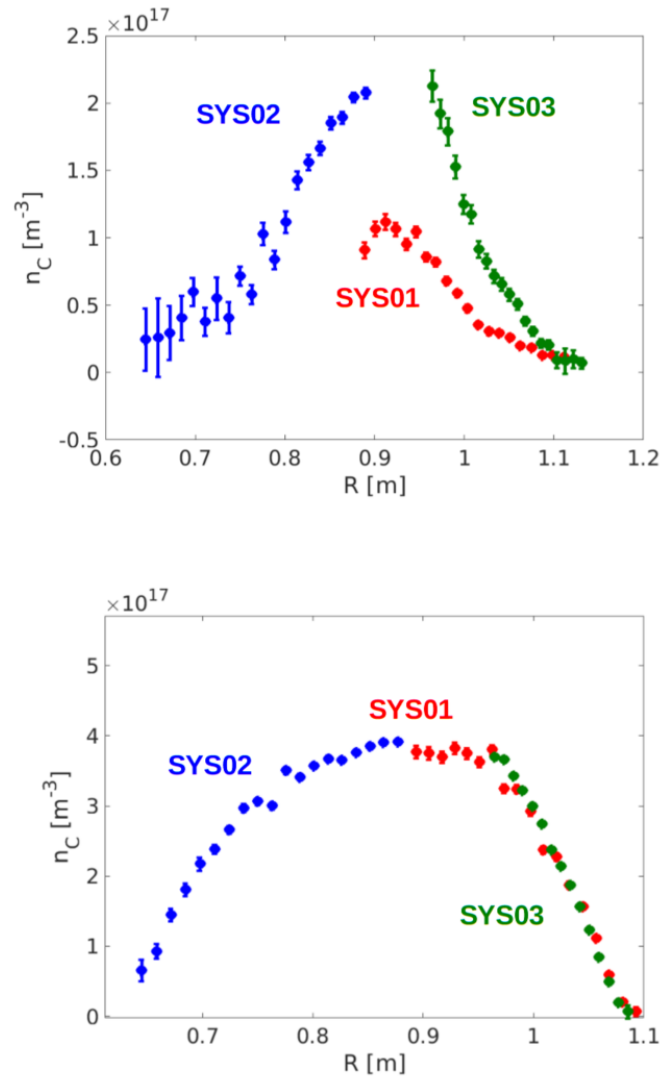


Figure 2.17 – Example of bad (top) and good (bottom) alignment of  $n_C$  profiles measured by different CXRS systems.

- a cold cathode arc-discharge plasma source from which hydrogen ions and charged molecules are extracted;
- an ion optical grid system to focus and accelerate all charged particles to the beam energy;
- a neutraliser tube where the charged molecules are dissociated and neutralised (50 % efficiency for the protons and better for the other extracted particles);
- an electric magnet and dump to remove the residual ions;



Figure 2.18 – Photo of the Diagnostic Neutral Beam Injector inside the TCV hall.

- a short beam duct interfacing with the TCV chamber.

Figure 2.18 shows a photo of the DNBI inside the TCV hall.

The beam is injected at the horizontal vessel mid-plane ( $Z = 0$ ), almost perpendicular to the torus but slightly inclined at an angle of 11.25 degrees to the normal to  $e_\phi$  (in the counterclockwise direction as seen from above). This prevents the trapping of the ionised injected neutral particles whilst minimising the injected toroidal momentum and maximising beam penetration across the plasma's poloidal plane. An estimate of the torque from the direct collisional momentum transfer and from the  $\mathbf{J} \times \mathbf{B}$  term due to the trapped particles was performed and revealed a maximum DNBI induced toroidal rotation  $\leq 1$  km/s for all of the normal situations, which is lower than the diagnostic accuracy and hence ignored. The estimated effect on poloidal rotation is lower and can also be neglected [111] [22].

The DNBI total injected power in TCV is limited to 80 kW, but only a fraction of that beam is absorbed by the plasma. The absorbed power is estimated by an attenuation code and normally varies from 20 % at low density ( $n_e = 1 \times 10^{19} m^{-3}$ ) to 80 % at high density ( $n_e = 6 \times 10^{19} m^{-3}$ ). Moreover, a large fraction of this power is transferred to the electrons, with often only  $\approx 10$  % absorbed to the plasma ions, resulting in a direct power transfer of only  $\approx 2$  kW to the ions. This is 1-2 orders of magnitude less than the electron-ion equipartition power, proving that the DNBI should not perturb any of the impurity kinetic parameters. Unlike a heating beam, it does not perturb plasma density, since it injects a small number of particles, as it is operated in pulsed mode. The total number of neutral atoms injected in a 12 ms DNBI pulse, estimated from the equivalent current, is  $N_{DNBI} \approx 2 \times 10^{17}$  [atoms], which is over an order of magnitude lower than the typical fuelling from the  $N_{NBH} \approx 2 \times 10^{18}$  [atoms]. The fuelling from the DNBI is negligible compared to the gas injected by the gas valve, which has typical flows of 10-30 [mbar l/s], typically corresponding to  $N_g \approx (2 \div 8) \times 10^{19}$  [atoms] in 12 ms.

The DNBI injects Hydrogen atoms (Deuterium operation is also possible) at full energy  $\leq 54$  keV/amu. The beam energy was chosen to optimise the CX CVI emissivity, as the CX cross

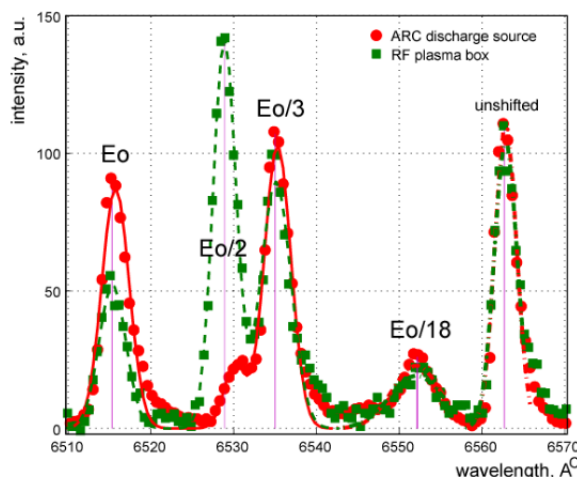


Figure 2.19 – Diagnostic neutral beam energy components.

section reaches the maximum value for that energy ( $\approx 48$  keV/amu, although recent ADAS data locate the peak at  $\approx 52$  keV/amu), whilst ensuring a good beam penetration at high plasma density ( $n_e \approx 10^{20} \text{ m}^{-3}$ ). An upgrade of the DNBI power supply unit (PSU) was performed in 2018 and could allow operation at beam energies  $\leq (53 \div 60)$  keV, but the present source arrangement tended to arc at these voltages so, for most of this reported work, the primary beam energy rarely exceeded 48 keV. Moreover, the beam current rise time was decreased from 1.8 ms to  $(400 \div 600) \mu\text{s}$  together with the minimal duration of individual pulses, which was decreased from 12 ms to 2 ms. This pulsed regime allows synchronisation of the DNBI injection with the CXRS in order to acquire active spectra during the ON phase and background spectra during the OFF time with minimal overlap.

The DNBI injects atoms with an energy spectra composed of four main components:  $E_0$ ,  $E_0/2$ ,  $E_0/3$  and  $E_0/18$ , corresponding to the acceleration of  $H^+$ ,  $H_2^+$ ,  $H_3^+$  and  $H_2O^+$ , respectively (as also shown in Figure 2.19), that are always present in a beam source but were minimised in the DNB by employing a hotter ARC plasma source configuration.

The measured energy fractions (in particle density) are [43.3 % 10 % 37.3 % 9.4 %] respectively. This relatively high fast ion fraction was achieved by replacing the initial RF ion source by the presently used Arc ion source. The injection fraction is monitored for each discharge using passive beam/neutral D- $\alpha$  doppler shifted intensity measurements from a dedicated Ocean-Optics spectrometer. The contribution to CX emissivity of the lower energy components is negligible for ground level donors, due to both a decrease in CX cross section and in the donor density, but can be substantial for the excited donors, since the CX cross section increases at those energies (as shown in the previous chapter).

The basic characteristics of TCV DNBI are listed in Table 2.1.



Table 2.1 – Main TCV DNBI technical specifications and parameters.

Parameter	Value
Maximum injected power	90 kW
Nominal energy	50 keV
Max NB pulse duration	1.4 s
Beam power range	[70 - 90] kW
Beam energy range	[48 - 51] keV Beam main species $D^0, H^0$
Full power modulation on-time	6 ms - 30 ms
Minimal modulation off-time	8 ms
Modulation rise/fall time	[1.5 - 2.5] ms
100% power modulation	up to 50 Hz

## 2.6 Passive signal subtraction - DNBI systems

A DNBI pulsed regime is employed during experimental operations and CXRS acquisition is synchronised so as to acquire active spectra during the ON phase and background spectra during the OFF one.

The raw spectra acquired after each shot have to be treated to subtract the background and thus to extract the active signal. Figure 2.20 shows the averaged charge exchange frames (in blue) overlapped to the modulated DNBI signal (in red). Every frame where the beam is OFF is considered as a passive frame, whilst those in-phase with the beam are the active frames (represented with green squares in the image).

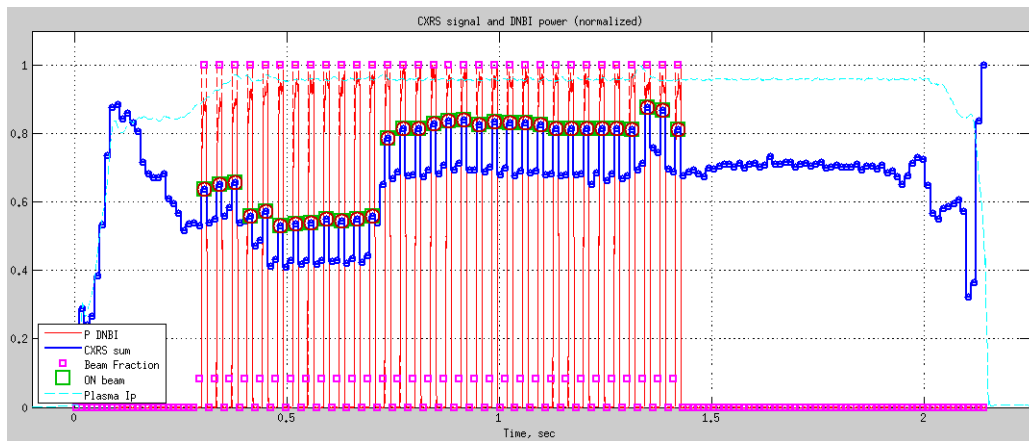


Figure 2.20 – Example of a plasma discharge with the CXRS signal in blue and the modulated DNBI in red. Notice that the only CXRS frames taken in consideration for the analysis are those contained into the DNBI modulation activity range.

Figure 2.21 shows an example of ON, passive and active spectra (obtained after the subtraction), respectively in red, green and blue. The two distinct lines correspond to the 529.1 nm main CVI line, one per slit. In order to evaluate the passive signal, the spectrum before and after the ON frames is selected. Each ON frame is therefore preceded and followed by a passive



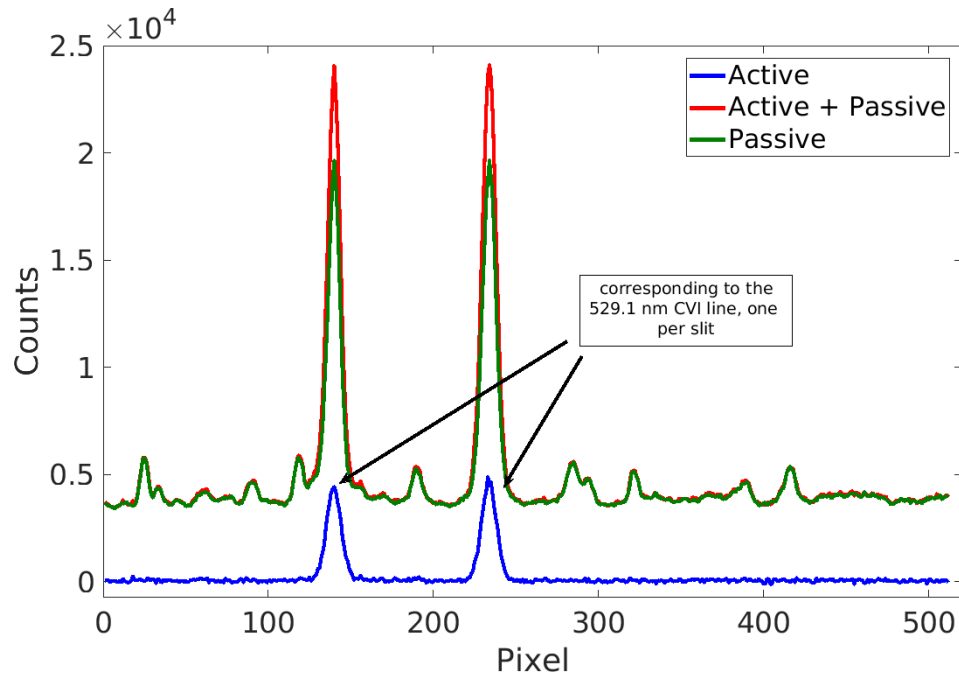


Figure 2.21 – Example of ON (red), passive (green) and active (blue) spectra. Raw spectra before calibration (that converts counts and pixels into photons and wavelength, respectively). The two blue lines correspond to the 529.1 nm CVI emission line, one per slit.

time frame (Figure 2.22).

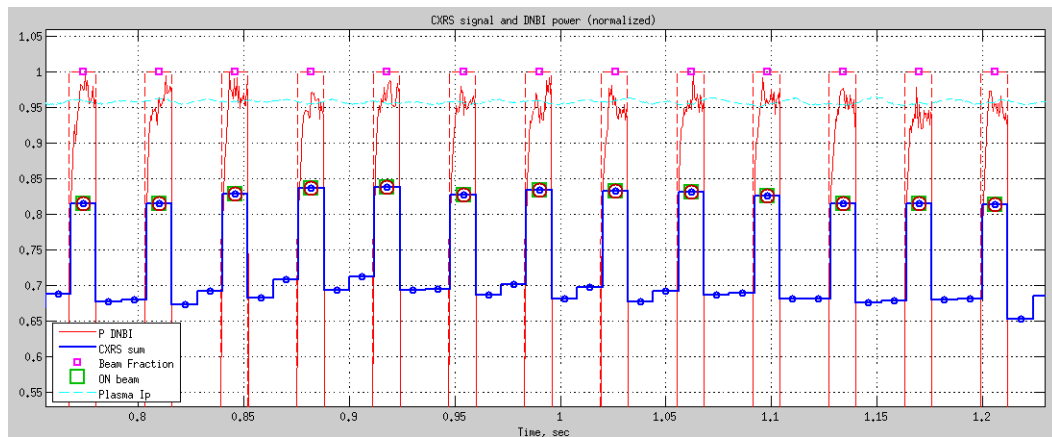


Figure 2.22 – Zoom on the previous image (Fig. 2.20) that shows the active and passive time frames.

A linear fit is performed between the background time frames and the spectra corresponding to the query points of the ON frames provide the passive signal. The fitted background is then subtracted from the ON spectrum to obtain the effective active signal. The active signal is just a few % of the entire spectrum, which is often dominated by passive plasma emission. In order

Table 2.2 – Main TCV NBI technical specifications and parameters.

Parameter	Value
Maximum injected power	1.3 MW
Nominal energy	28 keV
Max NB pulse duration	2 s
Beam power range	[0.25 - 1.30] MW
Beam energy range	[7 - 28] keV Beam main species D <sup>0</sup> , H <sup>0</sup>
Power sweep response ( $\frac{P}{\frac{dP}{dt}}$ )	$\leq 5$ ms
Full power modulation on-time	2.5 ms - 2 s
Minimal modulation off-time	5 ms
Modulation rise/fall time	[1 - 3] ms
100% power modulation	up to 300 Hz

to perform reliable Carbon measurements, the active to passive ratio should be at least  $\approx 8\%$ . However, during normal operations, this ratio was often  $\approx 20\%$ .

## 2.7 NBI-systems

As already mentioned in the introduction, TCV's external heating system comprises two neutral beam injectors. Although the first heating beam was installed in 2015, no spectroscopy system was developed to exploit it as a neutral source for charge exchange reactions until late 2019. After the successful installation of a spectrometer with lines of sight intersecting the main heating beam in 2019, another system was developed for installation on the second neutral beam injector. Both spectrometers are mainly used to measure C ions kinetic profiles but, in case of fast ions studies, can serve as FIDA systems.

The following paragraphs present in details the two neutral beam injectors and the corresponding CX spectroscopy systems.

### 2.7.1 Main heating beam

TCV's NBI was installed in 2015 to access higher  $T_i$  plasma regimes, decreasing the gap between mainly electron heated plasmas and fusion reactor conditions.

The injection geometry (already shown in Figure 1.9) with the tangential beam line at mid-plane was chosen to maximise heating efficiency whilst satisfying vessel access constraints [101]. The basic characteristics of TCV NBI are listed in Table 2.2.

As the DNBI, the NBI beam is also composed of a mix of species at full, half and 1/3 of acceleration energy. It reaches the ratio 76:17:7% at full power (Figure 2.23). Although the energy of injected particles is not optimised for the charge exchange reaction with C ions, the higher neutral density power compensates for the lower cross section value.

Fast beam modulation provides the possibility of using the same passive subtraction tech-

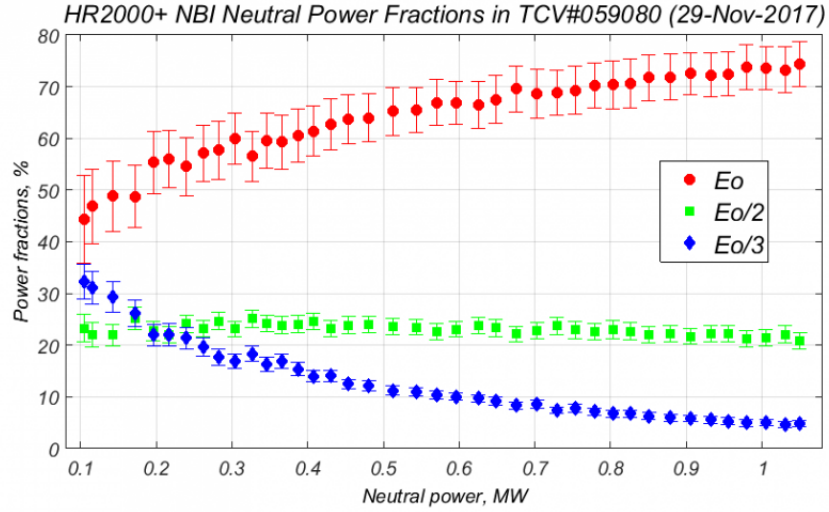


Figure 2.23 – Neutral beam energy components as a function of power.

nique used for the DNBI-systems. However, the main beam is usually exploited for heating purposes, where power is injected continuously. Both scenarios have been studied during commissioning shots.

### 2.7.2 NBI-1 CXRS

The recently installed SYS07 exploits the CX reaction between the C ions and the neutrals injected by the main heating beam (NBI-1) to measure impurity kinetic profiles. During an initial commissioning phase, that covered a large portion of the 2019 experimental campaign, measurements were performed with the Horizontal and Vertical FIDA systems. The FIDA diagnostic comprises two spectrometers whose lines of sight intersect the NBI trajectory in the plasma. It is designed to observe a CX reaction of the D- $\alpha$  emission. Since its geometry is very similar to that of SYS07, it was the perfect environment to test the installation of a new CXRS-dedicated spectrometer on NBH. Moreover, the two spectrometers were readily adapted to the C<sup>6+</sup> line.

The system was installed at the start of 2020 and it is now operational. Figure 2.24 shows the more recent in-vessel alignment performed during January 2020 TCV opening.

The system lines of sight are more complicated than the DNB systems, as they are tilted to intersect the beam path from the top of a vessel entrance aperture. The LOS intersect NBI-1 between  $R = [0.83 - 1.01]$  m, thus covering the region around the plasma core. Figure 2.25 shows NBI-1 and SYS07 LOS, intersecting the beam close to its entrance position in the vessel (labeled "NBI-1" in the picture).

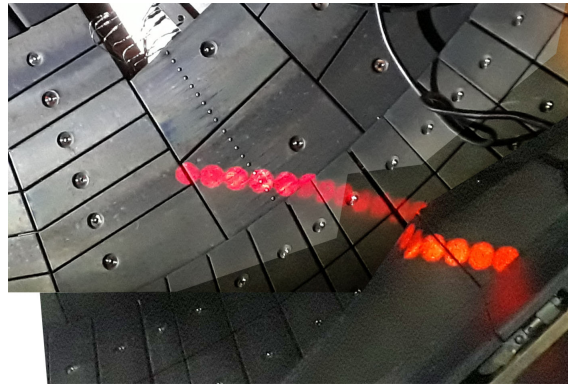


Figure 2.24 – Focusing of SYS07 lines of sight.

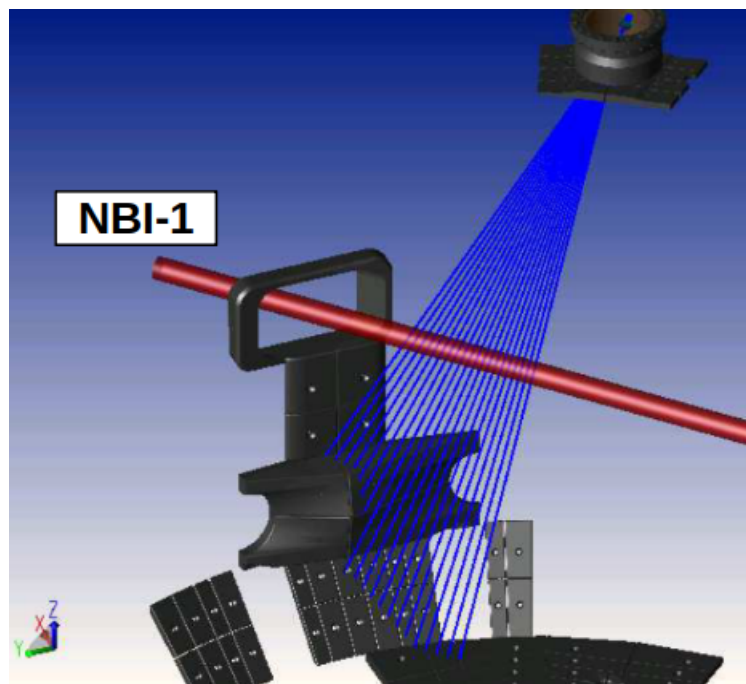


Figure 2.25 – CXRS SYS07 (NBI-1 system) lines of sight intersecting NBI-1.

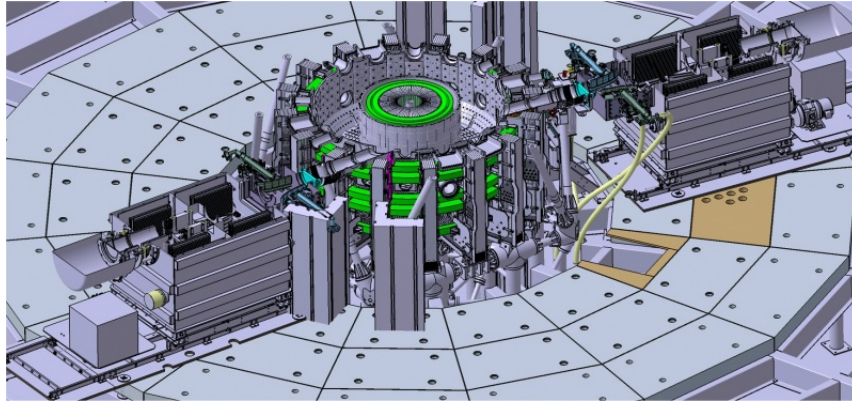


Figure 2.26 – Rendering of TCV and its neutral beam injectors (NBI-1 on the left and NBI-2 on the right).

Table 2.3 – Main TCV NBI-2 technical specifications and parameters.

Parameter	Value
Maximum injected power	1.1 MW
Nominal energy	51 keV
Max NB pulse duration	2 s
Beam power range	[0.25 - 1.30] MW
Beam energy range	[29 - 51] keV
Power sweep response ( $\frac{P}{dP}$ )	$\leq 5$ ms
Full power modulation on-time	3.5 ms - 2 s
Minimal modulation off-time	4.5 ms
Modulation rise/fall time	[1.5 - 3.5] ms
100% power modulation	up to 100 Hz

### 2.7.3 Second neutral beam injector

TCV's second neutral beam injector (NBI-2) was installed in 2021. Its nominal power is 1 MW whilst the energy of the injected neutrals at maximum power is  $\sim 50 - 60 \frac{\text{keV}}{\text{amu}}$ . This system further extends TCV capabilities for auxiliary ion heating. Moreover, it expands the possible scenarios for the investigation of fast ions and MHD physics together with the effects of plasma rotation.

Figure 2.26 shows the injection geometry of the two beams. NBI-2, on the right, injects neutrals in the opposite direction with respect to NBI-1. This choice was dictated specifically for the development of scenarios in which the externally induced torque can be balanced by the interplay of the opposing beams. Table 2.3 shows the basic characteristics of TCV NBI-2.

As for the DNBI, the energy of injected particles is near optimal for the observation of charge exchange reaction between NBI-2 neutrals and  $\text{C}^{6+}$  ions (see also Figure 2.1).

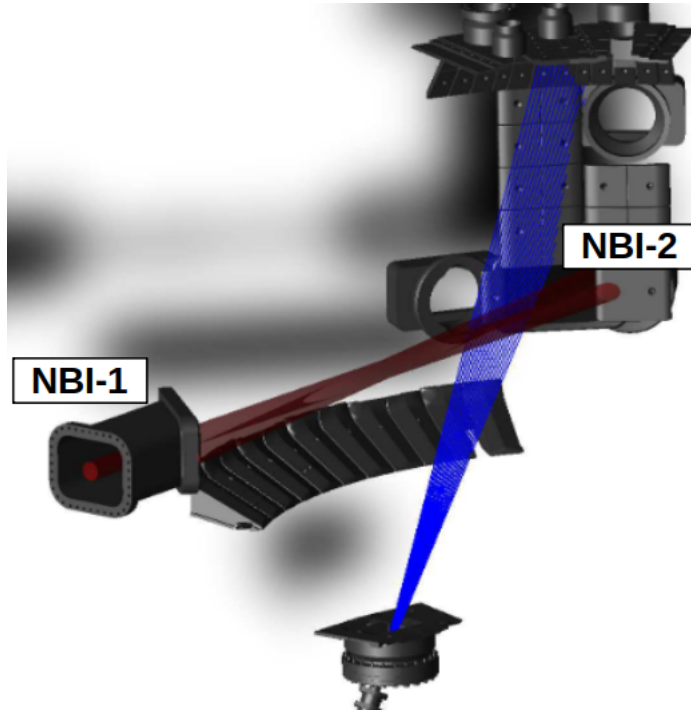


Figure 2.27 – CXRS SYS14 (NBI-2 system) lines of sight intersecting NBI-2.

#### 2.7.4 NBI-2 CXRS

The most recent CXRS system, named SYS14, was installed in 2021. It exploits the CX reaction between the C ions and the neutrals injected by the second heating beam (NBI-2) to measure impurity kinetic profiles. It features a poloidal view with 20 LOS slightly tilted from the vertical position. The LOS intersect NBI-2 between  $R = [0.87 - 1.08]$  m, thus covering the region around the plasma core. Figure 2.27 shows the two beams (NBI-1 and NBI-2) and SYS14 LOS, intersecting NBI-2 close to its entrance position in the vessel (labeled "NBI-2" in the picture). Unfortunately, at the time of writing this text, the beam has yet to be fully commissioned up to its nominal acceleration energy. Only preliminary, but highly encouraging data are presented herein.

#### 2.7.5 Commissioning discharges

A series of commissioning shots was performed after the installation of the second beam. The goal was to develop a stable scenario to test double beam injection. As the beams inject neutrals in opposite directions, torque can be driven in the co and counter-current direction simultaneously. In a generic ohmically heated TCV limited, positive triangularity D plasma, the measured intrinsic rotation is  $\sim 20 \frac{km}{s}$ , with direction depending on plasma configuration (limited or diverted) and density, as explained in detail in chapter 4. Figure 2.28 shows the

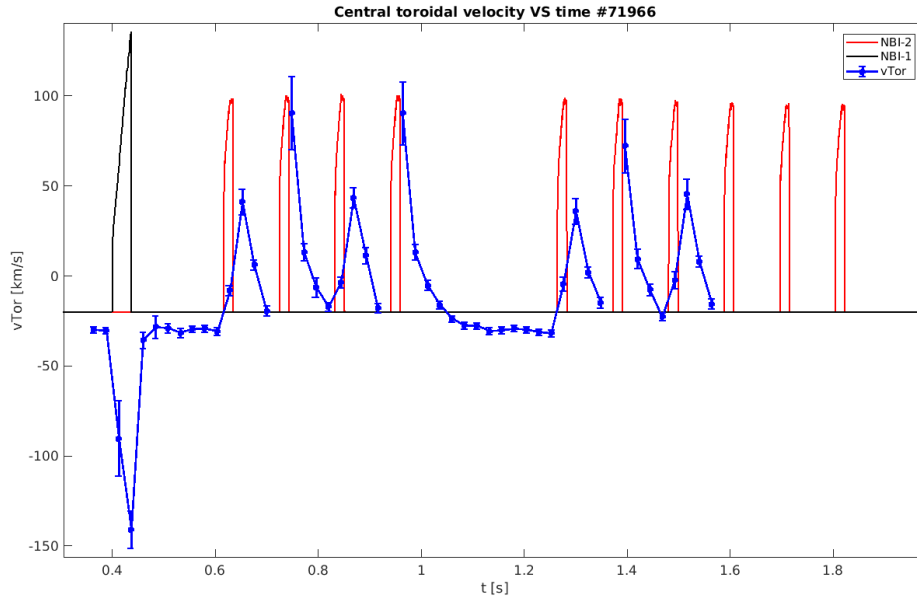


Figure 2.28 – Central toroidal velocity time trace, discharge #71966. NBI-1 and NBI-2 re-scaled traces (100 on y-axis  $\rightarrow$  1 MW) are shown in black and red, respectively. The effect of the two beams on toroidal velocity are visible: NBI-1 accelerates the plasma towards negative values of  $v_{tor}$  (counter-current direction, in this case), whereas NBI-2 pushes them in the opposite direction.

central toroidal velocity trace (in blue) for discharge #71966.

The beam power traces, re-scaled to fit on the graph, are depicted in black (NBI-1) and red (NBI-2). Both beams injected deuterium. The central toroidal velocity rapidly increases in the counter-current direction during the short NBI-1 burst, that was pre-programmed constant but ceased shortly after reaching 1.3 MW of peak power. The effect of NBI-2 is visible during the 18 ms blips at 0.93 MW.  $v_{TOR}$  relaxes back to pre-injection levels after  $\sim 150$  ms.

Figure 2.29 shows the central toroidal velocity trace for discharge #71974, where 18 ms NBI-2 blips were overlapped to two constant NBI-1 injection phases.

The power of each blip was 0.93 MW, whilst the two constant NBI-1 phases were 1.3 MW and 1.0 MW, respectively. This discharge shows how the driven torque is dominated by NBI-1. Central  $v_{TOR}$  remains in the counter-current direction throughout the discharge except for the interval without NBI-1 injection. The effect of the NBI-2 blips is nevertheless visible as the profile is pushed in the co-current direction during the injection phase. The power, as well as the blip durations, are insufficient to counter the torque induced by NBI-1. This can be expected based upon modelled neutron measurements and TRANSP simulations, that show that the deposition of the co-current injected beam is better (due to less first-orbit losses), hence showing how balancing the toroidal velocities induced by the two beams is complex.

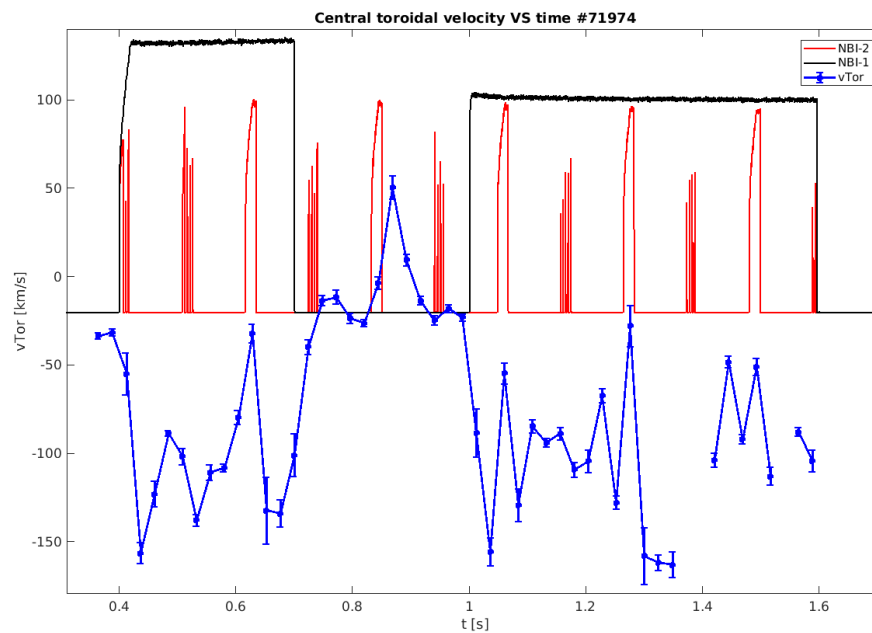


Figure 2.29 – Central toroidal velocity time trace, discharge #71974. NBI-1 and NBI-2 re-scaled traces (100 on y-axis  $\rightarrow$  1 MW) are shown in black and red, respectively. The effect of the two beams on toroidal velocity are visible: NBI-1 accelerates the plasma towards negative values of  $v_{tor}$  (counter-current direction, in this case), whereas NBI-2 pushes them in the opposite direction.



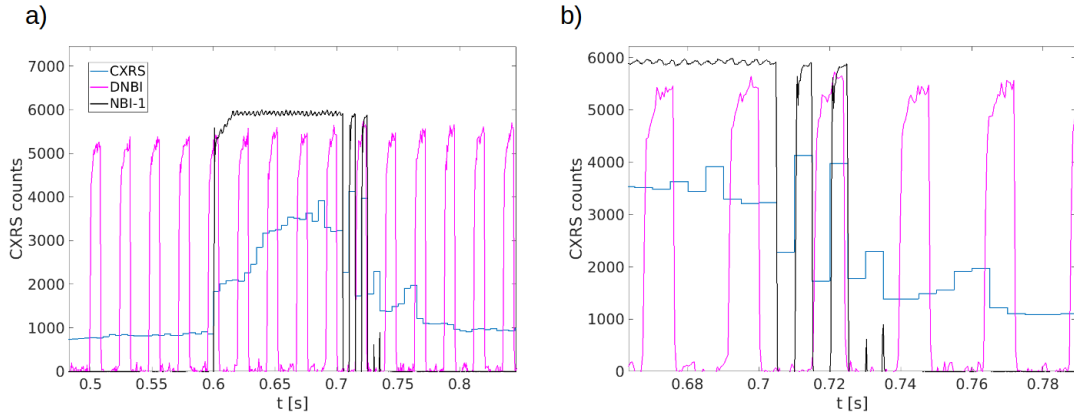


Figure 2.30 – a) CXRS counts over time and beam traces, discharge #64795; b) zoom over the NBI-1 blips.

### 2.7.6 Passive signal subtraction for NBI systems

TCV NBI system are ordinarily employed for heating purposes. Although high frequency modulation is available, it is more common to inject neutrals in long pulses to provide continual heating power. Without frequent OFF phases, it becomes difficult to estimate the background signal that evolves as the discharge progresses. In principle, if the active signal is high enough and dominates over the passive, the difference between the background spectra acquired during the initial ohmic phase or during short notches between long beam pulses should be negligible.

Commissioning discharges were performed with modulated and constant beam to investigate how the passive charge exchange signal is affected by the NBI and to develop a reliable background subtraction technique for CXRS measurements. The goal was to perform discharges comprising ohmic phases before and after the beam injection to see how long it takes for the passive CX signal to retrieve pre-injection levels. Simultaneously, the ordinary DNBI modulation scheme (52 pulses, 8 ms ON, 16 ms OFF, 1.2 s in total) was adopted to cover the relevant phases of the discharge, providing, when possible, additional measurements to compare the NBI and DNBI measurements.

Discharge #64795 was a diverted plasma with low positive triangularity,  $B_T = 1.4T$  and  $I_p = -220kA$ . The electron density was maintained fairly stable at  $n_e \sim 6 \times 10^{19} m^{-3}$  until 1.2 s to maintain similar conditions before and after the NBI injection. A 100 ms NBI pulse at 0.7 MW was injected from 0.6 s, followed by short blips (5 ms long,  $P = 0.7$  MW). Unfortunately, the beam injection stopped at 0.73 s, so only two short blips at 0.7 s and 0.72 s were available for analysis after the long beam pulse (Figure 2.30). DNBI-CXRS active signal acquisition started at 0.5 s, covering the pre and post-injection phases. The NBI significantly affects the passive signal and its effect persists for a certain period of time after the injection. This can be seen from the summed CCD counts trace in Figure 2.30-a: the blue line shows that a  $\Delta t$  of  $\sim 80$  ms is necessary for the background to relax back to pre-injection levels. Based on this observation, it is natural to ponder as to which passive spectrum should be employed for

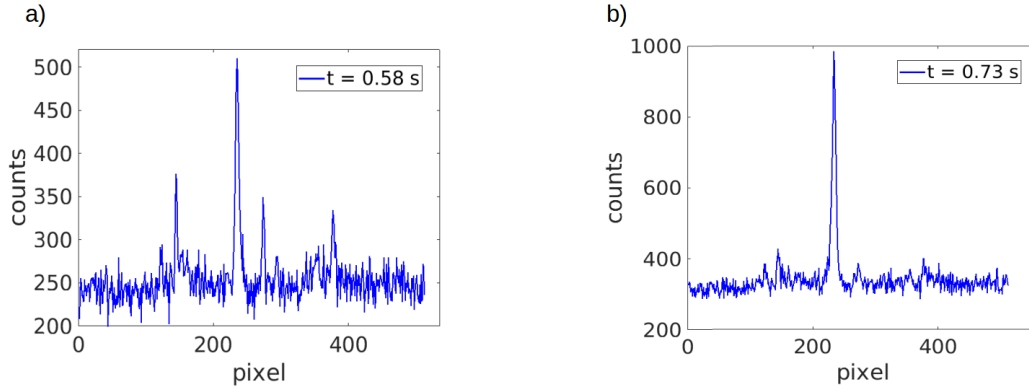


Figure 2.31 – a) CXRS background spectrum (NBI1-SYS07) at  $t = 0.58$  s, discharge #64795; b) CXRS background spectrum (NBI1-SYS07) at  $t = 0.73$  s.

background subtraction. Since the passive signal is highly affected by the NBI, it would be logical to evaluate the background just after high power injection ceases. CXRS background spectra before the injection and just after the last beam blip are compared in Figure 2.31. The difference between the two spectra, as expected, is significant: Figure 2.31-b shows that the passive C line intensity right after the last beam blip is almost double that of the pre-injection passive level. Therefore, the passive frame at  $t = 0.73$  s (*i.e.* the first CXRS frame available after the last beam blip) was subtracted from the acquired spectra. The raw and the fitted active C lines are shown in Figure 2.32.

An ion temperature profile was deduced from this spectra and shown in Figure 2.33, where it is compared to DNBI-CXRS  $T_i$  profiles. Note that the NBI-CXRS system here covers a smaller region of the plasma ( $R \sim [0.77 - 0.89]$  m) compared to the nominal spatial range described in section 2.7.2 "NBI-1 CXRS". These, in fact, were commissioning discharges, where a vertical FIDA system was adapted to measure C ion profiles.

It should be noted that discharge #64795 was a test discharge, that was not optimised for DNBI-CXRS measurements (diverted configuration, medium density and strong NBH power). The DNBI-CXRS data quality is relatively poor, especially in the core region. Nevertheless, the estimated NBI-CXRS  $T_i$  profiles match those from DNBI-CXRS. By analysing the ion temperatures from two different diagnostic beam/plasma interaction regions, we have now shown the measured ion temperatures to, as expected, be consistent, despite widely different operating conditions (low power VS high power beam as a neutral source for the charge exchange reaction).

As already mentioned, the DNBI-CXRS passive signal is strongly affected by ELMs. The perturbed background level is widely changing in these plasmas and can even exceed the active signal, irreversibly compromising the passive subtraction technique. One of the strongest advantages of NBI-CXRS is the higher active to passive ratio, which would allow for more reliable measurements during ELMy H-modes, adding a powerful tool for ion profiles estimations in high confinement regime that, fortunately, often employs NBH and, where not, could be

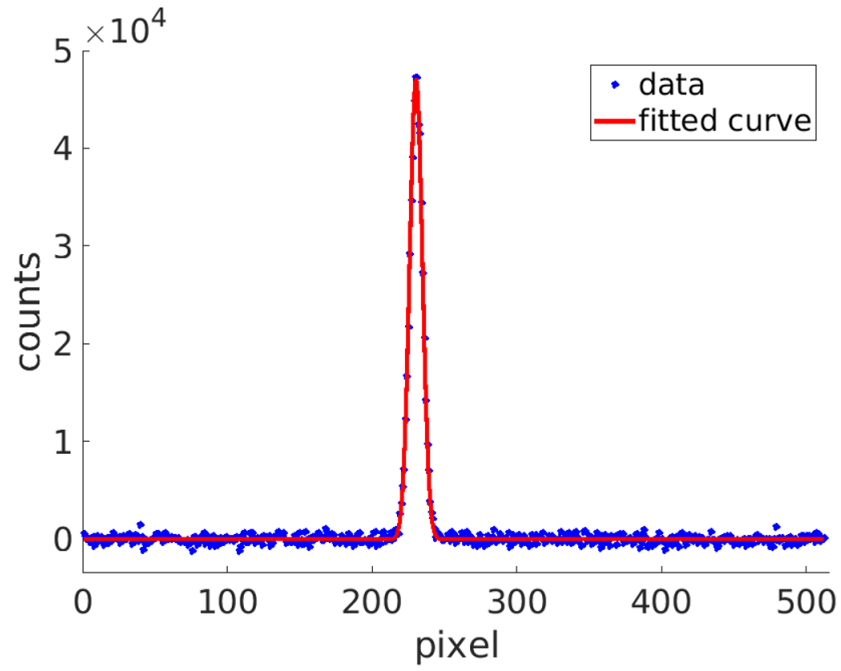


Figure 2.32 – Raw and fitted active C line, discharge #64795 (NBI1-SYS07).

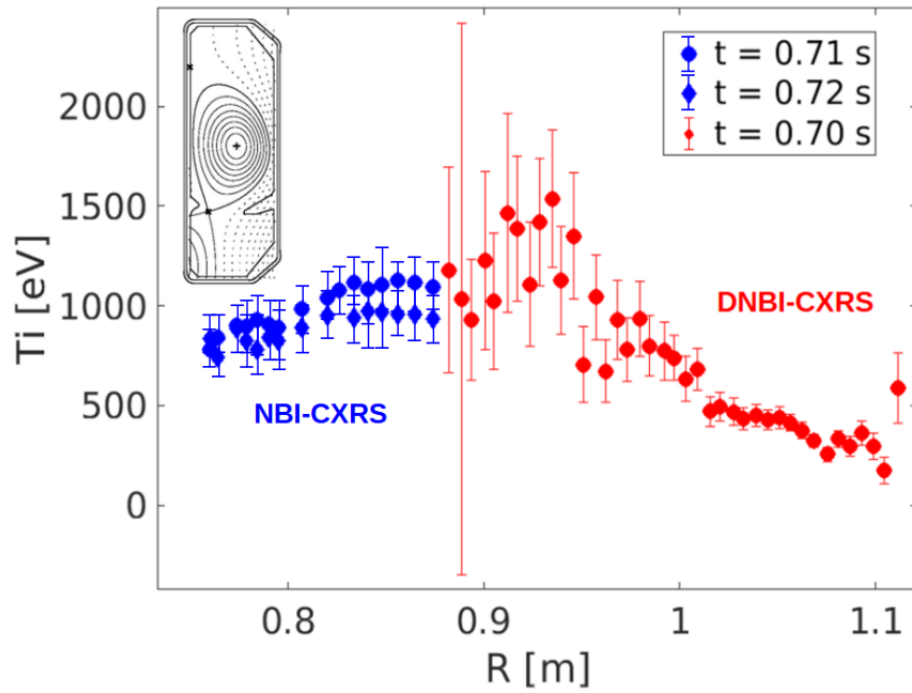


Figure 2.33 – Ion temperature profiles measured by the NBI-CXRS system (blue) and the DNBI-CXRS system (red), discharge #64795.

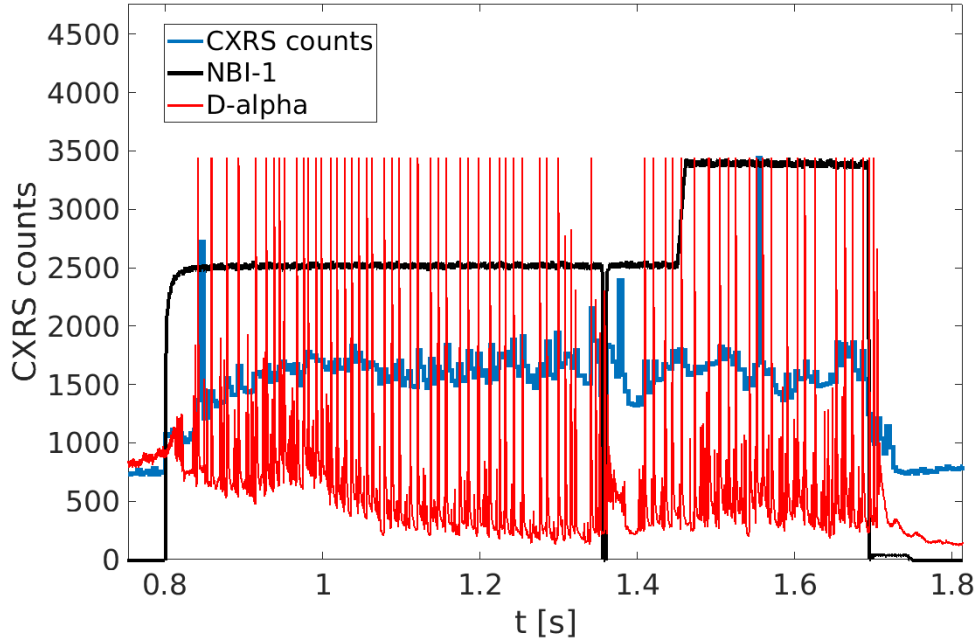


Figure 2.34 – CXRS counts over time, NBI-1 trace and D- $\alpha$  signal, discharge #66164.

augmented by short NBH pulses.

The NBI-1, despite its low energy per amu (not ideal for the CX reaction with C ions), is more powerful and generates denser neutral particle profiles than DNBI. Therefore, it provides a larger number of charge exchange reactions with the impurity ions, yielding a stronger active signal. A discharge with two long NBI power steps was performed to test the NBI-CXRS during ELMy H-modes (Figure 2.34). A 5 ms beam notch was included before the second power step to probe the passive signal. NBI-CXRS acquisition covered the entire beam phase due to the absence of OFF-frames (apart the 5 ms notch). Despite a high ELM frequency, the CXRS integration time was sufficiently low (5 ms) to discard the perturbed time frames whilst maintaining a high temporal coverage. Figure 2.35 shows the active signal percentage for each line of sight. The active signal reaches a peak between  $R = 0.85$  m and  $R = 0.9$  m ( $\sim 60\%$ ), where the beam penetration, and deposition, is highest. The active level never goes below 40%, a great result compared to the DNBI-CXRS, whose active signal is usually  $\leq 20\%$ . Ion temperature profiles during the two beam phases (0.65 MW and 0.85 MW) are shown in Figure 2.36. Unfortunately, DNBI did not fire during this discharge. Therefore, no DNBI-CXRS profiles are available for comparison. However, the increase in  $T_i$  between the two NB steps is compatible with the increasing injected power. This was the first measurement of  $T_i$  profiles performed during an ELMy H-mode with an NBI-CXRS system.

In order to better evaluate the background, a longer beam notch (100 ms) was included during the constant NB power injection (discharge #65424). Figure 2.37 shows the CXRS counts and beams time traces, as well as the D- $\alpha$  signal. As in the previous discharge #64795, a  $\Delta t$  of  $\sim 80$  ms is necessary for the background to relax to pre-injection levels. The discharge was operated

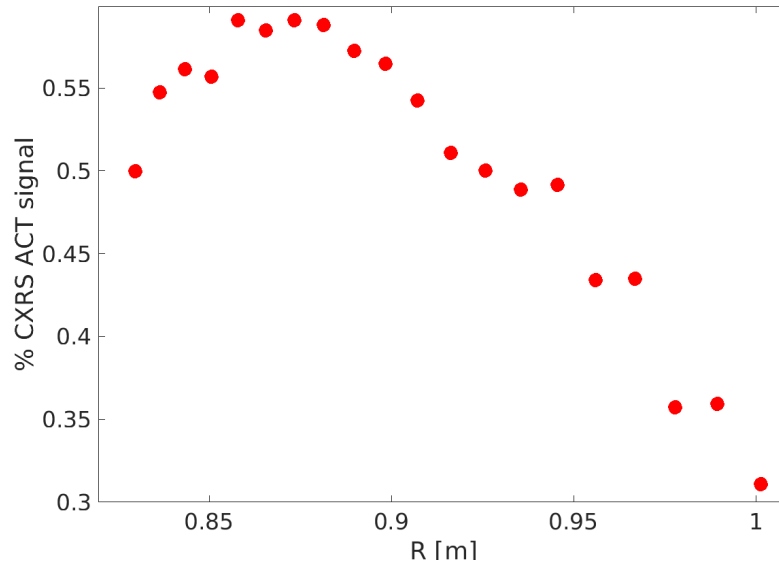


Figure 2.35 – Percentage of the active signal, discharge #66164.

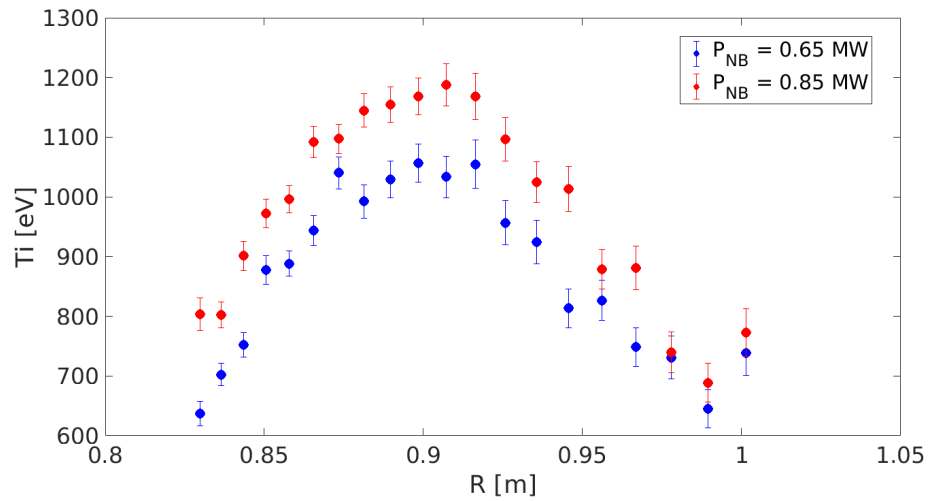


Figure 2.36 – Ion temperature profiles measured by the NBI-CXRS system, discharge #66164. In blue during the 0.65 MW beam phase, in red during the 0.85 MW one.

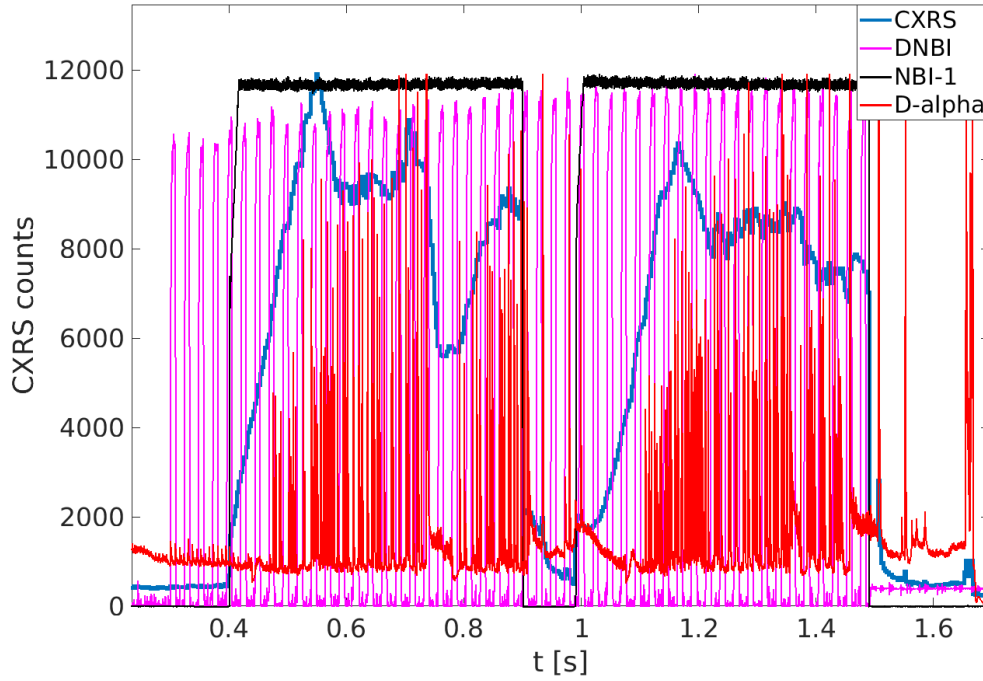


Figure 2.37 – CXRS counts over time, beam traces and D- $\alpha$  signal, discharge #65424.

in limited configuration and the injected NB power was 1.2 MW. Again, the high temporal coverage allows for the omission of ELMs perturbed frames. The active level was similar to the previous discharge. Figure 2.38 shows a comparison between the NBI and DNBI-CXRS  $T_i$  profiles during the first beam pulse. Since the toroidal systems were strongly perturbed by ELMs, the comparison is made with the DNBI-CXRS poloidal LFS system only, which was less affected.

The low values of  $T_i$  result from the executed plasma shape. As can be seen from the LIUQE reconstruction in Figure 2.38, the plasma was not positioned such as to allow on-axis NBI deposition. As the beams intersect the vessel at  $Z = 0$ , the measurements were not up to the core but from a lower temperature region.

Discharges with modulated beam were also performed to test the background subtraction technique and to evaluate how short blips at the maximum available power perturb the plasma. Discharge #66099 was a diverted configuration at high plasma current ( $I_p = -320$  kA) and high density. Six NBI-1 beam blips (6 ms long at 1.2 MW, separated by 12 ms OFF phases) were injected (Figure 2.39). The active signal was particularly high (60%) for the lower-R lines of sight ( $R \sim 0.85$  m), *i.e.* close to the vessel entrance where the beam is injected. However, it decreased rapidly to extremely low values (below 20%), insufficient for a reliable analysis (see the comparison between the active level and the ion temperature profiles in Figure 2.40). This is certainly due to the high density ( $n_e \sim 1.4 \times 10^{20} \text{ m}^{-3}$ ), which prevented optimal beam penetration. Moreover, the neutral beams strong divergence inevitably affects the CXRS active signal on the second-half of the beam path. Discharge #66099 also demonstrates that the beam perturbation is not negligible, despite the low blip period. The  $\beta_{tor}$  trace plotted in Figure

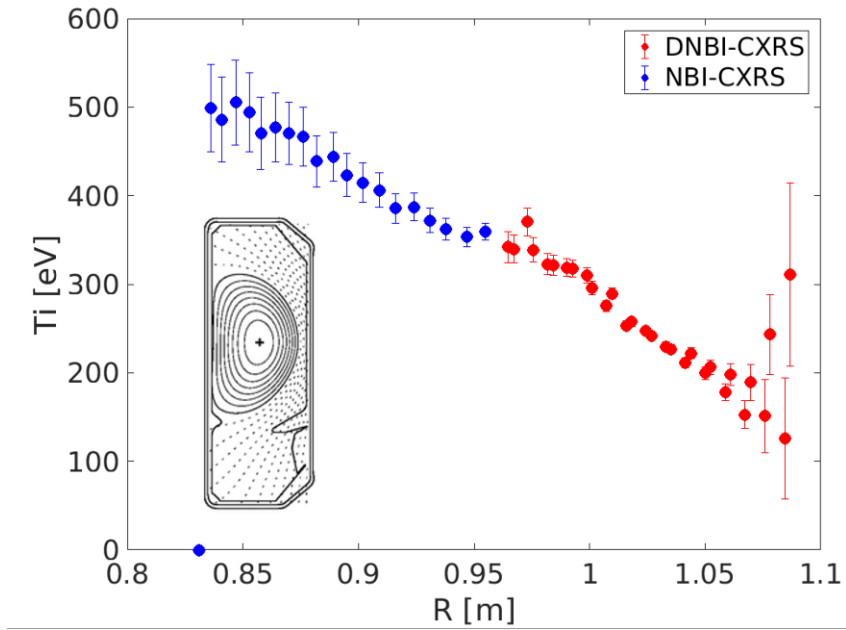


Figure 2.38 – Ion temperature profiles measured by the NBI-CXRS system (blue) and by the poloidal LFS DNBI-CXRS (red), discharge #65424.

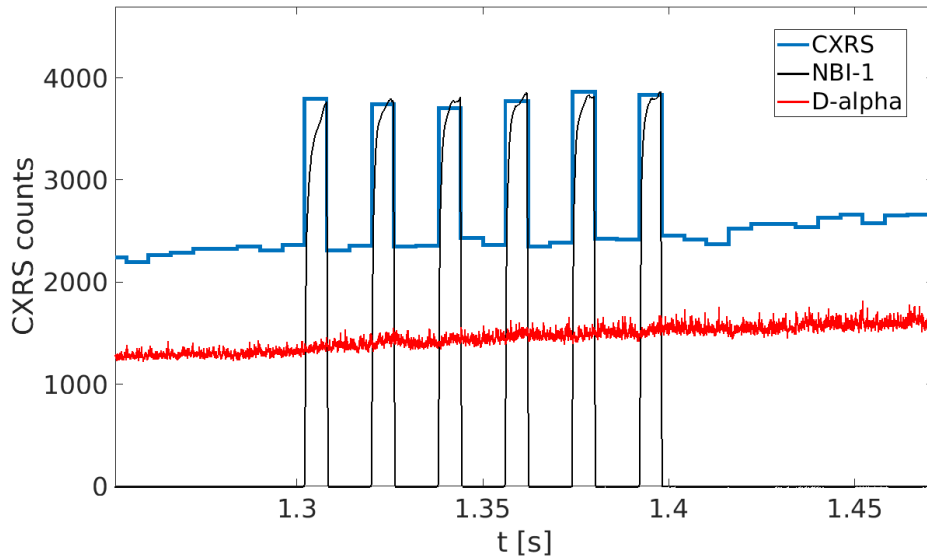


Figure 2.39 – CXRS counts over time, NBI-1 trace and  $D-\alpha$  signal, discharge #66099.

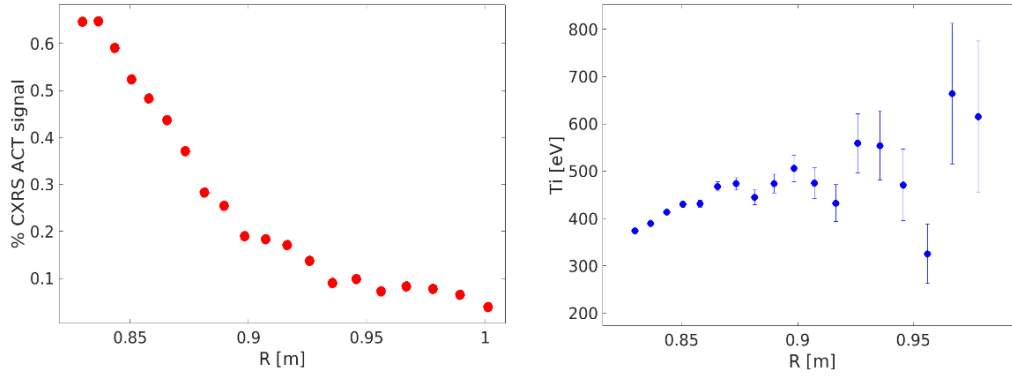


Figure 2.40 – NBI-CXRS active signal (left) and measured  $T_i$  profile, discharge #66099.

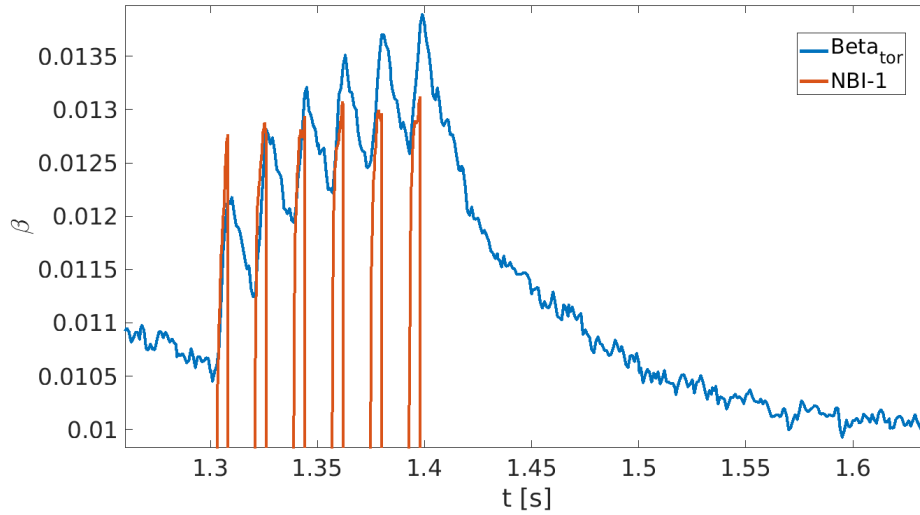


Figure 2.41 –  $\beta_{tor}$  trace and NBI-1 blips, discharge #66099.

2.41 shows a clear increment corresponding to the NBI-1 blips. Therefore, if perturbations must be kept low, for instance in ohmic shots, NBI blips should be short and separated by long OFF-phases. The injected power can then be maximal to provide a higher active CXRS signal. The low active signal, instead, strongly depends on the discharge parameters directly influencing the beam penetration, in particular plasma density, shape and configuration.

In conclusion, as long as short NBI blips are injected, the ordinary subtraction technique applied on the DNBI-systems and described in the previous paragraphs can be employed successfully. However, if the injection scheme envisages power ramps or power steps, short beam OFF-phases should be included to access a background frame for a reliable passive signal subtraction. In presence of constant power injection, instead, background frames can be acquired during the ohmic phases of the discharge or, for a more reliable passive signal subtraction, during short programmed power notches.

The results presented in this section showed that the NBI-CXRS systems yield a high active



signal, strong enough to make ELMs perturbations negligible. Therefore, differently from the DNBI-CXRS systems, they provide reliable measurements of ion temperature profiles during ELMy H-modes.

## **2.8 Impurity content tracking**

The following sections present two initial attempts to track multiple impurities in the same discharge. Since no absolute calibration was available for species other than C, only the intensity of the impurity spectral lines was monitored. The goal of the first experiment was to investigate whether impurities (C, B and O) coming from the vessel walls or from the NBI-2 duct are retained in the core, possibly affecting heating performances. DNBI-CXRS systems were employed during these discharges, with lines of sight in the LFS and HFS. The second experiment featured N seeding, ordinarily injected in TCV to increase the radiative losses in the divertor region and facilitate the access to detachment. Here, short high power NBI-1 blips were injected to monitor the N level, exploiting the higher active to passive ratio expected from NBI-CXRS systems.

The installation of two NBI-CXRS spectrometers opens the exciting possibility of monitoring multiple species during the same discharge, allowing for extended light impurity transport studies, previously performed only for C and B in TCV. The results presented in this section focus rather on the technical aspects of the CXRS impurity tracking system commissioning rather than the physics results of the respective missions.

### **2.8.1 C, B, and O tracking during NBI-2 injection**

After the installation of the second beam injector, it was observed that the neutron rate increased for a short period after the injection, until it reached a saturation level and drastically decreased, despite a supposed, continued, high power beam. The neutron rate decrease was also accompanied by a stagnation of  $T_i$ . A possible explanation for this behaviour could be linked to an increase in the impurity content during beam injection and/or some degree of beam-blocking within the beam's TCV access duct. Impurities, for instance O or B, can be sourced from the beam duct, which is further coated during cleaning processes and can retain impurity particles together with a B rich protection coating. CXRS systems were employed to track the O, B and C evolution.

Unfortunately, these impurity tracking experiments were not planned at the time of recent openings. As described in previous paragraphs, the absolute calibration is a demanding task, which requires access to TCV's vessel. Although the actual calibration measurements (recording of spectra) are quick and take only a few minutes, it can take hours to move the calibration lamp inside the vessel and set it properly for each CXRS system, thus requiring technical staff availability during TCV opening periods, which usually have an extremely tight schedule. Moreover, the LabSphere calibration lamp has a finite lifetime in terms of reliability of its radiance-wavelength spectrum. Therefore, the focus of the calibration measurements

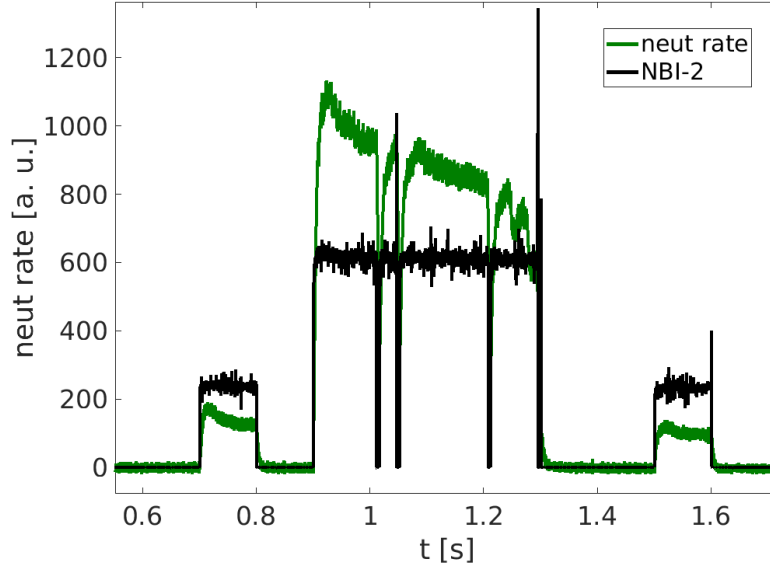


Figure 2.42 – Neutron rate (green) and NBI-2 time trace (black), discharge #73456.

remained on carbon. Other measurements were deemed unnecessary at that time and no absolute calibration on other impurity lines was performed. Consequently, only the active spectra lines intensity evolutions were tracked during these experiments.

Discharge #73456 was a medium density, low current ( $n_e \sim 6 \times 10^{19} m^{-3}$ ,  $I_p = 200 kA$ ) limited plasma configuration, centered close to  $Z = 0$ . NBI-2 was injected in three pulses of [0.24, 1.0, 0.25] MW. The first pulse was separated from the second by a 100 ms beam OFF-phase, whilst a further 200 ms passed between the central and the third pulse by using less perturbative test pulses. The goal was to track possible changes before and after the long powerful central pulse. The initial and final blip, in fact, were kept short and at low power to avoid strong perturbations. If the C, B or O level increased after the long and powerful pulse, that would mean that impurities are retained, providing some explanation for the  $T_i$  stagnation and the decrease in the neutron rate. The neutron rate for discharge #73456 is plotted in Figure 2.42. Figure 2.43 shows the C, B and O active line intensity (in CCD counts) time trace at mid-radius, where the highest line intensity was observed. The NBI-2 injection scheme is plotted in black. Carbon and boron levels increase whenever the beam is turned on or recovers after a short trip. However, no retention is observed, as the impurity level decreases after short spikes. The O level, in general, is not sufficient for a reliable analysis. Only a short spike is observed at mid-radius at the end of the central beam pulse. The C and B level decreases towards the core, whilst the oxygen active line disappears (Figure 2.44). Figure 2.45 shows the B, C and O active and passive spectra at  $t \sim 1.3$  s, where the highest active level was observed. Despite the long central pulse at high power, no significant difference was observed in the impurities level or in the neutron rate between the first and the last blip. The "spikes" in emission were ascribed to "flakes" falling out of the beam duct that were sometimes seen on a video camera view of the beam injection port.

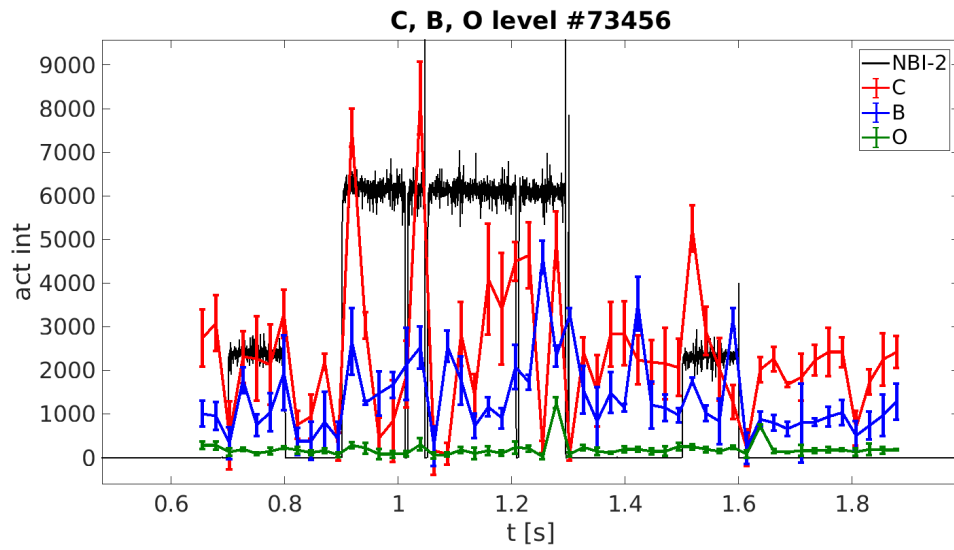


Figure 2.43 – C, B and O level (mid-radius) time trace, overlaid on the NBI-2 pattern, discharge #73456.

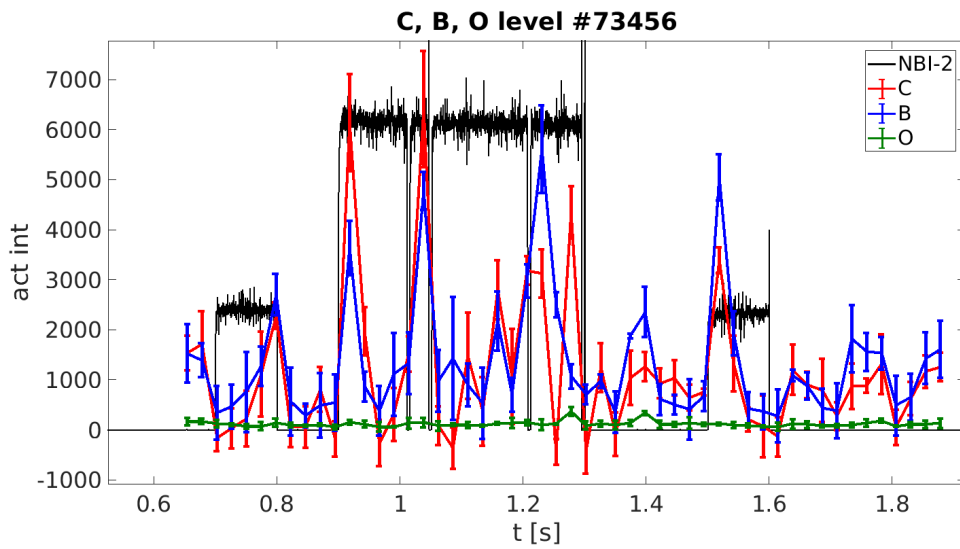


Figure 2.44 – C, B and O level (central  $\rho$ ) time trace, overlaid on the NBI-2 pattern, discharge #73456.

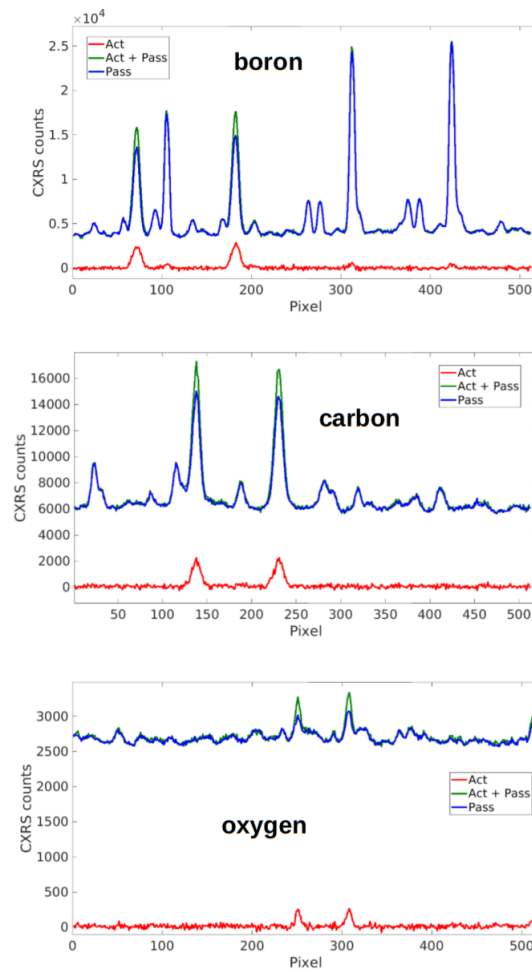


Figure 2.45 – B, C and O active and passive spectra at  $t \sim 1.3$  s, mid-radius, discharge #73456.

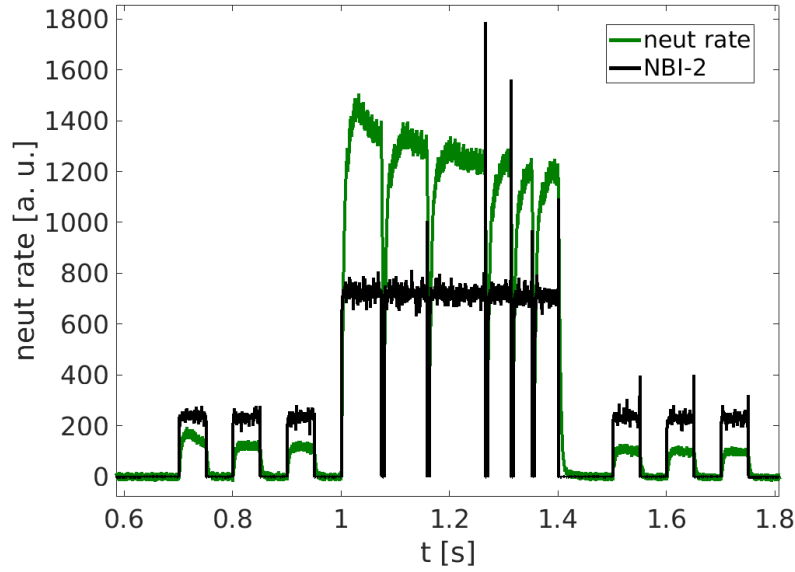


Figure 2.46 – Neutron rate (green) and NBI-2 time trace (black), discharge #73464.

A similar discharge was performed injecting three 0.25 MW short (50 ms) NBI-2 blips, followed by a long pulse at 1.0 MW and, again, three 0.25 MW blips (black line in Figure 2.47). The neutron rate for discharge #73464 is plotted in Figure 2.46. A similar outcome was observed: C and B level increases at the beginning of NBI-2 injection (red and blue traces), only to quickly recover pre-injection levels. The only change in the O active signal is observed at mid-radius (Figure 2.48), where a slight increase is observed during the beam pulses.

No impurity retention was observed during these experiments, disproving the hypothesis that the decrease in  $T_i$  and in the neutron rate was caused by the accumulation of impurities coming from the NBI vessel. The remaining hypothesis is that the beam is being, at least, partially blocked in the duct by a gas pressure build up that will be further probed by direct spectroscopy of the beam duct region. It also tells us that the whole beam has not yet entered the plasma, providing strong hope for increased plasma heating and an even stronger CXRS-NBHII signal in the future. In this situation, the C-level deduced from NBH high power injection will be far lower than from the DNB measurement since the delivered neutral density will be highly attenuated.

### 2.8.2 N tracking in detachment studies

Nitrogen level evolution was monitored during detachment experiments featuring N seeding. Since previous attempts with the DNBI-CXRS systems were unsuccessful, as the N active level was too low to be measured, the NBI-CXRS system was employed. Seven 5 ms beam blips at full power (1.3 MW) were injected every 100 ms from  $t = 0.5$  s until the disruption.

Figure 2.49 shows a spectrum acquired during one of the NBI-1 blips. The dashed line corresponds to the NVII ( $n = 9 \rightarrow 8$ ) line at  $\lambda = 566.9$  nm. The active to passive ratio was 70-80% until

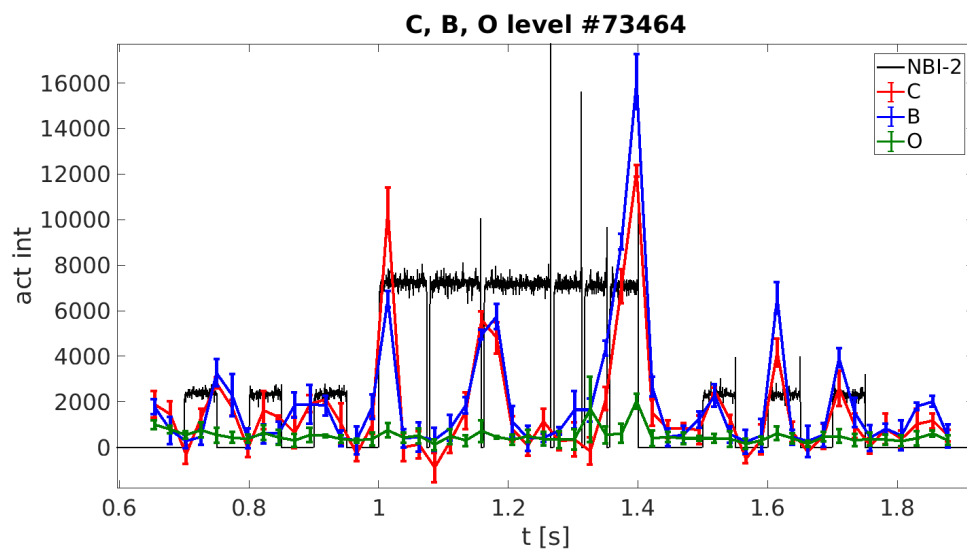


Figure 2.47 – C, B and O level (core region) time trace, overlaid on the NBI-2 pattern, discharge #73464.

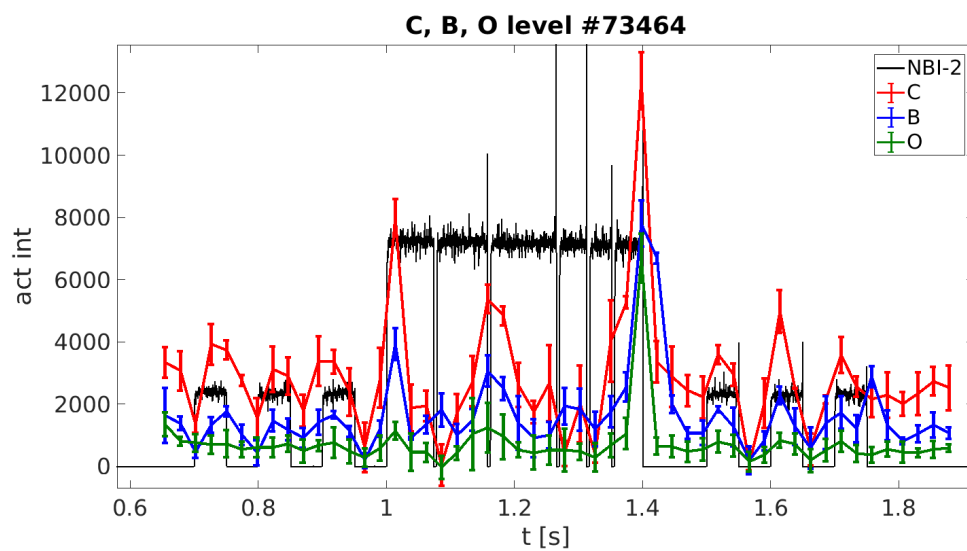


Figure 2.48 – C, B and O level (mid-radius) time trace, overlaid on the NBI-2 pattern, discharge #73464.

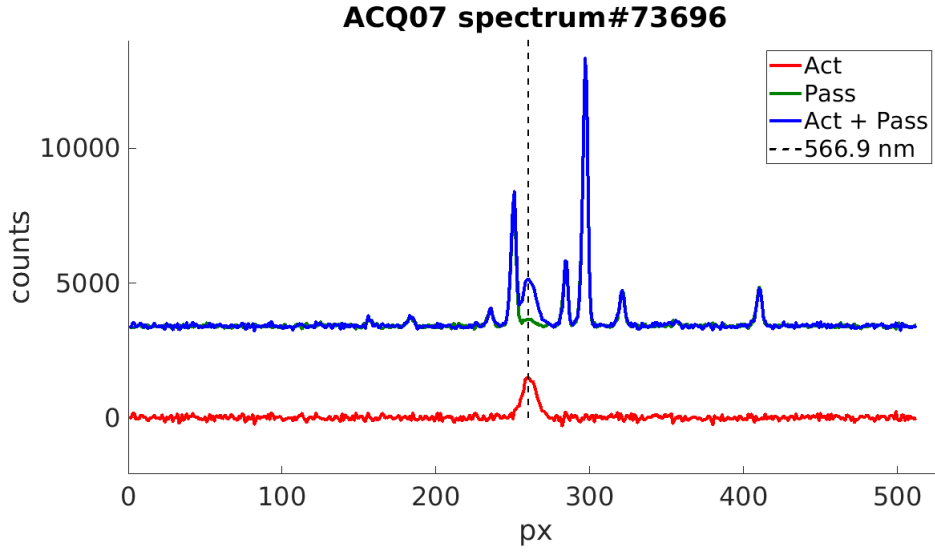


Figure 2.49 – N spectrum acquired during an NBI-1 blip, discharge #73696.

$R \sim 0.95$  m, *i.e.* at mid-radius, where it decreased to 55%. N seeding started at  $t = 0.8$  s. The intensity of the active N line is plotted in Figure 2.50 as a function of time at different positions. Interestingly, the intensity increases in the core region ( $R = [0.83 - 0.9]$  m) after N is injected, whilst only a slight increase is observed at mid-radius. As a test,  $T_i$  profiles were calculated from the N active spectra and compared to the DNBI-CXRS carbon impurity measurements. An example is shown in Figure 2.51. Despite the strongly scattered NBI-CXRS data points, the two profiles match, showing a good agreement between systems observing different impurity lines and installed at different positions and using different neutral beam sources.

These results strongly encourage further improvements of the NBI-CXRS systems, with the goal of employing them routinely during TCV operations. Since N injection will be further explored in TCV's divertor research program, this technique offers, for the first time on TCV, a method to assess N plasma core density evolution with the goal of using N to control divertor radiation/detachment whilst retaining sufficient plasma core performance.

## 2.9 ELMy H-modes: comparison between DNBI and NBI-CXRS systems

Following the promising results from the commissioning discharges, NBI-CXRS systems were employed during experiments involving high power neutral beam injection, including H-mode scenarios with strong ELMs that were, hitherto, inaccessible to CXRS. These experiments present an ideal scenario to compare DNBI and NBI-CXRS systems measurement capabilities in challenging discharges like those featuring ELMy H-modes.

Discharge #74257 was a diverted plasma configuration featuring an  $n_e$  and an  $I_p$  ramp, with the addition of NBI-1 injection as shown in Figure 2.52. The plasma accessed H-mode at 0.7

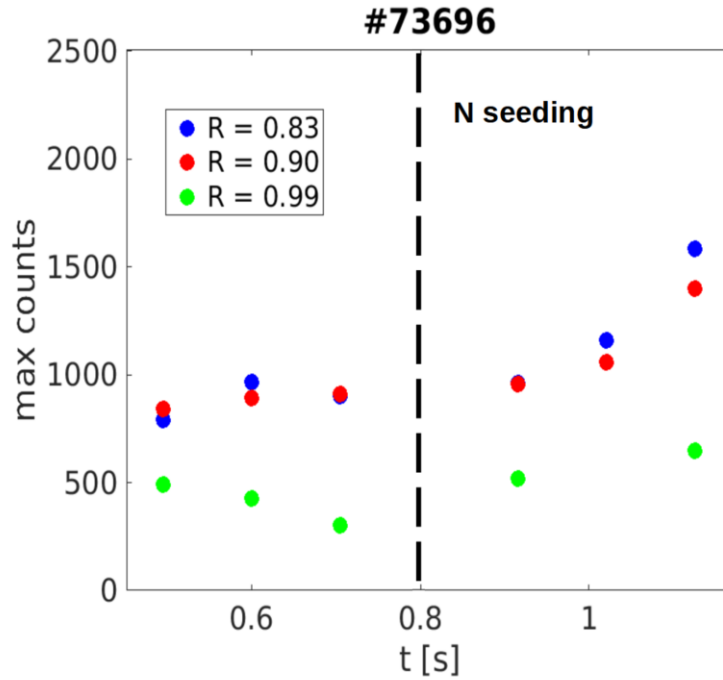


Figure 2.50 – Intensity of the active N line as a function of time and at different positions, discharge #73696. An increase of the measured spectral line intensity was observed after  $t = 0.8$  s, when N seeding started.

s, developing strong ELMs before a constant beam phase. Figure 2.53 shows a comparison between profiles measured by DNBI and NBI-1 systems before and during the ELM phase. During the early phase of the neutral beam injection, when the plasma was still in L-mode, a good agreement between the ion temperature profiles measured by the DNBI and the NBI-CXRS systems is observed (Figure 2.53-a). The poor data quality of DNBI-SYS02 is due to an unexpectedly low active signal, leading to highly scattered results with large uncertainties, caused by a strong DNBI attenuation in the LFS. As the plasma accesses H-mode ( $t = 0.7$  s), high frequency ELMs develop. Consequently, SYS01 (toroidal LFS) and SYS02 (toroidal HFS) background signal is strongly perturbed and their data quality plummets (Figure 2.53-b and c). This was the legacy situation on TCV when only DNBI was available. If the ELMs frequency was too high, multiple ELMs could occur during each CXRS time frame, making a reliable analysis impossible. As the active to passive ratio was already low, reducing the integration time was not viable. SYS03 (poloidal LFS) often provides a higher active signal compared to the other systems. However, its passive spectra were strongly affected by ELMs, reducing the number of reliable time frames available for analysis. Figure 2.53-b and c show the high quality of NBI-SYS07  $T_i$  profiles compared to DNBI-CXRS systems. As often occurs during ELMy H-modes, DNBI-CXRS systems overestimate  $T_i$  and provide highly unreliable profiles. It should be recalled that almost any error in the background subtraction will result in over-wide line profiles that will be interpreted as a higher temperature.

With high data quality, NBI-SYS07 was employed in these experiments to monitor the central



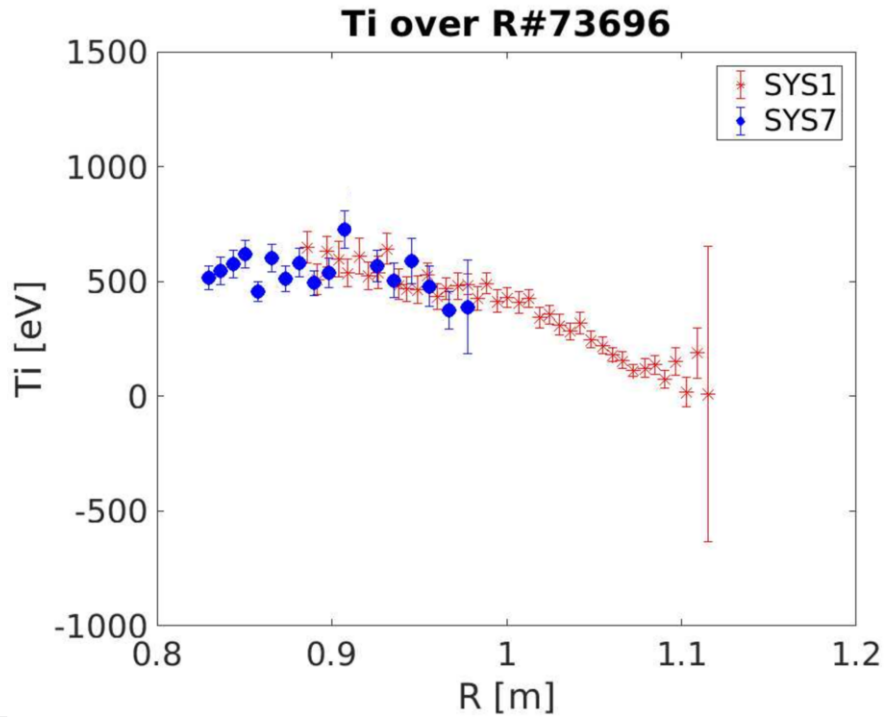


Figure 2.51 – Example of ion temperature profile measured by SYS07 (NBI, blue) and SYS01 (DNBI, red), discharge #73696. Despite the highly scattered data points, the two profiles match.

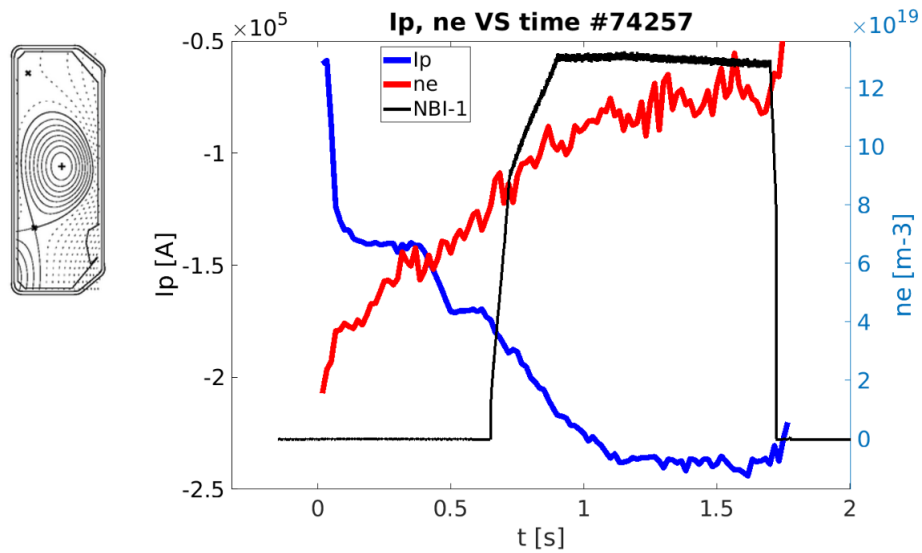


Figure 2.52 –  $I_p$ ,  $n_e$  and NBI-1 traces, discharge #74257.

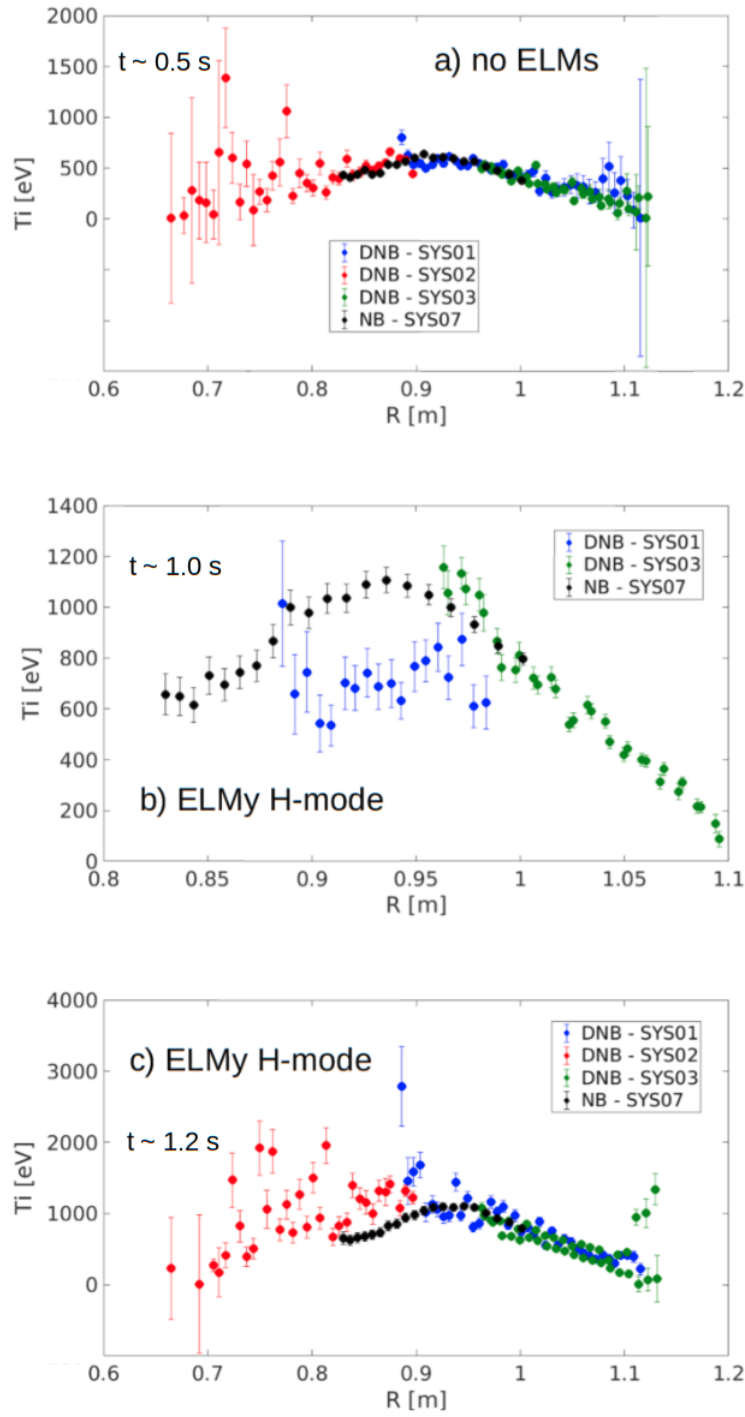


Figure 2.53 –  $T_i$  profiles measured by DNBI and NBI-1 CXRS systems before and during an ELMy H-mode, discharge #74257. The high quality of NBI-SYS07  $T_i$  profiles (compared to DNBI-CXRS systems) is visible. As often occurs during ELMy H-modes, DNBI-CXRS systems overestimate  $T_i$  and provide highly unreliable profiles.

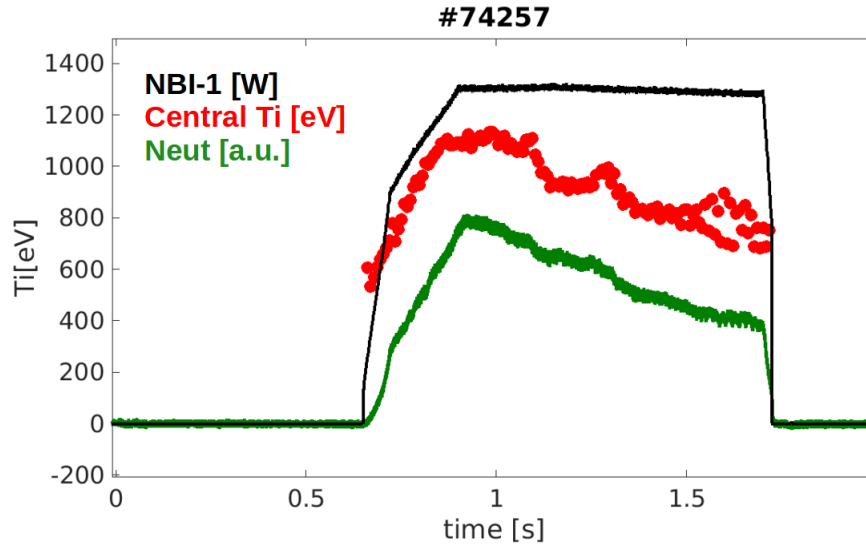


Figure 2.54 – Central  $T_i$  measured by NBI-SYS07 overlaid to the NBI-1 power time trace (black) and neutrons signal (green), discharge #74257. Small neutron rate changes during the constant beam phase are accompanied by small increases or decreases of  $T_i$ , proving the high quality of the NBI-CXRS system measurements.

ion temperature evolution, to track changes in  $T_i$  during the constant  $I_p$ -constant  $P_{NB}$  phase, where the density increase was expected to be accompanied by a decrease in heating and plasma  $\beta$ . The high quality of SYS07 data was supported by the comparison to the neutrons trace (green line in Figure 2.54), where even small neutron rate changes during the constant beam phase are accompanied by small increases or decreases of  $T_i$ .

## 2.10 Conclusions

The CXRS diagnostic systems were described in detail in this section. Measurement principles, calibrations and analysis techniques were explained. The low power diagnostic beam (DNBI), as well as the neutral beam heating systems (NBI-1 and NBI-2) were described and the most recently installed spectrometers which feature NBI-1 and NBI-2 as a source of neutrals for the CX reaction introduced.

The continuing advantage of TCV's CXRS DNBI-systems resides in the exploitation of a non perturbing beam as a source of neutrals, that remains an ideal tool for intrinsic rotation measurements. The downside of low power beams is the relatively lower active signal level. However, optimisation of the DNBI in terms of energy of the injected neutrals and the implementation of the DNBI modulation for the passive spectra subtraction technique often provides more than sufficient active to passive signal ratios for accurate spectra analysis. It is to be noted that, during this work, the DNB was concluded to have undergone a change in focal length (4 m  $\rightarrow$  2 m) and the full energy beam component was mostly limited to 48 kV or below. It can be expected that, with a refocussed beam and with a more appropriate power

supply, a S/N gain of 2-5 may be possible from DNBI-CXRS without increasing the plasma perturbation.

On the other hand, the heating beams, due to their high power and neutral density, provide a strong neutral source for CX reactions, yielding a higher active to passive ratio than DNBI-CXRS. The results presented in this chapter showed that spectra from multiple impurities can be robustly measured during the same discharge. C, B and O levels were monitored during NBI injection with the DNBI-CXRS systems, whilst a strong N active level was successfully observed during weak N seedings in TCV detachment studies with one of the NBI-CXRS spectrometers. These experiments showed that the NBI-CXRS systems yield robust signals even with species other than C, opening possibilities to multiple impurities transport studies in TCV. Moreover, the NBI-CXRS systems proved to provide reliable measurements during ELMy H-modes, where the legacy DNBI-CXRS spectra are ordinarily too strongly perturbed for reliable analysis. Therefore, the recently installed spectrometers are a powerful tool for ion temperature measurements in discharges involving high power heating beam injection and ELMy H-modes.

### 3 Rotation and particle transport: phenomenology and theoretical background

This chapter presents an overview of plasma rotation and particle transport in tokamaks from a theoretical perspective, focusing on fundamental aspects needed for the interpretation of the experimental results.

A tokamak plasma is a complex system in terms of rotation with two coupled privileged directions: parallel and perpendicular to the magnetic field. The former is the direction which charged particles are constrained (on average) to follow in absence of collisions and magnetic field line turbulence. The latter (perpendicular) is a preferential direction imposed by the symmetry of the system.

The two terms are coupled through collisions (fast time scales) or instabilities (long time scales). This separation is at the base of the physics determining the state of the plasma in terms of rotation.

The last section focuses on light impurity transport. In particular, momentum transport and turbulent fluxes are addressed, since these are the concepts that will be employed to discuss experimental results later on.

#### 3.1 Plasma rotation and momentum balance equation

Two main approaches are often used to describe a plasma: statistical mechanics and fluid models. The two methods, with due approximations, are equivalent in that they attempt to model the same phenomena.

From a statistical point of view, a plasma is a system composed of a variety of interacting charged and neutral particles: electrons, ions (main ions and impurities) and neutrals [38]. The behaviour of such a system is described by the Boltzmann equation 3.1 [26], which tracks the evolution of the distribution function  $f_\alpha(\mathbf{x}, \mathbf{v}, t)$  of the species  $\alpha$

$$\frac{\partial f_\alpha}{\partial t} + \mathbf{v} \cdot \nabla f_\alpha + \frac{\mathbf{F}}{m_\alpha} \cdot \nabla_{\mathbf{v}} f_\alpha = \left( \frac{\partial f_\alpha}{\partial t} \right)_{coll} \quad (3.1)$$

The distribution function changes as a function of forces  $\mathbf{F}$  and collisions (right hand side of equation 3.1). In a magnetically confined plasma, the main force is the Lorentz  $\mathbf{F} = q(\mathbf{E} + \mathbf{v} \times \mathbf{B})$ .

Collisions between particles of the same or different species result in phenomena that can be interpreted as friction forces, viscosity and electrical resistivity [82].

For a full description of a collisional plasma, it would be necessary to solve the Boltzmann equation together with Maxwell equations [97] with an appropriate model for the collisional term [82]. As this is a very complex problem (where many of the required parameters are, in themselves, complex), a fluid description is often employed as a reasonable approximation of the system.

A multi-fluid description is obtained evaluating moments of Boltzmann equation. The mass and momentum conservation equations for species  $\alpha$  are obtained from the first and second moments, respectively [38] [82]

$$\frac{dn_\alpha}{dt} + n_\alpha \nabla \cdot \mathbf{u}_\alpha \quad (3.2)$$

$$m_\alpha n_\alpha \frac{d\mathbf{u}_\alpha}{dt} = n_\alpha q_\alpha (\mathbf{E} + \mathbf{u}_\alpha \times \mathbf{B}) - \nabla \cdot \mathbf{P}_\alpha + \mathbf{R}_\alpha + \mathbf{S}_\alpha \quad (3.3)$$

where the total derivative is defined as  $\frac{d}{dt} = \frac{\partial}{\partial t} + \mathbf{u}_\alpha \cdot \nabla$ . The definitions for the number density  $n_\alpha$ , the fluid velocity of the species  $\mathbf{u}_\alpha$  and the pressure tensor  $\mathbf{P}_\alpha$  are the following:

$$n_\alpha = \int f_\alpha d\nu \quad (3.4)$$

$$\mathbf{u}_\alpha = \int \nu f_\alpha d\nu \quad (3.5)$$

$$\mathbf{P}_\alpha = n_\alpha m_\alpha (\nu - u_\alpha)(\nu - u_\alpha) \quad (3.6)$$

$\mathbf{R}_\alpha$  is the friction term (i.e. the momentum transfer due to collisions between different plasma species) and  $\mathbf{S}_\alpha$  is the momentum source (including any externally applied torques). Further considerations on momentum transport are described below.

A further simplification can be obtained by summing over all particle species to obtain a single fluid description, where mass, particle density and velocity are described as follows:

$$m = \sum_\alpha m_\alpha \quad (3.7)$$

$$n = \frac{\sum_\alpha m_\alpha n_\alpha}{\sum_\alpha m_\alpha} \quad (3.8)$$

$$\mathbf{u} = \frac{\sum_\alpha m_\alpha n_\alpha \mathbf{u}_\alpha}{\sum_\alpha m_\alpha n_\alpha} \quad (3.9)$$

Different species may flow with different vector velocities in an impure plasma. However, if the impurity concentration is low (i.e.  $n_i \gg n_\alpha$ ,  $\alpha \neq i$ ), given that  $m_e \ll m_i$ , the single fluid velocity often reduces well to that of the main ion species, thus  $\mathbf{u} \approx \mathbf{u}_i$  [77].

In a stationary situation ( $\frac{d}{dt} = 0$ ), neglecting friction forces between other species and considering isotropic pressure and no external momentum sources ( $\mathbf{R}_\alpha = 0$  and  $\mathbf{S}_\alpha = 0$ ), these

### 3.1. Plasma rotation and momentum balance equation

equations reduce to

$$n_\alpha \nabla \cdot \mathbf{u} = 0 \quad (3.10)$$

$$\nabla p_\alpha = q_\alpha n_\alpha (\mathbf{E} + \mathbf{u} \times \mathbf{B}) \quad (3.11)$$

Equation 3.11 is known as force balance equation [38] [73]. It shows that the Lorentz force is balanced by the plasma pressure, to lowest order. If we take the cross product between the force balance equation and the magnetic field  $\mathbf{B}$ , a formulation for the perpendicular velocity is found

$$\mathbf{u}_\alpha^\perp = \mathbf{u}_{\mathbf{E} \times \mathbf{B}} + \mathbf{u}_\alpha^* \quad (3.12)$$

$$\mathbf{u}_{\mathbf{E} \times \mathbf{B}} = \frac{\mathbf{E} \times \mathbf{B}}{B^2} \quad (3.13)$$

$$\mathbf{u}_\alpha^* = -\frac{1}{q_\alpha n_\alpha} \frac{\nabla p_\alpha \times \mathbf{B}}{B^2} \quad (3.14)$$

From the force balance equation, it is seen that  $\mathbf{u}_\alpha^\perp$  is determined by drift velocities due to  $q_\alpha n_\alpha \mathbf{E}$  and  $-\nabla p$ . The former is termed the  $\mathbf{E} \times \mathbf{B}$  drift and affects all particle species in the same way. The last term is the diamagnetic drift, which depends on the particle charge and, consequently, has opposite sign for ions and electrons.

$\mathbf{u}_\alpha^\perp$  is the lowest order solution of the force balance equation. It shows that electric fields and pressure gradients constitute the primary sources for plasma velocity equilibria.

The flow described by this equation is established in the fast compressional Alfvénic range ( $\tau_A \sim [1 - 100] \mu\text{s}$ ), representing the zero order of the gyroradius expansion [30]. On longer timescales, any plasma bulk motion evolves according to the parallel force balance equation on ion-ion collisional timescales ( $\tau_{i-i} \sim \mu\text{s}$ ) and upon the toroidal force balance on transport timescales ( $\tau_{tr} \sim [10 - 100] \mu\text{s}$ ) in TCV, determining the final rotation state [30]. It is for this reason that the momentum and ion equilibrium timescales are often close and closely linked. Rotation in tokamaks is often decomposed into perpendicular and parallel directions and, from symmetry measurements, into toroidal and poloidal directions, as explained in the following paragraph.

#### 3.1.1 Rotation decomposition

Rotation in tokamaks is often decomposed into perpendicular and parallel to the radial direction (see Figure 3.1)

$$\mathbf{u}_\alpha = u_{\alpha,\parallel} \mathbf{b} + \mathbf{u}_{\alpha,\perp} \quad (3.15)$$

Where  $\mathbf{b} = \frac{\mathbf{B}}{|\mathbf{B}|}$ .

Perpendicular velocity ( $\mathbf{u}_{\alpha,\perp}$ ) is described by equation 3.12. As both  $\nabla p_\alpha$  and  $\mathbf{E} = -\nabla \phi_{el}$  (radial electric field) are parallel to the radial direction  $\nabla \psi$  (see cross product in eq. 3.13 and 3.14),  $\mathbf{u}_{\alpha,\perp}$  is perpendicular to it. The fluid velocity ( $\mathbf{u}_\alpha$ ), therefore, lies on a magnetic flux surface. The parallel dynamics sets the value of poloidal rotation to ion collisional timescales, whilst

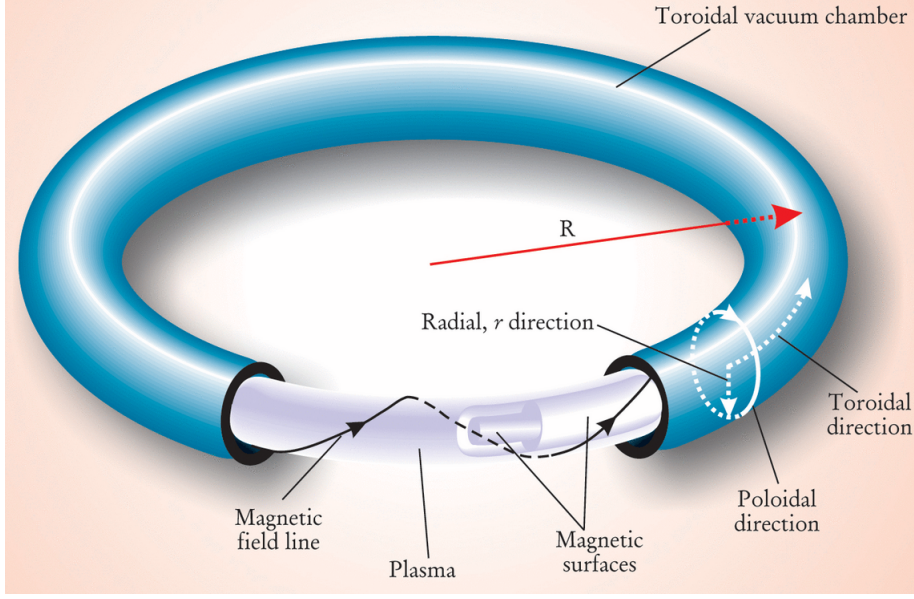


Figure 3.1 – Schematic of a tokamak, showing the toroidal, poloidal, and radial directions [80].

the toroidal dynamics generates the radial fluxes that determine the rotation evolution on transport timescales.

In tokamaks (from symmetry measurements), it is often useful to further decompose velocities into the toroidal and poloidal directions. The standard TCV coordinate system for equilibrium description is an  $(r, \theta, \phi)$  system where:

- $r = 0$  at the magnetic axis;
- $e_\phi$  is directed anti-clockwise viewing from the top;
- $e_\theta$  is directed downward in the Low Field Side region,  $\theta = 0$  at High Field side midplane;

Figure 3.2 is a schematic representation of the poloidal and toroidal directions, following the conventions used in TCV (see also [127] for details about TCV's sign convention).

Fluid velocity  $\mathbf{u}_\alpha$  can therefore be written as

$$\mathbf{u}_\alpha = u_{\alpha,\phi} \mathbf{e}_\phi + u_{\alpha,\theta} \mathbf{e}_\theta \quad (3.16)$$

where  $\mathbf{e}_\phi = \frac{1}{R} \nabla \phi$  and  $\mathbf{e}_\theta$  is the unit vector in the direction  $\nabla \phi \times \nabla \psi$ , which corresponds to the geometrical angle  $\theta$  direction for circular concentric flux surfaces. These two velocities lie on a magnetic flux surface and define plasma rotation [30].

To lowest order, the radial component is often neglected. It is, however, responsible for the radial particle flux  $\Gamma_\rho$  often addressed in momentum transport studies:

$$\Gamma_\rho = m_\alpha n_\alpha u_{\alpha,\rho} \quad (3.17)$$



### 3.1. Plasma rotation and momentum balance equation

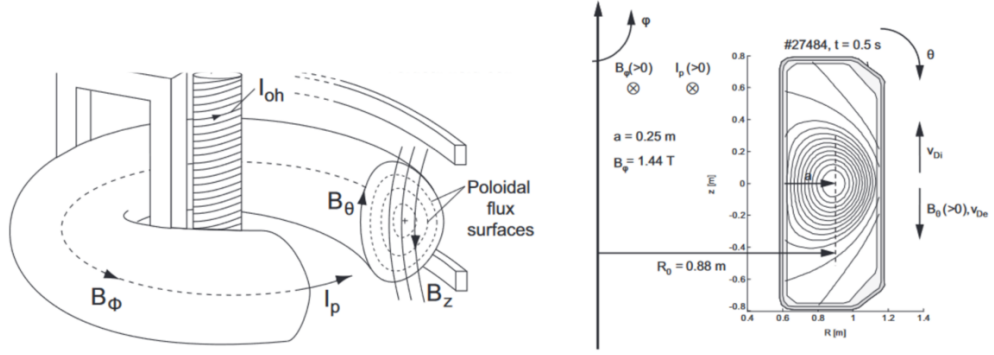


Figure 3.2 – Schematic of the directions of plasma current, magnetic fields, ion and electron diamagnetic velocities, following the conventions used in TCV.

where  $u_{\alpha,\rho} = \mathbf{u}_\alpha \frac{\nabla\psi}{|\nabla\psi|}$ .

Assuming incompressional rotational flow [82],  $\nabla \cdot (n_\alpha \mathbf{u}_\alpha) = 0$ , and considering impurity density to be constant over a flux surface, the following general expressions are found [79]:

$$\mathbf{u} = \omega(\rho) R \mathbf{e}_\phi + U_\theta(\rho) \mathbf{B} \quad (3.18)$$

$$u_\phi = \omega(\rho) R + U_\theta(\rho) B_\phi \quad (3.19)$$

$$u_\theta = U_\theta(\rho) B_\theta \quad (3.20)$$

$\omega$  (toroidal rotation frequency) and  $U_\theta$  (fluid velocity over the poloidal direction normalised to the poloidal magnetic field) are constant over a flux surface as they depend upon  $\rho$  alone. However, when we decompose the fluid velocity into its toroidal and poloidal components, equations 3.19 and 3.20 show that they depend explicitly upon the poloidal and toroidal magnetic fields, respectively. Therefore, neither the toroidal nor the poloidal velocities are flux surface constants and neither is the angular velocity  $\omega_\theta = \frac{u_\theta}{r}$ , often used to describe rotation. When the poloidal velocity is negligible, for instance when a strong external torque is applied, the approximation of a rigid rotation (like a spinning torus) holds. Nevertheless, a correction related to the poloidal velocity should be included whenever the toroidal velocity does not dominate. In the case of TCV intrinsic rotation, this approximation does not always hold, since the poloidal velocity is not negligible (it should be noted that, in many machines where the toroidal rotation is driven by tangential neutral heating beams, this approximation is often acceptable).

### 3.1.2 Momentum transport

Equation 3.3 can be recast as a continuity equation of the form [82]

$$\frac{\partial m_\alpha n_\alpha \mathbf{u}_\alpha}{\partial t} + \nabla \cdot \mathbf{\Pi}_\alpha = n_\alpha q_\alpha (\mathbf{E} + \mathbf{u}_\alpha \times \mathbf{B}) + \mathbf{R}_\alpha + \mathbf{S}_\alpha \quad (3.21)$$

$$\mathbf{\Pi}_\alpha = \mathbf{I}p_\alpha + \boldsymbol{\pi}_\alpha + m_\alpha n_\alpha \mathbf{u}_\alpha \mathbf{u}_\alpha \quad (3.22)$$

The three terms composing the momentum flux  $\mathbf{\Pi}_\alpha$  are the isotropic pressure, the viscosity and inertial terms.

Equation 3.21 describes the rate of momentum change in a given volume element. This quantity is determined by two factors. The first is the exchange of momentum through the given volume described by the divergence of  $\mathbf{\Pi}_\alpha$  and the second, the sum of all forces acting upon the volume: electromagnetic, friction and external forces. The momentum flux  $\mathbf{\Pi}_\alpha$  is composed of convective terms, proportional to the velocity, diffusive terms, proportional to the velocity gradient, and additional terms proportional to the temperature and density gradients known as residual stress, that neither fit with a convective nor diffusive term. This latter term is thought to be responsible for the intrinsic rotation that develops in tokamaks. Neoclassical predictions often disagree strongly with experimental observations [85], with the result that phenomena like the intrinsic rotation reversal remain unexplained [150] [119] [31] (see also [171] for an in depth discussion of neoclassical transport processes).

A more comprehensive treatment of particle and momentum transport was performed in the frame of gyrokinetic theory [137], including the effects of turbulence. In general, the mean field momentum flux driven by electrostatic turbulence is given by [49]:

$$\Pi_{r,\phi} = \langle n \rangle \langle \tilde{v}_r \tilde{v}_\phi \rangle + \langle \tilde{v}_r \tilde{n} \rangle \langle v_\phi \rangle + \langle \tilde{n} \tilde{v}_r \tilde{v}_\phi \rangle \quad (3.23)$$

Here the first term is the toroidal Reynolds stress and the second is the convective flux. The third term,  $\langle \tilde{n} \tilde{v}_r \tilde{v}_\phi \rangle$ , represents the nonlinear flux (as opposed to quasi-linear), driven by processes such as mode-mode coupling and turbulence spreading. The Reynolds term can be further decomposed as [96]:

$$\langle \tilde{v}_r \tilde{v}_\phi \rangle = -\chi_\phi \frac{\partial \langle v_\phi \rangle}{\partial r} + V \langle v_\phi \rangle + \Pi_{r,\phi}^R \quad (3.24)$$

Where  $\chi_\phi$  is the turbulent viscosity,  $V$  is the convective velocity (or velocity pinch) and  $\Pi_{r,\phi}^R$  is, again, the residual stress. The residual stress defines an effective local internal toroidal momentum source

$$\frac{\partial \langle P_\phi \rangle}{\partial t} = S_{\phi, internal} = -\frac{\partial}{\partial r} (\langle n \rangle \Pi_{r,\phi}^R) \quad (3.25)$$

It is, therefore, crucial for the development of intrinsic rotation. The residual stress is a function of ion and electron temperature, pressure and density gradients, and it converts part of the driving heat flux  $Q_i$  and  $Q_e$  to a net toroidal flow. A thorough overview of residual stress and turbulent momentum transport, that is beyond the scope of this thesis, can be found in [49] [153].

## 3.2 Radial electric field

The presence of a radial electric field  $E_r$  at the edge of tokamaks, especially in H-mode, has been well documented in many machines like AUG [182], C-MOD [121], DIII-D [72], JET [1], JFT-2M [92], NSTX [14] and MAST [126].

Although several processes have been investigated as possible sources of  $E_r$ , no comprehensive theory is able to predict its magnitude. One of the main reasons for this is that there is no single process leading to the formation of  $E_r$ , but rather a combination of multiple phenomena [168]: plasma heating, which causes charge imbalance by expanding ion orbits more than electrons', turbulent transport that may not be ambipolar [170], imperfections in the magnetic field surfaces that allow electrons to escape or, again, first orbit losses in fast particles generated by neutral beam injection, and more [184] [182].

However, the connection between plasma flow and  $E_r$  is paramount in tokamak physics. Such a radial electric field generates a strong rotation shear that helps suppressing turbulence and this is thought to be the mechanism that drives an edge transport barrier (ETB) that characterises the H-mode energy confinement improvement [18]. Moreover, all charged particles are directly affected by  $E_r$ . The radial electric field can be defined starting from the force balance equation 3.11 evaluating it in the radial  $\nabla\psi$  direction

$$E_r = \frac{1}{n_\alpha q_\alpha} \frac{\partial p_\alpha}{\partial r} - u_{\alpha,\theta} B_\phi + u_{\alpha,\phi} B_\theta \quad (3.26)$$

The magnetic field components  $B_\phi$  and  $B_\theta$  are retrieved from LIUQE magnetic reconstruction. All the other quantities are measured by CXRS.

Applying the first order flow equations 3.19 and 3.20 on 3.26 we obtain [23]

$$E_r = \frac{1}{n_\alpha q_\alpha} \frac{\partial p_\alpha}{\partial r} + \omega R B_\theta \quad (3.27)$$

which allows the determination of  $E_r$  even at poloidal positions not covered by any system. The shearing rate mentioned above can be quantified by the rate of change of  $E_r$  across the flux surfaces, i.e. the  $\mathbf{E} \times \mathbf{B}$  shearing rate defined as [76]

$$\omega_{\mathbf{E} \times \mathbf{B}} = \frac{r}{q} \frac{d}{dr} \left[ \frac{q}{r} \frac{E_r}{B} \right] \quad (3.28)$$

The shearing rate is widely accepted to be responsible for turbulence suppression [177], leading to the formation of a steep pressure gradient (pedestal) [18] that allows for higher

density and temperature in the plasma due to reduced transport [134]. Clearly, for stabilisation, this has to compete with the turbulent activity growth rate. This concept will be further addressed in Chapter 5, where a correlation between the shearing rate and the C density gradients in negative triangularity is highlighted, possibly related to turbulence suppression.

### 3.3 Sawteeth instability and rotation

In this section, recent results on sawteeth instability (ST) influence on rotation are summarised.

The ST is a macroscopic periodic instability that significantly affects the plasma core [78]. It is characterised by a periodic relaxation of the plasma core gradients resulting in the flattening of  $T_e$  and  $n_e$  profiles [111]. Its cycle is often divided into three phases:

- 1) Ramp phase, where the plasma core pressure increases with time;
- 2) A precursor phase, where a magnetic perturbation grows. This typically results in oscillatory traces detected by soft X-ray emission intensity or  $T_e$  and  $n_e$  diagnostics (DMPX, ECE, XTOMO...). The mode is  $n = 1$ ,  $m = 1$  (corresponding to a safety factor of 1, so the plasma current core density has to be high enough for such a magnetic field line to exist). This mode amplitude grows (on a range of scale times, depending upon the plasma configuration), until magnetic island like zones start to form. The flattening of electron temperature and density profiles (caused by high internal transport) within magnetic islands is well documented [37] and, since the plasma momentum is directly linked to the ions, also momentum transport is affected by it;
- 3) A crash phase (or fast phase), where magnetic reconnection [129] modifies the magnetic field topology by rupturing the nested flux surface configuration. This causes the plasma core gradients to collapse and flatten, often partially exhausting part of the previous pressure build up and often accompanied by a suddenly decrease in the core emissivity that, for a fusion grade plasma, is concentrated in the X-ray region corresponding to the core temperature. This Magneto Hydro Dynamic (MHD) activity has a strong influence on transport, since particles in the reconnection zone do not follow the previously aligned field lines and can move radially [67]. This flux across field lines adds to the radial transport [135].

The mixing radius  $r_{mix}$  and the inversion radius  $r_{inv}$  depicted in figure 3.3 define the regions where the plasma is perturbed by expelled particles. Particles and energy expelled from the core are redistributed in the region enclosed by  $r_{mix}$ , whilst the external region is often less perturbed. The region inside  $r_{mix}$  is in turn divided into two regions: one where particles and energy are expelled and a region that accomodates these fluxes. The inversion radius separates these two zones. This is so-called as the X-ray intensity increases and falls sharply

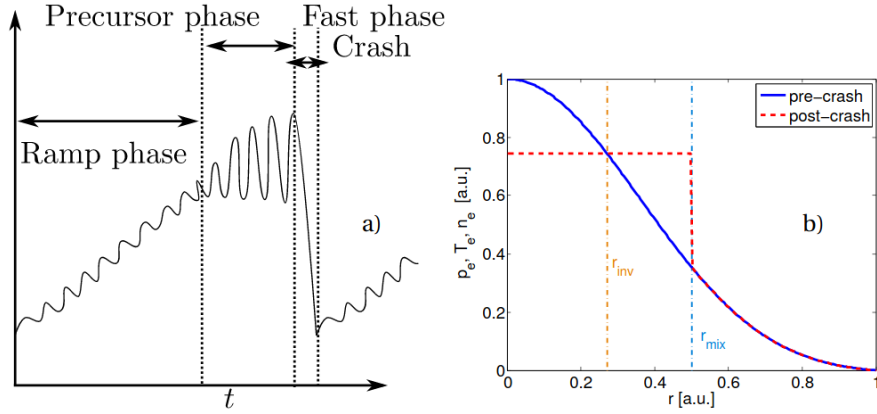


Figure 3.3 – (a) typical core FIR and/or soft-X ray time trace during a ST period, defining the three phases of the evolution. (b) sketch of a pre and post ST crash electron profile defining the inversion radius  $r_{inv}$  and the mixing radius  $r_{mix}$ .

within this radius whereas the opposite is true just outside  $r_{inv}$ .

Another important quantity in this characterisation is the sawteeth period  $\tau_{ST}$ . Its value depends on plasma parameters (especially  $I_p$  and  $q$ ) and the magnetic configuration, increasing with tokamak size,  $\sim 20$  ms in TEXTOR ( $R_0 = 1.75$  m) [166],  $\sim 100$  ms in JET ( $R_0 = 3$  m) [53]. In TCV, the natural ST period is of the order of a few ms, that is comparable, or lower, than typical CXRS integration times. However, the ST period can be considerably increased (stabilised) by ECRH deposition close to the  $q = 1$  flux surface [61] [74].

The ST is also stabilised by fast particles [81] such that, during high power NBH on TCV, the period is often 20ms and has been seen to exceed 30 ms [7] [71]. At TCV, the DMPX diagnostic is ordinarily employed to retrieve quantities such as  $r_{inv}$  or the sawteeth period  $\tau_{ST}$  [67] [74]. Most rotation diagnostics do not have sufficient time resolution to resolve these phenomena, so their effect is usually accounted for by simple additional diffusion or, often, neglected in transport models, where time-averaged profiles are used.

### 3.3.1 Overview of previous results

Previous results showed that ST-averaged velocity profiles are flat or hollow (for high  $I_p$ , low  $q$ ) inside the ST inversion radius. Outside  $r_{inv}$ , they linearly decrease towards the edge, where the toroidal velocity is small and usually in the  $I_p$  co-current direction [111].

Figures 3.4 and 3.5 (courtesy of A. Bortolon [22] and C. Marini [111]) show the effect of increasing  $I_p$  on the velocity profiles. In the first figure, positive and negative current cases are compared. These discharges, operated in limited configuration in TCV, display, in both cases, a plasma rotating in the counter-current direction with edge velocity close to zero. The net effect of increasing  $I_p$  is to decrease  $q$  and increase  $r_{inv}$ . This displacement of the  $q = 1$  surface is accompanied by a push of the toroidal velocity profiles towards the co-current direction. The  $v_{tor}$  profiles become progressively hollow inside  $\rho_{q=1}$ , whilst toroidal velocity remains close to zero at the edge. Carbon temperature and density profiles, instead, are flattened

within the region bounded by the inversion radius.

Figure 3.5 shows the same results, with the addition of ECRH (black profile). Here, ECRH power deposition results in the flattening of the profile and the increase of  $r_{inv}$ . Interestingly, ECRH injection results in increased  $T_e$  and  $n_e$ , but the shapes of their profiles remain unchanged. This suggests that employing ECRH does not modify the transport and that it can be safely employed to increase  $r_{inv}$ . In Marini's work, the time resolved ST was measured for different ECH powers and showed that their average mirrored the CXRS measurements for short ST periods. It was this that led to the conclusion that they were measuring the same phenomena [111].

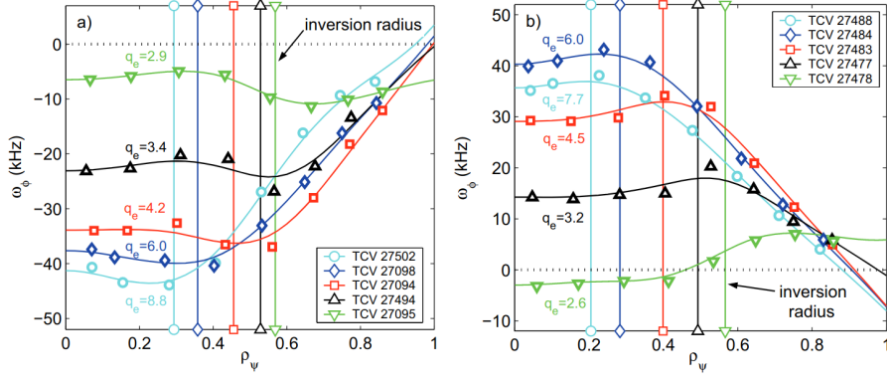


Figure 3.4 – Toroidal velocity profiles measured by CXRS for increasing current (decreasing  $q$ ). On the left for positive current case, with negative current on the right. In both cases, velocity profiles are bulged in the counter-current direction and flatten with increasing current (courtesy of A. Bortolon [22]).

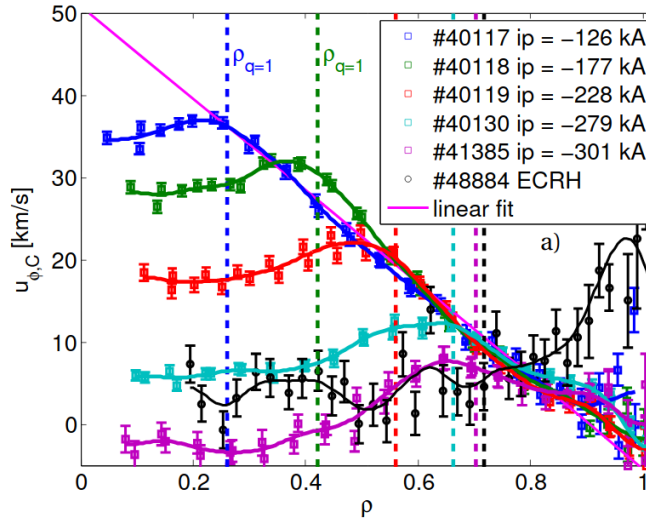


Figure 3.5 – Negative  $I_p$  scan. The net effect of increasing  $I_p$  is to "push" the profiles' region inside the inversion radius towards the co-current direction. Injecting ECRH also results in increased  $r_{inv}$  and flat velocity profile (courtesy of C. Marini [111]).

$T_C$  profile flattens inside  $\rho_{q=1}$  with the ST crash, although to a lesser degree than the electron temperature. Figure 3.6 shows the temperature profiles normalised to the carbon temperature measured at  $\rho_{q=0.8}$  ( $T_C(\rho = 0.8)$ ) to emphasise these flattenings.

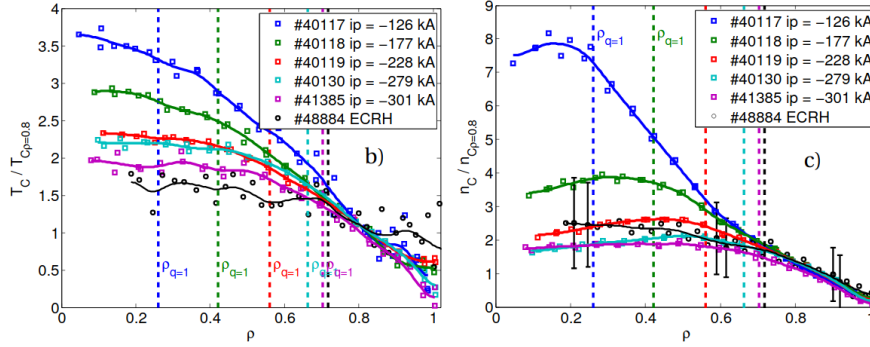


Figure 3.6 – Negative  $I_p$  scan.  $T_C$  and  $n_C$  normalised to their value inside the  $\rho_{q=0.8}$  regions are shown to emphasise the effect of  $I_p$ . Temperature increases with increasing current and its profile flattens inside the  $\rho_{q=1}$  region. Carbon density increases as well, but  $n_C$  profiles become hollow within the  $\rho_{q=1}$  region (courtesy of C. Marini [111]).

These results suggest that the net effect of ST crash is to generate a core torque in the co-current direction [22] [111]. Further investigations were made to ascertain the torque between ST crashes, *i.e.* resulting from modifications of transport characteristics, or whether the observed shape torque is localised at the time of the crash, and so readily ascribable to magnetic reconnection. A conditional sampling technique was applied in order to resolve pre and post crash profiles at the lowest CXRS integration time (2 ms).

The discontinuity across the crash observed in toroidal rotation profiles was confirmed by these experiments. The pre-crash profiles are peaked in the counter-current direction. During the ST evolution, the velocity increases until the crash. After the crash, profiles are pushed towards the co-current direction, suggesting the presence of a co-current torque acting through the crash, with the pre-crash profiles restored after the crash on timescales of the order of ms. This mechanism strongly affects profiles in the core region (between  $\rho = 0$  and  $\rho_{q=1}$ ). Moreover, impurities are expelled from the core by the ST crash. A high C density ring is formed between  $\rho_{mix}$  and  $\rho_{q=1}$  during the crash. Densities can reach values 120 % higher than pre-crash. The ring dissipates within 5 ms, probably through diffusion [135].

As the net effect of ST is to push  $v_{tor}$  profiles in the co-current direction, it is necessary to carefully discriminate it from other phenomena whenever investigating momentum transport. Chapter 4, for instance, presents an extensive study of the effect of plasma density on toroidal velocity profiles during density ramps in TCV Ohmic discharges operated in limited and diverted configuration in plasmas of different majority species. As the effect of density appears to be similar to that of ST, *i.e.* toroidal velocity profiles evolve towards the co-current direction as the density increases during Ohmic discharges operated in limited configuration in TCV, the two phenomena must be separated in order to assess which of these actuators is responsible for the experimental observations. Therefore, the results described in this section

will be addressed further in this thesis to explain how and why ST activity was monitored and its contribution separated from other effects.

### 3.4 Light impurity transport

One of the main problems of any confined plasma that limits its performances is associated with radial transport of particles and energy [84]. Even when macroscopic MHD instabilities (such as disruptions, sawteeth, tearing modes) are stabilised, the fusion device performance is degraded by energy conduction, convection and radiation. In this way, the fusion condition, set up by Lawson's triple product, can be seen as the most optimistic criteria for attaining fusion as it ignores all these effects. The objective of transport theory is to investigate such phenomena. In particular, impurity transport theory aims at describing the space-time evolution of density, temperature and rotation of species by identifying their sources and fluxes.

#### 3.4.1 Classical and Neoclassical transport

Transport processes are often considered to be dominated by diffusion [82] [84]. A Fick's type law is then assumed with the particle and heat fluxes written in the following way

$$\Gamma = -D\nabla n \quad (3.29)$$

$$Q = -n\chi\nabla T \quad (3.30)$$

with  $D$  and  $\chi$  of the form  $D, \chi = \frac{a^2}{\tau_E}$ . Here, the minor radius of the plasma  $a$  gives a value for the distance that energy and particles cover before exiting the plasma confined region (often taken as the plasma minor radius in a Tokamak).

Classical transport contribution, *i.e.* driven by collisional diffusion of particles across the magnetic field, is often small compared to experimentally measured fluxes. The probability that a particle undergoes a collision is equal in all directions. However, as the density is higher in the plasma core, a net outward flux develops. A random walk model can be employed to describe particle diffusivity

$$D = \frac{\Delta x^2}{\Delta t} \quad (3.31)$$

where  $\Delta x$  and  $\Delta t$  represent the typical distance and time step that, in magnetically confined plasmas, are of the order of the Larmor radius  $\rho$  and the inverse of the Coulomb collisional frequency  $\nu_C^{-1}$ , respectively. In fusion relevant conditions  $D_{class} \sim 10^{-3} m^2/s$ , which is negligible compared to often measured values  $\sim 1 m^2/s$  [82]. A similar discrepancy between classical theory and the experimental measurements is found for the energy diffusion. Note that the ion Larmor radius is larger than that of the electron by a factor  $\sqrt{m_i/m_e}$ . However, the diffusivity is balanced by a lower collision frequency of the order  $m_e/m_i$ .



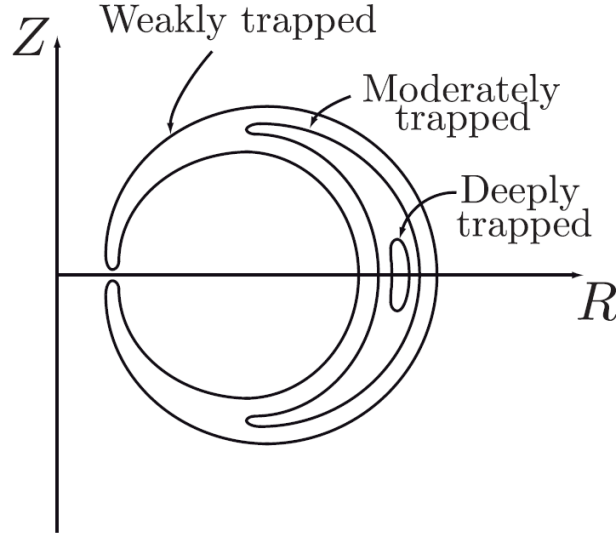


Figure 3.7 – Banana orbits of trapped particles (from [66]).

In tokamaks, the trajectory of charged particles is modified by the toroidal geometry and magnetic fields and their gradients. The theory that describes transport in toroidal geometry is called *neoclassical* and predicts higher heat and particle diffusivities than the classical calculation above [82].

One of the most important effects of the toroidal geometry is that particles can be trapped by the gradients in the magnetic field  $B$  as they follow the Tokamak's nested field lines. The toroidal magnetic field is proportional to  $1/R$ , and is stronger towards the center of the torus. Particles with a small  $v_{\parallel}/v_{\perp}$  on the outer region of the tokamak can "bounce" (the mirror effect) as their parallel motion brings them towards the high field region. This can be shown by the conservation of energy  $E$  and magnetic momentum  $\mu$ :

$$E = q\phi + \frac{1}{2}mv_{\parallel}^2 + \frac{1}{2}mv_{\perp}^2 \quad (3.32)$$

$$\mu = \frac{mv_{\perp}^2}{2B} \quad (3.33)$$

If  $\mu$  has to remain constant as the particle enters a region of denser magnetic field, the  $v_{\perp}$  must increase.  $E$  is, however, conserved. In regions where the electric field can, for the moment, be ignored, the velocity parallel to the magnetic field must decrease to maintain  $E$  constant, with some particles reaching stationary values, from where they can only be reflected. The resulting orbit has a shape of a banana in the poloidal plane, as shown in Figure 3.7. Particles with sufficiently high  $v_{\parallel}/v_{\perp}$  are not reflected and are termed passing particles as their parallel velocity carries them "over" the high field side magnetic potential "hill".

The neoclassical diffusion coefficient in the presence of trapped particles can be written as

$$D_{neo} = \alpha_t \frac{v_c}{c} \omega_b^2 \quad (3.34)$$

where  $\alpha_t \sim \sqrt{2\epsilon}$  is the fraction of trapped particles for a Maxwellian distribution,  $\epsilon = \frac{r}{R_0}$  and  $\omega_b$  is the bounce frequency of trapped particles [123].

The neoclassical impurity flux is often expressed by the following equation ([87] [158] [36] [27]):

$$\Gamma_Z^{neo} = D_{neo} \nabla n_Z + n_Z D_{neo} \left( \sum_j g_{j \rightarrow Z} \frac{\nabla n_j}{n_j} + g_{T_i} \frac{\nabla T_i}{T_i} + g_{T_e} \frac{\nabla T_e}{T_e} \right) \quad (3.35)$$

$g_{j \rightarrow Z}$ ,  $g_{T_i}$  and  $g_{T_e}$  are transport coefficients that depend upon momentum transport mechanisms due to collisions between different particles and/or species, and thus upon local plasma conditions. In presence of banana orbits,  $g_{e \rightarrow Z}$  and  $g_{T_e}$  can be neglected ([86] [12]) and, in steady state,  $\Gamma \rightarrow 0$  and 3.35 reduces to

$$\frac{n_Z(\rho)}{n_Z(0)} = \frac{n_D(\rho)}{n_D(0)} \frac{g_{D \rightarrow Z}}{g_{T_i}} \frac{T_i(\rho)}{T_i(0)} \quad (3.36)$$

$g_{D \rightarrow Z} \gg g_{T_i}$  in many discharges [12]. Therefore, if the main ion density profile is peaked, neoclassical transport models predict an accumulation of impurities in the core, regardless of  $T_i$  profiles.

As mentioned above,  $D_{neo}$  can be two orders of magnitude higher than the classical diffusion coefficients. However, measured values of the diffusivity are often one or two orders higher, showing that additional plasma transport processes must be included in a useful description of the experimental situation.

### 3.4.2 Turbulent flux, ITG and TEM microinstabilities

As described in the previous paragraph, impurity transport is affected by neoclassical (collisional and curvature) mechanisms. However, measured light impurity transport level largely exceeds neoclassical predictions, confirming that additional mechanisms are at play. This additional transport is termed "anomalous" and it is widely accepted due to plasma turbulence caused by microinstabilities, *i.e.* instabilities that develop on microscopic scale lengths, *i.e.* within the Debye scale length.

In addition, heavy and light impurity transport is driven by different phenomena. In particular, it has been demonstrated that heavy impurity transport is largely determined by their charge and neoclassical-like phenonema, whereas light impurities (like C or B), of interest in this work, are more determined by turbulence.

A general expression for impurity transport can be derived from first principles [2]. Equation 3.37 is a diffusion-convection equation which represents a model for turbulent particle flux:

$$\frac{R \Gamma_{nZ}^{TURB}}{n} = D_{nZ} \frac{R}{L_{nZ}} + D_{Th,Z} \frac{R}{L_{TZ}} + D_{uZ} u' + R V_{pZ} \quad (3.37)$$

where  $R$  is the major radius,  $n$  is the particle density,  $L_g = (\frac{\partial \ln(g)}{\partial r})^{-1}$  the normalised logarithmic gradient and  $u' = \frac{R^2}{v_{Th}} \frac{\partial \Omega_i}{\partial r}$  the gradient of the Mach number.

This is an appropriate physical decomposition, but not a linear relation. Consequently, it is

not simple to separate convective and diffusive terms [192].

Equation 3.37 shows how the turbulent flux cannot be referred to a single mechanism, but rather a combination of them. The density profile is consequently strongly affected by changes in the temperature and toroidal velocity gradients that, in turn, also affect each other. Therefore, a practical way of studying how the off-diagonal terms  $L_{TZ}$  and  $u'$  affect transport is to look for correlations between these terms and  $L_{nZ}$ .

The two diffusive terms, one proportional to the logarithmic temperature gradient, the other to the gradient of toroidal velocity (scaled to the Mach number), are termed thermo and roto-diffusion, respectively.

A first signature of turbulent transport can be found in the correlation between  $L_{nZ}$ ,  $L_{Te}$  and  $L_{TZ}$ . Turbulent transport is, in fact, mainly driven by the  $E \times B$  drift, which is determined by temperature gradients variations. The  $\nabla B$  drift velocity of a particle (caused by a gradient in the magnetic field) is proportional to the particle's kinetic energy. Hotter particles drift further than colder particles. Therefore, if a temperature gradient is aligned with a magnetic field gradient (as occurs in tokamaks), particles in the hotter region will drift further. Conversely, if there is a perturbation in the temperature gradient, then the difference in drift velocities will create charge separation. This charge separation creates an electric field that, in turn, creates an  $E \times B$  drift that increases the perturbation's amplitude. This is the principle of the Ion Temperature Gradient (ITG) instability (Figure 3.8) [123].

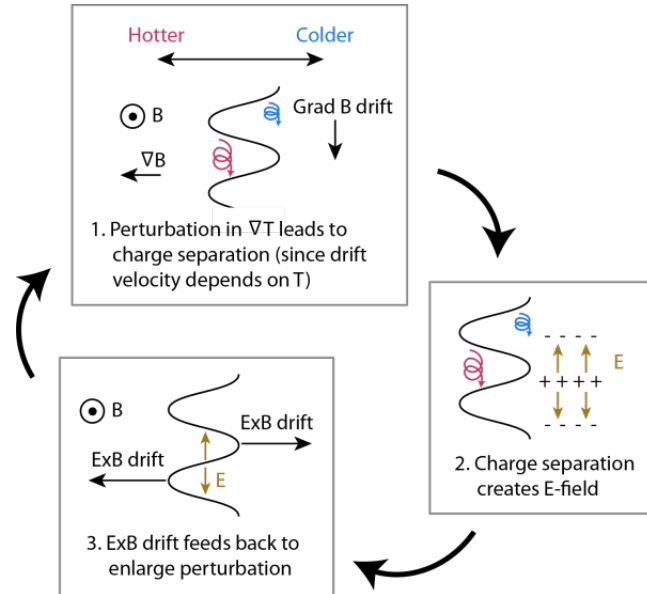


Figure 3.8 – Schematic picture showing the evolution of the ITG instability.

Thermo-diffusion proved to be related to both electron and ion microinstabilities, being directed inwards for TEM (Trapped Electron Modes) and outward for ITG.

TEMs are waves that can become unstable through a resonant interaction between an electrostatic perturbation and the toroidal precessional drift of electrons bouncing in trapped orbits [123], [100]. Today, it is universally accepted that TEMs are mainly responsible for anomalous

heat and particle transport in the electron channel.

In the same spirit, a simple explanation for the development of TEMs can be made in the following. Trapped electrons bounce back and forth in so-called banana orbits. The combination of parallel motion and vertical drifts results in a toroidal drift of the trapped particles after successive bounces. In the presence of a toroidal perturbation, for instance an  $E \times B$  drift, the effect of the associated field does not average out and a resonant interaction may lead to an instability.

Without toroidal velocity or velocity gradients, the roto-diffusion term should be zero from symmetry arguments. However, it has been already stated that tokamaks show a finite intrinsic rotation, implying that the roto-diffusion term is non-negligible [3]. Like thermo-diffusion, this term is also directed inwards for TEM and outwards for ITG [2]. This basic interpretation has been used in the literature, and will be revisited in later chapters, to suggest that changes in intrinsic rotation direction result from a change in the dominant turbulent mechanism, for instance going from TEM dominant at low density to more ITG related as the plasma density is increased. As will be shown, such a simple argument, although attractive from an interpretive viewpoint, is often too simplistic to explain experimental observations satisfactorily.

### 3.5 Conclusion

Some theoretical aspects of particle and momentum transport in a Tokamak were presented in this chapter. A classic rotation decomposition was performed, showing that both the poloidal and toroidal components of rotation are not flux surface quantities but depend upon their respective magnetic field components.

An equation for the momentum flux was derived (Eq. 3.3) to show and explain the coexistence of convection, diffusive and residual stress terms.

The radial electric field was defined and the shearing rate, considered at least in part responsible for turbulence suppression, derived. This will be further addressed in Chapter 5, where C transport studies in negative triangularity are presented.

The sawteeth instability was described, with emphasis on its effect upon momentum transport, and possible drive, induced at ST crashes. An overview of previous results obtained in TCV, relevant to this thesis, was presented.

Finally, the concept of transport was addressed, with a brief overview of classical, neoclassical and turbulent transport. A diffusion-convection equation (Eq. 3.37) was presented, explaining the interplay of terms depending upon the impurity ions temperature, velocity and density. The two main microinstabilities responsible for the turbulent transport of electrons and ions in Tokamaks, TEM and ITG, were described.

A more detailed description of residual terms can be found in [138] [139] [140]. Many of these terms are of the same order of magnitude and, therefore, discerning which are the most prevalent adds to the complexity and confusion in experimental interpretation. Moreover, as the curvature of rotation profiles (second derivative) is difficult to access experimentally due to limited diagnostic capabilities, these models pose a challenging scenario for experimental

investigations.

These concepts will be employed in the following chapters in the analysis and discussion of experimental results.



## 4 Isotope effect on rotation and confinement

The rotation reversal phenomenon was extensively studied in this work. Starting from the results obtained in 2008, a set of experiments was developed to compare previous studies in deuterium plasmas to other majority plasma elements. In particular, plasmas of majority hydrogen and helium were specifically operated for this work in the TCV tokamak.

One of the objectives of the study was to investigate the relation between the LOC/SOC transition and the rotation reversal. As the LOC/SOC transition is often seen near a plasma density threshold, typical scenarios to observe rotation reversal and/or LOC/SOC transitions were performed in Ohmic discharges that included density ramps.

These specific experiments were expanded to low current density ramps and current ramps at constant density to probe possible effects of plasma current and rational surfaces in the confined plasma. The effect of poloidal plasma shape was also investigated in negative triangularity plasmas and in diverted configurations. To further probe the effect of density peaking, X2 ECRH was employed in two specific cases to trigger a rotation reversal.

These results, and relevant discussions, are presented in this chapter. After a brief introduction to the LOC/SOC transition and the TEM/ITG bifurcation, the effect of majority gas isotope on confinement and toroidal rotation are described, together with an investigation on sawteeth activity during density ramps. Particular emphasis was placed on the exploration of possible connections between the density gradients and the evolution of  $v_{tor}$  profiles, as it was found to show the most relevant correlation in the discharges performed during this work. A final paragraph describes some results of linear gyrokinetic simulations, which provided useful insights into how turbulent mode dominance varies during density ramps. In particular, it was shown that the LOC/SOC transition was accompanied by a nearby (in density space) TEM/ITG bifurcation only in D discharges. A recap and discussion concludes the chapter.

### 4.1 LOC-SOC transition

Following early operations at high plasma temperature in the 70s, it was discovered that the global energy confinement time increases linearly with increasing electron density [130]. This regime was called linear Ohmic confinement (LOC). However, as tokamak performance im-

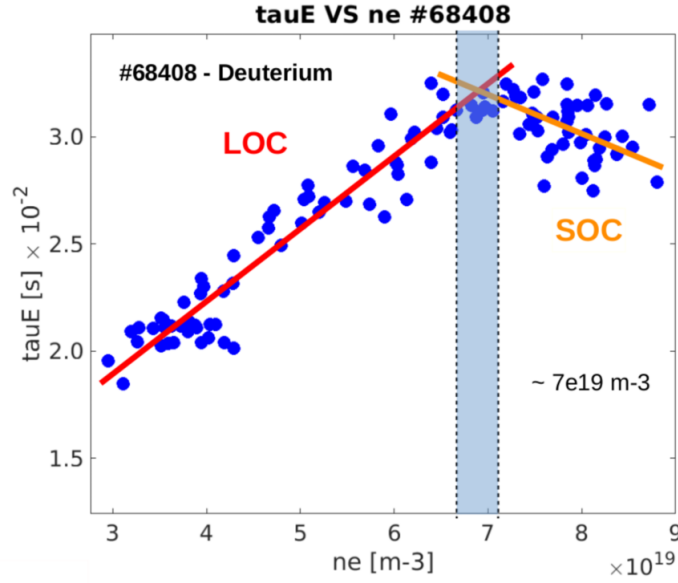


Figure 4.1 – Electron energy confinement time as a function of increasing density. The discharge consisted in a high current ( $I_p = 350$  kA) ohmically heated D density ramp. The density threshold at which the LOC-SOC transition is highlighted.

proved, the energy confinement time was found to saturate above a density threshold, leading to the Saturated Ohmic Confinement (SOC) regime (although termed "saturated" confinement often decreases further with increasing plasma density (Figure 4.1) [155] [69]. Optimism was soon restored when H-mode (High confinement) was discovered and tokamak operations started focusing on scenarios where external input power allowed for better performance rather than increased density.

Figure 4.1 shows an example of LOC-SOC transition during a high current ( $I_p = 350$  kA) ohmically heated D density ramp. The opaque band indicates the density region where the confinement is said to transition from LOC to SOC.

#### 4.1.1 TEM-ITG bifurcation

A theoretical explanation of the LOC/SOC transition observed during density ramps is conventionally linked to changes in the plasma's turbulent state [10] [9]. A transition of the dominant turbulent transport from trapped electron mode (TEM) to ion temperature gradient (ITG) mode is often concluded during density ramps. Ions and electrons are weakly thermally coupled at low density, where the collisionality is low, and TEMs are particularly virulent, leading to the poor confinement observed in the early phases of the discharge. As the density increases, the coupling between ions and electrons grows from the increasing collisionality, which also serves to decrease the growth rate of TEMs through collisional detrapping of electrons [34]. As



shown in [157], the growth rate of the dissipative trapped electron modes can be written as

$$\gamma = \epsilon \frac{\omega_n^* \omega_T^*}{\nu_{e-i}} \quad (4.1)$$

with  $\epsilon = \frac{r}{R}$ ,  $\omega_n^* = \frac{cT_e}{eB} k_\perp \left| \frac{\nabla n}{n} \right|$ ,  $\omega_T^* = \omega_n^* \frac{d \ln(T)}{d \ln(n)}$  and  $\nu_{e-i}$  the electron-ion collision frequency. Equation 4.1 shows that the increasing collisions between ions and electrons lead to a reduction in the TEM growth rate.

The higher collisionality is also accompanied by a decrease in the impurity content, that reduces the ion dilution by  $1 - \frac{n_D}{n_e}$ . This strongly affects the ITG stability. At low collisionality, the relatively high  $Z_{eff}$  and ion dilution are universally observed to stabilise ITG modes. Conversely, as  $\nu$  increases, decreasing ion dilution leads to an increase of the ITG growth rate [57] [176]. After the LOC/SOC transition, the thermal diffusivity of electrons and ions becomes independent of the electron density and ITG now dominates over TEM in the confinement scaling [169]. Although the ITG growth rate increases with collisionality, it still provides a strong ITG drive, as the ion temperature gradients tend to be pinned near marginal stability [34]. This, in part, contributes to the confinement saturation.

Gyrokinetic simulations performed at AUG [106][58] suggest that the LOC/SOC transition is, however, not determined by a change from TEM to ITG. The  $\tau_E$  saturation is rather explained by stronger ion energy transport at higher densities caused by the decreasing plasma dilution. A TEM to ITG transition is still, however, necessary to explain the observation of the electron density peaking in the parameter regime of the LOC to SOC bifurcation.

Such a TEM/ITG bifurcation cannot occur punctually (or in this case at a single density threshold) at all radial positions in the plasma. It rather develops at the plasma periphery and moves in to encompass the core [159]. Experimental and modeling works performed in AUG [58] and Alcator-C Mod [172] suggest that such transition may only occur in the edge region, with the plasma core still dominated by ITG inside  $\rho_{pol} < 0.8$  [106].

#### 4.1.2 Isotope effect on the LOC-SOC transition

A deuterium reference discharge (#68408:  $I_p = 350$  kA,  $B_T = 1.4$  T) was developed in a limited configuration with positive triangularity (Figure 4.6). The discharge density ramp commenced at  $n_e \sim 3 \times 10^{19} m^{-3}$ . The electron density was increased by gas puffing from the TCV floor, until a major plasma disruption, where it reached a maximum of  $n_e \sim 9 \times 10^{19} m^{-3}$ .

The same discharge was replicated in H and He. Figure 4.2 shows a comparison of the energy confinement times  $\tau_E$  as a function of electron density for all three discharges.

The LOC/SOC transition, here highlighted by opaque bands, occurred at different densities in all discharges. The highest density was obtained in He, preceded by D and H ( $n_e^{sat}(H) < n_e^{sat}(D) < n_e^{sat}(He)$ ). Whilst the LOC/SOC transition occurs at lower density, and for lower  $\tau_E$ , in H, the energy confinement time saturation value in D and He is similar, albeit slightly higher in He, thus following the same ordering as the saturation density:  $\tau_E^{sat}(H) < \tau_E^{sat}(D) < \tau_E^{sat}(He)$ .

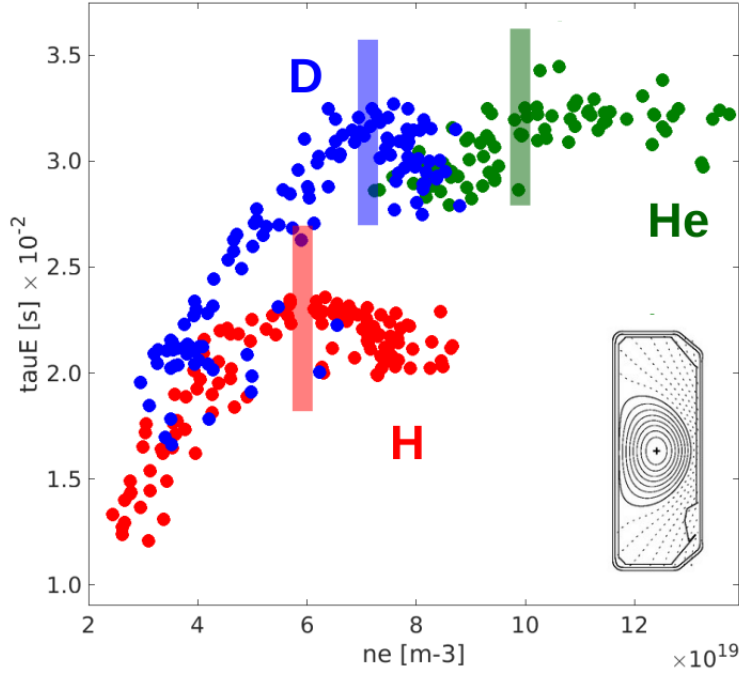


Figure 4.2 – Energy confinement time plotted as a function of increasing electron density for deuterium discharge # 68408 (blue), hydrogen discharge # 68428 (red) and helium discharge # 68536 (green). The density region where the LOC/SOC transition occurs is highlighted by the opaque areas. The LOC/SOC transition occurred at different densities in all discharges, also displaying different values of the energy confinement time at this threshold. Confinement time and density threshold follow the same ordering:  $\tau_E^{sat}(H) < \tau_E^{sat}(D) < \tau_E^{sat}(He)$  and  $n_e^{sat}(H) < n_e^{sat}(D) < n_e^{sat}(He)$ .

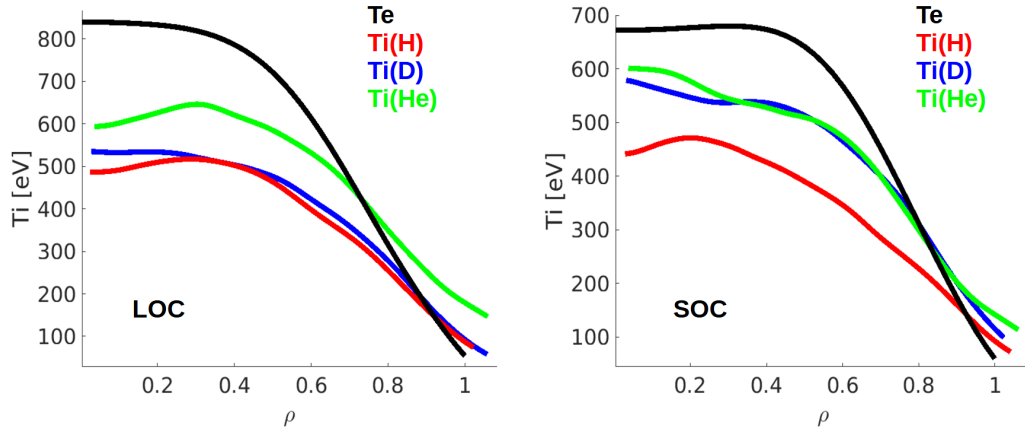


Figure 4.3 – Electron temperature (black), H (red), D (blue) and He (green) ion temperature. The  $T_e$  profile was similar between the three discharges, thus it is plotted only once. a) during the LOC phase; b) during the SOC phase. Experimental uncertainties were low ( $|\Delta T_{e,i}| \leq 15$  eV) and, for a better clarity of the plot, error bars are not drawn. The lower energy confinement observed in H may possibly be explained by a drop in electron temperature that is not fully compensated by an increase in ion temperature, *i.e.* a reduction in the total energy confinement. A similar trend is observed in the early phase of the density ramp, where the H ion temperature is comparable to that of D. At the LOC/SOC transition, however, the D and He core ion temperatures are similar, whilst H is lower, possibly correlated to the closer energy confinement times of D and He.

This result is confirmed by experimental observations from other machines (JET [110], AUG [162] [17], LHD [175], TEXTOR [190]). The mass dependence appearing in the  $e-i$  heat transfer  $p_{e-i}$  may, at least, partially explain the reduced confinement in hydrogen majority plasmas [162]:

$$p_{e-i} = 3 \frac{m_e}{m_i} \frac{n}{\tau_E} (T_e - T_i) \propto \frac{Z_i^2}{m_i} \frac{n^2}{T_e^{3/2}} (T_e - T_i) \quad (4.2)$$

where  $\tau_E$  is the collision time for electrons and  $Z_i$  the ion charge number.

When comparing isotopes, a decrease in  $T_e/T_i$  with increasing density is also an indicator of stronger  $e-i$  coupling. Figure 4.3 shows the electron and isotopes' ion temperature profiles before and after the LOC/SOC transition. Colours indicate the different majority species for each discharge. The three discharges displayed similar  $T_e$  profiles, here plotted in black. The lower energy confinement observed in H may possibly be explained by a drop in electron temperature that is not fully compensated by an increase in ion temperature, *i.e.* a reduction in the total energy confinement. A similar trend is observed in the early phase of the density ramp, where the H ion temperature is comparable to that of D. At the LOC/SOC transition, however, the D and He core ion temperatures are similar, whilst H is lower, possibly correlated to the closer energy confinement times of D and He.

It must, however, be mentioned that these observations were exclusively performed in the L-mode confinement regime. Recent works show that any isotope effect is weak in L-mode

discharges and depends mostly upon the  $e-i$  energy exchange or the external heating scheme and less on any change of transport caused by a differences due to isotope mass. A stronger confinement dependence on the isotope mass appears, instead, for H-mode [162] [110] [186].

### 4.2 Intrinsic rotation reversal

A curious phenomenon often observed during density ramps is a change of direction of intrinsic toroidal rotation. Intrinsic rotation is a non-zero toroidal rotation that tokamak plasmas can achieve without external momentum input [153]. TCV is particularly suited for the study of intrinsic rotation as CXRS measurements are obtained by means of a non-perturbative beam (the DNBI) that does not apply a significant external torque.

TCV's plasmas in limited configuration usually rotate in the counter-current direction (with edge rotation close to zero) over a wide range of parameters ( $I_p$  and  $n_e$ ). Rotation reversal consists in the relatively sudden change of toroidal rotation direction at a highly repeatable density threshold ( $n_e \sim 10 \times 10^{19} m^{-3}$  in TCV's 2006 shots), as shown in Figure 4.4. Here, the toroidal rotation profile reverses from counter to co-current direction in a discharge performed in a limited plasma configuration in TCV in 2006. This critical density value depends upon plasma current, magnetic field and machine size [56].

The best indicator of rotation reversal is a change in the sign of the gradient of the toroidal velocity profile. The simple observation of a change in the toroidal rotation direction, in fact, can lead to misleading results, as  $v_{tor}$  profiles that evolved from co to counter-current direction without changing their concavity were observed in TCV's diverted discharges (see section 4.5). In this case, although the absolute value of  $v_{tor}$  changes sign, the gradient of the toroidal rotation profile remains unchanged. The  $v_{tor}$  profiles show a slow, rigid displacement towards the counter-current direction (see, for instance, Figure 4.41, further in section 4.5), but no change in the gradients is observed, *i.e.* no profile reversal occurs. Therefore, whenever the absolute value of the toroidal velocity is employed (instead of its gradient) to discuss experimental results in this thesis, the entire toroidal rotation profile is also plotted to clarify whether the change in  $v_{tor}$  is describable as a "rotation reversal".

A rotation reversal was first reported at the TCA (Tokamak Chauffage Alfvén) tokamak in 1992 [54], but it was only in 2006 that it was extensively studied [22] [24] [55] [56], and has since been replicated in several other devices [156] [150] [31] [69].

In Figure 4.4, the two toroidal velocity profiles are nearly inverted, with the pre-inversion profile (in blue) showing a core velocity of  $\sim -10 \frac{km}{s}$  in the counter-current direction. The post-inversion profile (in red) has a similar shape but the rotation is now flipped in the co-current direction. It has to be mentioned here that this is the opposite of what has been seen on other devices (as also reported in [31]): co-current rotation at low density, then reversing to counter-current direction at high density [156] [119]. However, TCV's discharges were performed in limited configurations, conversely to the other devices that mostly operated in diverted configurations. As described in this chapter, also TCV's discharges in diverted configuration display co-current rotation at low density and counter-current at higher  $n_e$ . This

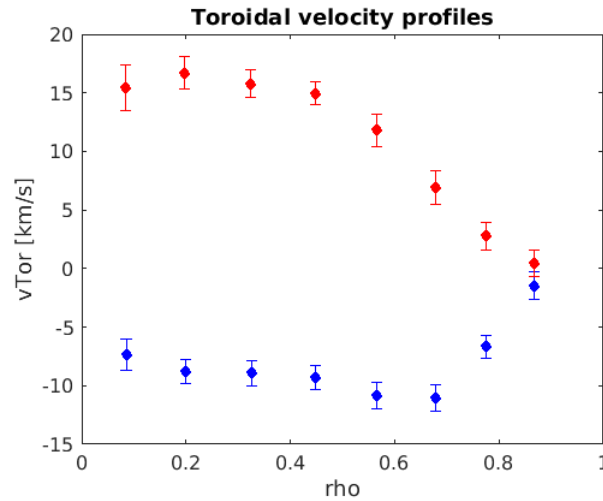


Figure 4.4 – Toroidal velocity profiles before and after the reversal during a D density ramp in limited configuration.

suggests that plasma configuration strongly affects plasma rotation direction. Therefore, the effects of plasma shape (positive and negative triangularity) and configuration (limited and diverted configuration) are addressed and discussed in detail in this chapter.

Since rotation reversal in D often occurs near the same parameter range (especially density) of the LOC/SOC transition, it has been recently suggested, strongly, that a causal relation between the two phenomena exists [34] [149], so that rotation reversals were then used as a precise indicator for the confinement time saturation that remains, itself, less easy to define. However, cases of toroidal rotation reversal occurring at different densities than the LOC/-SOC transition were already reported [106], as well as toroidal velocity profiles evolving back towards pre-reversal direction when the plasma confinement was already deep in the SOC regime [119], making the suggested relation controversial.

Turbulent momentum transport was reported as the most likely candidate to explain the reversal, with modelling and experiments still ongoing [106] [33]. However, the range of parameters that had been studied, including on TCV, was, to date, rather limited. Experiments performed during this work focused on a scan of parameters and shapes (such as negative triangularity) that had not yet been fully explored. Further such experiments were also performed to study the same phenomena with different majority species (D, He, H). One of the main objectives of these studies was to add further examples in the investigation of a possible relation between rotation reversal and the LOC-SOC (Linear to Saturated Ohmic Confinement) transition.

#### 4.2.1 Rotation reversal in deuterium plasmas

The set of experiments performed in TCV in 2006 clearly showed that rotation reversal was a highly reproducible physical phenomenon. A D density ramp from the 2006 set was replicated in 2020.

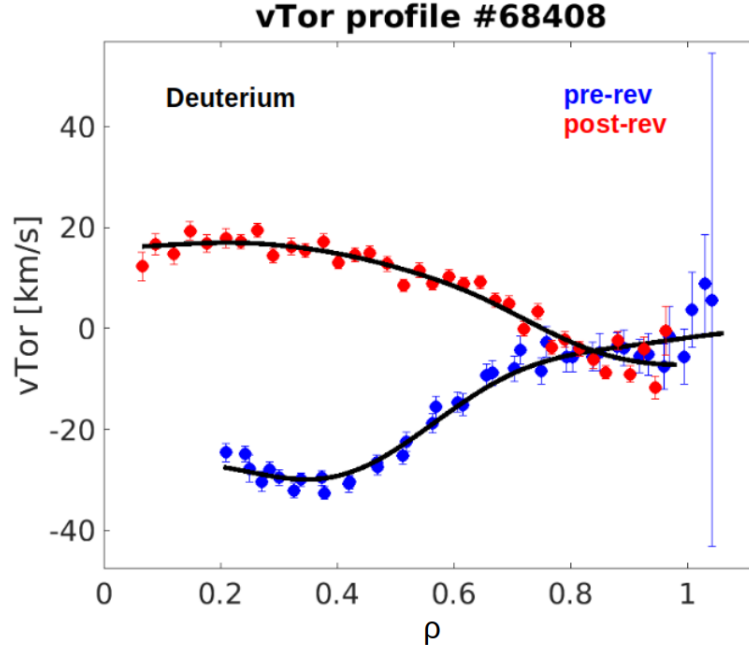


Figure 4.5 – Toroidal velocity profile before and after the reversal (blue and red, respectively), D discharge #68408. The discharge was a high current ( $I_p = 340$  kA) ohmically heated D density ramp in limited configuration.

Figure 4.5 shows the toroidal velocity profiles before (blue) and after (red) such a reversal during a D Ohmic density ramp in limited configuration in TCV.  $I_p$  was constant at 340 kA. Here, the density ramp was initiated at  $\sim 3 \times 10^{19} \text{m}^{-3}$  and reached  $\sim 9 \times 10^{19} \text{m}^{-3}$  (Figure 4.6). As the current flat-top is reached, central  $v_{TOR}$  increases linearly with density. The edge rotation remains close to zero, whilst the core rotation evolves from  $\sim -30 \frac{\text{km}}{\text{s}}$  to  $\sim +20 \frac{\text{km}}{\text{s}}$ , *i.e.* from co-current to counter-current direction. The reversal consists in inverting the profiles derivative at mid-radius, which then evolves from positive (hollow) to negative (peaked). Profiles are fully reversed after  $\sim 1.3$  s, at  $n_e \sim 6.5 \times 10^{19} \text{m}^{-3}$ , concomitantly with a LOC/SOC transition (Figure 4.7, showing the central toroidal velocity and energy confinement time traces). The density threshold found here was lower than for the 2006 case. This value was confirmed by repetitions of the same discharge with longer, and thus slower, density ramps. This relatively slow density ramp also showed that the rotation reversal is not a sudden bifurcation, as the  $v_{tor}$  profiles evolved progressively towards the counter-current direction following the plasma density variation. It is considered probable that the difference with legacy measurements may be ascribed to the higher temporal resolution of the present CXRS that has allowed for a more accurate coverage of density throughout the profiles' evolution.

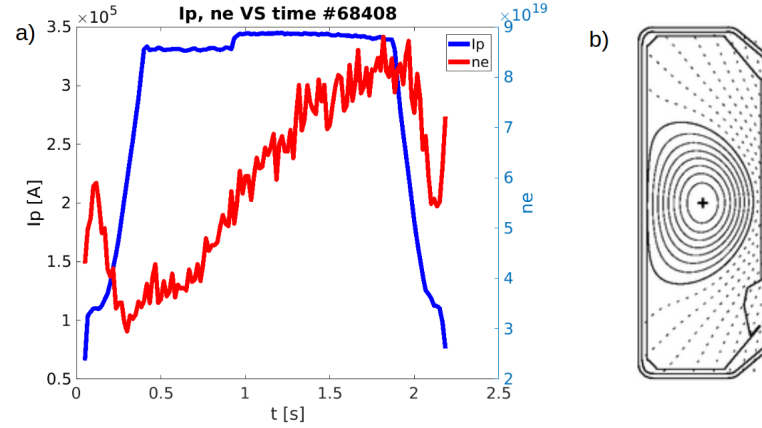


Figure 4.6 – Deuterium discharge #68408: a) electron density and plasma current traces; b) plasma equilibrium reconstruction.

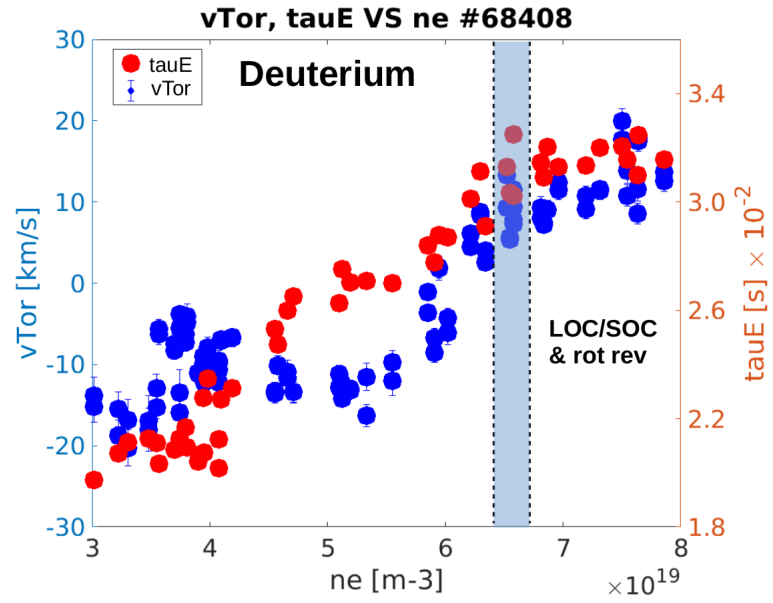


Figure 4.7 – Central toroidal velocity and energy confinement time as a function of increasing density, D discharge #68408. The discharge was a high current ( $I_p = 340$  kA) ohmically heated D density ramp in limited configuration. The density threshold at which the LOC-SOC transition and the rotation reversal occur is highlighted.

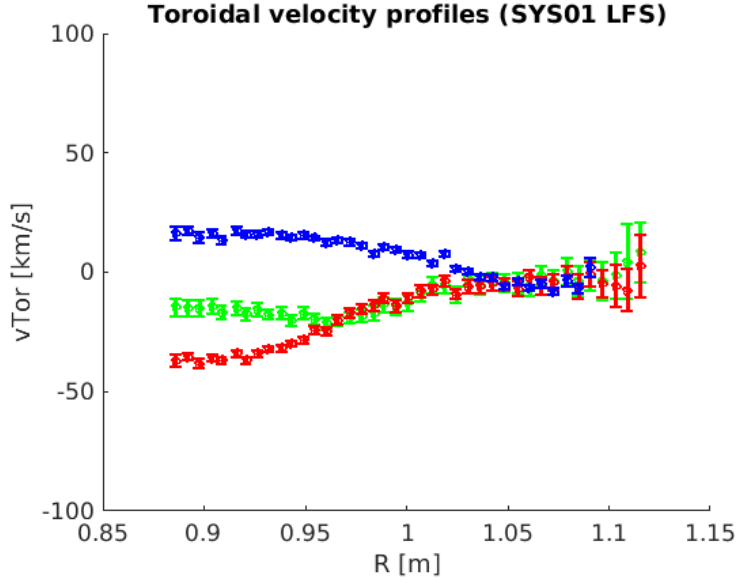


Figure 4.8 – Radial toroidal velocity profiles for discharge #68408. In blue, before the density ramp start (0.3 s), in red, the fully reversed profile at the end of the density ramp (1.3 s). The green profile was measured during the early phase of the density ramp (0.4 s).

#### 4.2.2 Rotation reversal in hydrogen plasmas

Deuterium discharge #68408 showed a clear LOC/SOC transition accompanied by a reversal of the toroidal rotation profiles in the same core plasma density range (Figure 4.7).

The same behaviour was not observed in hydrogen discharge #68428, where the LOC/SOC transition clearly occurred at a lower density with respect to the deuterium discharge, but was not accompanied by a rotation reversal (Figure 4.9).

Although a general trend in the  $v_{tor}$  trace can be seen (despite the large scatter within the data set), no evident causal correlation between the two phenomena can be inferred.

The same discharge was replicated at a higher current ( $I_p = 350$  kA) and then by extending the density ramp to the plasma discharge disruption limit. Higher density was accompanied by a degradation of the data quality in the latter part of the discharge, and no effect on the toroidal velocity profiles was discerned.

These observations strengthen the suspicion that no general causal correlation exists between the LOC/SOC transition and the rotation reversals.

#### 4.2.3 Rotation reversal in helium plasmas

He density ramps were challenging as starting at densities below  $n_e \sim 8 \times 10^{19} \text{ m}^{-3}$  was difficult in this configuration. Therefore, the D reference shot was adapted and two density ramps performed.

In the first (#68531), a long phase at constant  $n_e$  was followed by a short density ramp from  $n_e \sim 8.0 \times 10^{19} \text{ m}^{-3}$  to  $n_e \sim 1.1 \times 10^{20} \text{ m}^{-3}$ . The aim here was to establish whether the profiles



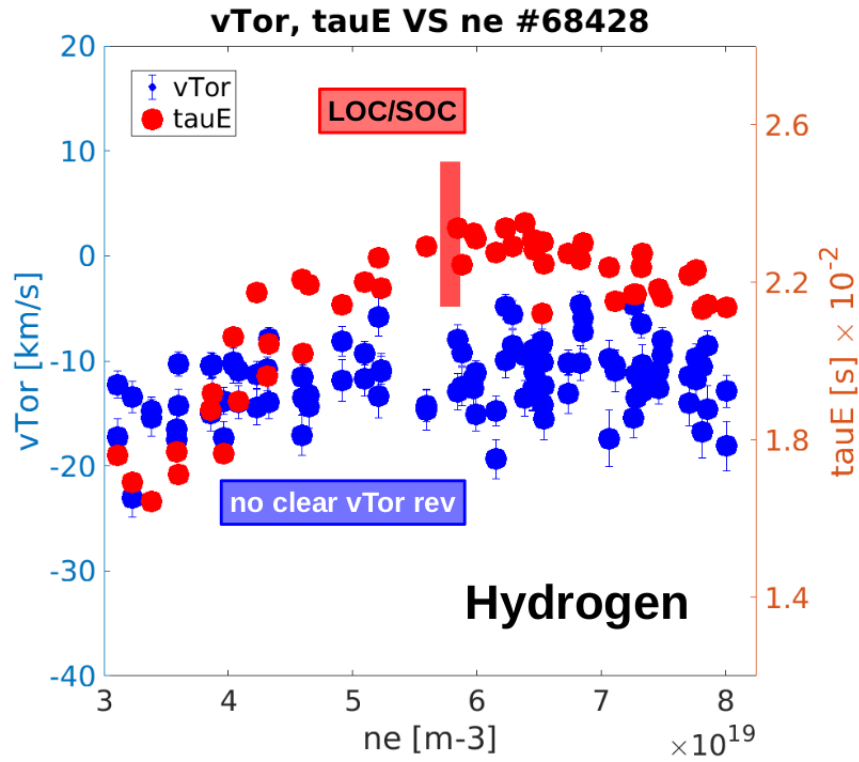


Figure 4.9 – Toroidal velocity and energy confinement time as a function of increasing density, H discharge #68428. The discharge was a high current ( $I_p = 340$  kA) ohmically heated hydrogen density ramp in limited configuration. The density threshold at which the LOC-SOC transition occurs is highlighted in red. No rotation reversal was observed in this discharge. Therefore, no causal correlation between the two phenomena was observed.

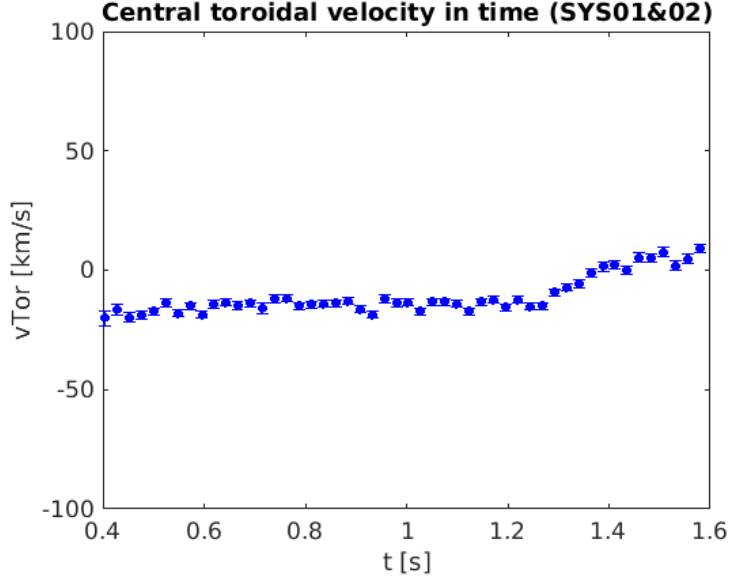


Figure 4.10 – Toroidal velocity evolution, discharge #68531. A long constant density phase is followed by a short density ramp starting at 1.3 s.

had already reversed during the early ramp phase and whether any change could be seen during the short ramp at the end of the discharge. Figure 4.10 shows the temporal evolution of the central toroidal velocity.

$v_{Tor}$  maintained a value of  $\sim -20 \frac{\text{km}}{\text{s}}$  throughout the constant density phase. At 1.3 s, when the density ramp commenced,  $v_{Tor}$  increased until it reached  $\sim 0 \frac{\text{km}}{\text{s}}$ . At 1.5 s ( $n_e \sim 1.0 \times 10^{20} \text{m}^{-3}$ ) the linear increase seems to cease but the discharge ended shortly after.

The density ramp was extended in the following discharge (#68536), starting at 0.6 s and from  $n_e \sim 8.0 \times 10^{19} \text{m}^{-3}$  to  $n_e \sim 1.3 \times 10^{20} \text{m}^{-3}$ . The linear increase stopped again at  $n_e \sim 1.0 \times 10^{20} \text{m}^{-3}$  and  $t \sim 1$  s, confirming the previous observation. After  $n_e \sim 1.1 \times 10^{20} \text{m}^{-3}$ , background fluctuations started to increase and the data fluctuations increased, although remaining in the zero velocity region.

Here, the toroidal rotation reversal occurred before the LOC/SOC transition (Figure 4.11).

Both phenomena are better separated in He with respect to their D and H counterparts. This result now implies that the correlation observed for D was circumstantial/fortuitous and restricted to a specific kinds of situations.

Figure 4.12 shows the toroidal velocity profiles in the He discharge at the start of the density ramp (blue, counter-current direction) and after the rotation reversal (red, slightly co-current in the core, but close to zero). Interestingly, here, the profile shape differs from the D case. The rotation at the edge is, again, close to zero. However, the reversal is not symmetrical as for D. The gradient flips sign at mid-radius but the post-reversal profile (red) is nearly flat in the core, highlighting the diverse phenomenology of the rotation reversal phenomenon. The profiles continued to evolve in the co-current direction but, as the density increases further, so does  $v_{Tor}$  experimental scatter. These observations also show that the absolute value of  $v_{tor}$  does

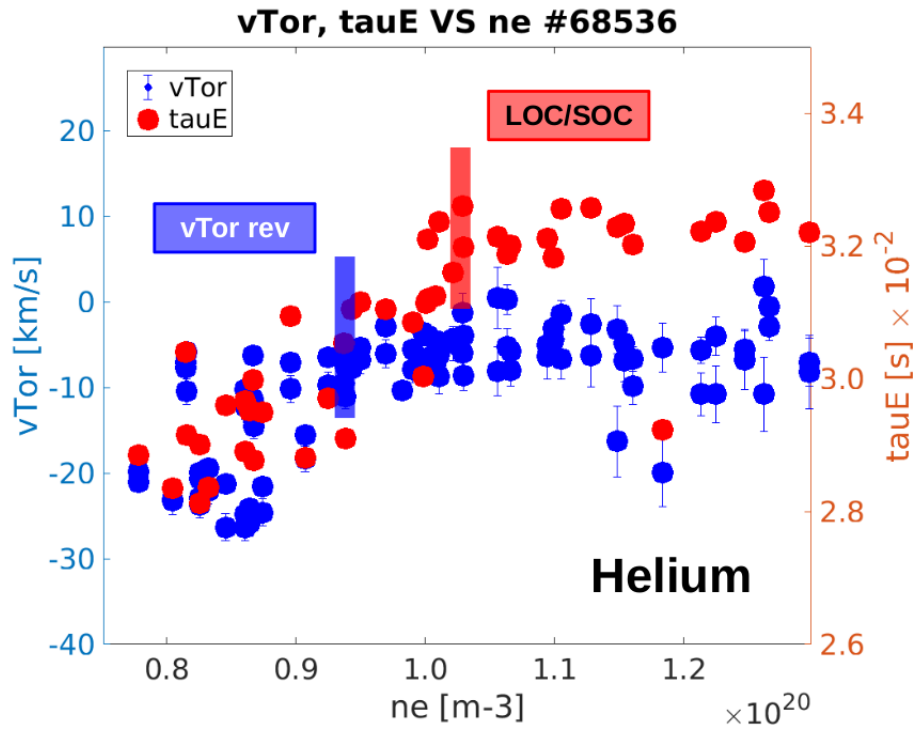


Figure 4.11 – Toroidal velocity and energy confinement time as a function of increasing density, He discharge #68536. The discharge was a high current ( $I_p = 340$  kA) ohmically heated helium density ramp in limited configuration. The density threshold at which the rotation reversal and the LOC-SOC transition occur are highlighted in blue and red, respectively. The two phenomena are better separated in this discharge with respect to their D and H counterparts and no causal correlation was observed.

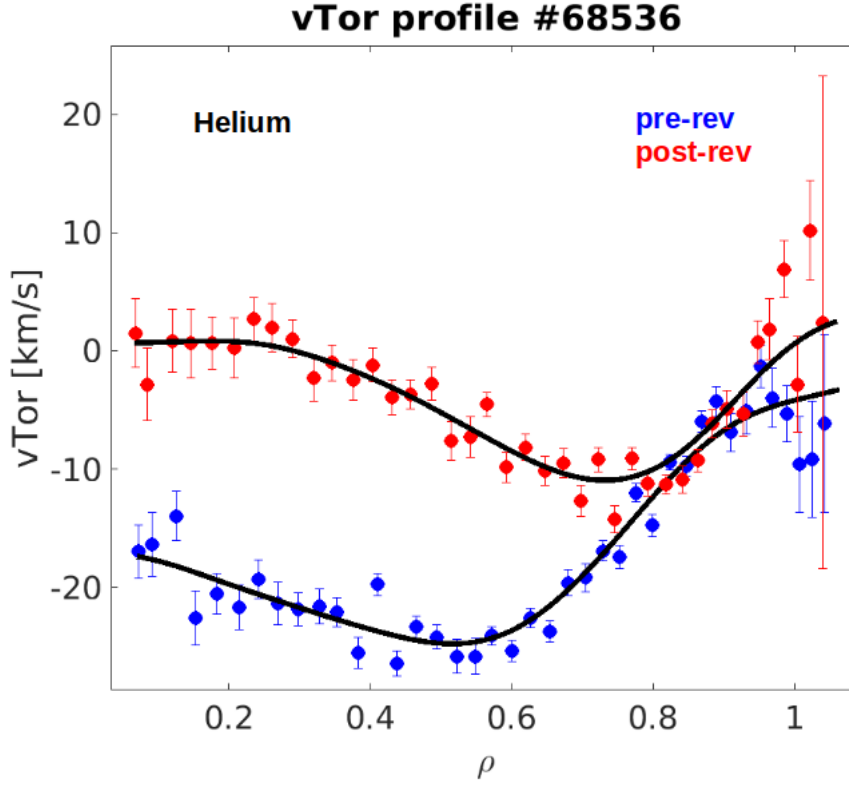


Figure 4.12 – Toroidal velocity profile before and after the reversal (blue and red, respectively), He discharge #68536. The discharge was a high current ( $I_p = 340$  kA) ohmically heated He density ramp in limited configuration.

not necessarily need to change sign, and thus rotation direction, to call the profile variation a reversal. A change in concavity (sign of the profile gradient), in fact, can occur before the saturation of  $|v_{tor}|$ , with the plasma still rotating in the co-current direction.

### 4.3 Effect of Sawteeth activity on rotation

The effect of sawteeth crashes, already described in detail in chapter 3, was explored during the experiments on rotation reversal. In particular, the maximum toroidal velocity scales linearly with plasma current.  $v_{TOR}$  profiles tend to be bulged in the counter-current direction at low  $I_p$ . As the plasma current increases, the central toroidal velocity evolves in the co-current direction, together with the simultaneous outward displacement of the  $q = 1$  surface. The rotation profiles develop a gradient outside the ST inversion radius, whilst remaining flat within.

It is, thus, natural to consider whether sawteeth activity plays a role in the reversal. CXRS spectra are acquired over a time window set by the diagnostic integration time that is, mostly, longer than the ST period. Therefore, the recorded  $v_{TOR}$  profiles are averages over several ST periods and the observed rotation reversal could result from an accumulation of multiple ST

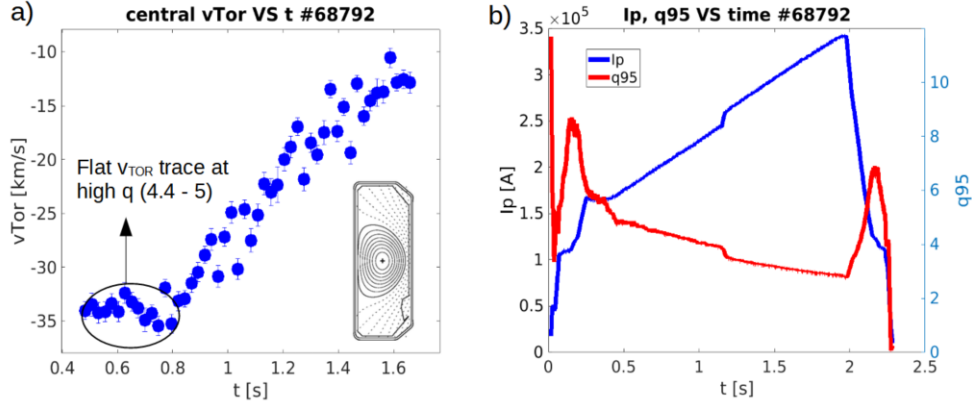


Figure 4.13 – a)  $v_{tor}$  time trace, discharge #68792. The trace is flat above  $q = 4.4$ ; b)  $q_{95}$  and  $I_p$  time trace.

crashes within the same integrated frame.

To investigate this possibility, the following approach was adopted. A current ramp at constant density was performed, allowing for a scan of the safety factor that should reveal any  $q$ -threshold for the reversal. The shape was copied from the D reference discharge and  $n_e$  was chosen to be above the previously identified reversal threshold, so that profiles should reverse when a certain value of  $I_p$  was exceeded. Once this  $q$ -threshold was found, a density ramp was repeated at constant  $I_p$ , at a value lower than the reversal threshold. If our assumptions are correct, no rotation reversal should be observed in this discharge, although the LOC/SOC transition still occurs, as before.

#### 4.3.1 $q$ -threshold for rotation reversal

The  $q$ -threshold was found by monitoring the central velocity evolution with time (Figure 4.13-a). Figure 4.13-b also shows the  $q_{95}$  and  $I_p$  evolutions with time, where the density was maintained at  $\sim 5.5 \times 10^{19} \text{m}^{-3}$ .

The  $v_{TOR}$  profile remains continually peaked at  $-30 \frac{\text{km}}{\text{s}}$  (counter-current direction) until  $q \sim 4.4$ . With further increasing plasma current, central  $v_{TOR}$  increases linearly towards the co-current direction until a maximum value of  $-10 \frac{\text{km}}{\text{s}}$  was attained at the highest current (340 kA).

The reference density ramp was repeated at low current (190 kA), where  $q$  was, now, constant and above 4.4. Central  $v_{tor}$  and  $\tau_E$  are shown as a function of density in Figure 4.14.

As expected from our assumptions,  $v_{TOR}$  does not change direction and its profile remains peaked in the counter-current direction despite the increasing density. Encouragingly, the LOC/SOC transition occurs at the previously obtained density threshold. Therefore, yet again, no direct correlation between the LOC/SOC transition and the rotation reversal was observed at low current and high  $q$ , confirming the  $I_p$  scalings reported in [149] and [55].

These results strongly encouraged extending this investigation of the rotation reversal phe-

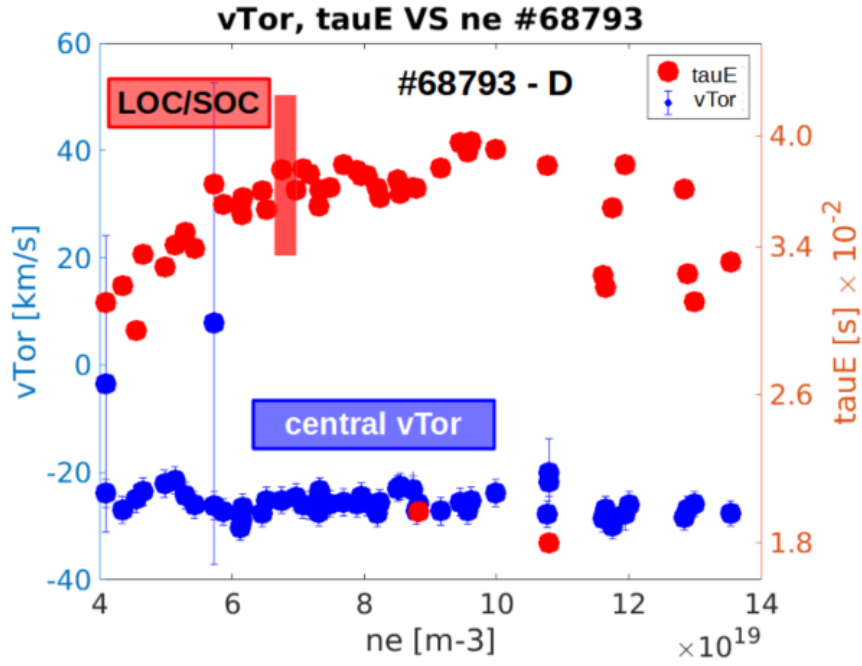


Figure 4.14 – Evolution of central toroidal velocity during a density ramp at low current ( $I_p = 190$  kA), discharge #68793. As expected for such a high value of  $q$ ,  $v_{Tor}$  profiles remained constantly peaked in the counter-current direction. The energy confinement time shows a clear LOC/SOC transition. The density threshold is similar to that observed in the high plasma current discharge. Experimental uncertainties are small and, when not visible, are within the dimension of the data marker.

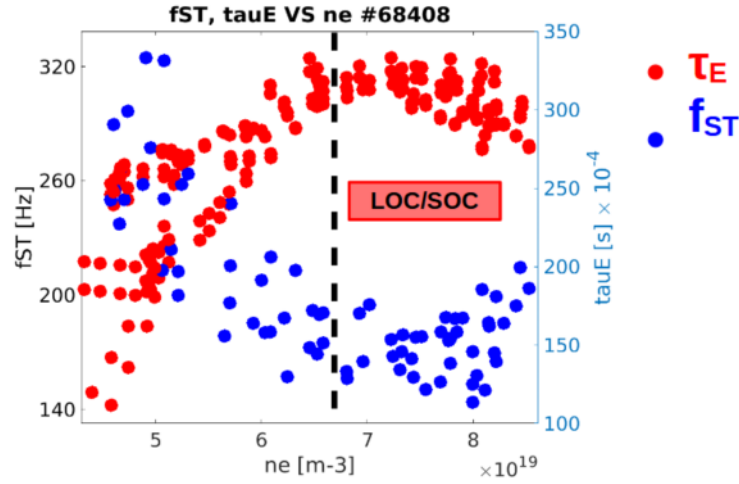


Figure 4.15 – Sawtooth frequency (blue) and energy confinement time (red) evolution during a D density ramp, discharge #68408.

nomenon and its correlation with the LOC/SOC transition and the ST activity for H and He discharges. To monitor any effect of ST crashes on the toroidal rotation profiles, the ST frequency and inversion radius were recorded for all these D, H and He discharges.

### Deuterium

Figure 4.15 shows the ST frequency  $f_{ST}$  evolution during D density ramp #68408 and compares its evolution with the energy confinement time.

As previously shown in Figure 4.7, the LOC/SOC transition in D discharges occurs at  $n_e \sim 7 \times 10^{19} \text{ m}^{-3}$ . The ST inversion radius remained constant throughout the shot ( $\rho_\psi \sim 0.42$ ), as did the position of the  $q = 1$  surface at  $\rho_\psi \sim 0.57$ . The ST frequency decreases linearly until the LOC/SOC density threshold, where it plateaus.

### Hydrogen

Figure 4.16 shows the ST frequency  $f_{ST}$  evolution (blue dots) during H density ramp #68428. The energy confinement time as a function of density is overlaid in red.

The LOC/SOC transition in the H density ramp occurred at  $n_e \sim 6 \times 10^{19} \text{ m}^{-3}$ , lower than for D (Figure 4.9). The ST inversion radius, together with the position of the  $q = 1$  surface, was monitored through Soft X-ray emission and remained constant throughout the shot at  $\rho_\psi \sim 0.4$  and  $\rho_\psi \sim 0.55$ , respectively, slightly displaced radially inwards compared to the D case. The ST frequency, similar to the density ramp performed in deuterium, decreases until the LOC/SOC transition, after which it remains constant. This correlation, albeit being seemingly present in all three discharges, is only circumstantial, as proven by other density ramps performed

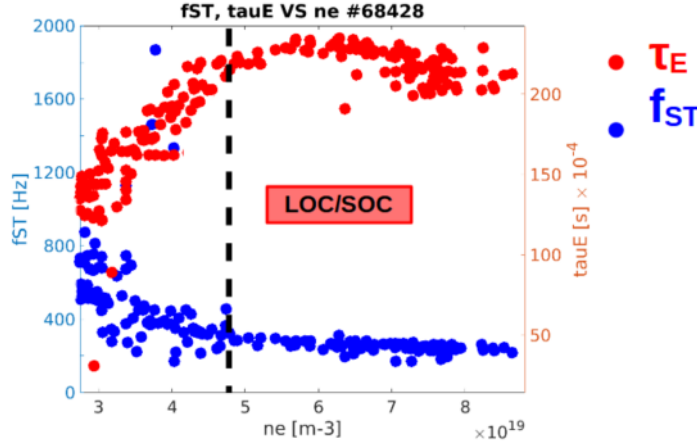


Figure 4.16 – Sawtooth frequency (blue) and energy confinement time (red) evolution during a H density ramp, discharge #68428.

during this work in which a LOC/SOC transition was often not accompanied by any plateau or saturation of the ST frequency. Experimental investigations in the CTH (Compact Toroidal Hybrid) stellarator showed a similar increase in the ST period during a density ramp, but no evident correlation between plasma density and ST activity [83]. A possible explanation may be linked to the changes of the ohmic heating rate inside the  $q = 1$  surface during strong plasma density and current variations. The opposite behaviour was observed in the past in TCV [147], where the ST frequency decreased with density. In general, strong changes of the ST period with varying density are often observed in D plasma discharges [16] [164] [50], and were reported also in H and He [94].

As no rotation reversal was observed during this discharge (Figure 4.9), an eventual effect of the ST crashes on velocity profiles cannot be ascribed to the change in the ST period.

## Helium

Figure 4.17 shows the ST frequency  $f_{ST}$  evolution (blue dots) during He density ramp #68536. The energy confinement time, as a function of density, is overlaid in red.

The LOC/SOC transition in the He density ramp occurred at  $n_e \sim 10 \times 10^{19} \text{ m}^{-3}$ , higher than both the D and H cases (Figure 4.11). The ST inversion radius, as well as the position of the  $q = 1$  surface, remained constant throughout the shot at  $\rho_\psi \sim 0.42$  and  $\rho_\psi \sim 0.57$ , respectively, similar to the D discharge. The ST frequency, as in the density ramps performed in deuterium and hydrogen, decreases until the LOC/SOC transition, after which it remains constant. Again, no correlation between the increase in the ST period and the rotation reversal can be inferred. The saturation of the ST frequency, in fact, occurs close to the LOC/SOC transition, whilst the rotation reversal occurs earlier.



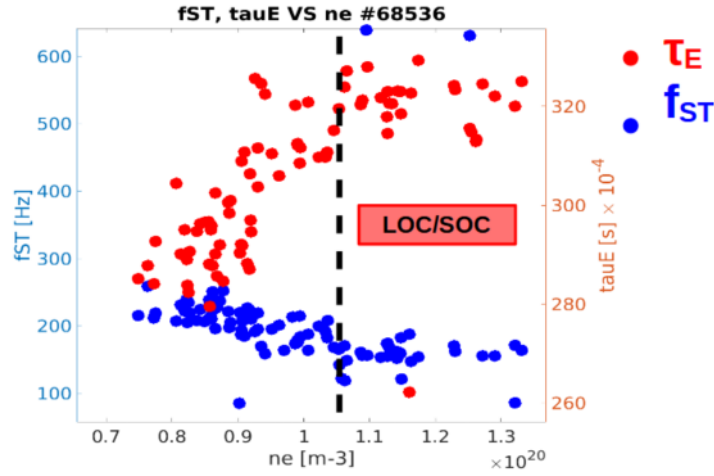


Figure 4.17 – Sawtooth frequency (blue) and energy confinement time (red) evolution during a He density ramp, discharge #68536.

#### 4.4 Effect of density peaking

The results presented in the previous sections showed no distinguishable causal correlation between the LOC/SOC transition and rotation reversal at low current in D or in high current H and He discharges.

The bifurcation from TEM to ITG dominated transport was previously proposed as a possible explanation for both the rotation reversal and the LOC/SOC transition [150] [33]. In particular, adding to the complexity of these phenomena, the C-Mod group reported the observation of co and counter-current rotating plasmas with the same density profiles, obtained through a turbulent suppression technique [33]. Their conclusion was that rotation reversal and LOC/SOC transition are both ascribable to a TEM/ITG bifurcation. However, recent developments in modelling of intrinsic rotation in ohmic discharges in AUG suggest that changes in the curvature (*i.e.* the second derivative) of density profiles can strongly alter the residual stress (see equation 3.21, chapter 3) and that this could explain the rotation reversal [89]. A strong correlation between the toroidal rotation reversal and density peaking, observed in AUG discharges, added credence to this idea. In particular, it was shown that a core toroidal rotation reversal occurred after the LOC/SOC transition and was concomitant with higher peaking of the electron density [6] [106] [119]. These works also showed that the TEM/ITG bifurcation can help in explaining the density peaking but not the entirety of the LOC/SOC transition, as explained in 4.1.1. These hypotheses will be further discussed in the following sections.

The results presented herein confute any causal correlation between the LOC/SOC transition and the rotation reversal.

The density peaking was calculated for all TCV's discharges used herein and its evolution compared to the toroidal velocity and its gradient.

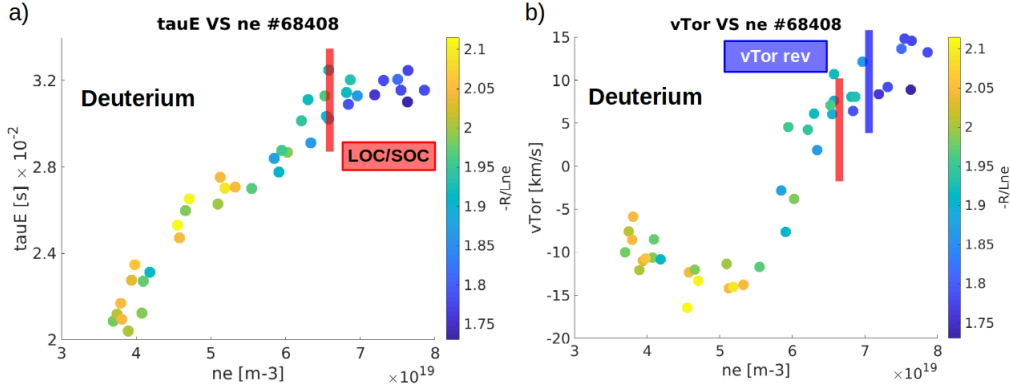


Figure 4.18 – a) Energy confinement time as a function of increasing density, D discharge #68408. The colourbar indicates the logarithmic density gradient. The LOC/SOC transition is highlighted in red. b) Toroidal velocity as a function of increasing density. The opaque red band highlights the LOC/SOC transition, whilst the blue band indicates the toroidal rotation reversal. Here, experimental uncertainties were small (see Figure 4.5, where discharge #68408 toroidal velocity profiles are plotted with error bars) and, for a better clarity of the plot, are not drawn.

#### 4.4.1 Density peaking in D plasma

Figure 4.18 shows D discharge #68408 energy confinement time and toroidal velocity as a function of density. Toroidal velocity is, again, monitored through its central value (combination of toroidal LFS and HFS core lines of sight). Although this is arguably not the best indicator of a reversal, it shows the evolution of the magnitude of the plasma core toroidal rotation, including a sign variation, indicating a change in rotation direction. A better indicator of rotation reversal is the toroidal rotation gradient, which shows how the velocity profile changes its concavity (*i.e.* it "flips"). This term was also calculated and employed further on this chapter to discuss the results. The colourbar indicates the inverse of the logarithmic density gradient scaled with TCV's major radius, *i.e.*  $-\frac{R}{L_{ne}}$ , with  $L_{ne} = \frac{d \ln(n_e)}{dr}^{-1}$ .

The velocity profiles start to reverse at  $n_e \sim 5 \times 10^{19} \text{ m}^{-3}$ , as  $-\frac{R}{L_{ne}}$  reaches its maximum. Although the LOC/SOC transition, and the rotation reversal, occur in the same parameters range in this shot, Figure 4.18-b shows that the rotation reversal occurs slightly after the energy confinement time saturation, concomitantly with the minimum of the  $-\frac{R}{L_{ne}}$  (also seen in [151]), that, itself, corresponds to the maximum steepness in the electron density profiles.

As stated earlier, a better indicator of the reversal is the sharp change in sign of the gradient of the toroidal velocity, here normalised to the thermal Mach number [47]. Assuming rigid plasma rotation on a flux surface, the angular velocity  $\Omega$  can be evaluated from the measured toroidal rotation velocity:  $\Omega = \frac{v_{tor}}{R}$  [62]. The Mach number is defined as  $u = \frac{R\Omega}{v_{thi}}$ , where  $v_{thi} = \sqrt{\frac{2T_i}{m_i}}$  is the ion thermal velocity and  $R$  is the major radius. The gradient of the Mach number is, therefore,  $u' = -\frac{R^2}{v_{thi}} \nabla \Omega$ . Note that  $u$ , differently from the toroidal velocity directly measured by the CXRS (see also chapter 3), is constant over a flux surface. The Mach number,

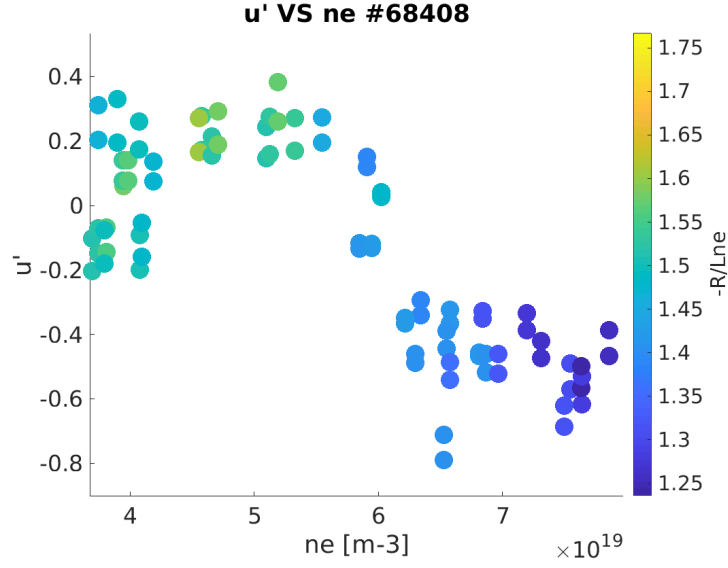


Figure 4.19 – Gradient of the Mach number as a function of density. The gradient is evaluated at the maximum steepness ( $\rho \sim 0.6$ ). The flipping sign indicates a transition from hollow (positive  $u'$ ) to peaked (negative  $u'$ ).

being a dimensionless quantity normalised to the tokamak major radius, is often employed for a practical comparison between different machines [35] [117] [46], also easing comparison between TCV discharges operated in different scenarios.

Figure 4.19 shows the evolution of the gradient of the Mach number in D discharge #68408. The gradient is not taken where the profiles tend to be flatter, but at  $\rho \sim 0.6$  where the profiles tend to be steepest for this safety factor profile. The change in sign starts after central  $n_e \sim 5.5 \times 10^{19} m^{-3}$  and, according to Figure 4.19, the rotation reversal occurs slightly before the LOC/SOC transition and the maximum density peaking but still close to the same parameter range.

The relation between the gradient of the Mach number and the normalised logarithmic gradient is highlighted in Figure 4.20, with a linear regression added in red. The density peaking was also evaluated from the ratio between the plasma density at  $\rho = 0.3$  and  $\rho = 0.8$ . To further highlight the strong correlation with rotation reversal, Figure 4.21 plots this density peaking (blue dots) overlaid on the derivative of the Mach number (red dots) as a function of central density. Here, again, the similar evolution of  $u'$  and the density peaking is highlighted.

Figure 4.22 shows the ratio of the electron and ion temperatures, here evaluated at  $\rho = 0.55$ .  $\frac{T_e}{T_i}$  decreases with increasing density, similarly to the density peaking. This is in agreement with AUG findings [6], where the density peaking and  $\frac{T_e}{T_i}$  decreased with increasing collisionality (and, therefore,  $n_e$ ) in ohmically heated plasmas. Moreover, the density peaking is not affected by the increasing collisionality at high density, *i.e.* in the SOC regime, as was also reported from TCV discharges.

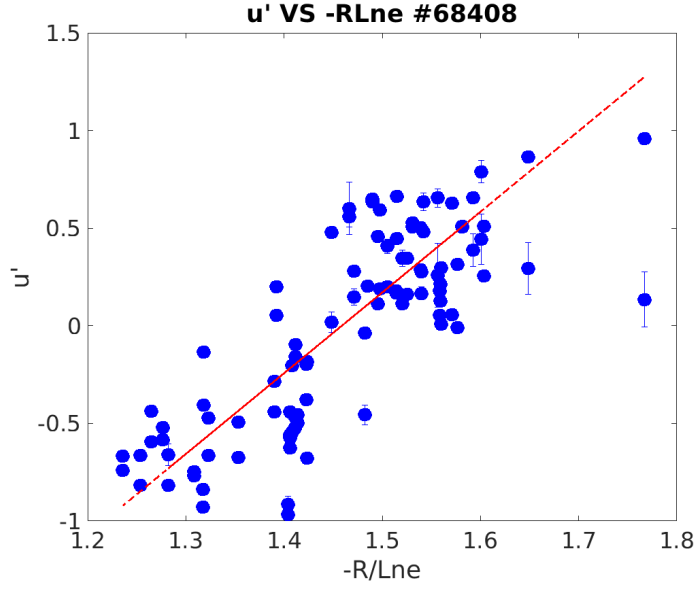


Figure 4.20 – Gradient of the Mach number as a function of the logarithmic density gradient, deuterium discharge #68408. The strong correlation between the two parameters is highlighted by the linear regression in red. Experimental uncertainties are small and, when not visible, error bars are within the data marker dimension.

#### 4.4.2 Density peaking in He plasma

He discharge #68536 shows a well separated (within 10%) LOC/SOC transition and rotation reversal, with a similar correlation to density peaking (Figure 4.23).

The gradient of the Mach number, shown in Figure 4.24, follows the same trend, changing sign when the density profiles are steepest.

For the He discharge, Figure 4.25 shows the relation between the gradient of the Mach number and the  $-\frac{R}{L_{ne}}$  factor.  $\frac{n_e(\rho=0.3)}{n_e(\rho=0.8)}$  is plotted as a function of central density in Figure 4.26, showing, again, a strong correlation between the density peaking and changes in the toroidal velocity. Interestingly, the  $\frac{T_e}{T_i}$  decrease is smaller than the D case (Figure 4.27). This is reflected in the collisionality plot (Figure 4.28), where  $\nu$  in D increases at a different rates compared to the He case.

#### 4.4.3 Density peaking in H plasma

The same analysis was performed for H discharge #68428, where no rotation reversal was observed, although a clear saturation of the energy confinement time is clearly visible in the  $\tau_E - n_e$  plot in Figure 4.29.

Increasing plasma density and current had no effect on the rotation profiles in H, which remained peaked in the co-current direction.  $\frac{n_e(\rho=0.3)}{n_e(\rho=0.8)}$  is plotted as a function of central density in Figure 4.30. Here, for clarity, the  $-\frac{R}{L_{ne}}$  factor is shown without the Mach number gradient

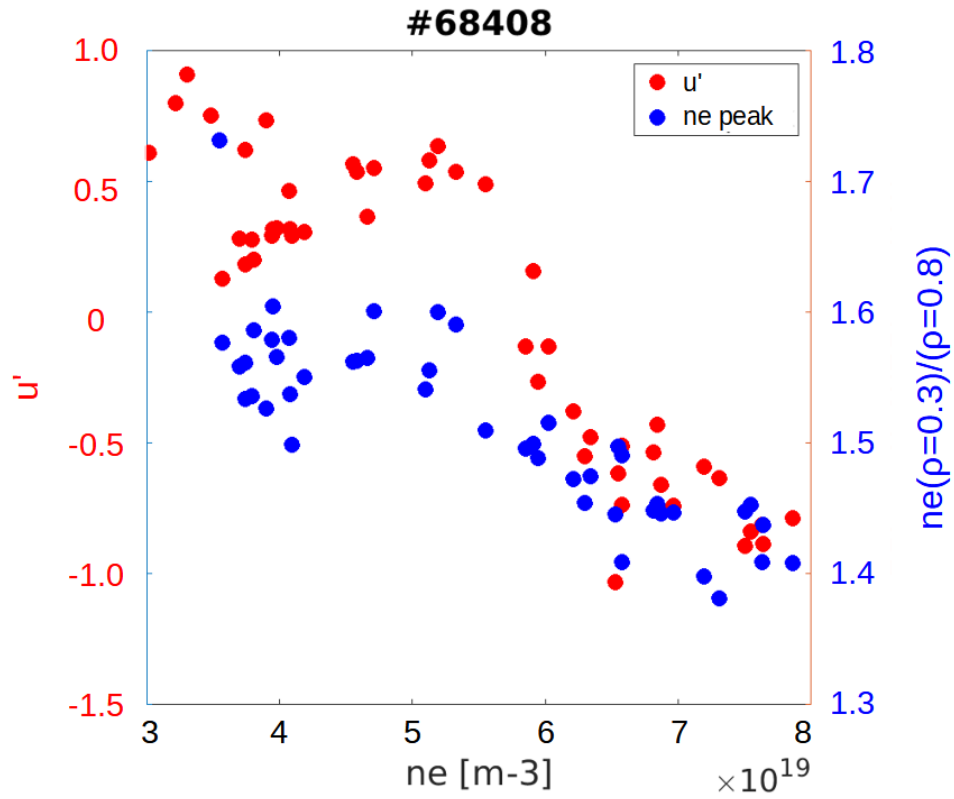


Figure 4.21 – Gradient of the Mach number (red) and  $\frac{n_e(p=0.3)}{n_e(p=0.8)}$  (blue) as a function of central density, deuterium discharge #68408. Experimental uncertainties are small and, most of the time, within the dimensions of the data marker (see Figure 4.20).

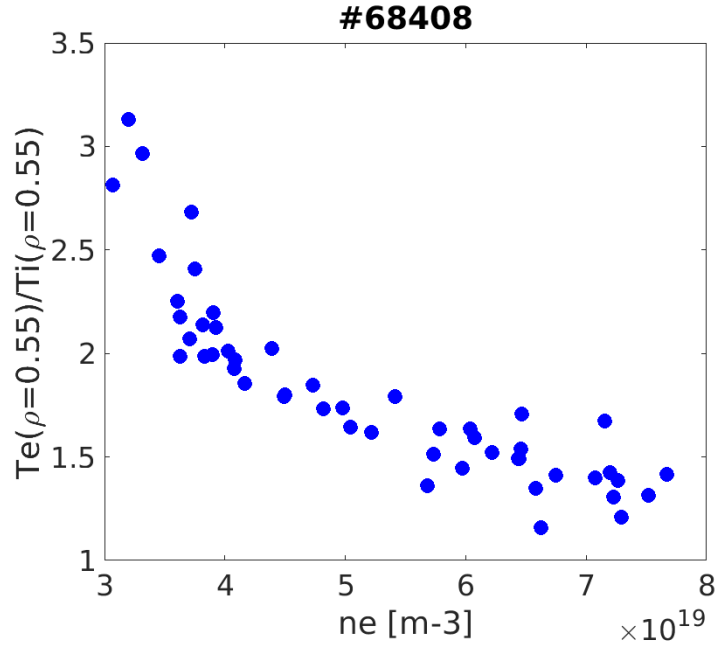


Figure 4.22 –  $\frac{T_e}{T_i}$  as a function of central density, deuterium discharge #68408.

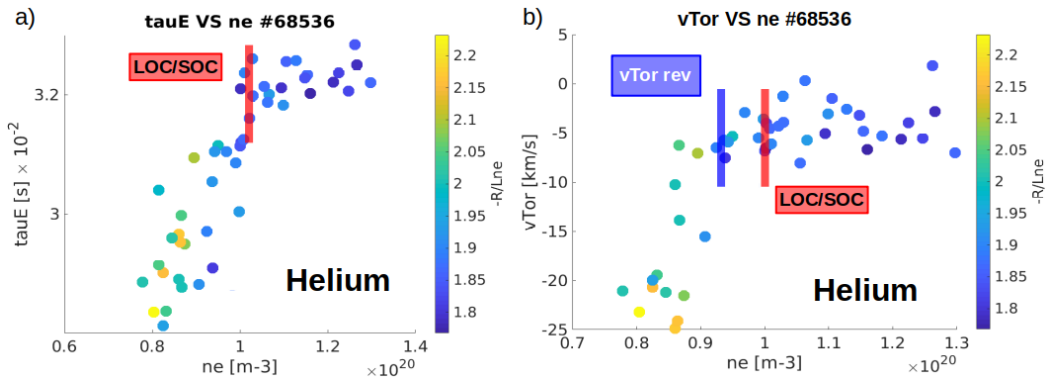


Figure 4.23 – a) Energy confinement time as a function of increasing density, He discharge #68536. The colourbar indicates the logarithmic density gradient. The LOC/SOC transition is highlighted in red. b) Toroidal velocity as a function of increasing density. The opaque red band highlights the LOC/SOC transition, whilst the blue band indicates the toroidal rotation reversal. Here, experimental uncertainties were small (see Figure 4.12, where discharge #68536 toroidal velocity profiles are plotted with error bars) and, for a better clarity of the plot, are not drawn.

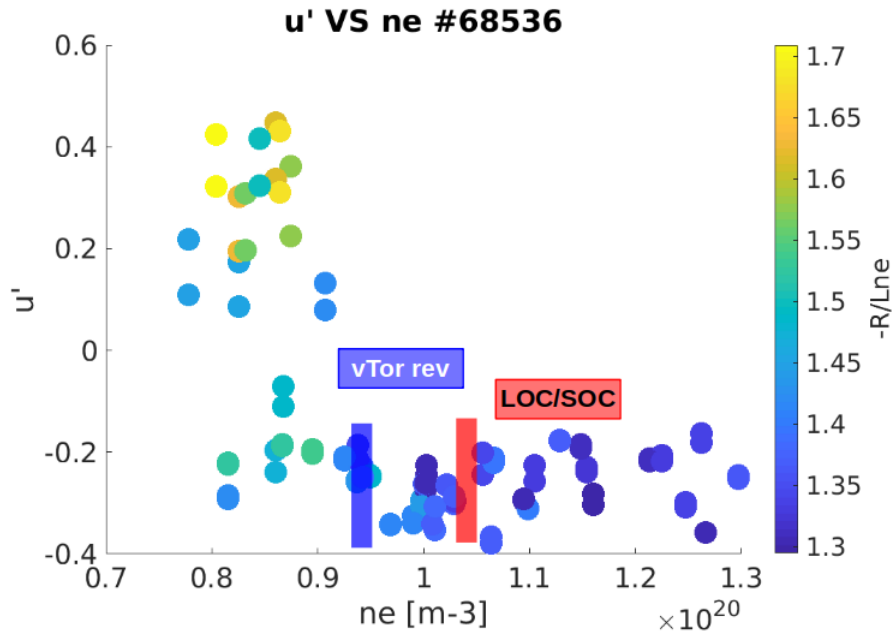


Figure 4.24 – Gradient of the Mach number as a function of density. The rotation reversal and the LOC/SOC transition are highlighted in blue and red, respectively.

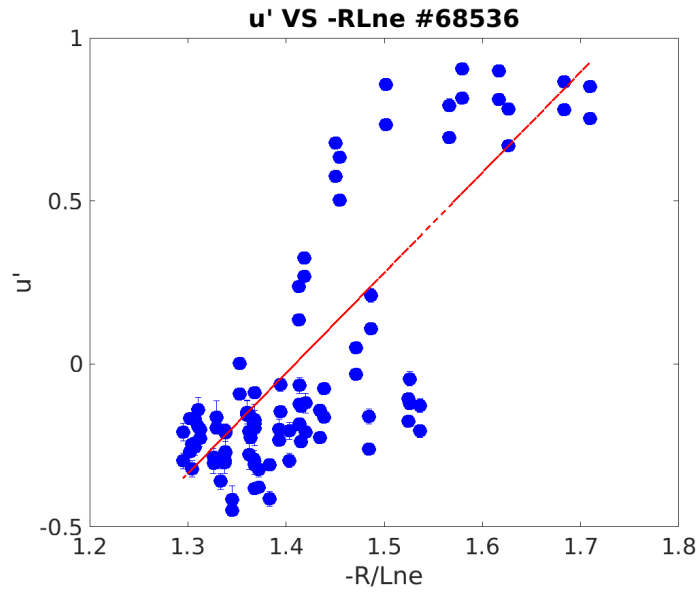


Figure 4.25 – Gradient of the Mach number as a function of the logarithmic density gradient, helium discharge #68536. The strong correlation between the two parameters is highlighted by the linear regression in red. Experimental uncertainties are small and, when not visible, error bars are within the data marker dimension.

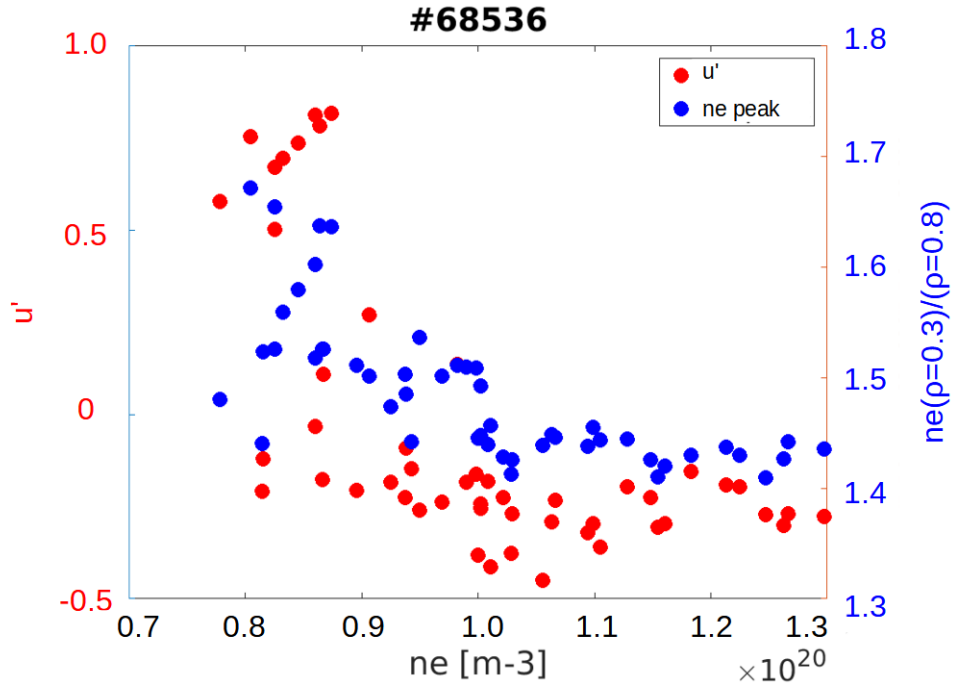


Figure 4.26 – Gradient of the Mach number (red) and  $\frac{n_e(\rho=0.3)}{n_e(\rho=0.8)}$  (blue) as a function of central density, helium discharge #68536. Experimental uncertainties are small and, most of the time, within the dimensions of the data marker (see Figure 4.25).

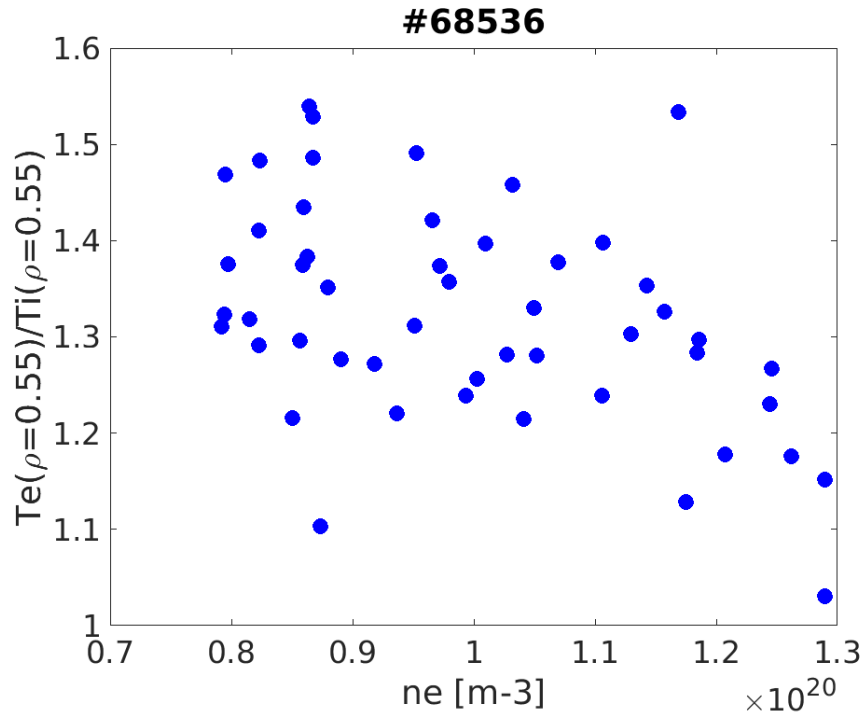


Figure 4.27 –  $\frac{T_e}{T_i}$  as a function of central density, deuterium discharge #68536.



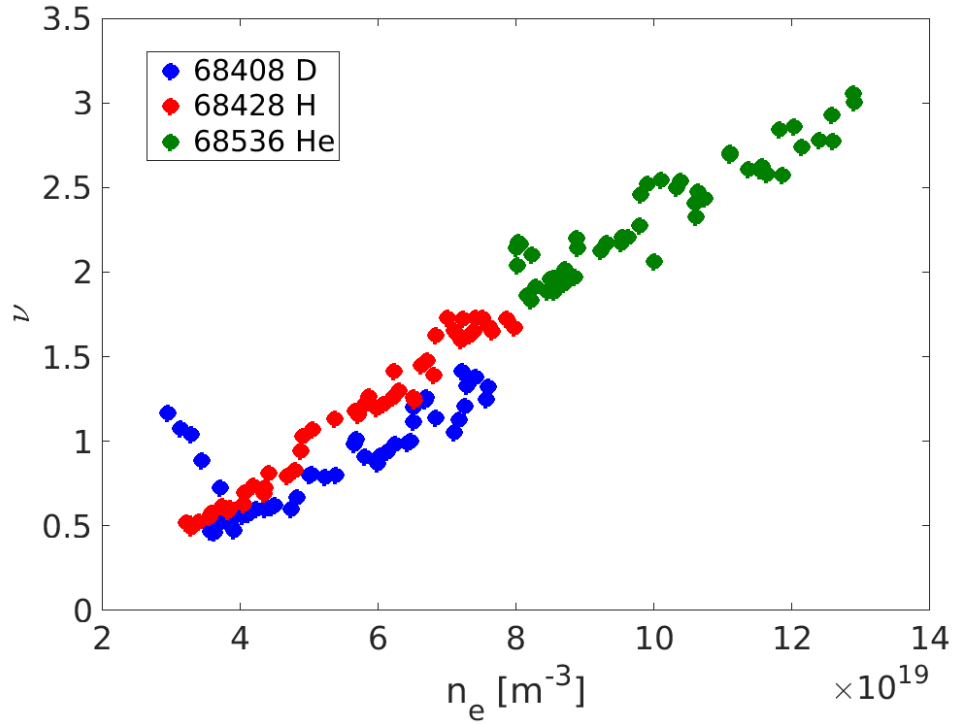


Figure 4.28 – Collisionality VS central electron density for D, H and He discharges (#68408 #68428 #68536).  $\nu$  increases linearly in all three discharge, but at different rates in D.

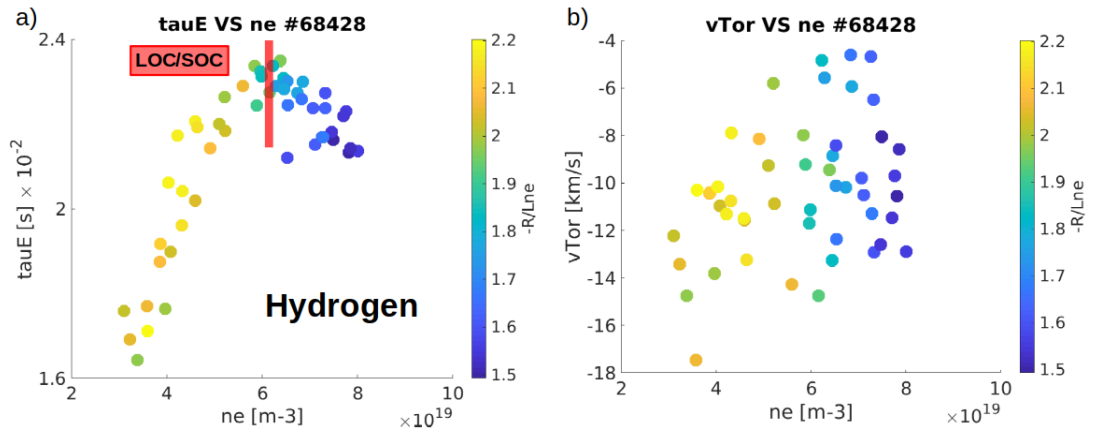


Figure 4.29 – a) Energy confinement time as a function of ramped density, H discharge #68428. The colourbar indicates the logarithmic density gradient. The LOC/SOC transition is highlighted in red. b) Toroidal velocity as a function of increasing density. No rotation reversal was observed in H. Here, experimental uncertainties were small (see Figure 4.9, where discharge #68428 central toroidal velocity is plotted with error bars) and, for a better clarity of the plot, are not drawn.

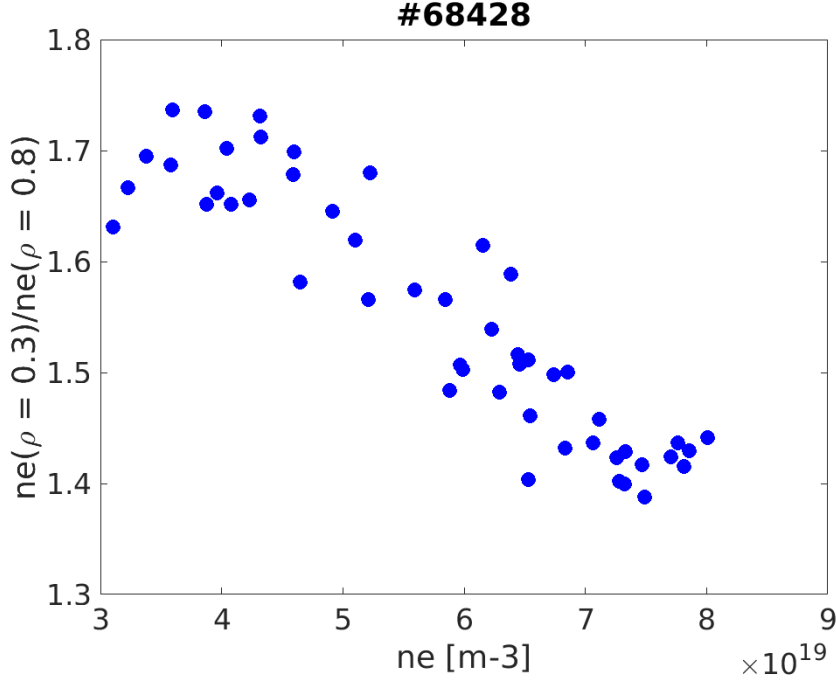


Figure 4.30 – Density peaking factor  $\frac{n_e(\rho=0.3)}{n_e(\rho=0.8)}$  as a function of central density, hydrogen discharge #68428.

trace.  $\frac{n_e(\rho=0.3)}{n_e(\rho=0.8)}$  appears to saturate only at the very end of the density ramp, in clear contrast to D and He. This may suggest that stronger changes in the rotation profiles would be observed if the density were further increased. However, the D and He discharges also displayed a continuous change of the toroidal velocity gradient accompanied by a change in the density peaking, which is not the case here.

The  $\frac{T_e}{T_i}$  ratio, instead, shows a decreasing trend, as in the D discharge (Figure 4.31).

To further probe any effect of peaking, additional X2 ECRH was deposited close to the  $q = 1$  surface with the double objective of displacing this surface radially outwards and increasing the density peaking. The average density was kept near constant to avoid the ECRH cut-off. Three 300 ms pulses were injected with increasing launch power (0.17 MW, 0.5 MW and 0.6 MW), whilst ensuring that the CXRS temporal coverage also included the Ohmic phase before ECH injection. As discharge #69898 did not feature a density ramp, the evolution of the toroidal velocity is better shown as a function of time in Figure 4.32, with the ECRH injection scheme overlaid on the time axis. Figure 4.33 shows the evolution of the gradient of the Mach number in time. The density peaking increases similarly to the density ramp discharges. Toroidal velocity profiles start to reverse with the first ECRH pulse. The complete reversal from the co to counter-current direction occurs during the second 0.5 MW ECRH pulse, whilst no further change is observed during the injection of the final 0.6 MW pulse. Interestingly, the  $q = 1$  surface was displaced from  $\rho = 0.22$  at  $t = 0.4$  s and  $\rho = 0.6$  at  $t = 0.9$  s, *i.e.* before the full reversal, whereas the ST inversion radius remained unchanged. Consequently, although the

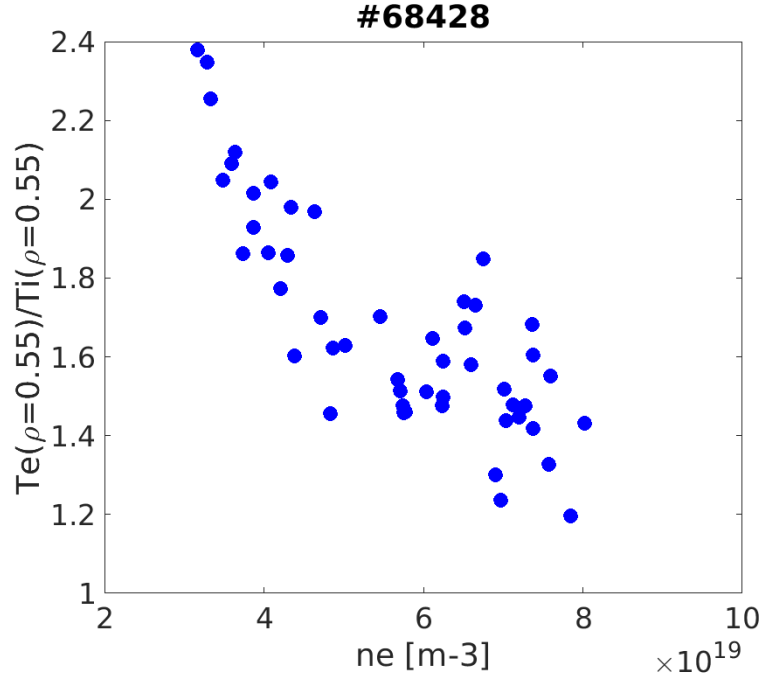


Figure 4.31 –  $\frac{T_e}{T_i}$  as a function of central density, deuterium discharge #68428.

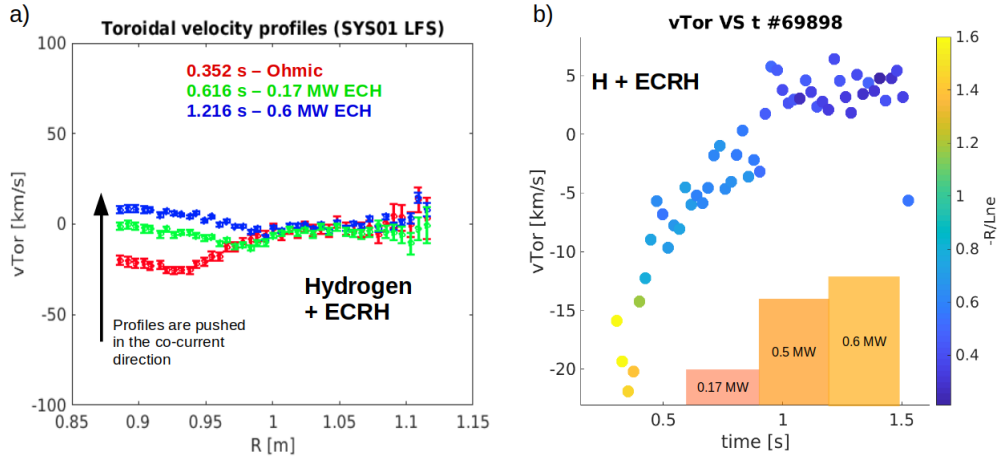


Figure 4.32 – a) Toroidal velocity profiles plotted over major radius. The three profiles correspond to three different phases: early ohmic phase (red), 0.17 MW ECRH pulse (green) and 0.6 MW ECRH pulse (blue). b) Central toroidal velocity evolution in time. The ECRH injection scheme is overlaid on the time axis. The colourbar indicates the logarithmic density gradient.

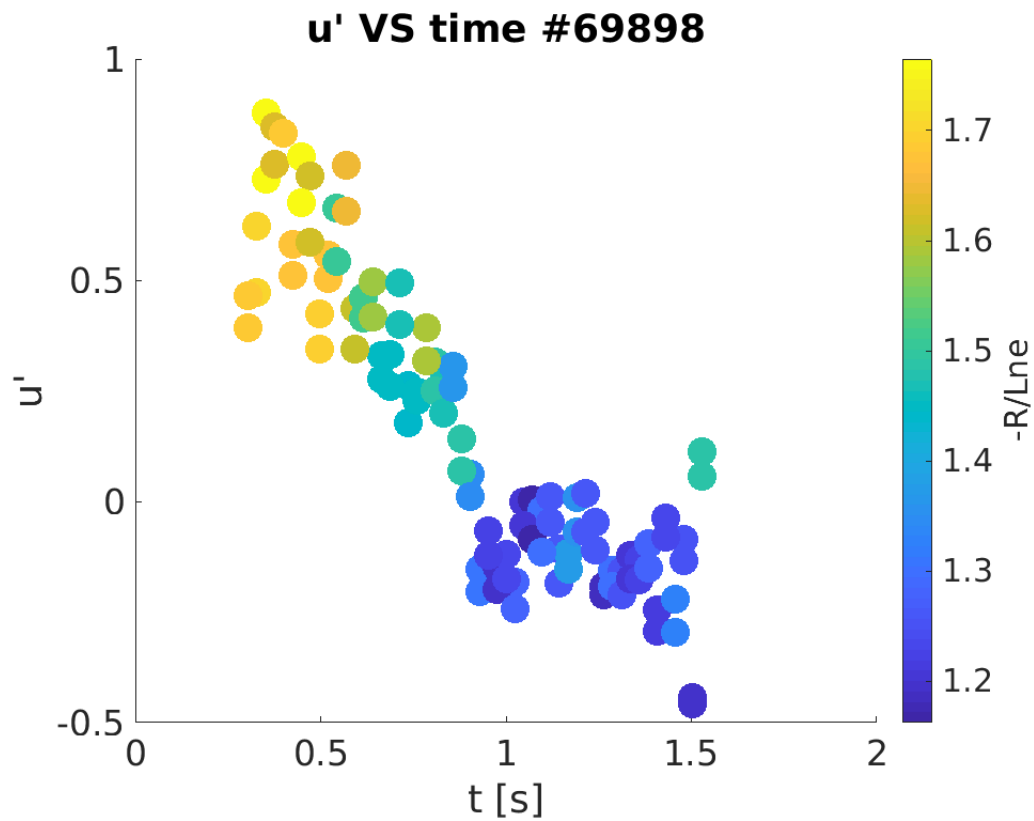


Figure 4.33 – Evolution of the gradient of the Mach number in time, hydrogen discharge #69898. Experimental uncertainties are small and error bars are within the data marker dimension.

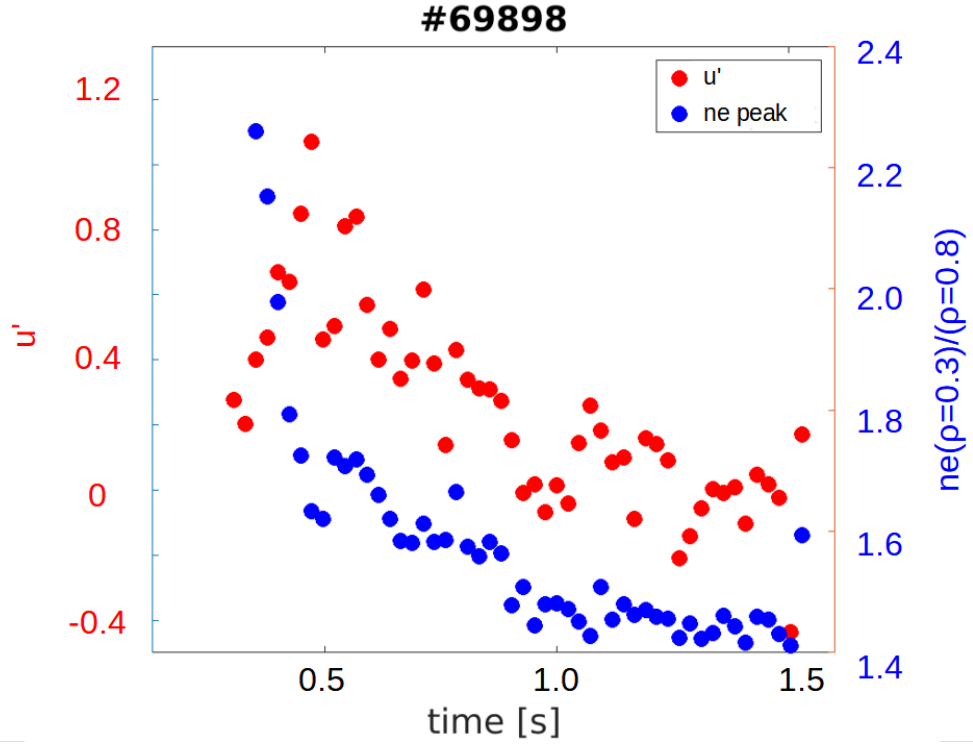


Figure 4.34 – Density peaking factor  $\frac{n_e(\rho=0.3)}{n_e(\rho=0.8)}$  (blue) and gradient of the Mach number (red) as a function of central density, hydrogen discharge #69898.

minimum of the toroidal rotation profile is displayed outwards along with the  $q = 1$  radius, the reversal is unlikely to be well explained by ST activity.

The correlation between the density peaking and the gradient of the velocity profiles is further highlighted in Figure 4.34. However, it should be mentioned here that, during the H density ramp (#68428), the density peaking factor decreased, yet the temperature profiles became steeper. This, however, was not accompanied by any change in the toroidal velocity profiles. The strong changes in the electron and ion temperatures do not seem to play an important role in driving changes in the rotation profiles. The strong decrease in  $\frac{T_e}{T_i}$  observed during the D and H density ramps is less pronounced in He. However, whilst D and He displayed a clear rotation reversal, the ohmic H discharge did not. During ECRH injection, as expected,  $\frac{T_e}{T_i}$  increased (Figure 4.35), the density peaking factor decreased and rotation profiles reversed concomitantly with the maximum steepness in the electron density profiles.

The discharge was repeated in D with a similar outcome: the toroidal rotation profile reversed concomitantly with the maximum density peaking. Density was kept constant at  $\sim 3.5 \times 10^{19} \text{m}^{-3}$ , again, to avoid the ECRH frequency cutoff. Although the density was below the rotation reversal threshold,  $v_{Tor}$  profiles were fully reversed already from the start of the first power step injection (0.17 MW, Figure 4.36), with no meaningful differences seen in the rotation profiles between the three ECRH power steps.

During the Ohmic phase, and during the Ohmic density ramp discharge, the position of the

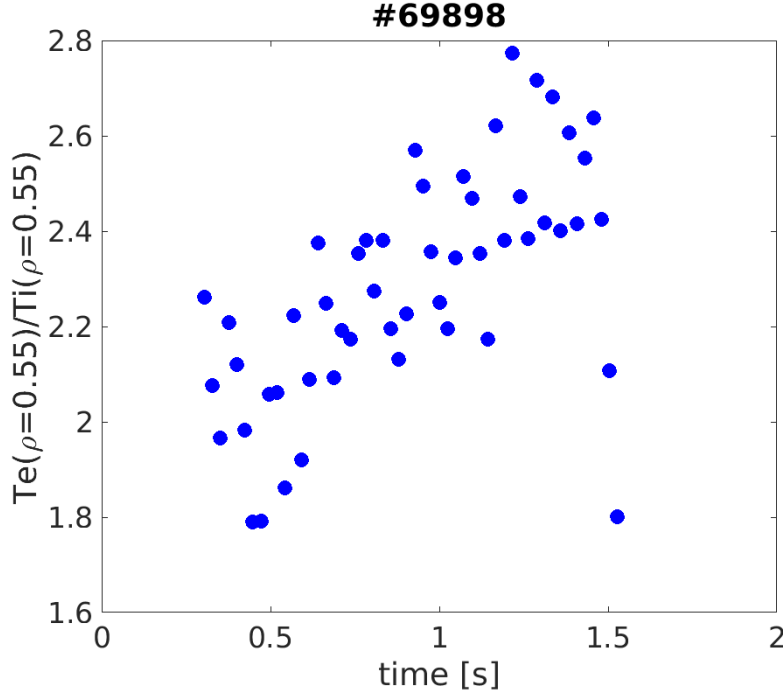


Figure 4.35 –  $\frac{T_e}{T_i}$  as a function of time, hydrogen discharge #69898.

$q = 1$  surface remains between  $\rho_{q=1} = 0.550$  and  $\rho_{q=1} = 0.575$  and the ST radius is the same as in the reference ohmic density ramp (#68408). The addition of ECRH power steps has the effect of displacing the  $q = 1$  surface to  $\rho_{q=1} = 0.650$ . The ST period and inversion radius both decrease during the ECRH injection phase.

Figure 4.37 shows the gradient of the Mach number as a function of the logarithmic density gradient for the H + ECRH discharge (left) and D + ECRH (right). The linear relation described above is recovered in these cases too.

The correlation between density peaking and the gradient of the velocity profiles is again highlighted in Figure 4.38, and Figure 4.39 plots the  $\frac{T_e}{T_i}$  trajectory.

These observations suggest that, wherever the change in  $v_{Tor}$  is not difficult to separate from the ST activity, density peaking is the main actuator for the rotation reversal for this plasma configuration (limited, positive triangularity, L-mode). It is to note here that this result is in contrast with the work reported in [33] (C-Mod), where turbulent modes were suppressed and co and counter-current rotation profiles were observed in plasmas with same density and temperature profiles. The conclusion of the C-Mod group was that both the LOC/SOC transition and the rotation reversal are the consequence of a TEM/ITG bifurcation. However, in the opinion of the author, the experiments presented in this thesis explored a larger number of scenarios, highlighting the complex phenomenology of the LOC/SOC transition, the TEM/ITG bifurcation and the rotation reversal that, although seemingly related to a common phenomenon, cannot be ascribed to the same cause. Linear gyrokinetic simulations performed in TCV will be presented in the following paragraphs, showing that discharges that presented a

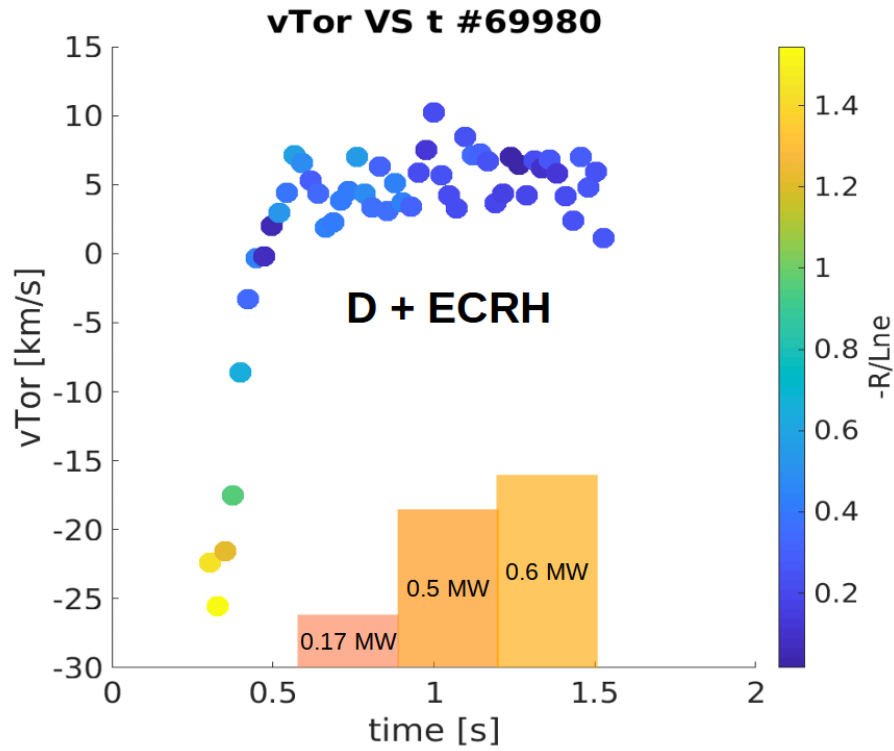


Figure 4.36 – Central toroidal velocity evolution in time, discharge #69980. The ECRH injection scheme is overlaid on the time axis. The colourbar indicates the logarithmic density gradient.

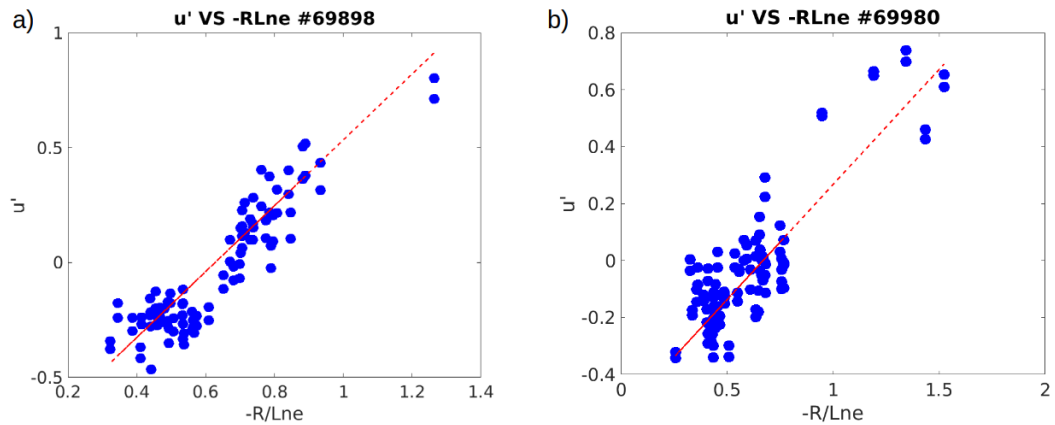


Figure 4.37 – Evolution of the gradient of the Mach number in time: a) H discharge + ECRH #69898; b) D discharge + ECRH #69980. Experimental uncertainties are small and error bars are within the data marker dimension.

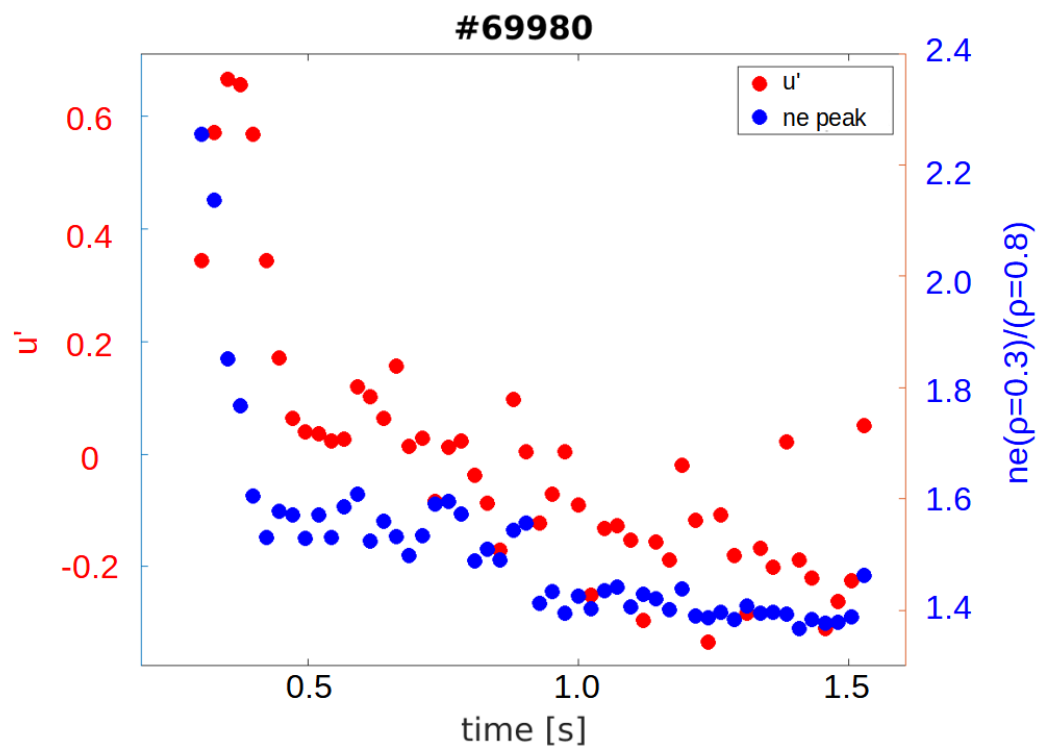


Figure 4.38 – Density peaking factor  $\frac{n_e(\rho=0.3)}{n_e(\rho=0.8)}$  (blue) and gradient of the Mach number (red) as a function of central density, hydrogen discharge #69898.

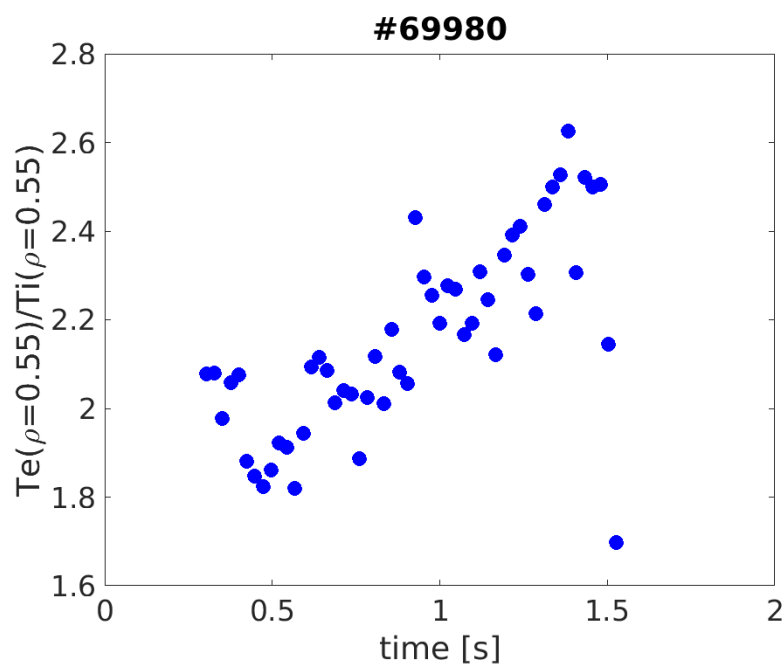


Figure 4.39 –  $\frac{T_e}{T_i}$  as a function of time, deuterium discharge #69980.



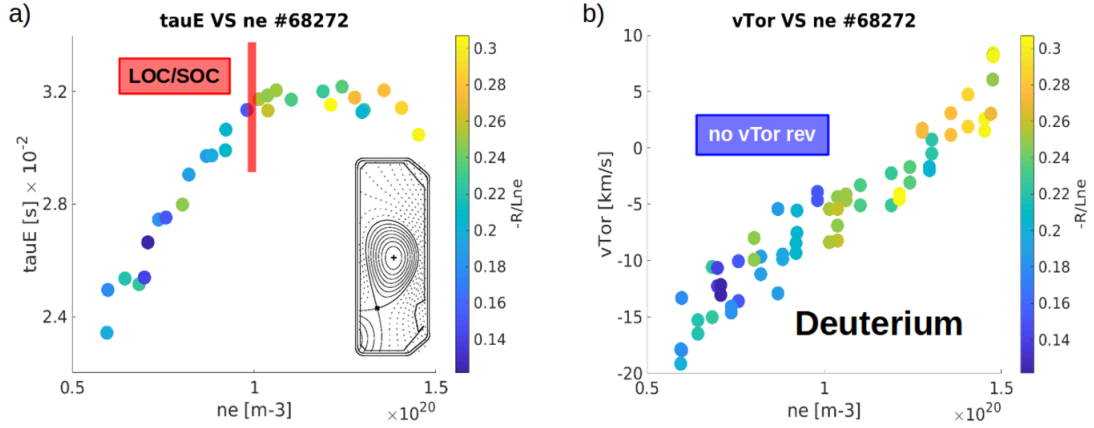


Figure 4.40 – a) Energy confinement time as a function of increasing density, diverted D discharge #68272. The red band indicates the LOC/SOC transition; b) Central toroidal velocity as a function of increasing density, diverted D discharge #68272. Experimental uncertainties are of the order  $\sim \pm 3 \frac{km}{s}$ , see Figure 4.41 where toroidal velocity profiles are plotted at different time frames.

rotation reversal were not necessarily accompanied by a TEM/ITG bifurcation. These results, albeit preliminary, emphasise the need for further exploration of these phenomena.

## 4.5 Diverted configuration

Plasma discharges were performed in diverted configuration in D and H to further explore the effects of isotopes, plasma shape and configuration on rotation. Previous experiments showed that diverted plasmas usually rotate in the co-current direction and that a reversal occurs in the counter-current direction [56] [31]. The same behaviour was observed in these experiments, confirming the highly reproducibility of the involved physics.

Figure 4.40 shows the energy confinement time and the central toroidal velocity evolution as a function of density in a deuterium discharge at negative plasma current ( $I_p = -320 kA$ ) and diverted configuration. The LOC/SOC transition occurs at higher density than for the limited discharge. However, the central toroidal velocity monotonically evolves in the counter-current direction without displaying a reversal.

Figure 4.41-a also shows that the velocity gradient (here calculated at  $\rho \sim 0.3$ ) in the diverted configuration does not display a correlation with the density peaking. The evolution of toroidal velocity is shown in Figure 4.41-b, where three  $v_{tor}$  profiles are shown at different times during the density ramp. Despite the relatively large error bars, probably due to the rapid variation in  $n_e$ , there is no change in sign of the gradient at any  $\rho$ . The change towards the counter-current direction is, here, more of a rigid displacement of the entire profile than a reversal, differently from that reported in [55] (TCV 2007), where a clear reversal in diverted configuration was observed. In that case, however, the plasma shape was highly elongated, almost limited,

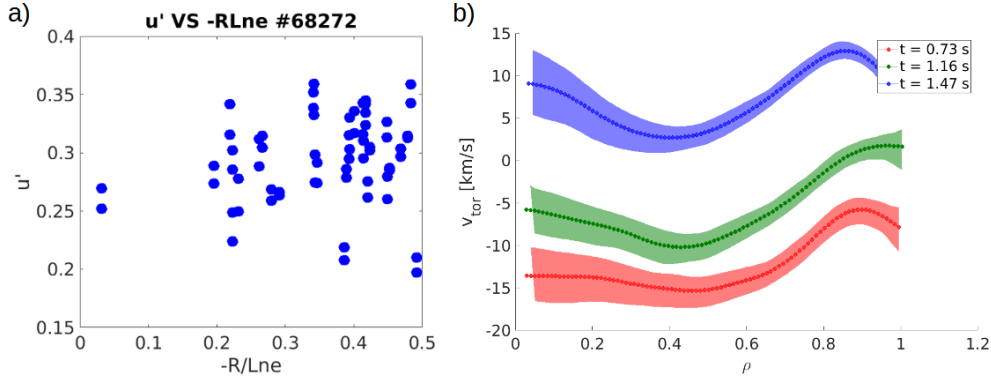


Figure 4.41 – a) Gradient of the Mach number as a function of logarithmic density gradient, diverted D discharge #68272; b) Toroidal velocity profiles at different moments of a density ramp, diverted D discharge #68272.

and with shorter divertor legs compared to #68272 (see Figure 4.40). As shown in [56], the plasma shape parameters (elongation, triangularity) and, possibly, the wall gaps (since they appear to provide an edge  $v = 0$  that gets approached by some of the diverted regimes), appear to be crucial for the observation of a rotation reversal. Therefore, a density ramp in diverted configuration was performed adjusting the shape in order to seek a possible reversal in the toroidal velocity profiles. This plasma discharge was challenging due to a locked mode appearing in the early phase that engendered early discharge disruptions. Several attempts were required to perform the full  $n_e$  ramp. Eventually, a full discharge was performed and a rotation reversal was indeed observed, although the data quality was not optimal (Figure 4.42). Interestingly, the LOC/SOC transition occurs at  $n_e \sim 5.8 \times 10^{19} m^{-3}$  and  $t \sim 0.8$  s but no rotation reversal was observed until  $t \sim 1.2$  s, at  $n_e \sim 7.1 \times 10^{19} m^{-3}$ . The observation of a toroidal rotation reversal from co to counter-current direction agrees with results reported in other machines [151] [119], showing, again, the importance of plasma shape and configuration, as stated at the beginning of the chapter.

A similar behaviour was observed in H discharges performed in the frame of a study on "isotope effect on transport in presence of TEMs and ITGs". In this mission, a series of diverted discharges was performed at  $I_p = -200$  kA and  $B_T = -1.4$  T. The aim was to explore the effect of isotopes in the presence of different turbulent modes. Assuming that the plasma is dominated by TEMs in the LOC phase and ITGs in the SOC, a series of discharges was performed at increasing density in D and H. The toroidal velocity at fixed  $\rho$  was taken from each discharge and plotted as a function of central electron density (Figure 4.43).

The linear increase in  $v_{tor}$  observed in the D density ramp is retrieved in H as well. The main difference between the D density ramp (Ohmic discharge #68272,  $n_e$  ramp in diverted configuration) and the D density scan (experiment "isotope effect on transport in presence of TEMs and ITGs", multiple Ohmic discharges at different  $n_e$ ) was the current, which affected the value of the density at the LOC/SOC transition threshold. The Ohmic density ramp in diverted configuration #68272 was performed at  $I_p = -320$  kA, whilst the Ohmic density

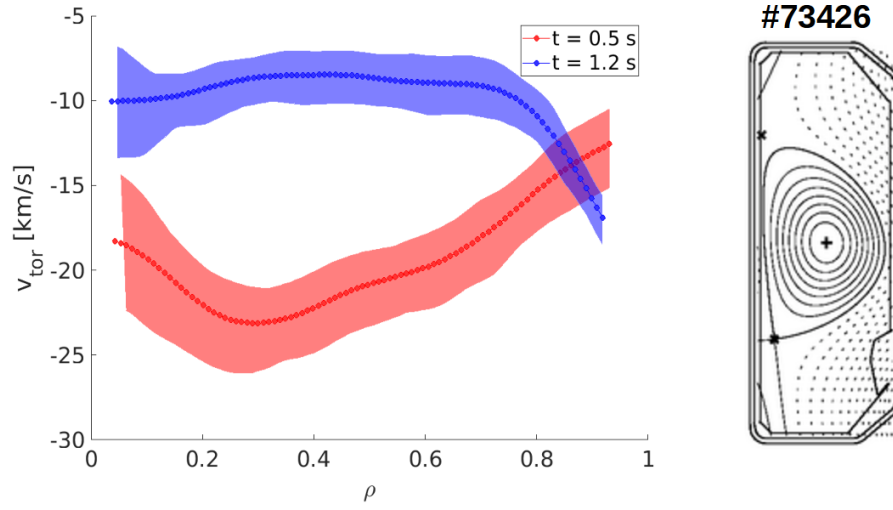


Figure 4.42 – Toroidal velocity profiles before and after the rotation reversal, diverted D discharge #73426. A rotation reversal occurs from co to counter-current direction.

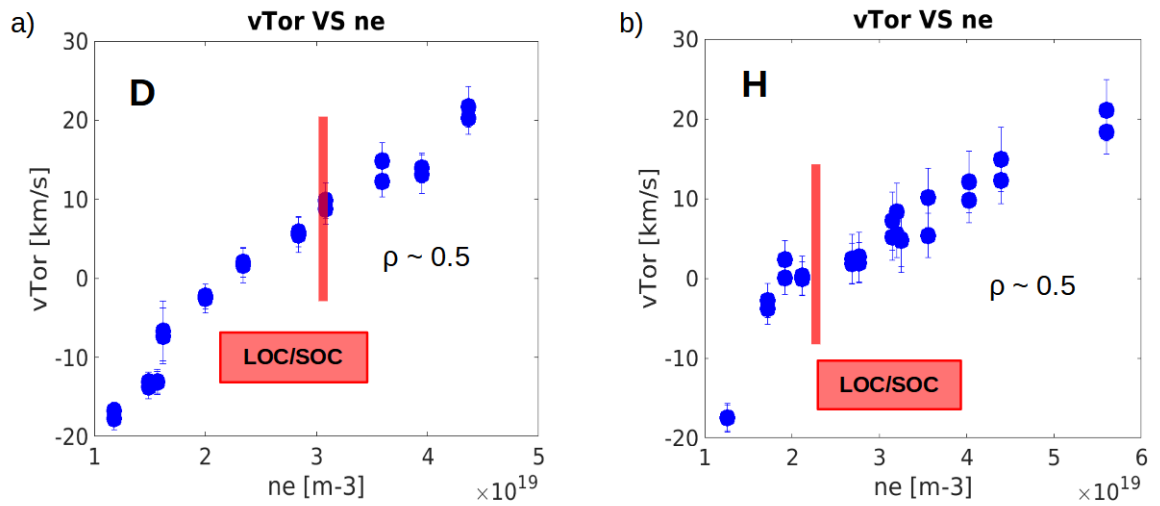


Figure 4.43 – Toroidal velocity at  $\rho \sim 0.5$  extrapolated from a series of discharges in diverted configuration at increasing density. a) D discharges; b) H discharges.

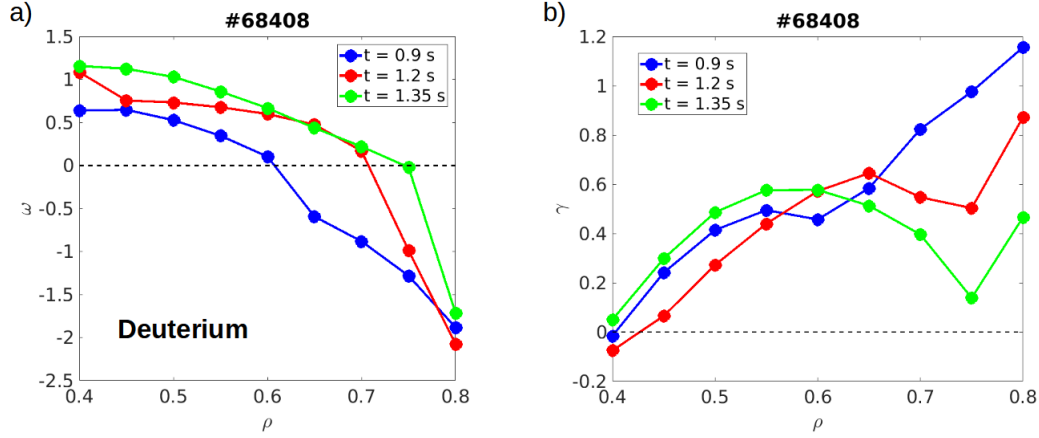


Figure 4.44 – Frequency (a) and growth rate (b) of the most unstable mode across the LOC/SOC transition, D discharge #68408.

scan in diverted configuration (experiment "isotope effect on transport in presence of TEMs and ITGs") was performed at  $I_p = -200$  kA. As expected [56], the density at the LOC/SOC transition threshold was higher for the high current case. The LOC/SOC transition occurred earlier in H than in D, as was observed also for limited configuration. No rotation reversal was observed but, again, a slow, rigid displacement of the toroidal velocity profiles towards the counter-current direction without changes in the gradients.

## 4.6 Linear gyrokinetic simulations

Linear gyrokinetic simulations were performed with the GENE code to explore the TEM/ITG dominance across the LOC/SOC transition and the rotation reversals for the experiments reported above.

Figure 4.44-a shows the frequency of the most unstable mode (the contribution of sub-dominant mode was not explored) as a function of  $\rho$  for D discharge #68408. Its evolution across the LOC/SOC transition was monitored by performing the calculation at specific shot times ( $t = [0.9, 1.2, 1.3]$  s).

The central region of the plasma is clearly dominated by ITG ( $\omega > 0$ ) in all three time frames. However, moving towards the plasma edge, where the ion temperature profiles are steeper, a significant difference appears.

The plasma is dominated by TEM ( $\omega < 0$ ) for  $\rho > 0.6$  in the LOC phase. As the density increases, a mode appears to develop at the edge in the ion direction and, after  $t = 1.2$  s, ITGs dominate also in the external region ( $\rho < 0.7$ ). Although it is hard to observe a precise transition from TEM to ITG dominance with time, it is clear from the simulations that a change in turbulence occurs across the LOC/SOC transition parameters. These results provide support to the hypothesis that the TEM/ITG bifurcation is a local phenomenon [106] and, as argued in the chapter introduction, does not occur over the entire plasma profile simultaneously.

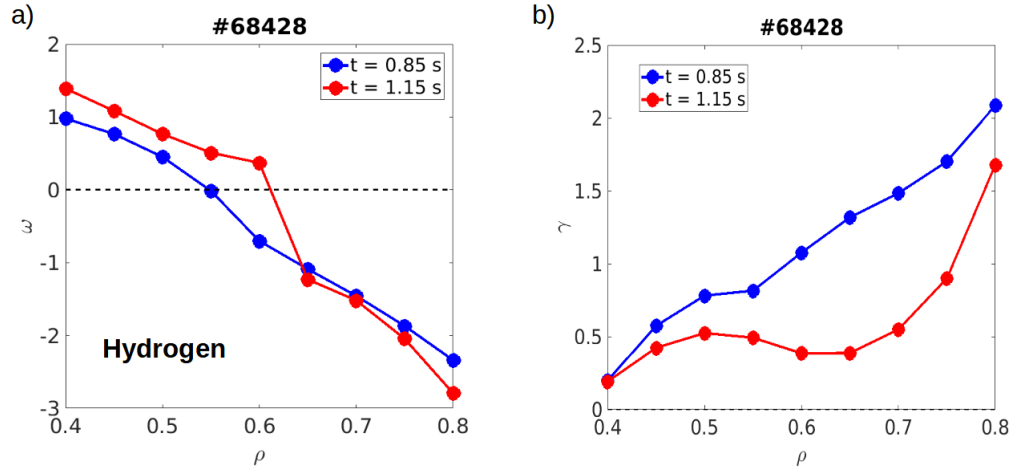


Figure 4.45 – Frequency (a) and growth rate (b) of the most unstable mode across the LOC/SOC transition, H discharge.

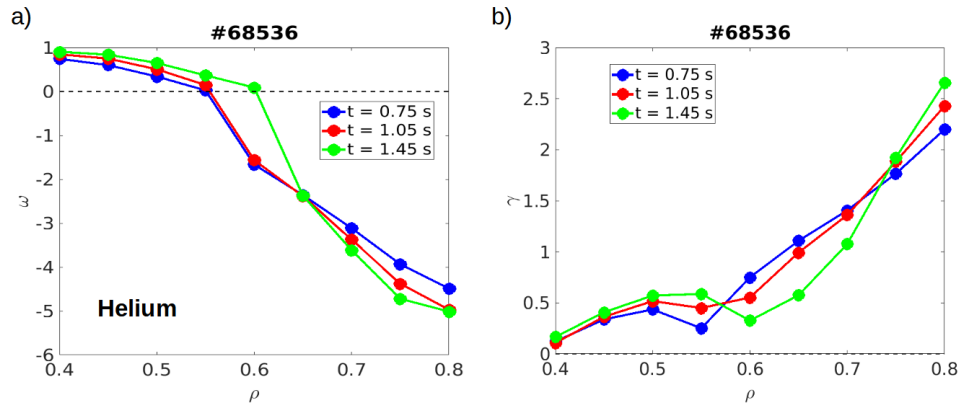


Figure 4.46 – Frequency (a) and growth rate (b) of the most unstable mode across the LOC/SOC transition, He discharge.

A similar analysis was performed for H discharge #68428, where the LOC/SOC transition occurred earlier than the D discharge, but where no rotation reversal was observed (Figure 4.45). The transition from TEM to ITG is less pronounced here with no difference observed above  $\rho \sim 0.6$ .

Finally, the He discharge #68536 analysis yielded a similar outcome. Figure 4.46 shows just a minor change in the frequency of the most unstable mode across the LOC/SOC transition and almost no change across the rotation reversal.

The three discharges exhibit different mode growth rate (Figures 4.44-b, 4.45-b, 4.46-b).  $\gamma$  strongly decreases above  $\rho = 0.6$  across the LOC/SOC transition in D discharge #68408. Finally, just a mild decrease is observed at mid-radius in H and He, with the difference between the LOC and the SOC phases less pronounced than for the D discharge.

As no evident TEM/ITG bifurcation was found in H and He, an interchange between dominant

turbulent modes must be excluded as the fundamental cause for either a  $\tau_E$  saturation or the rotation reversal. These results agree with AUG's findings [106] that suggested that the LOC/SOC transition is not directly related to the TEM/ITG bifurcation, but rather the stronger ion energy transport at higher densities, caused by the decreasing plasma dilution, that leads to a saturation of  $\tau_E$ . The strong correlation between density peaking and profiles steepness, instead, supports the hypothesis that it is rather the change in  $n_e$  induced by turbulence that drives the reversal rather than any change in LOC/SOC [89].

### 4.7 Discussion and conclusions

Experimental observations made during 2020/2021 TCV campaign were presented in this chapter. Data analysis focused on the study of toroidal rotation profiles of plasmas of three majority species: D, H and He. The main objective of the study was to explore the possibility of a relationship between the LOC/SOC transition and the rotation reversal phenomena previously observed during density ramps. The two phenomena were reported to occur in the same parameters range ( $n_e, B_T, I_p$ ) at least in high current D discharges. Based upon these observations, a causal relation was suggested to exist between the two phenomena. Furthermore, a commonly accepted explanation for the saturation of the energy confinement time above a density threshold was a change in the plasma turbulent state with the Ohmically plasma dominated by TEM at low density. As the density is raised, the TEM instability is stabilised due to collisional detrapping of electrons, whilst the ITG instability growth rate increases. Following this reasoning, above a certain density threshold, ITGs overtake TEMs as the dominant turbulent mode, becoming the main contributor to the ion confinement scaling [169]. Such a TEM/ITG bifurcation has been also suggested to explain the toroidal rotation reversal, as this change in the turbulent regime is associated with a change in the direction of the residual stress [149] and hence rotation direction. However, as cases of LOC/SOC transition occurring without a TEM/ITG bifurcation were reported [119], this story was thought to require refinement. Recent results, in fact, suggested that the energy confinement time saturation is rather caused by the stronger (compared to electrons) ion energy transport at high density [106]. These and other works [89] would indicate no causal relation between the LOC/SOC transition and the rotation reversal should exist, and that an explanation for the inversion of the  $v_{tor}$  gradient would be found in a correlation with the electron density gradient and/or its peaking.

In addition, previous results obtained from TCV suggested that ST crashes may push the  $v_{Tor}$  profiles in the co-current direction for sufficiently low  $q$ , providing another possible toroidal drive term. The ST period was observed to increase with increasing density until the LOC/SOC transition, after which it plateaus, or decreases, as does the energy confinement time. Initially, it was supposed that the absolute values of the ST period and the ST inversion radius were determinant in the development of an associated rotation reversal. This conclusion also required refinement when plasma operated in majority H and He showed contradictory behaviour. Based on results presented herein, possible actuators for the rotation reversal were identified

to be  $n_e$ , the density peaking, the TEM/ITG bifurcation and ST activity.

The measurements presented in this chapter show clearly that rotation reversal occurs concomitantly with the LOC/SOC transition for a very restricted number of cases, with that only for D majority discharges. In fact, a change in  $v_{Tor}$  from the counter-current to the co-current direction was observed only during D density ramps at high current (low  $q$ ) and for a limited configuration. Moreover, the direction of rotation and reversal is opposite to that usually observed in other machines. This seems to depend on the plasma configuration. Diverted configuration in TCV, in fact, displayed co-current rotation at low density in the LOC regime and counter-current rotation at high density in the SOC regime, similar to what is usually observed in diverted plasmas in other machines [151] [119].

$I_p$  ramps were performed to find a  $q$ -threshold for the reversal. A density ramp then was repeated at low  $I_p$  such that the  $q$  value was higher than this reversal threshold. No change in rotation was observed, with profiles continually peaked in the counter-current direction although a LOC/SOC transition was observed at the usual density. This strengthened the suspicion that no direct causal relation between the LOC/SOC transition and the rotation reversal exists.

If such a relation did exist, it should occur in other types of plasma. Since the turbulent nature is known to depend upon the majority plasma, similar experiments were performed in D, H and He majority plasmas to seek such evidence. He discharges were characterised by a higher overall density. The lowest achievable value at ramp initiation was  $n_e = 8.0 \times 10^{19} \text{m}^{-3}$  that, however, did not prevent us from observing a reversal (that occurred at  $n_e \sim 9.5 \times 10^{19} \text{m}^{-3}$ ), although, at these higher densities ( $n_e \geq 1.1 \times 10^{20} \text{m}^{-3}$ ), fluctuations in the plasma behaviour were detrimental to the data quality. As in the D case,  $v_{Tor}$  linearly increased towards the co-current direction with increasing density and ST period until the LOC/SOC transition. The position of the  $q = 1$  surface was naturally higher in He ( $\rho_{q=1} \sim 0.6$ ).

A strong correlation between the  $\frac{-R}{L_{ne}}$  and toroidal rotation profiles was observed in D and He. This relation was suggested and supported by previous results from AUG ([106] [6]), in which it was shown that the LOC/SOC transition did not directly result from a TEM/ITG bifurcation. This bifurcation should, however, drive the changes in the peaking and the steepness of the  $n_e$  profile that act as the main actuators for the rotation reversal.

Conversely, experiments and simulations reported in [33] suggested that a TEM/ITG bifurcation is responsible for both the toroidal rotation reversal and the LOC/SOC transition. Those experiments employed a turbulence suppression technique to show that co and counter-current toroidal rotation, as well as LOC and SOC like energy confinement times, can be observed in plasmas with the same density and temperature profiles. However, the experiments performed in this thesis, that employed high resolution diagnostics to explore a wide range of scenarios, did not reveal any such similar relation. Consequently, in the opinion of the author, the existence of a causal relation between the TEM/ITG bifurcation and the rotation reversal (and the LOC/SOC transition, too) needs to be further explored. This could be

done in the near future employing TCV's TPCI (Tangential Phase Contrast Imaging) diagnostic, that can measure radial and temporally resolved profiles of turbulent fluctuations, possibly revealing TEM/ITG bifurcations in Ohmic density ramps. Based on the current results, the plasma density gradient appears to be the main actuator for any strong variation in toroidal rotation observed in TCV's Ohmic plasmas during this work.

The H discharges presented a challenging scenario. The LOC/SOC transition occurred at a lower density threshold in H than for D. However, this was not followed by any change in the rotation profiles. The plasma current could not be further increased, as the discharge was already at the current limit (close to  $q_{edge} = 2$ ). The density ramp was extended to higher values ( $\sim 25\%$ ) but the  $v_{Tor}$  profiles remained unchanged.

A solution to generating a rotation reversal in H was found using high power ECRH deposition. As previously shown in [111], ECRH deposited close to the  $q = 1$  surface displaces this surface outwards without changing the normalised  $T_e$  and  $n_e$  profiles, *i.e.* the transport mechanisms remain unchanged. This should result in an increased ST inversion radius with a consequent increased bulging of the  $v_{Tor}$  profiles in the co-current direction. An additional effect of ECRH injection should be to increase the density profile steepness, with a possibility of retrieving the correlation between rotation and  $\frac{-R}{L_{ne}}$  observed in D and He.

ECRH was injected in three increasing power steps from 0.17 MW to 0.6 MW. Rotation reversal was observed at constant density, which was required for continued ECH heating. With constant density, no LOC/SOC transition was induced. The  $q = 1$  surface was displaced from  $\rho_{q=1} = 0.55$  to  $\rho_{q=1} = 0.60$ , where the rotation profile continued to evolve even after the displacement of the  $q = 1$  surface, saturating concomitantly with the maximum value of  $\frac{R}{L_{ne}}$ . The same discharge was repeated in D and yielded similar results, showing, yet again, a strong correlation between rotation reversal and  $\frac{-R}{L_{ne}}$ .

These observations are concluded to prove that the rotation reversal phenomenon is not caused by a single component of the ST activity and that, whenever the change in  $v_{Tor}$  can be separated from the ST activity, density peaking and steepness are the main actuators for rotation reversal in this plasma configuration (limited, positive triangularity, L-mode).

The absolute value of the pre-reversal and the reversed toroidal velocity profile changes from species to species ( $\sim 15 \frac{\text{km}}{\text{s}}$  in D,  $\sim 10 \frac{\text{km}}{\text{s}}$  in H,  $\gtrsim 0 \frac{\text{km}}{\text{s}}$  in He), suggesting that the torque derived from the actuator (or possibly actuators) can induce more or less velocity depending upon the majority species. This would also indicate that the almost symmetrical shape of the pre-reversal and reversed  $v_{Tor}$  profiles in D is accidental or, at best, fortuitous. The observations made in the He discharge also showed that the  $v_{tor}$  profile can change the sign of its gradient (and, thus, reverse) without necessarily changing rotation direction.

The LOC/SOC transition was also observed in diverted D and H discharges. Here, however, rotation reversal (from co to counter-current direction, *i.e.* opposite to what was observed in limited configuration in TCV) was observed only for highly elongated plasmas in D, in agreement with the results reported in [55]. Diverted discharges with low elongation showed



an evolution of toroidal rotation profiles similar to  $\delta = 0$  plasmas in limited configuration that display an increase of toroidal velocity towards the counter-current direction with no visible change in their gradients. Here again, a causal relationship between rotation reversals and the LOC/SOC transition appears unfounded.

Finally, linear gyrokinetic simulations were performed to assess the dominance of TEMs and ITGs across the LOC/SOC transitions. The D density ramp #68408 showed the development of a mode in the ion direction between the LOC and the SOC phase. The mode appears to develop locally and then propagate radially, which means that the TEM/ITG bifurcation is not a global phenomenon occurring at all radial positions simultaneously, in agreement with reports from AUG [106]. As stated earlier, the results reported in [106], [6] and [58] also suggested that a TEM/ITG bifurcation is not directly responsible for the LOC/SOC transition, but it drives the changes of the density peaking that could possibly lead to the rotation reversal. In particular, the results in [58] showed that the maximum peaking of the density profiles occurs before the LOC/SOC transition, when the plasma remains dominantly TEM. During the early phases of the discharge, the  $n_e$  profile is naturally less peaked, likely due to the density pump out associated with strong TEM turbulence. As the density increases and the LOC/SOC transition approaches, the density profile becomes more peaked, eventually reaching its maximum and showing a strong counter-current rotation. At higher density (and  $v_{eff}$ ), the plasma is in the SOC regime and, possibly, dominated by ITG. Here, the density peaking has reduced, the  $n_e$  profile flattens and co-current plasma rotation is observed [59]. This hypothesis appears to be confirmed by the H density ramp experiments presented herein, where a LOC/SOC transition was clearly observed but not accompanied by a rotation reversal. Here, simulations did not indicate any TEM/ITG bifurcation either. Comparing the peaking factor and the  $\frac{-R}{L_{ne}}$  evolution in H, D and He, both quantities do not reach saturation, with the  $n_e$  profile remaining peaked at mid-radius and  $v_{TOR}$  profiles remaining in the counter-current direction throughout the discharge (see Figure 4.47). In D and He, conversely, the saturation of  $\frac{-R}{L_{ne}}$  is accompanied by rotation reversal. The H (and D) discharges with ECRH injection further strengthen this view, displaying rotation reversal at maximum  $n_e$  profile steepness accompanied by flattening of the central density profile (as shown in [5]), whilst remaining clearly in TEM dominated conditions due to the added temperature and pump out associated with electron cyclotron heating.

The stabilisation (or destabilisation) of turbulent modes plays a major role in understanding rotation reversal in plasmas with different majority species. Investigations on isotope effects reported in [190] (TEXTOR) showed how increasing the isotope mass would reduce transport due to a decrease in the step size of collisional transport and turbulent structures with the ion gyroradius  $\rho_s$ , consistently with [144] and [131], where the improved confinement in D (compared to H) was suggested to be caused by the higher zonal flow levels. Further studies, based on analytic calculations, suggested that TEM turbulence is also influenced by the isotope mass [75]. An extensive study of the isotope effects of trapped electron modes [163], which also included the presence of impurities, showed that the maximum growth rate of the TEM scales

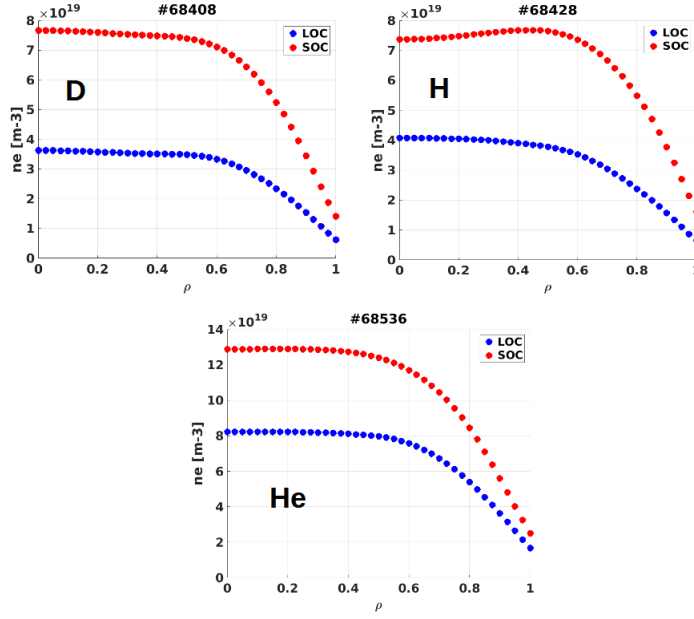


Figure 4.47 – Comparison between D, H and He density profiles in the LOC and in the SOC regime.

as  $\gamma_{max} \propto M_i^{-0.5}$  for purely hydrogenic plasmas, and  $\gamma_{max} \propto M_{eff}^{-1.0}$  in presence of impurities with moderate ion charge number like C ( $Z = 6.0 - 8.0$ ), where  $M_{eff} = (1 - f_z)M_i + f_z M_z$  and  $f_z = \frac{Z n_{0z}}{n_{0e}}$  the charge concentration of impurity ions. This implies that TEMs are more unstable in H than D and He. A similar scaling was reported for ITG [52] [51] [143].

As described in this chapter, the plasma tends to be dominated by virulent TEMs in the early phases of density ramps, where the plasma is characterised by low collisionality and a higher impurity content. If the growth rate of TEMs scales with mass as  $\gamma \propto \frac{1}{\sqrt{M_i}}$ , it is likely that the stabilisation of TEMs by collisional detrapping is less effective in H than in D and He, thus reducing the effects on density profiles that, in turn, induce variations in plasma toroidal rotation and, eventually, lead to a rotation reversal.

In conclusion, the measurements and the discussion presented in this chapter provided new insights into the LOC/SOC transition and its relation with the rotation reversal and the TEM/ITG bifurcation. In particular, discharges performed in H and He extended previous scenarios to different majority species, showing that even the limited correlation between LOC/SOC transition and rotation reversal supposed from D is not found in H nor He. As no evident TEM/ITG bifurcation was found in simulations in H and He, these models imply that a change in dominant turbulent modes cannot be the cause for either the  $\tau_E$  saturation nor the rotation reversal. A strong correlation between density peaking and profiles steepness was, however, highlighted, confirming a previously published hypothesis that it is the change in  $n_e$ , induced by turbulence, that drives the reversal rather than the LOC/SOC transition itself.

To further probe any correlation between the LOC/SOC transition and the rotation reversal, the scenarios presented in this chapter were extended to negative triangularity. A change in turbulent modes appears to be necessary to explain the observed changes in density peaking that lead to rotation reversal, but not the LOC/SOC transition. This may be the fundamental ingredient required to explain why rotation reversal was not observed in negative triangularity discharges (despite a clear saturation of  $\tau_E$ ). Therefore, the next chapter will focus on impurity transport in positive and negative  $\delta$  plasmas, with an extensive investigation of possible correlations between the local density gradients and the plasma rotational shear.



## 5 Impurity transport in negative triangularity

Impurities are unavoidable components of tokamak plasmas. The strength of their sources (such as the vessel walls) and transport mechanisms determine their concentration, which can strongly vary depending upon the plasma region. Whilst their accumulation has detrimental effects, reducing confinement and diluting the fuel, their presence, if kept under control, can have beneficial effects. The seeding of impurities into the plasma, in fact, was observed to improve confinement. Moreover, in a fusion reactor, their presence at the plasma periphery is considered necessary to increase the radiative emissions, and thus the radiated power fraction, that help decrease the heat load to the divertor region.

Impurity transport also presents an interesting subject for physics research, as it is concomitantly driven by both collisional and turbulent mechanisms. Plasma conditions, together with impurity charge and mass, determine the dominance of some mechanisms over others.

This work focused on the study of light impurity transport, in particular carbon, which is naturally present in TCV due to plasma edge interaction with its graphite tiled walls. TCV's flexible shaping capabilities were exploited to cover a large range of poloidal triangularity shapes, from positive to extremely negative. This possibility is unique in TCV using its open chamber and generous poloidal field coil array, providing the capacity to generate extremes of plasma shaping whilst naturally accommodating the changes in divertor geometry.

This chapter is organised as follows: the concept of negative triangularity is first introduced. Recent results from TCV and other machines are briefly reviewed, with particular emphasis on improved confinement and turbulence suppression in negative  $\delta$  plasmas. A comparison between positive and negative  $\delta$  discharges is then presented. As described in chapter 3, light impurity transport is dominated by turbulent mechanisms. The turbulent flux described by equation 3.37 is the sum of convective and diffusive contributions. Ion temperature and velocity gradients govern this turbulent flux and the correlations between them and density gradients are at the root of light impurities transport studies. Therefore, C ions kinetic profiles were measured during  $\delta$  scans in both limited and diverted configurations to explore how temperature, density and velocity profiles behave for positive and negative triangularity. The effects of plasma rotation and shearing were investigated both from intrinsic rotation and through NBI pulsed injection pulses. The remainder of the chapter is dedicated to the study

of the LOC/SOC transition and rotation reversal at negative  $\delta$  to complement the results presented in the previous chapter.

### 5.1 Negative triangularity

One of TCV's initial and continued objectives is to study the effects of plasma shape on confinement and plasma stability. Experiments conducted in TCV in the late 1990's ushered in the investigation of negative triangularity, and showed that creating an inverse D-shape led to increased energy confinement due to reduced transport with respect to a near symmetric positive  $\delta$  counterpart. Since then, record performances were obtained for L-mode plasmas with auxiliary heating directed at both electrons (ECRH) and ions (NBH). Global confinement sometimes approached H-mode levels whilst remaining in L-mode [42], with normalised  $\beta$  reaching values of 2.8 transiently and 2 in steady state. Fluctuation measurements revealed that the enhanced confinement was accompanied by (or perhaps the result of) turbulence suppression [64][65][91] and gyrokinetic simulations have provided initial insights into the origin of this phenomenon [114] [125]. More recently, results from DIII-D [11][113] and ASDEX Upgrade confirmed TCV's findings, albeit with more compromises required on available shapes to satisfy local machine limits.

DIII-D experiments focused on the study of the L-H transition at negative triangularity. In particular, an extreme resilience of negative  $\delta$  plasmas to stay in L-mode well beyond the L-H power threshold observed in positive  $\delta$  discharges was recently confirmed by the DIII-D team [160]. The widely accepted paradigm for the L-H transition is linked to turbulence suppression by  $E \times B$  flow in the edge region, that leads to the formation of a steep pressure gradient (pedestal) [18], allowing for higher density and temperature in the plasma due to reduced transport [134]. DIII-D experiments were performed in diverted configuration and showed that plasmas with slightly different top triangularity (from  $\delta = -0.18$  to  $\delta = -0.36$ ) required a higher pedestal temperature to access the so-called 2nd stability where the ideal  $n = \infty$  ballooning mode stability limit for the pressure gradient disappears [19], possibly explaining the observation of high negative  $\delta$  plasmas remaining in L-mode, despite a significantly higher heating power compared to their positive triangularity counterparts [160].

These results agree with TCV's findings reported in [42], where H-mode was accessed maintaining a lower positive  $\delta$  and varying only the upper triangularity. In this configuration, no evident difference in the L-H power threshold was observed, and the H-mode could be sustained reliably with constant heating. This work showed other beneficial effects of NT, this time in H-mode, resulting in less virulent, but more frequent, ELMs [142]. These results, similar to those reported by the DIII-D team, were also explained by a reduced access to the 2nd ballooning mode stability limit, which caused the instability to develop sooner during the pedestal growth, eventually limiting its development and reducing the impact of the, now smaller, ELMs [122].

Starting from the results presented in the previous chapter, that showed an evident correlation between the plasma rotational shear and the local density gradient in Ohmic and ECRH

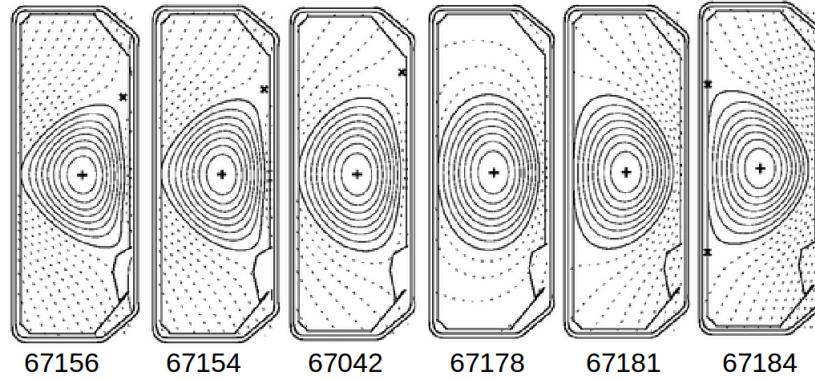


Figure 5.1 – Triangularity scan in limited configuration from  $\delta \sim -0.6$  to  $\delta \sim +0.6$ .

heated discharges, confirming AUG's findings [5] [3], TCV's research was extended to negative triangularity with NBI heating.

### 5.1.1 Triangularity scan in limited configuration

A complete triangularity scan in limited configuration between  $\delta \sim -0.6$  and  $\delta \sim +0.6$  was performed (Figure 5.1) to investigate the evolution of C ion kinetic profiles with  $\delta$ .

Figure 5.2 shows a comparison between positive (blue) and negative (red) triangularity carbon ion density profiles. The image on the left displays the  $\delta = \pm 0.3$  discharges profiles, whilst the image on the right displays those for  $\delta = \pm 0.6$ .

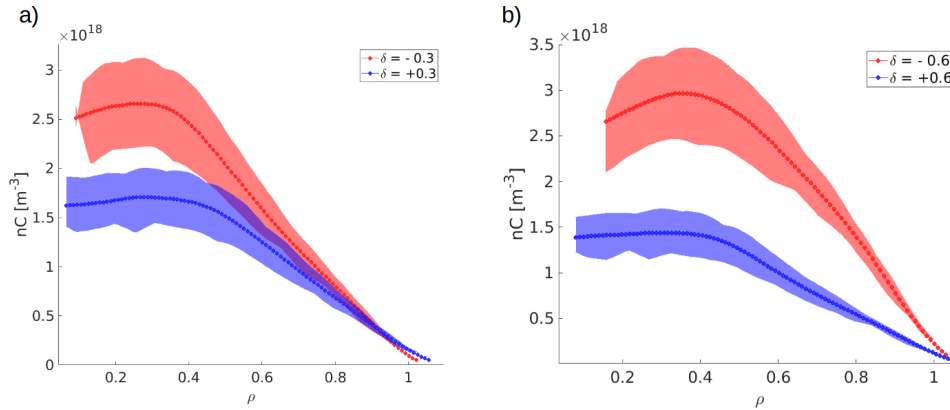


Figure 5.2 – Carbon ion density profiles in positive (blue) and negative (red) triangularity discharges. On the left, comparison between  $\delta = -0.3$  and  $\delta = +0.3$  discharges. On the right, comparison between  $\delta = -0.6$  and  $\delta = +0.6$  discharges. Positive  $\delta$  plasmas show a flat C density profile in the core region, with no major difference between the  $\delta = +0.3$  and  $\delta = +0.6$ . Conversely, negative  $\delta$  discharges display hollow core profiles, with a peak around  $\rho \sim 0.4$ . The peaking is stronger in the  $\delta = -0.6$  discharge compared to  $\delta = -0.3$ , and is accompanied by a steeper gradient.

Positive  $\delta$  plasmas show a flat C density profile in the core region, with no major difference between the  $\delta = +0.3$  and  $\delta = +0.6$ . Conversely, negative  $\delta$  discharges display hollow core profiles, with a peak around  $\rho \sim 0.4$ . The peaking is stronger in the  $\delta = -0.6$  discharge compared to  $\delta = -0.3$ , and is accompanied by a steeper gradient. Moreover, negative  $\delta$  discharges display significantly higher C densities with respect to their positive triangularity counterparts. The same behaviour is observed in discharge #67817, for a triangularity scan from  $\delta = -0.6$  to  $\delta = +0.6$  (Figure 5.3).

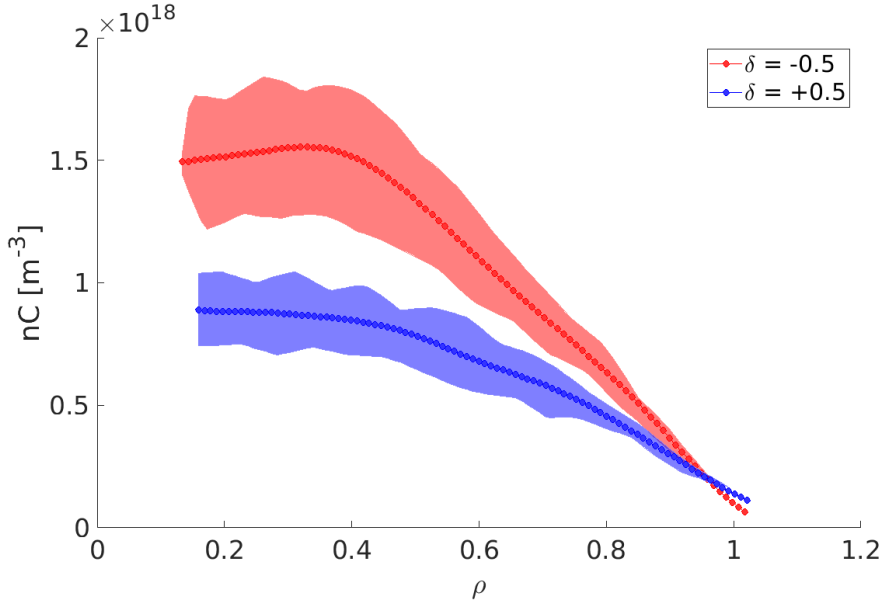


Figure 5.3 – Carbon ion density profiles in positive (blue) and negative (red) triangularity discharges during a  $\delta$  scan from -0.6 to +0.6 (discharge #67817). C density profiles at positive  $\delta$  are, again, flat, whereas negative triangularity  $n_C$  profiles display a peak at mid-radius, accompanied by a steeper gradient.

There was no significant difference between positive and negative  $\delta$  ion temperature profiles.  $T_i$  is higher in the  $\delta = -0.6$  discharge, but the gradients in positive and negative triangularity configurations are similar (Figure 5.4).

Toroidal velocity and Mach number gradient profiles show different behaviour between positive and negative triangularity discharges, especially for the more strongly probed cases  $\delta = \pm 0.6$  (Figure 5.5).  $v_{Tor}$  profiles are hollow in the core region ( $\rho < 0.3$ ) in the positive  $\delta$  discharge. At mid-radius ( $\rho \sim 0.5$ ), the profile becomes peaked and tending, after a strong gradient region, to a slow edge region rotation in the co-current direction. The negative  $\delta$  discharge also has a peaked profile at mid-radius but its gradient is not as steep and the edge rotation is slightly positive (counter-current direction). A similar behaviour is observed for higher  $\delta$  ( $\pm 0.6$ ). Here, the steepness of the gradients is more pronounced for the positive triangularity discharge, whilst its  $\delta < 0$  counterpart displays a smaller peak at mid-radius followed by a more gentle gradient.

These observations suggest that transport of light impurities (in this specific case carbon



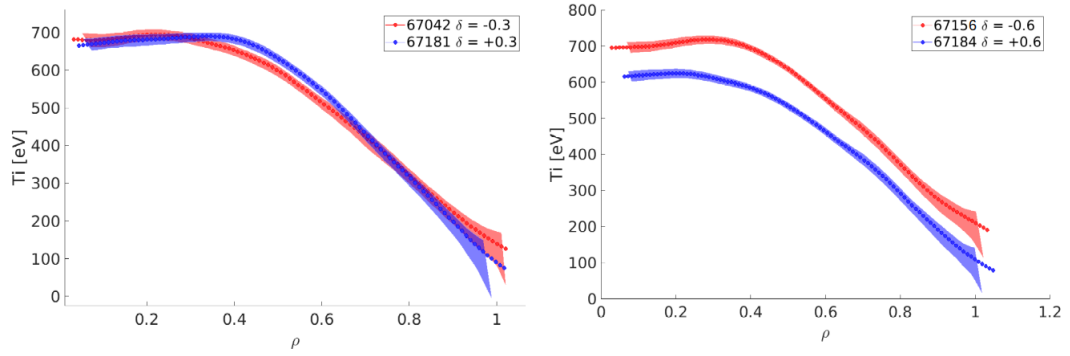


Figure 5.4 – Ion temperature profiles in positive (blue) and negative (red) triangularity discharges mapped to the reconstructed  $\rho$  coordinate. On the left, comparison between  $\delta = -0.3$  and  $\delta = +0.3$  discharges. On the right, comparison between  $\delta = -0.6$  and  $\delta = +0.6$  discharges. Temperature profiles do not show a large difference between positive and negative triangularity discharges, except for the absolute value, that is higher at  $\delta \sim -0.6$ .

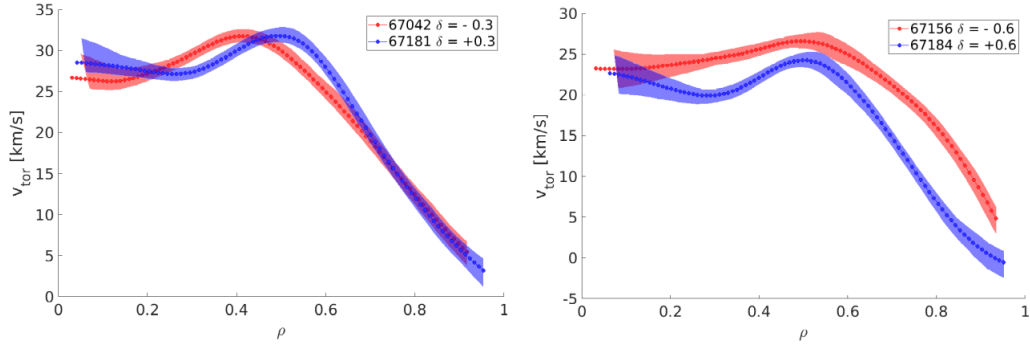


Figure 5.5 – Ion toroidal velocity profiles in positive (blue) and negative (red) triangularity discharges. On the left, comparison between  $\delta = -0.3$  and  $\delta = +0.3$  discharges. On the right, comparison between  $\delta = -0.6$  and  $\delta = +0.6$  discharges.  $v_{tor}$  profiles at  $\delta < 0$  are hollow in the region  $0.1 < \rho < 0.4$  and develop a peak at  $\rho \sim 0.6$ . This behaviour is enhanced at lower  $\delta$ .

ions) changes significantly between positive and negative triangularity. Previous experiments in TCV showed reduced transport in negative  $\delta$ , such that discharges at  $\delta = -0.4$  displayed electron diffusivities ( $\chi_e$ ) a factor of two lower than their positive triangularity counterparts ( $\delta = +0.4$ ) [32]. As mentioned in the introduction, this smaller  $\chi_e$  was attributed to turbulence suppression and reduction in TEM strength directly resulting from the reversed D shape. This hypothesis has been strengthened by experimental observations [65] and theoretical investigations [125]. Recent results from DIII-D confirmed these trends, showing reduced  $\chi_e$  in the confinement region ( $0.4 < \rho < 0.8$ ) and, although still under investigation with gyrokinetic simulations, demonstrate once again that the reduction in transport stems from a suppression of turbulent modes that is ascribed to the shape change.

Whilst  $\delta > 0$  discharges display flat core C density profiles, regardless of the absolute value of  $\delta$ ,  $n_C$  profiles in negative triangularity show an accumulation of C ions at mid-radius that tends to become stronger with increasing absolute values of  $\delta < 0$ . The mid-radius peak is also

accompanied by stronger gradients, with similar results reported in past campaigns (2006, [22]). It is important to recall that ion density measurements are delicate and depend heavily upon a reliable absolute calibration (see chapter 2). Herein, calibrations must be performed close to the time of measurement due to uncertainties in on-vessel window transmission changes. Therefore, comparisons between  $n_C$  profiles in positive and negative triangularity discharges performed during different experimental campaigns should be made with particular care, ensuring that the absolute calibration did not evolve significantly due to possible deterioration of elements in the complete optical chain (mirrors, lenses, fibers, etc.).

As described in chapter 3, light impurity transport is deemed to be driven by turbulence. Eq. 3.37 showed that the turbulent flux is described by a combination of diffusive and convective terms. The diffusive terms, in particular, depend upon the impurity ion temperature, density and toroidal rotation gradients, that can all be obtained from the kinetic profiles measured by the CXRS diagnostic. As all these terms influence each other, a practical way of studying how transport is affected by their changes is to seek correlations between them. The normalised logarithmic density gradient  $\frac{R}{L_{nZ}}$  is plotted as a function of the normalised logarithmic temperature gradient  $\frac{R}{L_{Ti}}$ , the thermal Mach number  $u$  and its derivative  $u'$  (Figures 5.6, 5.7, 5.8). The Mach number is defined as the toroidal velocity normalised to the sound speed ([47], see also section 4.4.1, where the Mach number is first introduced), here used, together with its derivative, to ease inter-machines scaling [39] [152] and comparison with other TCV scenarios. The Figures depict normalised gradients at different  $\rho$ . The colour scale corresponds to the different values of  $\delta$  to better highlight any trend in positive (green-yellow dots) or negative (turquoise-blue dots) triangularity.

The correlation plots tend to reflect the observations made comparing kinetic profiles at different  $\delta$ . Zero and positive  $\delta$  plasmas tend to populate the region of low or zero logarithmic density gradient, corresponding to flat core profiles. Remarkably, negative  $\delta$  plasmas not only show systematically hollow core  $n_C$  profiles, but also a trend in the density-temperature logarithmic gradients plot, particularly pronounced at mid-radius, for hollowness to increase with decreasing  $\delta$ .

Correlations are also visible between the logarithmic density gradient, the Mach number and its derivative. Plasmas at  $\delta < -0.4$  tend to span a wide region of  $u$  for the same  $\frac{R}{L_{ni}}$  value, showing little correlation between  $\frac{R}{L_{ni}}$  and  $u$ . However, a near-linear trend is visible in the  $\frac{R}{L_{ni}}$  VS  $u'$  plot, particularly marked at mid-radius. In a similar fashion,  $\delta < 0$  discharges tended to populate different regions of the  $\frac{R}{L_{ni}}$  VS  $\frac{R}{L_{Ti}}$  plot, again depending on the absolute value of negative  $\delta$ . These results suggest that transport in negative delta plasmas is mainly driven by temperature and toroidal velocity gradients, with profiles becoming increasingly hollow for increasing  $\nabla T$  and  $\nabla v_{Tor}$ . Conversely, no marked change was observed in  $n_C$ ,  $T_i$  and  $v_{tor}$  profiles from zero to the highest positive triangularity. Consequently, these plasma discharges did not show the same strong variations and/or correlations observed as their negative  $\delta$  counterparts. Figure 5.9 recaps these observations.

To better highlight correlations and trends at negative triangularity,  $\frac{R}{L_{ni}}$  is plotted as a function of  $\frac{R}{L_{Ti}}$ ,  $u$  and  $u'$  in Figure 5.10 for the  $\delta < 0$  discharges only. All plots compare values at  $\rho = 0.3$ , where the differences were more pronounced. A linear correlation between  $\frac{R}{L_{ni}}$  and  $u'$  is high-

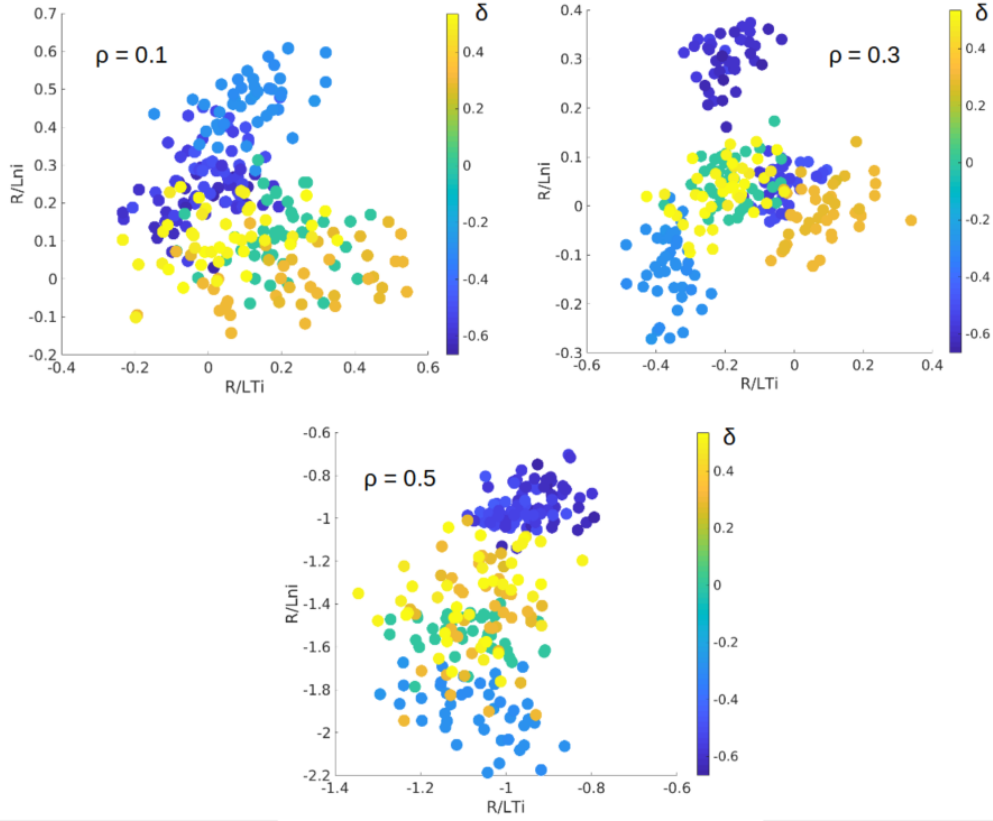


Figure 5.6 –  $\frac{R}{L_{ni}}$  as a function of  $\frac{R}{L_{Ti}}$  for different  $\rho$ . A linear trend is visible for the negative triangularity cases (blue shaded data points), especially towards mid-radius. Density profiles tend to be more peaked for stronger negative  $\delta$  with respect to the slightly negative and positive  $\delta$  cases.

lighted with a dotted line. The other plots ( $\frac{R}{L_{ni}}$  VS  $u$  and  $\frac{R}{L_{ni}}$  VS  $u'$ ), although not displaying a similar linear trend, show that discharges at different  $\delta < 0$  populate different regions of the plot, *i.e.* a strong change in transport with increasingly negative triangularity. Positive and zero triangularity discharges (Figures 5.6, 5.7 and 5.8), again, did not show a similar tendency. Furthermore, it would appear reasonable to speculate that this trend would continue to evolve if the value of  $\delta < 0$  is extended further ( $\delta < -0.6$ ).

As the sawteeth crashes can alter the magnitude and the gradients of the toroidal velocity profiles, two discharges from the scan in limited configuration were repeated to assess whether the ST instability plays a role in the peaking or flattening the observed profiles. The period of a complete ST cycle  $\tau_{ST}$  depends upon plasma parameters and the magnetic configuration, and increases with the machine size. In TCV the natural ST period in ohmic discharges is of few ms, which is comparable to the minimal, 20 chord, CXRS integration time. Discharge #67154, at  $\delta \sim -0.5$  and #67184, at  $\delta \sim +0.5$ , were repeated with lower CXRS integration times. The ST period varied between 4 ms and 6 ms in these plasmas. CXRS IT was lowered to 3 ms, allowing for a partial temporal discrimination within the ST period. Statistically, CXRS time frames

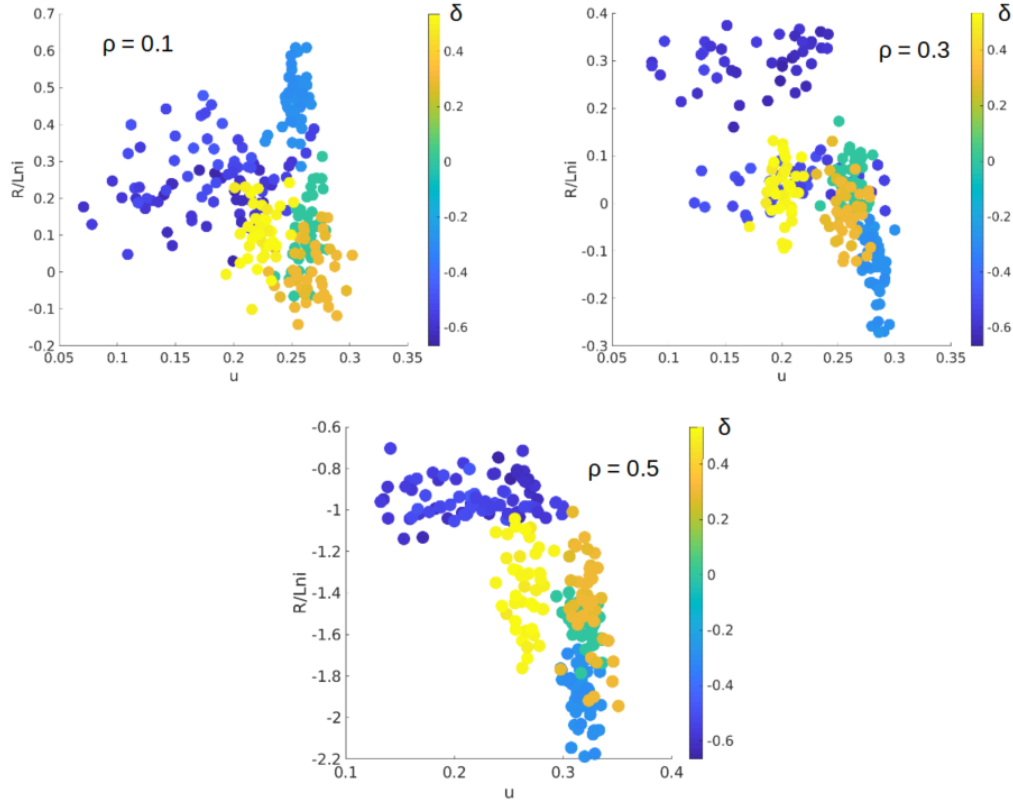


Figure 5.7 –  $\frac{R}{L_{ni}}$  as a function of  $u$  for different  $\rho$ . High negative  $\delta$  shots tend to span a wider range of Mach number values for the same logarithmic density gradient.

should fall randomly during ST crash phases or pre/post crash phases. A conditional sampling was performed to assess possible correlations between sawteeth crash and logarithmic density gradients (Figure 5.11).

The distribution of data points for the same  $\delta$  but as a function phase in the ST cycle (before or after the crash) in the  $\frac{R}{L_{ni}}$  VS  $\frac{R}{L_{Ti}}$  plot is uniform with no correlation observed. Nevertheless, data points fit well the  $\frac{R}{L_{ni}}$  VS  $\frac{R}{L_{Ti}}$  plot obtained from the delta scan and recover the previously described trend.

### 5.1.2 External torque injection through Neutral Beam

The scan in triangularity for a limited plasma configuration was repeated with the addition of NBH injection. The goal here was to explore how external torque injection affects carbon ions' kinetic profiles in positive and negative triangularity since we are expecting the plasma confinement to be altered.

The beam power injection scheme is shown in Figure 5.12. Five NBH pulses of 100 ms each were applied during the scan. Each pulse was separated from the previous one by a 100 ms beam OFF-phase, with injected power increasing at each step by 0.25 MW. The DNBI covered

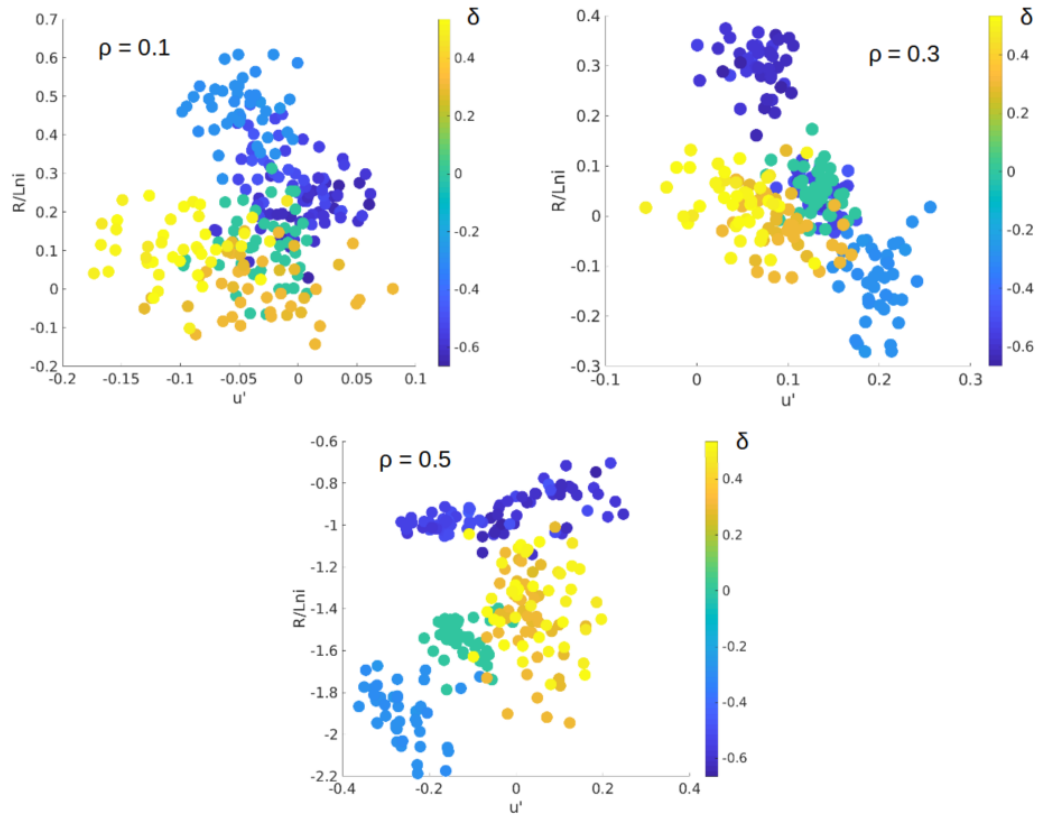


Figure 5.8 –  $\frac{R}{L_{ni}}$  as a function of  $u'$  for different  $\rho$ . A linear trend appears between the logarithmic temperature gradient and the gradient of the Mach number, suggesting that there is a strong correlation between the steepness of the toroidal velocity profiles and the peaking of the density profiles.

NO NBH	$\delta > 0$	$\delta < 0$
nC	flat, lower	hollow, higher
Ti	slightly hollow, lower	flat, higher
vTor	hollow, highly peaked at mid-radius	hollow, slightly peaked at mid-radius

Figure 5.9 – Recap table of observations on impurity profiles during a scan in triangularity of Ohmically heated limited plasmas.

the shot time window between 0.5 ms and 1.6 ms, allowing for non-perturbative C kinetic

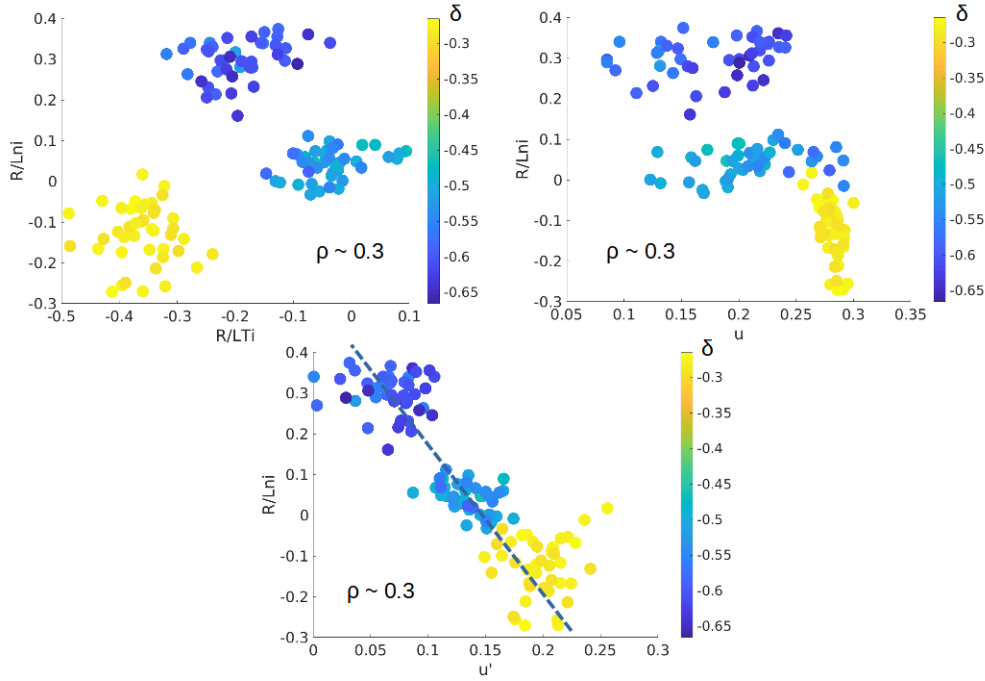


Figure 5.10 –  $\frac{R}{L_{ni}}$  as a function of  $\frac{R}{L_{Ti}}$ ,  $u$  and  $u'$ . The colour scale corresponds to the different values of  $\delta < 0$ . A linear trend is highlighted in the  $\frac{R}{L_{ni}}$  VS  $u'$  plot. The other plots, although not displaying any linear correlation, show how discharges at different  $\delta < 0$  populate different regions of the plot.

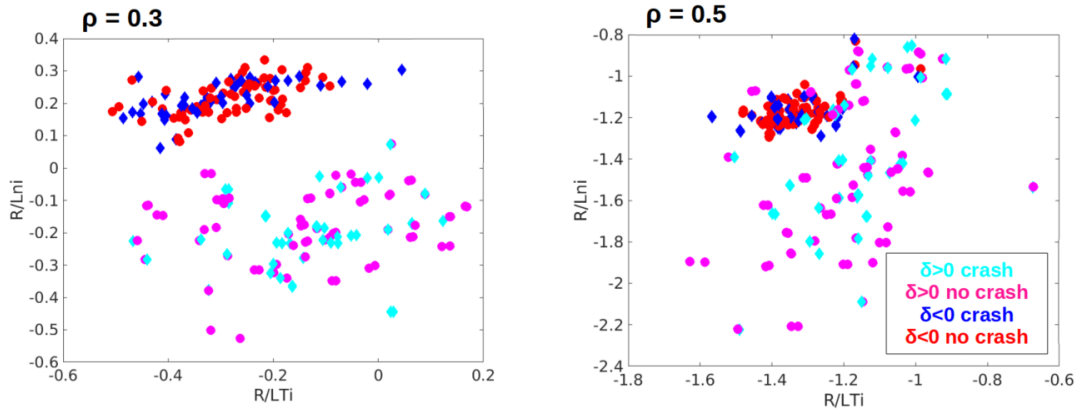


Figure 5.11 – Conditional sampling of CXRS time frames happening during a ST crash or not. No correlation is visible between data points at same triangularity (68323,  $\delta \sim -0.5$  and 68341,  $\delta \sim +0.5$ ). Nevertheless, data points fit well the  $\frac{R}{L_{ni}}$  VS  $\frac{R}{L_{Ti}}$  plot obtained from the delta scan.

profiles measurements during both the ON and OFF NBI-1 phases, to provide insights into the evolution of the profiles during and after neutral injection for a range of powers. All discharges were performed in the unfavorable  $B_T$  configuration to avoid H-mode access and the resulting ELMs, that would compromise the CXRS data quality (see chapter 2).

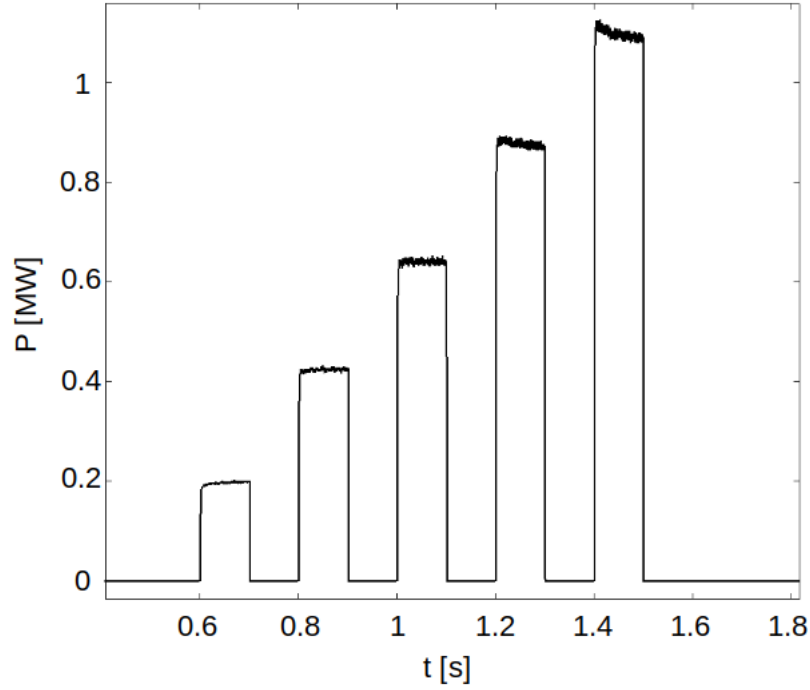


Figure 5.12 – Trace of neutral beam power injection during a triangularity scan in limited configuration.

Two C ions density profiles in negative triangularity are compared in Figure 5.13. The red profile is from a  $\delta = -0.5$  Ohmic discharge in limited configuration, with blue profile a repeat of that discharge with the addition of NBH following the injection pattern previously described. Here, the absolute value of  $n_C$  is not indicative of a change in transport, as the electron density underwent moderate variations due to the beam injection. However, the  $n_C$  gradient was seen to change dramatically with NBI-1. The C ion density profiles tend to be peaked at mid-radius ( $\rho \sim 0.4$ ) and hollow in the core in the absence of NBH. The addition of NBI-1 (0.5 MW, in the particular case of Figure 5.13) results in the peaking of  $n_C$  in the core and a consequential strong gradient region bend of the profile at mid-radius, where the gradient flips sign compared to its ohmic counterpart.

The same discharge (limited configuration + NBH) was repeated at positive triangularity (Figure 5.14), keeping the same  $n_e$  and  $I_p$  of the ohmic discharge. Interestingly, here, NB injection has a less dramatic effect on the  $n_C$  profiles shape. The  $n_C$  profiles are further flattened with their steepness decreasing for  $\rho > 0.5$ , but the sign of the gradient does not change. The absolute value of carbon density, instead, decreases dramatically from  $n_e \sim 1.4 \times 10^{18}$  at  $\rho = 0.1$  without the NBH to  $n_e \sim 0.5 \times 10^{18}$  with 0.5 MW of NBH.

To further probe these differences, two  $n_C$  profiles, acquired during the 0.75 MW NB injection phase, are compared in Figure 5.15. Here, the  $n_C$  profile at positive  $\delta$  is depicted in blue, with the negative triangularity counterpart in red.

The striking difference, temporarily ignoring the absolute C ion density, is in the shape of

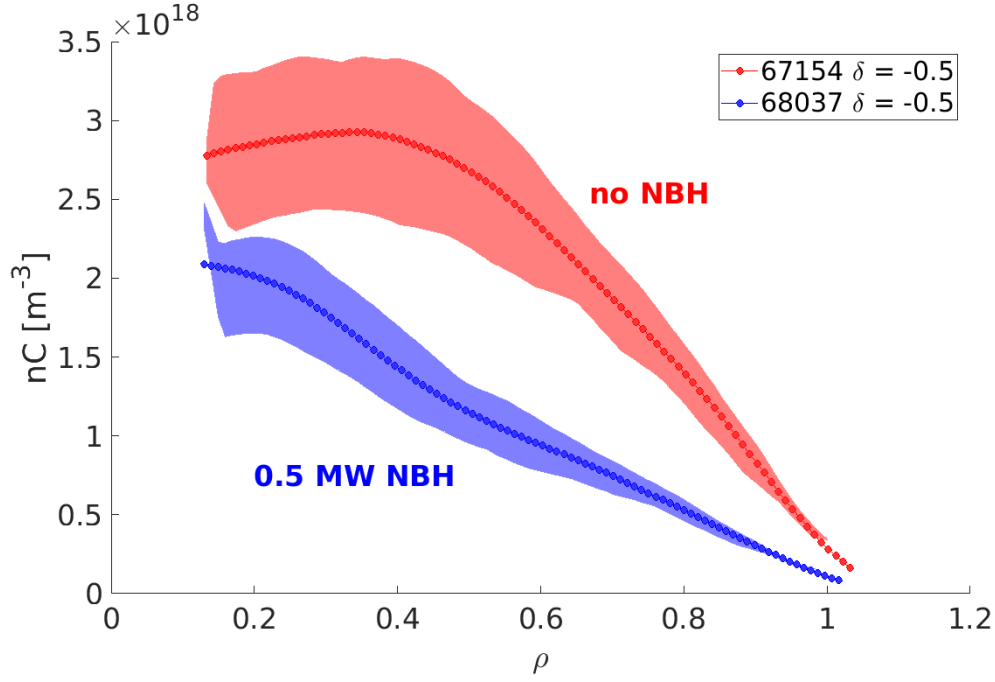


Figure 5.13 – Ion density profiles in negative triangularity discharges. In red without NBH, in blue with the addition of 0.5 MW NBH. The addition of NBI-1 (0.5 MW, in this particular case) results in the peaking of  $n_C$  in the core and a consequential strong gradient region bend of the profile at mid-radius, where the gradient flips sign compared to its ohmic counterpart.

the profiles. The  $\delta = -0.5$  discharge displays a peaked core profile with a steep gradient until  $\rho \sim 0.6$ , where the profile gradient relaxes. Increasing NBI power further strengthens these changes, enhancing the  $n_C$  peaking and profile steepness. Conversely, not only does NBI have the opposite effect by flattening  $n_C$  profiles at positive  $\delta$ , but increasing NBI power appears to engender only little further change in the absolute values of the C density and its gradients. This can also be seen in Figure 5.16, where two central C ion density time traces, one at positive (blue) and one at negative triangularity (red) are compared. The blue trace remains continually near-flat, whereas the red trace varies throughout the discharge, likely affected by changes in the NBI power and deposition profile.

Similar to the C impurity ion density profiles, the  $n_e$  profiles are peaked in the negative triangularity discharge and flat at positive  $\delta$ , as shown in Figure 5.17. Although the shape of the  $n_C$  and  $n_e$  profiles at negative triangularity is similar, the C ion density profile appears to be more peaked at negative triangularity, with a steeper gradient at mid-radius (Figure 5.15).

The higher impurity content observed in TCV's negative triangularity discharges is in disagreement with DIII-D TRANSP simulation results previously mentioned [11] that show a higher C concentration in  $\delta > 0$  plasmas, leading to a lower measured neutron rate with impurity retention and D dilution. It has to be mentioned, again, that the absolute value of carbon ions density is not indicative of a strong change in impurity transport, especially when the plasma density is not kept constant between positive and negative  $\delta$  discharges. Moreover, a higher C



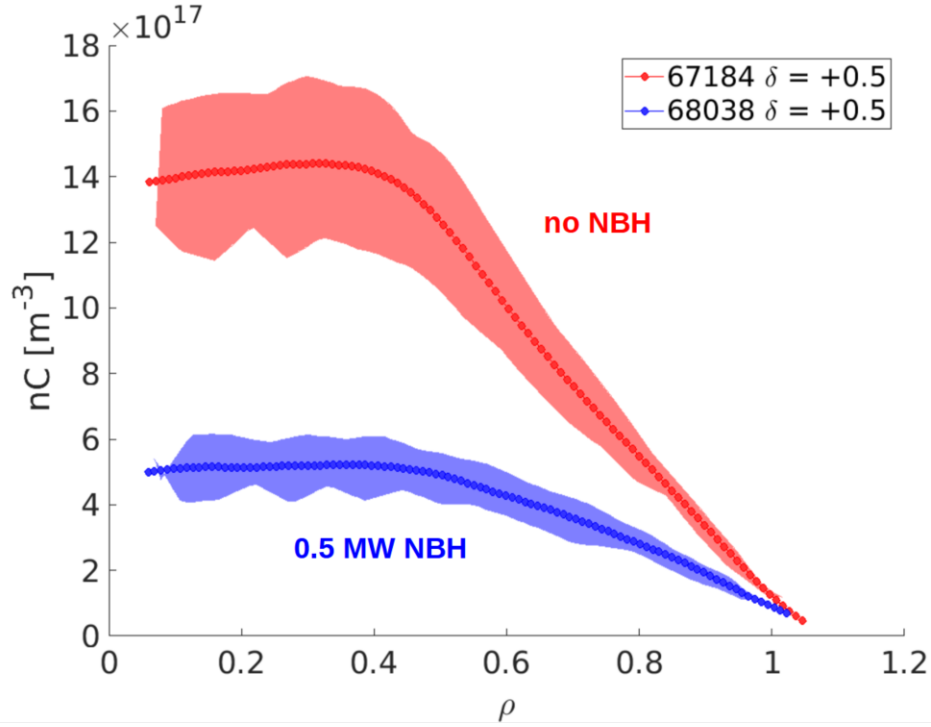


Figure 5.14 – Ion density profiles in negative triangularity discharges. In red without NBH, in blue with the addition of 0.5 MW NBH. Here, NB injection has a less dramatic effect on the  $n_C$  profiles shape. The absolute value of carbon density, instead, decreases dramatically from  $n_e \sim 1.4 \times 10^{18}$  at  $\rho = 0.1$  without the NBH to  $n_e \sim 0.5 \times 10^{18}$  with 0.5 MW of NBH.

concentration in negative  $\delta$  plasmas was also observed in past TCV discharges with matching profiles [63] [22]. As shown in [124] and [125], impurities are crucial in simulations to retrieve the actual transport level. An increase in  $Z_{eff}$  (and, thus, in collisionality  $\nu^* \propto \frac{n_e Z_{eff}}{T_e^2}$ ) causes a reduction of ion and electron fluxes from ion dilution and collisional stabilisation of TEMs, as discussed in the previous chapter (section 4.1.1 "TEM-ITG bifurcation"). Therefore, the experimental observations presented here appear to agree with this results.

Electron density profiles, and other ion kinetic parameters ( $T_i$ ,  $v_{tor}$ ), were surveyed to find an explanation for the different behaviour of  $n_C$  profiles in positive and negative triangularity plasmas. Figure 5.18 shows the electron density measured at  $\rho = 0.1$ , again for  $\delta = \pm 0.5$ .

Moving on to the effect on ion temperature,  $T_i$  profiles become peaked during beam injection in both positive and negative  $\delta$  discharges (see Figure 5.19), with the core temperature increasing with power (ion heating).

Before NBH, negative  $\delta$  toroidal velocity profiles are hollow in the core and slightly peaked at mid-radius. A similar shape is displayed by  $v_{Tor}$  profiles at positive triangularity, albeit with a more marked peak at mid-radius. During the Ohmic phase, the plasma rotates in the counter-current direction in both negative and positive  $\delta$  plasma discharges, as seen in the pre-reversal profiles presented in the previous chapter. During NBH injection,  $v_{Tor}$  evolves towards negative values, displaying a strong plasma rotation in the co-current direction, *i.e.*

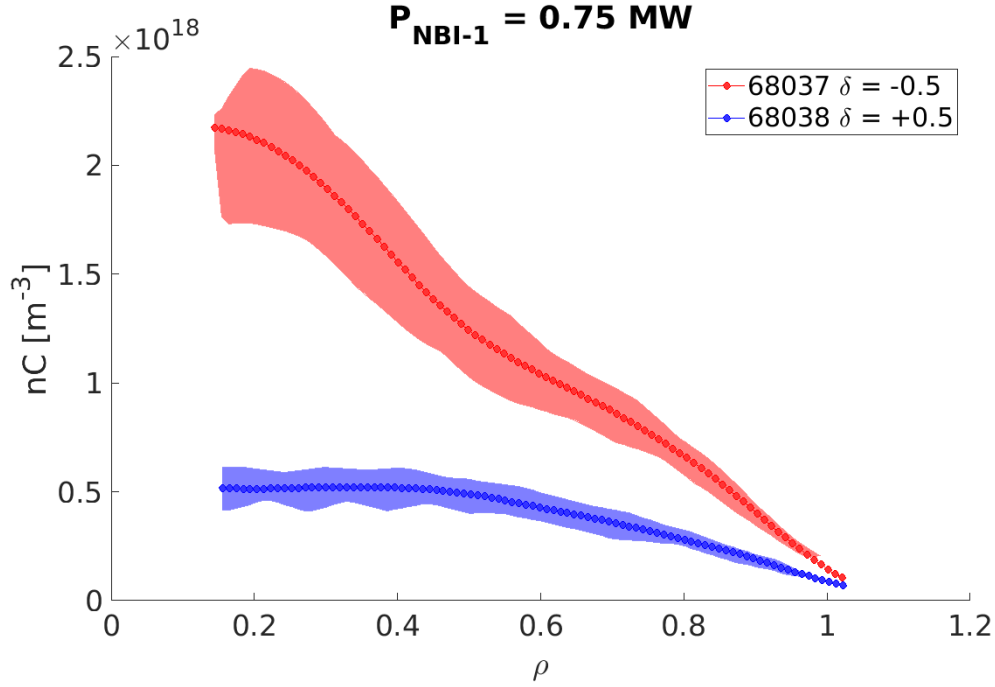


Figure 5.15 – Comparison between ion density profiles in positive (blue) and negative (red) triangularity. Both profiles were acquired during the injection of a 0.75 MW NBH pulse. The  $\delta = -0.5$  discharge displays a peaked core profile with a steep gradient until  $\rho \sim 0.6$ . Increasing NBI power further strengthens these changes, enhancing the  $n_C$  peaking and profile steepness. Conversely,  $n_C$  profiles at positive  $\delta$  are flat until  $\rho \sim 0.4$  and increasing NBI power appears to engender only little further change in the absolute values of the C density and its gradients.

the direction of momentum drive from NBH (Figure 5.20). Toroidal velocity progressively increases with power due to the additional toroidal torque applied by the beam injection itself.

The negative  $\delta$  discharge with NBH injection is now compared to its positive  $\delta$  counterpart. Figure 5.21 shows the evolution of toroidal rotation profiles before, during, and after the injection of a 1.0 MW NBH pulse.

As before, negative  $\delta$  toroidal velocity profiles are hollow in the core and peaked at mid-radius before NBH. During beam injection, both positive and negative  $\delta$  toroidal velocity profiles become hollow in the co-current direction, as expected from the dominant momentum injection. However, negative  $\delta$  plasmas tend to rotate faster than their positive  $\delta$  counterparts. After beam injection ends, both rotation profiles tend to relax and flatten. However, negative  $\delta$  plasmas maintain a strong rotation in the co-current direction following beam termination, indicating increased momentum confinement in negative triangularity discharges. Also, the  $\delta < 0$  plasma continues to rotate in the co-current direction after the beam injection, but it quickly slows down, eventually retrieving pre-injection rotation levels, *i.e.*  $v_{\text{Tor}} > 0$ , within  $t \lesssim 100 \text{ ms}$ .

The higher plasma rotation observed in negative triangularity is accompanied by a higher

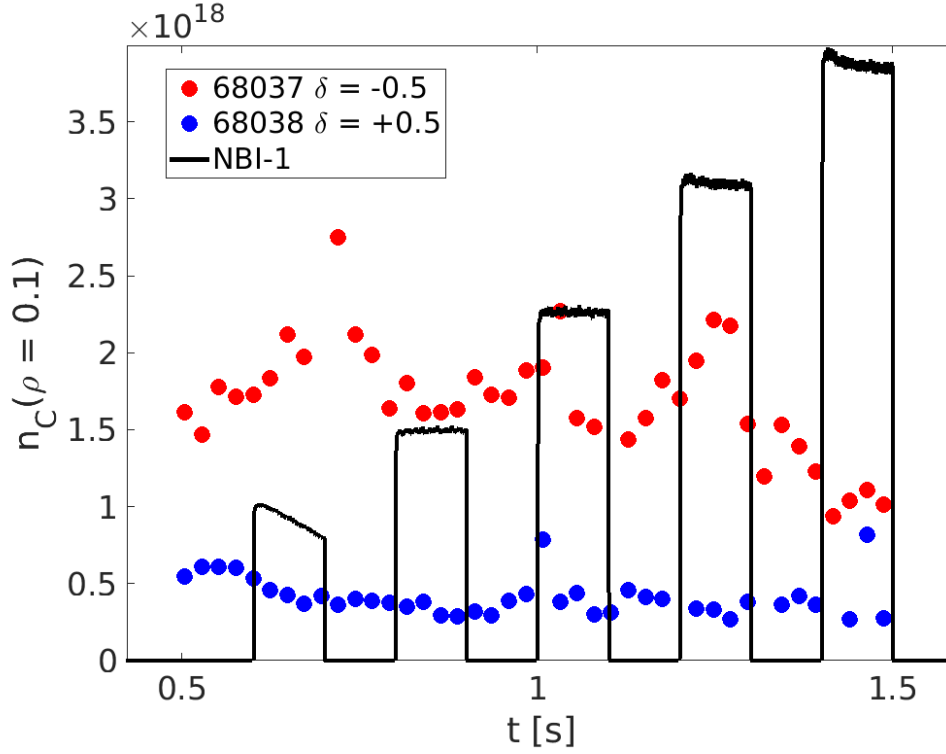


Figure 5.16 – Comparison between central C ion density traces in positive (blue) and negative (red) triangularity. The blue trace remains nearly continually flat, whereas the red trace varies throughout the discharge, likely affected by changes in the NBI power and deposition profile. For a better clarity of the plot, error bars are not drawn (for an estimation of experimental uncertainties, see Figure 5.15, where error bars are shown on the  $n_C - \rho$  profiles).

energy confinement time (Figure 5.22).

All these observations are reflected in the correlation plots. Figure 5.23 shows that negative  $\delta$  plasmas tend to populate more the region of peaked temperature and density profiles, especially towards mid-radius. Conversely, positive  $\delta$  plasmas  $n_C$  and  $T_i$  profiles tend to remain flat and do not change shape during beam injection.

A linear correlation between density peaking and the toroidal rotation velocity can be discerned at low radius (Figure 5.24). Plasmas with enhanced negative triangularity ( $\sim -0.3$ ) rotate faster than those with only slightly negative  $\delta$  ( $\delta \sim -0.1$ ) that populate the same region of flat density profiles and lower rotation of the zero and positive  $\delta$  cases. Also, the logarithmic density gradient decreases towards more negative values with decreasing triangularity, showing that highly rotating, negative  $\delta$  plasmas also exhibit highly peaked density profiles.

Figure 5.25 shows the logarithmic density gradient as a function of Mach number and its gradient. Negative  $\delta$  plasmas density peaking occurs for a slightly higher rotation than the positive cases. The RHS plot also shows how negative  $\delta$  plasmas populate a wider range of the gradients of the Mach number, although no correlation between  $\frac{R}{Ln_i}$  and  $u'$  is inferable.

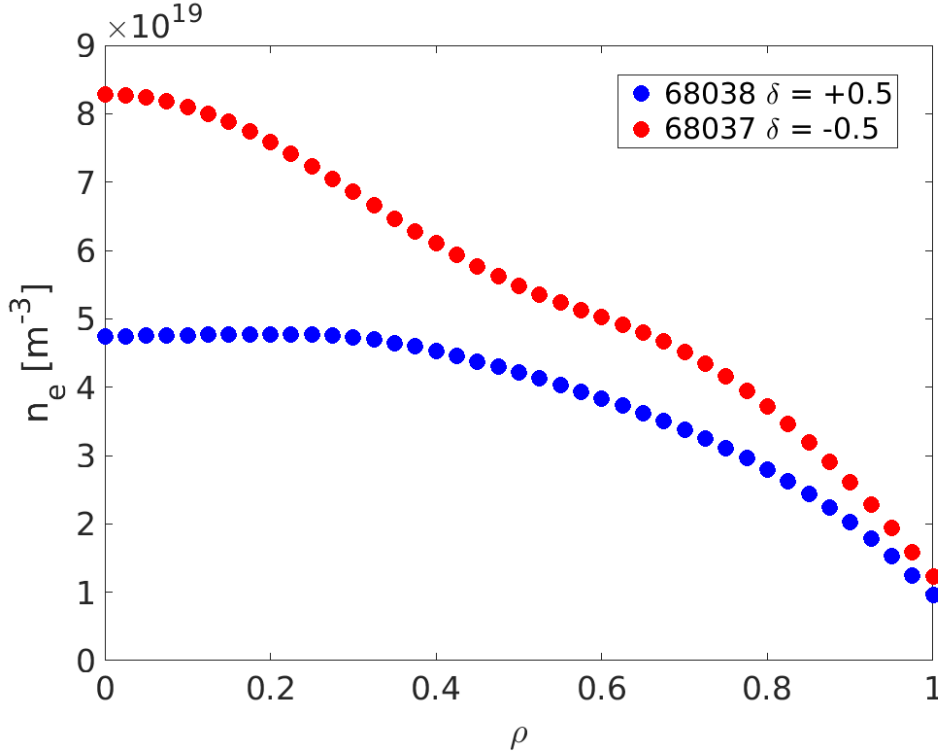


Figure 5.17 – Comparison between electron density profiles in positive (blue) and negative (red) triangularity. Both profiles were acquired during the injection of a 0.75 MW NBH pulse.

### 5.1.3 Triangularity scan in diverted configurations

Similarly to the experiments performed in limited configurations, a complete upper delta scan from  $\delta_{top} \sim -0.5$  to  $\delta_{top} \sim +0.5$  was performed with a diverted plasma configuration. Figure 5.26 shows an upper delta sweep performed during a single shot. Separate discharges at fixed  $\delta_{top}$  were also performed to avoid making conclusions on transitory phenomena.

Similar differences between positive and negative triangularity to those extensively described in the previous paragraph were observed in the diverted scan. Figures 5.27, 5.28 and 5.29 show the  $R/L_{ni}$  VS  $R/L_{ti}$ ,  $R/L_{ni}$  VS  $u'$  and  $R/L_{ni}$  VS  $u$  correlations plots, respectively, here all measured at  $\rho = 0.4$ . In particular, a strong variation of  $R/L_{ni}$  with decreasing negative  $\delta$  can again be highlighted. The linear trends highlighted during the triangularity scan in limited configuration remain strongly pronounced in diverted configurations. However, it has to be mentioned here that no extreme values of positive triangularity were accessed during this diverted scan. For completeness, a scan in diverted plasma configuration should be performed, expanding the previous scan to  $\delta = +0.6$ .

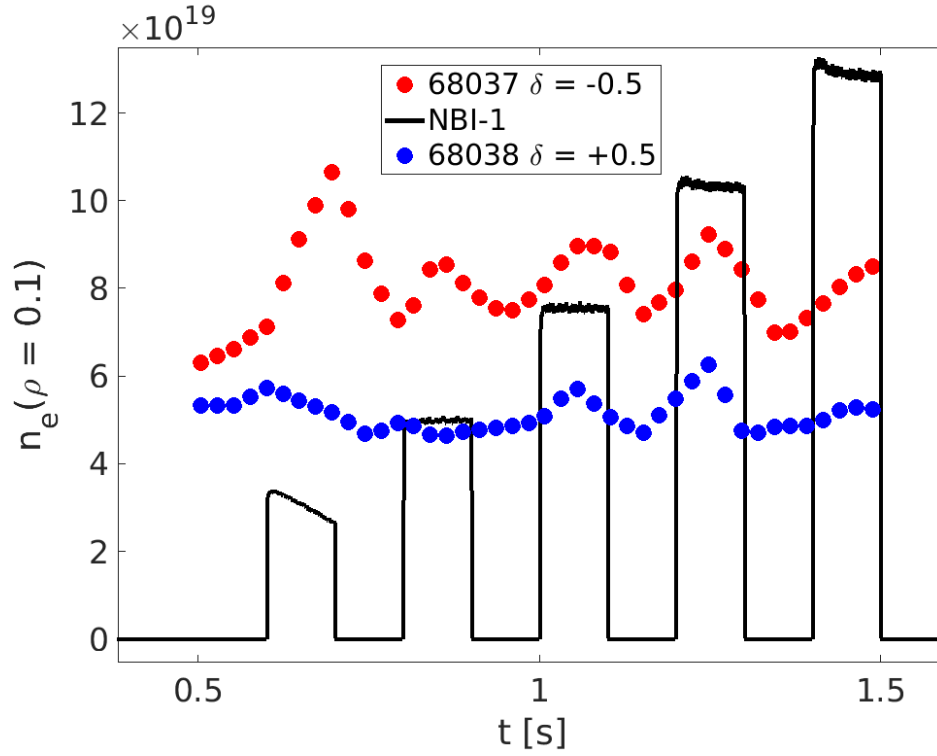


Figure 5.18 – Comparison between central electron density traces in positive (blue) and negative (red) triangularity.

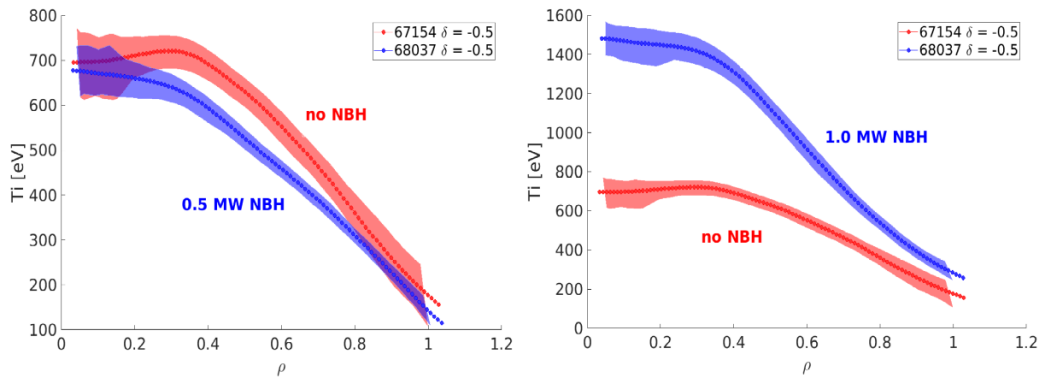


Figure 5.19 – Comparison of ion temperature profiles between an Ohmic plasma and a discharge with different NBI power injection pulses at negative triangularity.

#### 5.1.4 LOC/SOC transition in negative triangularity

Ohmic density ramps were performed with negative triangularity to expand previous scenarios and explore plasma rotation and LOC/SOC transitions for  $\delta < 0$ .

Previous attempts to study the phenomenon of rotation reversal in negative triangularity did not provide reproducible results. A suspicion of rotation reversal was seen in shot #32129,

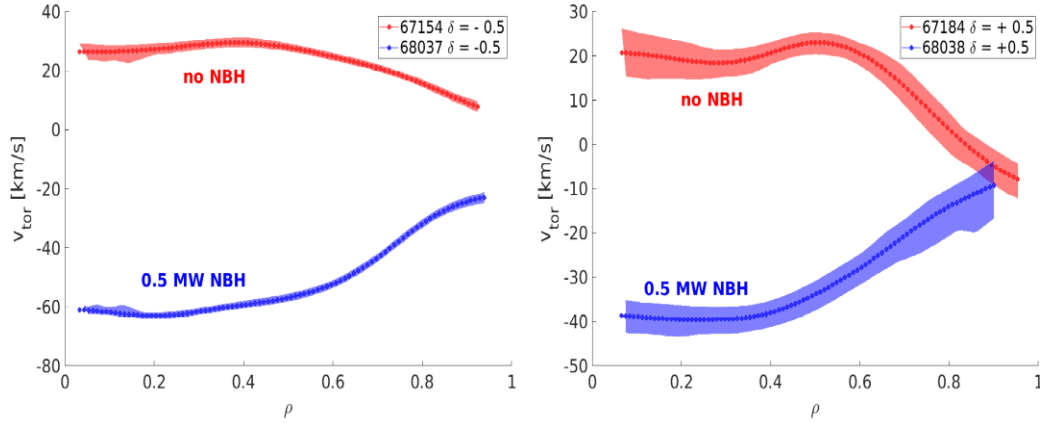


Figure 5.20 – Toroidal velocity profiles before (red) and during the injection of a 0.5 MW NBI pulse (blue), at negative (left) and positive triangularity (right).  $v_{Tor}$  evolves towards negative values during the NBH injection, displaying a strong plasma rotation in the co-current direction, *i.e.* the direction of momentum drive from NBH. Conversely, during the Ohmic phase, the plasma rotates in the counter-current direction, as shown in the pre-reversal profiles presented in the previous chapter.

although it seemed to be more of a rigid displacement of the toroidal velocity profile than a reversal [22]. As stated in the previous chapter (section 4.2), a rotation reversal is better defined by a change in the sign of the toroidal rotation profile gradient (*i.e.* the profile's concavity) rather than a change in the rotation direction. One of the interesting aspects of negative  $\delta$  is that TCV's plasmas in limited configuration usually rotate in the co-current direction. Therefore, any rotation reversal would be required to occur from co to counter-current direction. Figure 5.30 shows the evolution of the energy confinement time and the toroidal velocity at mid-radius for a negative triangularity deuterium discharge. The density peaking is shown in the colourbar. A LOC/SOC transition occurs at higher density than for the positive triangularity case. No rotation reversal is observed, although there remains a decrease in the absolute value of  $v_{tor}$ .

Figure 5.31 shows toroidal velocity profiles at three different times during a density ramp. The profiles appear increasingly pushed in the co-current direction but no change in the sign of the gradient is obtained at any  $\rho$ .

The absolute triangularity and the elongation were both then varied, showing that even small changes of  $\delta$  and  $\kappa$  were able to generate strong variations of  $v_{tor}$ , as shown in Figure 5.32. None of these discharges displayed a clear inversion in the gradient of the rotation profiles, although strong variations in the electron density peaking were observed. The elongation was further increased in discharge #69306, keeping the triangularity at -0.34. Although the absolute value of the central velocity saturated at relatively low density ( $n_e \sim 4.2 \times 10^{19} m^{-3}$ ), no correlation with the LOC/SOC transition, that occurred at  $n_e \sim 7 \times 10^{19} m^{-3}$ , and no rotation reversal were observed (Figure 5.33-b).

A triangularity scan was performed to complete this investigation (Figure 5.34). The D dis-

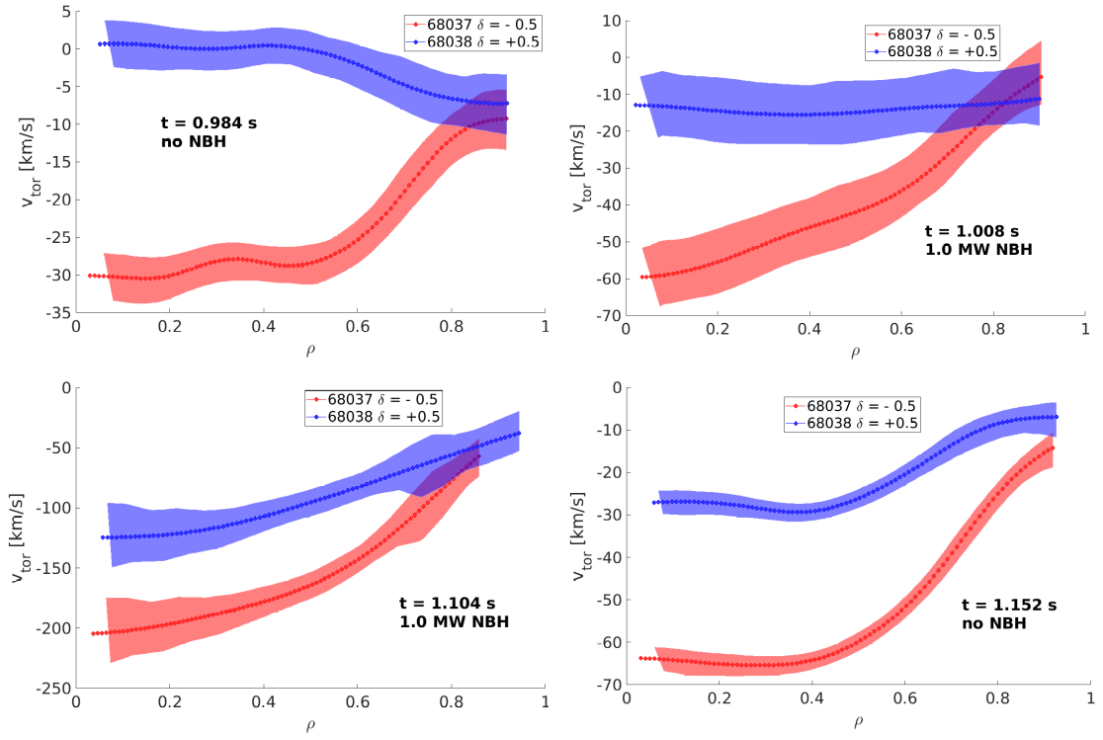


Figure 5.21 – Evolution of toroidal rotation profiles during and after beam injection. Negative and positive triangularity discharges compared. Negative  $\delta$  plasmas tend to rotate faster than their positive  $\delta$  counterparts, also maintaining a strong rotation in the co-current direction following beam termination, indicating increased momentum confinement.

charge, as before, featured high current ( $I_p = 340\text{ kA}$ ), standard magnetic field ( $B_T = 1.4\text{ T}$ ) and a  $\delta$  scan from 0 to  $-0.4$ . The density was kept constant at  $n_e \sim 7 \times 10^{19}\text{ m}^{-3}$ .

As deduced from previous discharges, small variations of  $\delta$  induce changes in  $v_{tor}$  that, although not large, remain well outside the experimental uncertainties.

For all cases, no strong change nor inversion in the rotation profile gradients were observed. All variations consisted in a near rigid displacement of the entire profile and/or variations in the absolute value of  $v_{tor}$ .

## 5.2 Discussion and conclusions

Following the results presented in the previous chapter, the study of C impurity transport, with particular focus on the effects of rotation, was extended to negative triangularity. Extensive  $\delta$  scans were performed in limited and diverted configurations. As reported in previous works performed at TCV, negative triangularity exhibits improved confinement compared to matching discharges at positive  $\delta$  [64] [65] [125]. Less external heating, by means of NB injection, is required to obtain similar values of  $\tau_E$  at negative  $\delta$ , compared to positive. These observations were supported by recent observations made at the DIII-D tokamak [11], that extended

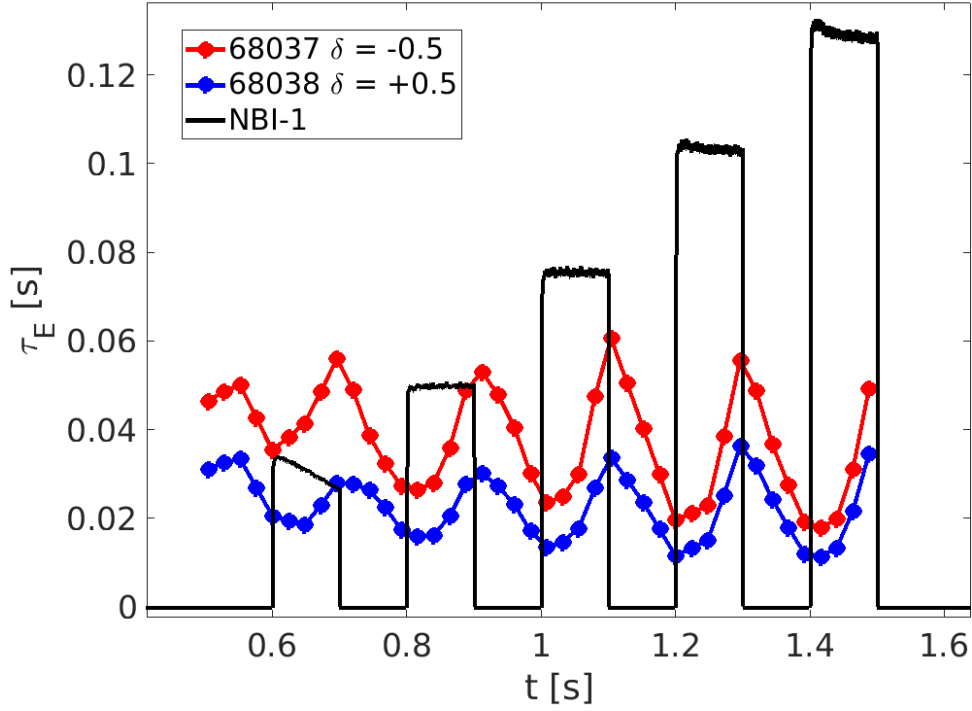


Figure 5.22 – Energy confinement time trace for a negative (red) and a positive (blue) triangularity discharge with neutral beam injection. As expected, a higher energy confinement time is observed at negative triangularity.

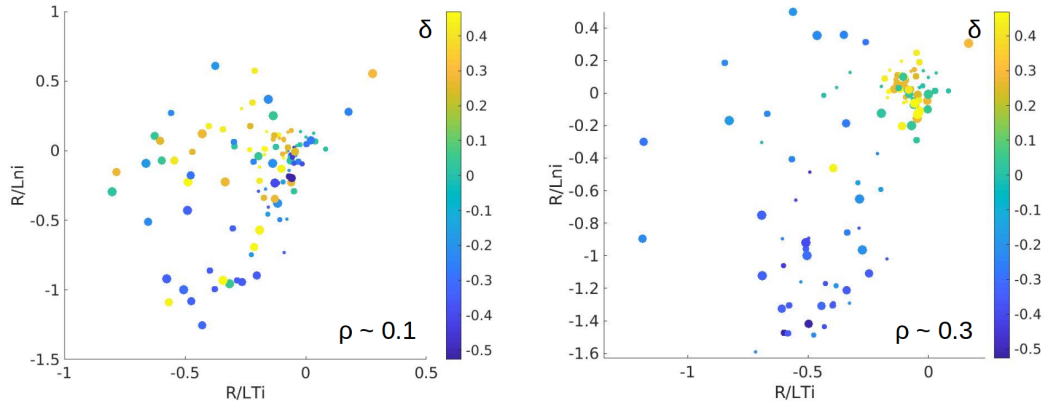


Figure 5.23 –  $\frac{R}{Ln_i}$  VS  $\frac{R}{LT_i}$  correlation plot. Different colour correspond to different triangularity. Each data point was acquired during NBH pulses of various intensity. Increasing size of the spot corresponds to increasing injected power ([0.25 0.5 0.75 1.0 1.25] MW).

previous measurements to  $\frac{T_e}{T_i} \sim 1$ , also achieved in TCV's 2021 experimental campaign and reported in [42].

The improved confinement in negative triangularity is commonly associated with reduced



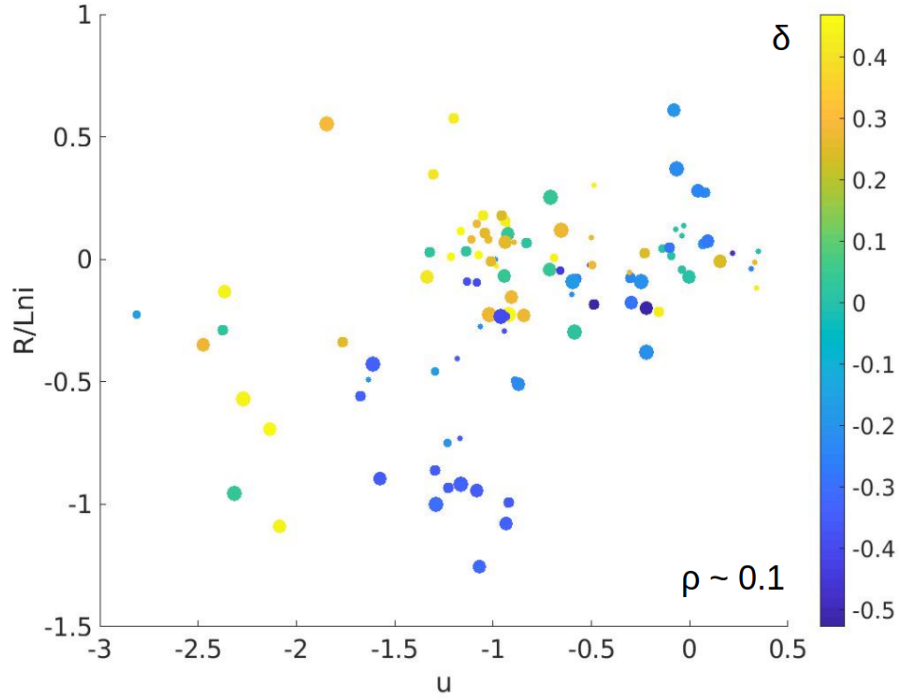


Figure 5.24 –  $\frac{R}{L_{ni}}$  VS  $u$ . Colours correspond to triangularity. Each data point was acquired during NBH pulses of various strength. Increasing spot size corresponds to higher injected power ([0.25 0.5 0.75 1.0 1.25] MW).

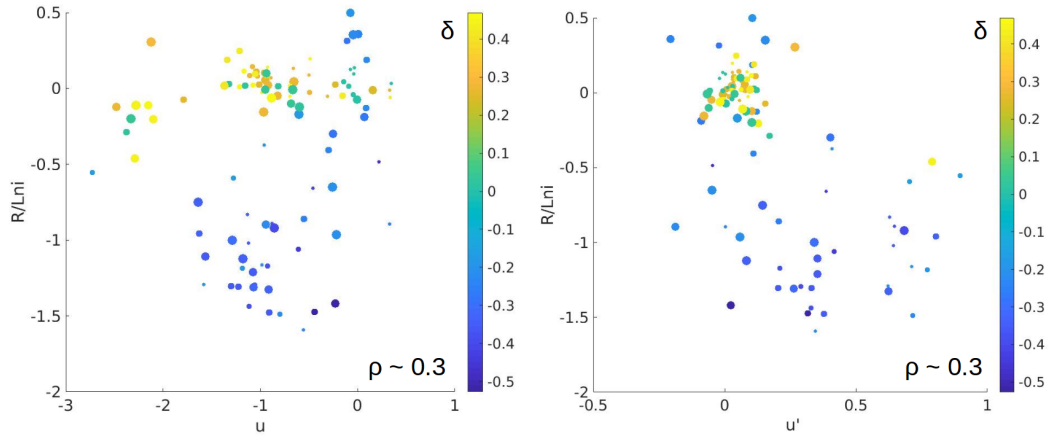


Figure 5.25 –  $\frac{R}{L_{ni}}$  VS  $u$  and  $u'$ . Colour correspond to triangularity. Each data point was acquired during NBH pulses of various strength. Increasing spot size corresponds to higher injected power ([0.25 0.5 0.75 1.0 1.25] MW).

turbulent fluctuations levels [125] and TEM dominance, as observed from gyrokinetic simulations [125] and measured by fluctuation diagnostics such as PCI (Phase Contrast Imaging [115]) at DIII-D [11] or CECE (Correlation Electron Cyclotron Emission [44]) at TCV [65]. Turbulence suppression is often accompanied (and thought to result from) strong  $E \times B$  shear

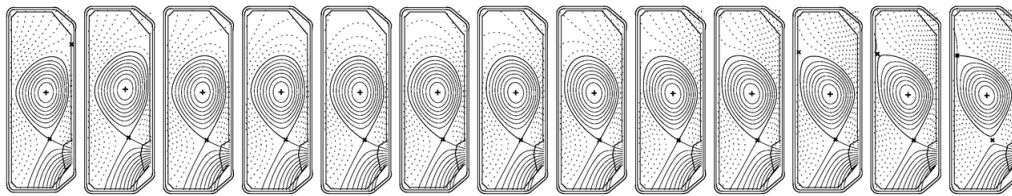


Figure 5.26 – Upper triangularity scan in diverted configuration from  $\delta_{top} \sim -0.5$  to  $\delta_{top} \sim +0.5$ , discharge #67254.

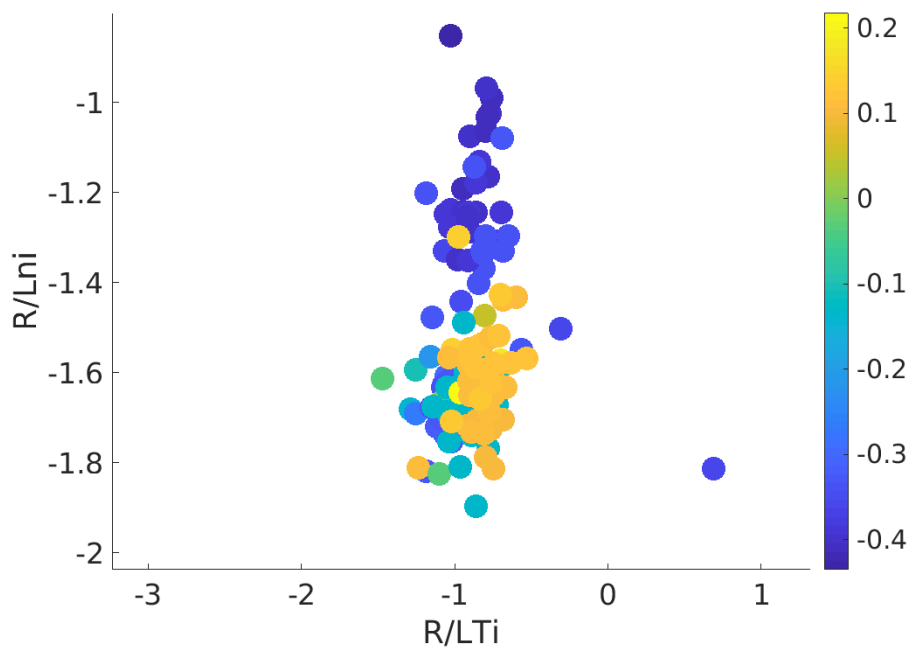


Figure 5.27 – Upper triangularity scan in diverted configuration from  $\delta_{top} \sim -0.5$  to  $\delta_{top} \sim +0.5$ , discharge #67254. Plasmas at positive  $\delta$  populate a small region of the plot, whereas plasmas at  $\delta < 0$  display strong variations, similar to what was observed in limited configuration.

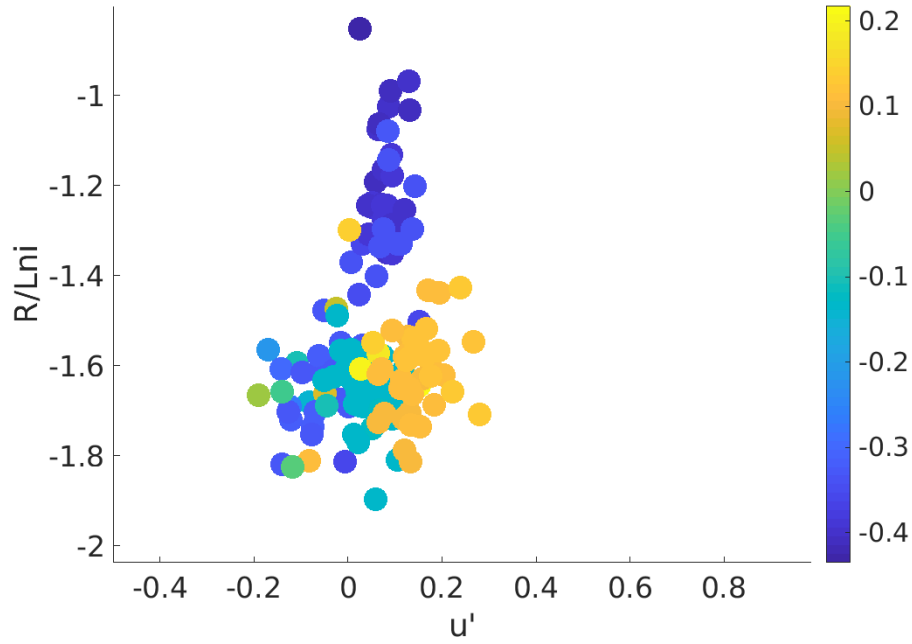


Figure 5.28 – Upper triangularity scan in diverted configuration from  $\delta_{top} \sim -0.5$  to  $\delta_{top} \sim +0.5$ , discharge #67254. Plasmas at positive  $\delta$  populate a small region of the plot, whereas plasmas at  $\delta < 0$  display strong variations, similar to what was observed in limited configuration.

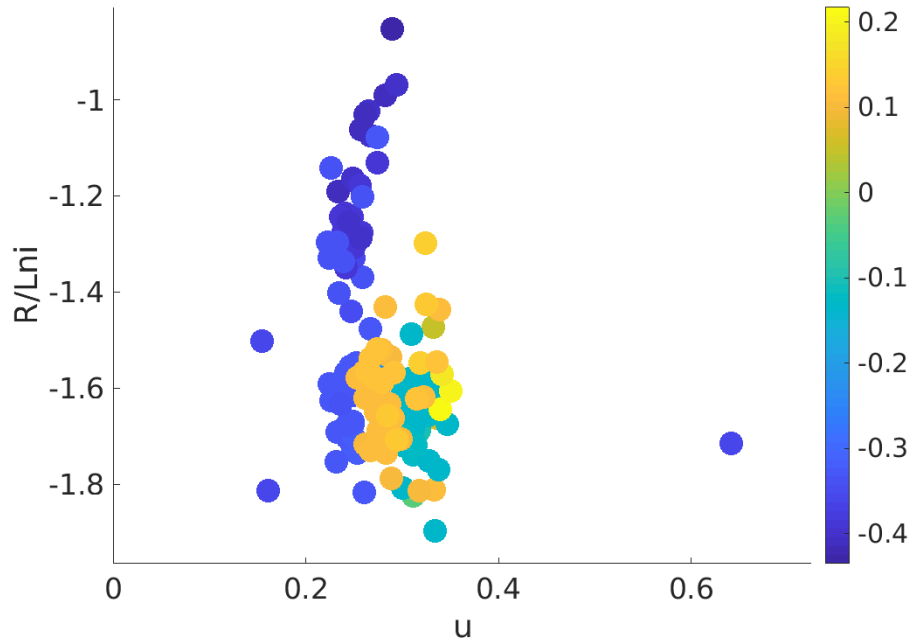


Figure 5.29 – Upper triangularity scan in diverted configuration from  $\delta_{top} \sim -0.5$  to  $\delta_{top} \sim +0.5$ , discharge #67254. Plasmas at positive  $\delta$  populate a small region of the plot, whereas plasmas at  $\delta < 0$  display strong variations, similar to what was observed in limited configuration.

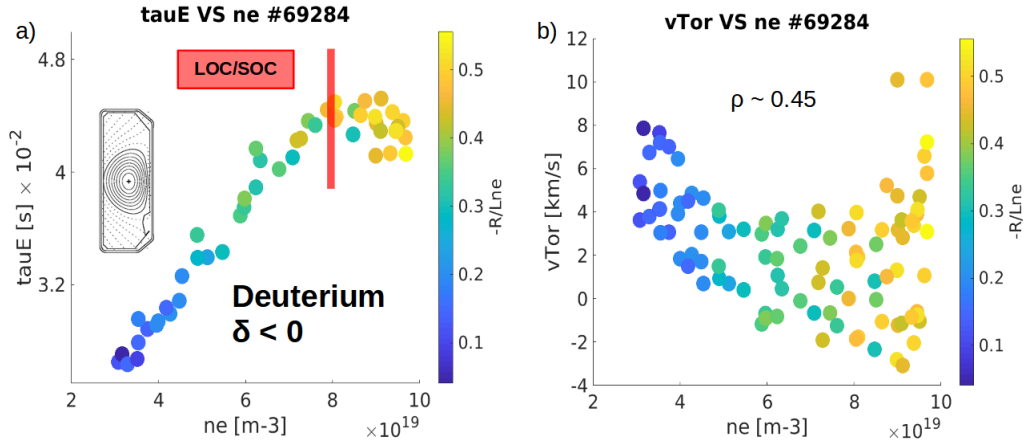


Figure 5.30 – D discharge #69284, negative triangularity,  $I_p = 330$  kA,  $B_T = 1.4$  T. a) Energy confinement time as a function of increasing density; b) Toroidal velocity as a function of density. The colourbar represents the logarithmic density gradient. The LOC/SOC transition occurs at a higher density compared to the positive triangularity case, but is not accompanied by any rotation reversal. For a better clarity of the plot, error bars are not drawn. See Figure 5.33-b for an estimation of experimental uncertainties.

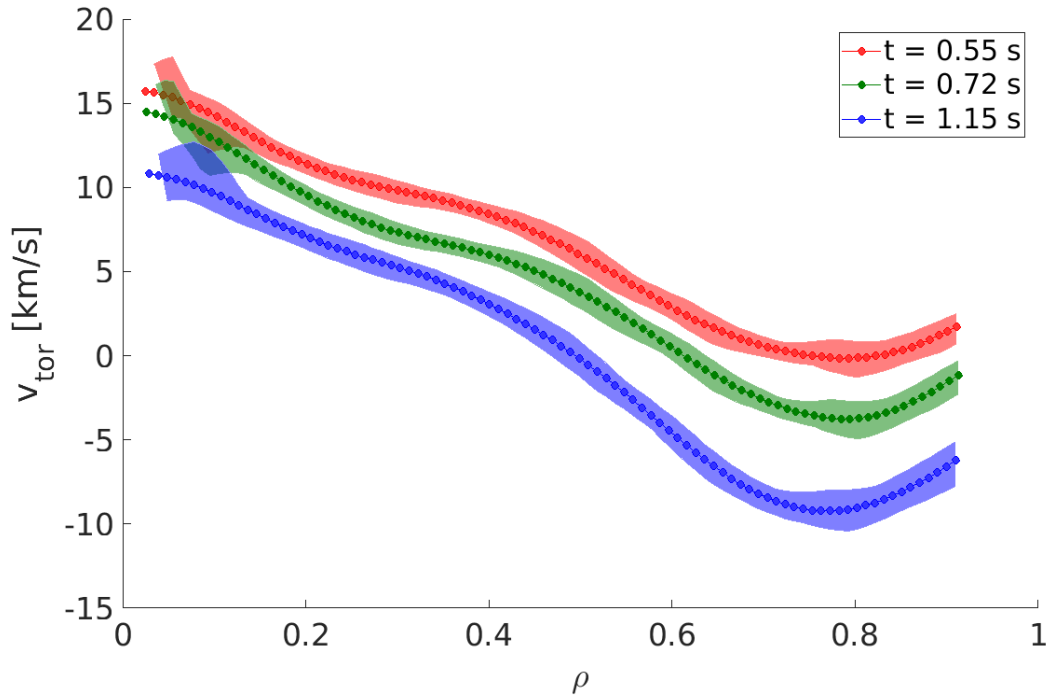


Figure 5.31 – Toroidal velocity profiles at different times during a density ramp. The  $v_{tor}$  profile evolves towards the counter-current direction without showing any change in its gradient, *i.e.* no rotation reversal is observed.

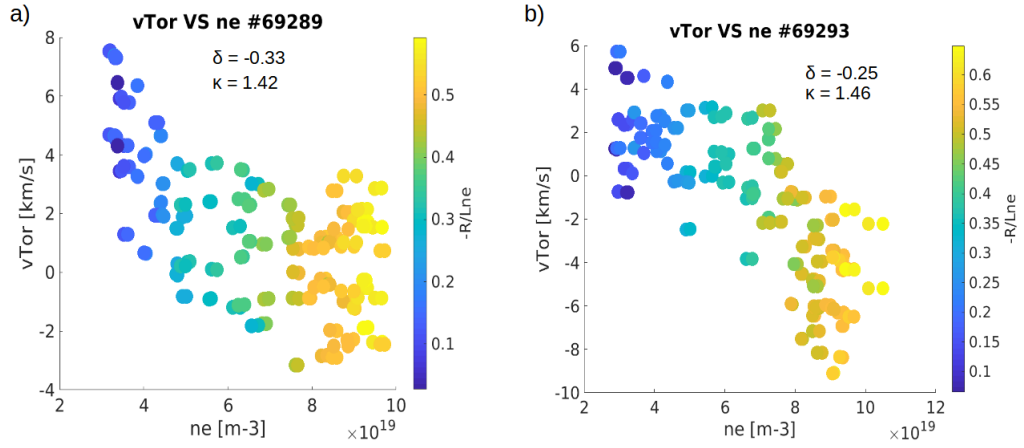


Figure 5.32 – Comparison of the absolute value of the toroidal velocity at mid-radius ( $\rho \sim 0.4$ ) between two discharges at different  $\delta$  and  $\kappa$ . Small variations of  $\delta$  and  $\kappa$  can result in strong changes in  $v_{tor}$ . For a better clarity of the plot, error bars are not drawn. See Figure 5.33-b for an estimation of experimental uncertainties.

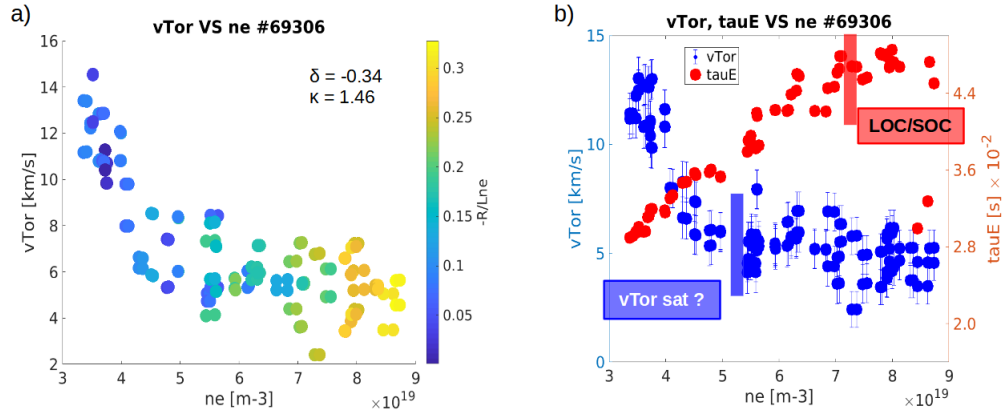


Figure 5.33 – a) Toroidal velocity at  $\rho \sim 0.4$  as a function of increasing density; b) toroidal velocity (blue) and energy confinement time (red) plotted as a function of density. The LOC/SOC transition is not accompanied by any toroidal rotation reversal.

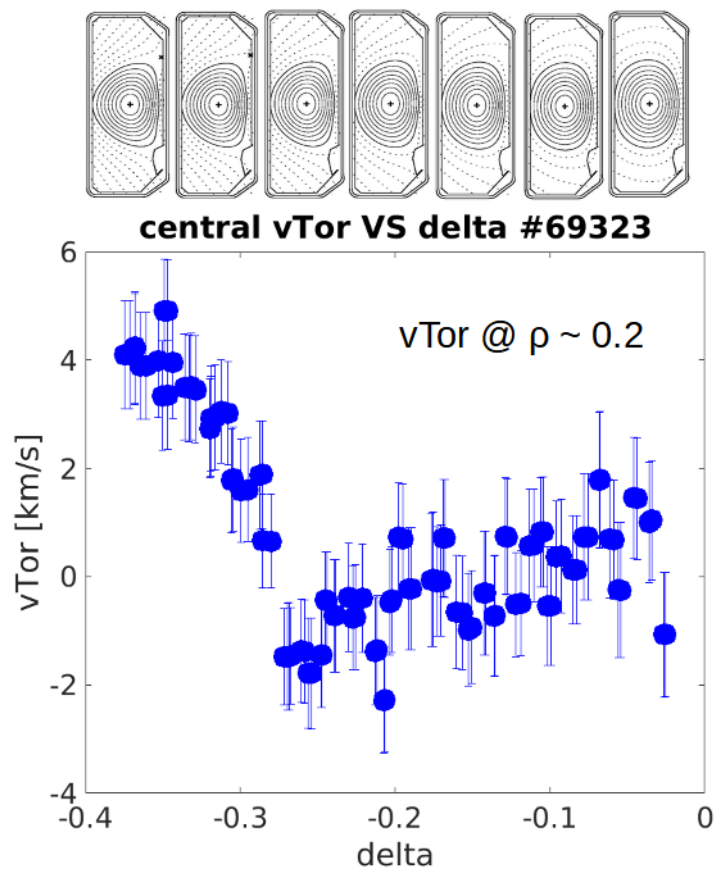


Figure 5.34 – Toroidal velocity at  $\rho \sim 0.2$  evolution during a triangularity scan from 0 to -0.4. As deduced from previous discharges, small variations of  $\delta$  induce changes in  $v_{tor}$  that, although not large, remain well outside the experimental uncertainties.

measured in highly rotating plasmas [154] [185] [43] [13] [20]. The improved confinement, often associated with negative triangularity plasma configurations in TCV, was systematically accompanied by higher toroidal rotation, hinting at the possibility that the higher plasma rotation and momentum confinement measured at negative  $\delta$  in TCV plays a major role in the improved  $\tau_E$  or is, itself, a result of changed radial momentum transport.

A linear correlation between the plasma rotational shear and the local density gradient in Ohmic discharges at different negative triangularity was highlighted in this chapter. In particular, increasing the absolute value of  $\delta$  led to a higher logarithmic density gradient. A large range of negative  $\delta$  was explored, and this effect, particularly visible at mid-radius ( $0.3 < \rho < 0.6$ ), appears to increase continuously with decreasing  $\delta < 0$ . Conversely, the same correlation was not observed for positive triangularity, where  $\delta$  variations resulted in mild changes in the density gradients and no evident trend in the correlation plots.

Studies on particle transport showed that the behaviour of the  $n_e$  profile and the type of turbulence dominating the plasma are strongly connected [4]. As explained in the previous chapter, the turbulence variations (that, eventually, lead to the TEM/ITG bifurcation in D density ramps) are also necessary to explain the changes in the density gradient, which appears to be the main actuator for the observed changes in plasma toroidal velocity [5]. This was reflected in the linear correlation between the rotational shear and the local density gradient observed in D, He and H + ECRH discharges and reported in chapter 4. Such strong correlations between the logarithmic density gradients and the toroidal velocity profiles encouraged the investigation of the turbulent regimes that appear to be present in all of the plasma discharges performed during this work.

Negative delta plasmas, as shown by gyrokinetic simulations [125] and experimental measurements [11], are dominated by TEM turbulence that are less prone to see a transition to ITG, even when NBH is applied. The stabilising effect of  $\delta < 0$  on TEM was speculated to be partially caused by a modification of the toroidal precessional drift [112] which, however, has a strong impact only close to the plasma edge, due to the finite penetration depth of triangularity (as for all poloidal shaping) [114].

The higher impurity content at negative triangularity can also contribute to explain the stabilisation of TEMs and the strong reduction in ITG's dominance. During the  $\delta$  scan reported in this chapter, in fact, an increase of the C concentration was observed for more negative values of  $\delta$ , whilst no strong variation was observed in their positive  $\delta$  counterparts. Such an increase in  $Z_{eff}$  causes a reduction of ion and electron heat fluxes due to ion dilution and increased collisional stabilisation of TEMs [125]. As the ion dilution increases with decreasing negative  $\delta$ , ITGs are maintained stable and TEMs remain the dominant modes. The opposite effect was observed during the D density ramps for positive triangularity reported in chapter 4, where the increase in collisionality (caused by the increasing plasma density) was accompanied by a decrease of  $Z_{eff}$  (often observed during density ramps) and, consequently, ITGs were further destabilised thanks to a lower ion dilution.

This change in the C concentration (and in density gradients) would explain why the linear correlation between  $u'$  and  $\frac{R}{Ln}$  was observed only during the negative  $\delta$  scan and not in posi-

tive triangularity discharges, as only mild changes were observed when varying  $\delta > 0$ . The ITG stabilisation with higher ion dilution could also contribute in determining why no rotation reversal was observed for negative triangularity. The LOC/SOC transition at  $\delta < 0$ , in contrast, was maintained and occurred at a higher density compared to its  $\delta > 0$  counterpart. However, this transition was not followed by any rotation reversal. If strong variations in turbulence are necessary to explain the changes of local density gradients [5] (that, in turn, cause the changes in plasma toroidal rotation), the suppression of turbulence, the dominance of TEM and the stabilisation of ITG due to ion dilution at  $\delta < 0$  could explain why such a rotation reversal was not observed.



## 6 Conclusions and outlook

This thesis, carried out at the Swiss Plasma Center in Lausanne, focused on the study of impurity transport in the TCV tokamak. The work is based on measurements performed with TCV's CXRS diagnostic that, employing a low power diagnostic neutral beam injector, allows for spatial and temporal resolved measurements of impurity ions temperature, density and rotation from the spectroscopic analysis of C CX emission lines in a non-perturbative manner. Since the start of this work, significant effort was dedicated to improve the quality of the impurity density measurements. This was achieved by performing accurate absolute calibrations that, requiring a direct access to TCV's vessel, could not be performed regularly, but only during machine openings. These calibrations were essential to obtain reliable C concentration measurements, crucial for the transport studies performed during this work.

A CXRS system, that exploits the CX reaction between the C ions and the neutrals injected by the main heating beam (NBI-1), was developed and successfully operated on TCV in 2019. Following installation of a second neutral heating beam injector (NBI-2), a further CXRS spectrometer, with lines of sight intersecting NBI-2 beam path, was installed in 2021. These two systems provided, for the first time on TCV, reliable measurements of ion temperature profiles during ELMy H-modes, where the DNBI-CXRS systems' background signals are often too strongly perturbed, inevitably compromising the measurements.

The NBI-CXRS systems, due to their higher, in plasma, neutral density, that provides a stronger active signal, were also employed, again for the first time, for impurity tracking, opening to the possibility of performing intensity measurements of multiple impurities (C, B, N, O) simultaneously. In the continuous effort made in fusion research to improve diagnostic capabilities, these system can provide a powerful tool to perform more accurate estimations of  $Z_{eff}$  and improve impurity content tracking measurements in TCV. This, however, requires the inclusion of a precise beam (DNBI, NBI-1 and NBI-2) model in the analysis routines [120], as well as regular accurate intensity calibrations, that should be envisaged in future experimental campaigns.

In the future, these NBI-systems are more likely to be employed for high performance discharges and will become continually requested, so further development is inevitable. The

## Conclusions and outlook

---

possibility to monitor core N densities for TCV's extensive detachment experiments, alone, merits the addition of a dedicated diagnostic system when TCV's high energy NBH-2 system is finally commissioned.

At the time of this writing, TCV's CXRS comprises 6 systems: 4 DNBI-spectrometers, with lines of sight covering the entire LFS and HFS regions in the toroidal and poloidal directions, including a system dedicated to the LFS edge region, and 2 NBI-spectrometers.

The legacy DNB, non-perturbing, system remains TCV's workhorse, despite the beam power and divergence degradation reported herein. Intriguingly, a recent development, that exploits TCV's CCD cameras to provide data in a real-time compatible format, opened new horizons to use this information for Real-Time discharge optimisation. This will allow many of the measurements and analyses presented in this thesis to be coupled to TCV's already highly developed real-time, diagnostic-based, control system.

One of the goals of this thesis was to investigate impurity transport in negative triangularity. TCV's extreme flexible shaping capabilities were exploited to perform triangularity scans in limited and diverted configurations. Based on recent models [2], light impurities transport is deemed to be mainly driven by turbulent transport. The turbulent flux (eq. 3.37) can be described as a combination of diffusive and convective terms and evolves according to the interplay of ion temperature, rotation and density gradients that mutually affect each-other. A practical way of studying turbulent transport is to investigate the correlations between these impurity ion gradients.

This study highlighted significant differences between positive and negative  $\delta$  plasmas. In particular, no correlation between C temperature, rotation and density gradients was found at positive triangularity. This stiff response with  $\delta > 0$  is relieved in negative triangularity, where a linear correlation between  $\nabla T_i$  and  $\nabla n_C$ , and  $\nabla v_{tor}$  and  $\nabla n_C$ , was observed over a range of negative  $\delta$ , suggesting that transport in NT is mainly driven by temperature and toroidal velocity gradients. A large range of negative  $\delta$  was explored, and this effect, particularly visible at mid-radius ( $0.3 < \rho < 0.6$ ), appears to increase continuously with decreasing  $\delta < 0$ .

A possible explanation to this phenomenon could be linked to turbulence suppression and stabilisation of TEM often observed for  $\delta < 0$  [125] [65]. During the  $\delta$  scan, in fact, C density appeared to increase with negative triangularity, whilst no particular effect was observed in positive  $\delta$  plasmas. Such an increase in  $Z_{eff}$  causes a reduction of ion and electron heat fluxes due to ion dilution and collisional stabilisation of TEMs [125]. ITGs are therefore maintained stable by the increasing ion dilution and TEMs remain the dominant modes.

These speculations are supported by observations made during  $n_e$  ramps at  $\delta < 0$ . Density ramps in D plasmas at positive  $\delta$  are usually accompanied by changes in toroidal rotation and, in some specific cases, by the reversal of the rotation direction. This phenomenon was not observed at  $\delta < 0$ . If strong variations in turbulence are necessary to explain the changes of local density gradients [5] (that, in turn, cause the changes in plasma toroidal rotation), the suppression of turbulence, the dominance of TEMs and the stabilisation of ITGs due to ion dilution in negative triangularity could explain why no rotation reversal was observed.

To further probe this effect, future studies should focus on experimental investigations of

turbulent fluctuations. TCV is equipped with turbulence diagnostics (PCI, CECE) that, unfortunately, were not yet fully available at the time of this writing. The PCI diagnostic, in particular, can provide signatures of turbulence nature and dominant modes as functions of plasma radius. Such measurements, supported by gyrokinetic simulations, may then be exploited to better understand the interplay of TEMs and ITGs in presence of strong changes of ion temperature, rotation and density gradients and, of course, poloidal shape.

The rotation reversal phenomenon was extensively studied in this thesis. A set of experiments was extended to compare previous studies in deuterium plasmas to discharges of majority hydrogen and helium. One of the main goals was to investigate any relation between the LOC/SOC transition and the rotation reversal, as both phenomena are often observed around a plasma density threshold that, in some specific cases, appears to coincide, with most data reported from D majority plasmas only.

High quality measurements from CXRS allowed for a clear separation of the two phenomena in D and He. Furthermore, no rotation reversal was observed in H or in low current D discharges, despite a clear transition from linear to saturated Ohmic confinement. These results demonstrated that no causal relation between these two phenomena exists. Consequently, although these two phenomena may occur in similar plasma situations, their explanation should be found by separate mechanisms.

A strong correlation between toroidal rotation gradients and plasma density peaking was observed. Strong variations of turbulence are, again, necessary to explain the changes of local density gradients. Therefore, the stabilisation (or destabilisation) of turbulent modes plays a major role in understanding rotation reversal also in plasmas with different majority species. Experimental [190] and theoretical [163] [52] studies reported an increase of the maximum growth rate of TEMs with decreasing mass, suggesting that TEMs are more unstable in H compared to D and He. Similar results were found for ITGs [51]. As a consequence, it is likely that the stabilisation of TEMs by collisional detrapping is less effective in H than D and He, thus reducing any effect on density profiles that induce variations in plasma toroidal rotation and, eventually, may lead to rotation reversal.

This work also highlighted the role of plasma shape and configuration, confirming previous results reported in TCV, where D plasmas in limited configuration displayed counter-current rotation at low density in the LOC regime and co-current rotation at higher density in the SOC regime. This behaviour was only apparently disagreeing with other devices, which usually show co-current rotation in low density plasmas in diverted configuration, reversing towards the counter-current direction at higher density. Similar discharges were repeated in TCV in diverted configuration, showing co-current rotation direction in the low density LOC regime and counter-current rotation in the higher density SOC regime. This dependency of rotation direction on plasma configuration should be further explored in other devices that usually operate only in diverted configuration.

Based on these results, the experimental investigation of turbulent modes with PCI should be extended to plasmas of majority D, H and He. Furthermore, discharges of majority H could be performed at  $\delta < 0$ , trying to favour destabilisation of ITGs and, possibly, rotation reversal.

## Conclusions and outlook

---

Permitting measurements with and without the presence of concomitant strongly perturbing NBI heating has been used to probe well known results, such as LOC/SOC transitions and separate their physics from more recent, and still intriguing phenomena, such as rotation reversal. With CXRS currently a standard TCV diagnostic, now extended to a much wider range of plasma scenarios, it can be expected that these complex diagnostics will continue to provide insight, and hopefully guidance, in the future.

# Acknowledgements

After 4 years and a half, it is with great satisfaction that I complete this thesis and feed it to the ferocious world of research. Though it is true that “it goes without saying that this work would have not seen light without the help and support of many people”, I will try to avoid clichés as much as possible, but I cannot make any promises. When I started the PhD I underestimated the importance of acknowledgments and I saw the thesis as a mere report of a scientific work. However, 4 years and a half are a tremendously long time, a PhD is a hard, often overwhelming experience, and all the people that accompanied you to the end, supporting and believing in you, deserve to be acknowledged. These acknowledgments are sincere, and even if you feel like you did not have an impact on the outcome of my PhD, I assure you had it on my life, helping me to face the pitfalls of existence in these last years.

First, I have to thank my supervisor, and mentor, Basil, whose wise tutelage guided me through this journey. Basil has the impressive skill of teaching science and research without lecturing. Many people say that when you visit his office you enter with a question and you leave with existential doubts (and many more questions). However, once you find the answer you were seeking, and you feel like you have done that by yourself, it is in that moment that you realise how valuable his maieutics is. But the most important lesson that I learnt from Basil is to laugh about our own mistakes, because “if you cannot laugh doing scientific research (that most of the time is about failing), you are probably not enjoying what you are doing”.

Secondly, I have to thank my family, my mum, my dad and my sister. My family has always supported my decisions. Even when I was doubting my choices, they made me feel like they were 100 % sure I was doing the right thing. I left my parents’ house in 2018 to start the PhD, moving to another country, finally feeling independent. It is in that independence that I understood the value of having a place to call home, somewhere to return to whenever you want. The joy I witnessed whilst driving in the snow through the Grand St Bernard, leaving Martigny and reappearing in sunny Aosta, knowing that I was going back home to my family for Christmas holidays, is an emotion that I will always cherish. In particular, I have to thank my mum, who would have loved to see me earning just another piece of paper (she used to collect them...) and to whom this thesis is dedicated.

I thank Valentina for her support, her love, her patience and the incredible strength she demonstrates whilst fighting the unfair situations that this precarious life as a researcher forces us to undergo. In the last years, we discovered mountains, islands and new countries together, things that made me a better person and that I would have never done without her.

## Acknowledgements

---

My friends, Fabrizio, Stefano, Luca, who have known me for years, are another reason why it is worth going back home. No matter how much time passes, it always feels like yesterday that we were in school.

A special thanks goes to Matteo R. “CAI” (what a curse...), with whom I shared an incredible amount of adventures (and many more are yet to come). The bond we created through climbing, during hardcore sport sessions or in sketchy alpine situations, shaped some of the best memories of my life.

I thank my friends at the SPC, Aylwin, Paolo, Dario, Lorenzo, Claudia, that always managed to make every day less boring. I started my PhD with Aylwin and Paolo, and shortly after Dario joined our group. After a few weeks, Paolo and I were sharing the office, and a short time later also Dario joined it (unofficially, but he was spending more time there than at the third floor, so it counts...). When Paolo and Dario left it was heartbreaking, a real turning point. Fortunately, Aylwin, Lorenzo and Claudia stayed and, eventually, I got kicked out of my old office to join the latter two in the infamous PPH277. I also had the privilege to share a significant part of my job in the spectroscopy lab with Lorenzo. I would have never thought that I would end up working side by side with someone from Verbania, TI, but side by side with a friend, I could do that.

I thank my officemates, friends and colleagues: Arsène, Curdin, Sophie, Guillaume, Stefano, Jesús, Federico, Mack, Margherita, Jean, Simon, Nico, Matteo, Carrie, Justin, Anna. Such a diversified and international environment is what makes the SPC strong, and teaches you more than a thousand PhDs.

I thank Yanis and Dmytry for their incredible knowledge about optics and spectroscopy, that more than once saved me some hundreds hours of work.

My flatmates, those from the present and those from the past: Bryan, Francesco, Stelios, Chris, Eleni, Davide, Mirko, Oscar, Solène, Léa, JL, Gabriel, Rönja. It was definitely easier to survive the pandemic with your company. I learnt a lot about other countries’ traditions, like the refined French housekeeping skills, the subtle German sense of humour, or the gargantuan American culinary heritage that built the foundation of the Italian culture.

I thank my climbing buddies, Flo, Mateusz, Théo, Aaron, with whom I shared a good amount of training and outdoor climbing sessions that made life easier.

Last but not least, I thank Remi “Mojo” Morange, great dog (not the best, there is still room for improvement) and best bouldering partner that witnessed all my hardest ascents.

Well, here at last, dear friends, on the shores of these pages comes the end of my thesis. Go in peace! I will not say: do not weep; for not all tears are an evil.

*Lausanne, August 26, 2022*

F. B.

# Bibliography

- [1] Andrew, Y., Hawkes, N. C., Biewer, T., Crombe, K., Keeling, D., de la Luna, E., Giroud, C., Korotkov, A., Meigs, A., Murari, A., Nunes, I., Sartori, R., and Tala, T. (2008). Evolution of the radial electric field in a JET h-mode plasma. *EPL (Europhysics Letters)*, 83(1):15003.
- [2] Angioni, C. (2021). Impurity transport in tokamak plasmas, theory, modelling and comparison with experiments. *Plasma Physics and Controlled Fusion*, 63(7):073001.
- [3] Angioni, C., Camenen, Y., Casson, F., Fable, E., McDermott, R., Peeters, A., and Rice, J. (2012). Off-diagonal particle and toroidal momentum transport: a survey of experimental, theoretical and modelling aspects. *Nuclear Fusion*, 52(11):114003.
- [4] Angioni, C., Fable, E., Greenwald, M., Maslov, M., Peeters, A. G., Takenaga, H., and Weisen, H. (2009). Particle transport in tokamak plasmas, theory and experiment. *Plasma Physics and Controlled Fusion*, 51(12):124017.
- [5] Angioni, C., McDermott, R. M., Casson, F. J., Fable, E., Bottino, A., Dux, R., Fischer, R., Podoba, Y., Pütterich, T., Ryter, F., and Viezzer, E. (2011). Intrinsic toroidal rotation, density peaking, and turbulence regimes in the core of tokamak plasmas. *Phys. Rev. Lett.*, 107:215003.
- [6] Angioni, C., Peeters, A. G., Ryter, F., Jenko, F., Conway, G. D., Dannert, T., Fahrbach, H. U., Reich, M., Suttrop, W., Team, A. U., and Fattorini, L. (2005). Relationship between density peaking, particle thermodiffusion, ohmic confinement, and microinstabilities in asdex upgrade l-mode plasmas. *Physics of Plasmas*, 12(4):040701.
- [7] Angioni, C., Pochelon, A., Gorelenkov, N. N., McClements, K. G., Sauter, O., Budny, R. V., de Vries, P. C., Howell, D. F., Mantsinen, M., Nave, M. F. F., Sharapov, S. E., and contributors to the EFDA-JET Workprogramme (2002). Neutral beam stabilization of sawtooth oscillations in JET. *Plasma Physics and Controlled Fusion*, 44(2):205–222.
- [8] ARC (2022). Sparc website. <https://www.psfc.mit.edu/sparc/faq>. Accessed: 14-07-2022.
- [9] Arnichand, H., Sabot, R., Hacquin, S., Krämer-Flecken, A., Bourdelle, C., Citrin, J., Garbet, X., Giacalone, J., Guirlet, R., Hillesheim, J., and Meneses, L. (2015). Discriminating the trapped electron modes contribution in density fluctuation spectra. *Nuclear Fusion*, 55(9):093021.

## Bibliography

---

- [10] Arnichand, H., Sabot, R., Hacquin, S., Krämer-Flecken, A., Garbet, X., Citrin, J., Bourdelle, C., Hornung, G., Bernardo, J., Bottereau, C., Clairet, F., Falchetto, G., and Giacalone, J. (2014). Quasi-coherent modes and electron-driven turbulence. *Nuclear Fusion*, 54(12):123017.
- [11] Austin, M. E., Marinoni, A., Walker, M. L., Brookman, M. W., deGrassie, J. S., Hyatt, A. W., McKee, G. R., Petty, C. C., Rhodes, T. L., Smith, S. P., Sung, C., Thome, K. E., and Turnbull, A. D. (2019). Achievement of reactor-relevant performance in negative triangularity shape in the diiii-d tokamak. *Phys. Rev. Lett.*, 122:115001.
- [12] Baker, D. R. et al. (2001). Transport of Particles and Impurities in DIII-D Discharges with Internal Regions of Enhanced Confinement. *IAEA*.
- [13] Beer, M. A., Hammett, G. W., Rewoldt, G., Synakowski, E. J., Zarnstorff, M. C., and Dorland, W. (1997). Gyrofluid simulations of turbulence suppression in reversed-shear experiments on the tokamak fusion test reactor. *Physics of Plasmas*, 4(5):1792–1799.
- [14] Bell, R. E., Andre, R., Kaye, S. M., Kolesnikov, R. A., LeBlanc, B. P., Rewoldt, G., Wang, W. X., and Sabbagh, S. A. (2010). Comparison of poloidal velocity measurements to neoclassical theory on the national spherical torus experiment. *Physics of Plasmas*, 17(8):082507.
- [15] Bell, R. E., Levinton, F. M., Batha, S. H., Synakowski, E. J., and Zarnstorff, M. C. (1998). Poloidal rotation in tftr reversed shear plasmas. *Phys. Rev. Lett.*, 81:1429–1432.
- [16] Bernardo, J., Fenzi, C., Bourdelle, C., Camenen, Y., Arnichand, H., Bizarro, J. P. S., Cortes, S., Garbet, X., Guimarães-Filho, Z. O., Aniel, T., Artaud, J.-F., Clairet, F., Cottier, P., Gunn, J., and and, P. L. (2015). Density impact on toroidal rotation in tore supra: experimental observations and theoretical investigation. *Plasma Physics and Controlled Fusion*, 57(3):035002.
- [17] Bessenrodt-Weberpals, M., Wagner, F., Gehre, O., Giannone, L., Hofmann, J., Kallenbach, A., McCormick, K., Mertens, V., Murmann, H., Ryter, F., Scott, B., Siller, G., Soldner, F., Stabler, A., Steuer, K.-H., Stroth, U., Tsois, N., Verbeek, H., and Zoohm, H. (1993). The isotope effect in ASDEX. *Nuclear Fusion*, 33(8):1205–1238.
- [18] Biglari, H., Diamond, P. H., and Terry, P. W. (1990). Influence of sheared poloidal rotation on edge turbulence. *Physics of Fluids B: Plasma Physics*, 2(1):1–4.
- [19] Bishop, C., Kirby, P., Connor, J., Hastie, R., and Taylor, J. (1984). Ideal MHD ballooning stability in the vicinity of a separatrix. *Nuclear Fusion*, 24(12):1579–1584.
- [20] Boedo, J., Gray, D., Terry, P., Jachmich, S., Tynan, G., and and, R. C. (2002). Scaling of plasma turbulence suppression with velocity shear. *Nuclear Fusion*, 42(2):117–121.
- [21] Bonanomi, N., Mantica, P., Giroud, C., Angioni, C., Manas, P., and and, S. M. (2018). Light impurity transport in JET ILW l-mode plasmas. *Nuclear Fusion*, 58(3):036009.
- [22] Bortolon, A. (2009). *Plasma rotation and momentum transport studies in the TCV tokamak based on charge exchange spectroscopy measurements*. PhD thesis, EPFL, Lausanne.



- [23] Bortolon, A., Camenen, Y., Karpushov, A., Duval, B., Andrebe, Y., Federspiel, L., and and, O. S. (2013). Indirect measurement of poloidal rotation using inboard–outboard asymmetry of toroidal rotation and comparison with neoclassical predictions. *Nuclear Fusion*, 53(2):023002.
- [24] Bortolon, A., Duval, B. P., Pochelon, A., and Scarabosio, A. (2006). Observation of spontaneous toroidal rotation inversion in ohmically heated tokamak plasmas. *Phys. Rev. Lett.*, 97:235003.
- [25] Bosshard, P. (2003). *Confinement ionique dans le tokamak TCV mesuré par spectroscopie d'échange de charge*. PhD thesis, EPFL, Lausanne.
- [26] Braginskii, S. I. (1965). Transport Processes in a Plasma. *Reviews of Plasma Physics*, 1:205.
- [27] Buller, S., Mollén, A., Newton, S. L., Smith, H. M., and Pusztai, I. (2019). The importance of the classical channel in the impurity transport of optimized stellarators. *Journal of Plasma Physics*, 85(4):175850401.
- [28] Burrell, K. H., Austin, M. E., Brennan, D. P., DeBoo, J. C., Doyle, E. J., Gohil, P., Greenfield, C. M., Groebner, R. J., Lao, L. L., Luce, T. C., Makowski, M. A., McKee, G. R., Moyer, R. A., Osborne, T. H., Porkolab, M., Rhodes, T. L., Rost, J. C., Schaffer, M. J., Stallard, B. W., Strait, E. J., Wade, M. R., Wang, G., Watkins, J. G., West, W. P., and Zeng, L. (2002). Quiescent h-mode plasmas in the DIII-d tokamak. *Plasma Physics and Controlled Fusion*, 44(5A):A253–A263.
- [29] Buzhinskij, O. I. and Semenets, Y. M. (1997). Review of in situ boronization in contemporary tokamaks. *Fusion Technology*, 32(1):1–13.
- [30] Callen, J. D. (2006). Plasma Descriptions I : Kinetic , Two-Fluid. In *Fundamentals of Plasma Physics*, chapter 5. University of Wisconsin, Madison, Wisconsin, draft edition.
- [31] Camenen, Y., Angioni, C., Bortolon, A., Duval, B. P., Fable, E., Hornsby, W. A., McDermott, R. M., Na, D. H., Na, Y.-S., Peeters, A. G., and Rice, J. E. (2017). Experimental observations and modelling of intrinsic rotation reversals in tokamaks. *Plasma Physics and Controlled Fusion*, 59(3):034001.
- [32] Camenen, Y., Pochelon, A., Behn, R., Bottino, A., Bortolon, A., Coda, S., Karpushov, A., Sauter, O., Zhuang, G., and the TCV team (2007). Impact of plasma triangularity and collisionality on electron heat transport in TCV I-mode plasmas. *Nuclear Fusion*, 47(7):510–516.
- [33] Cao, N., Rice, J., Diamond, P., White, A., Baek, S., Chilenski, M., Hughes, J., Irby, J., Reinke, M., and and, P. R.-F. (2019). Hysteresis as a probe of turbulent bifurcation in intrinsic rotation reversals on alcator c-mod. *Nuclear Fusion*, 59(10):104001.
- [34] Cao, N. M., Rice, J. E., Diamond, P. H., White, A. E., Chilenski, M. A., Ennever, P. C., Hughes, J. W., Irby, J., Reinke, M. L., and Rodriguez-Fernandez, P. (2020). Evidence and modeling of turbulence bifurcation in I-mode confinement transitions on alcator c-mod. *Physics of Plasmas*, 27(5):052303.

## Bibliography

---

- [35] Casson, F. J., Peeters, A. G., Angioni, C., Camenen, Y., Hornsby, W. A., Snodin, A. P., and Szepesi, G. (2010). Gyrokinetic simulations including the centrifugal force in a rotating tokamak plasma. *Physics of Plasmas*, 17(10):102305.
- [36] Chang, C. S. and Hinton, F. L. (1986). Effect of impurity particles on the finite-aspect ratio neoclassical ion thermal conductivity in a tokamak. *The Physics of Fluids*, 29(10):3314–3316.
- [37] Chapman, I. T., Scannell, R., Cooper, W. A., Graves, J. P., Hastie, R. J., Naylor, G., and Zocco, A. (2010). Magnetic reconnection triggering magnetohydrodynamic instabilities during a sawtooth crash in a tokamak plasma. *Phys. Rev. Lett.*, 105:255002.
- [38] Chen, F. F. (1984). *Introduction to Plasma Physics and Controlled Fusion*. Springer US, Boston, MA.
- [39] Chrystal, C., Grierson, B., Haskey, S., Sontag, A., Poli, F., Shafer, M., and deGrassie, J. (2020). Predicting the rotation profile in ITER. *Nuclear Fusion*, 60(3):036003.
- [40] Clery, D. (2020). U.K. seeks site for world’s first fusion power station. *Science magazine*.
- [41] Clery, D. (2021). Laser-powered fusion effort nears ‘ignition’. *Science*, 373(6557).
- [42] Coda, S., Merle, A., Sauter, O., Porte, L., Bagnato, F., Boedo, J., Bolzonella, T., Février, O., Labit, B., Marinoni, A., Pau, A., Pigatto, L., Sheikh, U., Tsui, C., Vallar, M., and Vu, T. (2021). Enhanced confinement in diverted negative-triangularity l-mode plasmas in TCV. *Plasma Physics and Controlled Fusion*, 64(1):014004.
- [43] Conway, G. D., Borba, D. N., Alper, B., Bartlett, D. V., Gormezano, C., von Hellermann, M. G., Maas, A. C., Parail, V. V., Smeulders, P., and Zastrow, K.-D. (2000). Suppression of plasma turbulence during optimized shear configurations in jet. *Phys. Rev. Lett.*, 84:1463–1466.
- [44] Creely, A. J., Freethy, S. J., Burke, W. M., Conway, G. D., Leccacorvi, R., Parkin, W. C., Terry, D. R., and White, A. E. (2018). Correlation electron cyclotron emission diagnostic and improved calculation of turbulent temperature fluctuation levels on asdex upgrade. *Review of Scientific Instruments*, 89(5):053503.
- [45] Creely, A. J., Greenwald, M. J., Ballinger, S. B., Brunner, D., Canik, J., Doody, J., Fülöp, T., Garnier, D. T., Granetz, R., Gray, T. K., and et al. (2020). Overview of the sparc tokamak. *Journal of Plasma Physics*, 86(5):865860502.
- [46] de Vries, P., Salmi, A., Parail, V., Giroud, C., Andrew, Y., Biewer, T., Crombé, K., Jenkins, I., Johnson, T., Kiptily, V., Loarte, A., Lönnroth, J., Meigs, A., Oyama, N., Sartori, R., Saibene, G., Urano, H., and and, K.-D. Z. (2008). Effect of toroidal field ripple on plasma rotation in JET. *Nuclear Fusion*, 48(3):035007.
- [47] de Vries, P. C., Rantamäki, K. M., Giroud, C., Asp, E., Corrigan, G., Eriksson, A., de Greef, M., Jenkins, I., Knoop, H. C. M., Mantica, P., Nordman, H., Strand, P., Tala, T., Weiland, J.,

- and Zastrow, K.-D. (2006). Plasma rotation and momentum transport studies at JET. *Plasma Physics and Controlled Fusion*, 48(12):1693–1708.
- [48] Delabie, E. (2021). 63rd aps-dpp meeting, 2021. 11-2021.
- [49] Diamond, P., McDevitt, C., Gurcan, O., Hahm, T., Wang, W. X., Yoon, E., Holod, I., Lin, Z., Naulin, V., and Singh, R. (2009). Physics of non-diffusive turbulent transport of momentum and the origins of spontaneous rotation in tokamaks. *Nuclear Fusion*, 49(4):045002.
- [50] Ding, B. J., Shan, J. F., Wang, M., Xu, H. D., Wu, Z. W., Sun, Y. W., Zhao, Y. P., Kuang, G. L., Li, J. G., and the HT-7 Team (2007). Investigations of sawtooth behaviour in ramp-up plasma assisted by lower hybrid current drive in the HT-7 tokamak. *Plasma Physics and Controlled Fusion*, 49(5):563–572.
- [51] Dong, J. Q. and Horton, W. (1995). Studies of impurity mode and ion temperature gradient mode in toroidal plasmas. *Physics of Plasmas*, 2(9):3412–3419.
- [52] Dong, J. Q., Horton, W., and Dorland, W. (1994). Isotope scaling and  $\eta_i$  mode with impurities in tokamak plasmas. *Physics of Plasmas*, 1(11):3635–3640.
- [53] Duperrex, P., Pochelon, A., Edwards, A., and Snipes, J. (1992). Global sawtooth instability measured by magnetic coils in the JET tokamak. *Nuclear Fusion*, 32(7):1161–1180.
- [54] Duval, B., Joye, B., and Marchal, B. (1992). Behaviour of plasma rotation and radial electric field with density ramp rate in an ohmically heated tokamak. *Nuclear Fusion*, 32(8):1405–1419.
- [55] Duval, B. P., Bortolon, A., Karpushov, A., Pitts, R. A., Pochelon, A., and and, A. S. (2007). Bulk plasma rotation in the TCV tokamak in the absence of external momentum input. *Plasma Physics and Controlled Fusion*, 49(12B):B195–B209.
- [56] Duval, B. P., Bortolon, A., Karpushov, A., Pitts, R. A., Pochelon, A., Sauter, O., Scarabosio, A., and Turri, G. (2008). Spontaneous l-mode plasma rotation scaling in the tcv tokamak. *Physics of Plasmas*, 15(5):056113.
- [57] Ennever, P., Porkolab, M., Candy, J., Staebler, G., Reinke, M. L., Rice, J. E., Rost, J. C., Ernst, D., Fiore, C., Hughes, J., and Terry, J. (2015). The effects of dilution on turbulence and transport in c-mod ohmic plasmas and comparisons with gyrokinetic simulations. *Physics of Plasmas*, 22(7):072507.
- [58] Erofeev, I., Fable, E., Angioni, C., and and, R. M. (2017). Theory-based modeling of LOC–SOC transitions in ASDEX upgrade. *Nuclear Fusion*, 57(12):126067.
- [59] Fable, E., Angioni, C., and Sauter, O. (2009). The role of ion and electron electrostatic turbulence in characterizing stationary particle transport in the core of tokamak plasmas. *Plasma Physics and Controlled Fusion*, 52(1):015007.

## Bibliography

---

- [60] Fasoli, A., Reimerdes, H., Alberti, S., Baquero-Ruiz, M., Duval, B., Havlikova, E., Karpushov, A., Moret, J.-M., Toussaint, M., Elaian, H., Silva, M., Theiler, C., and and, D. V. (2019). TCV heating and divertor upgrades. *Nuclear Fusion*, 60(1):016019.
- [61] Felici, F. et al. (2012). Real-time control of multiple MHD instabilities on TCV by ECRH/ECCD. *EPJ Web of Conferences*, 32.
- [62] Fischer, R. et al. (2015). Effect of measured toroidal flows on tokamak equilibria. *42nd EPS Conference on Plasma Physics*, 42.
- [63] Fontana, M. (2018). *Turbulence studies in TCV using the Correlation ECE diagnostic*. PhD thesis, EPFL, Lausanne.
- [64] Fontana, M., Porte, L., Coda, S., and and, O. S. (2017). The effect of triangularity on fluctuations in a tokamak plasma. *Nuclear Fusion*, 58(2):024002.
- [65] Fontana, M., Porte, L., Coda, S., Sauter, O., Brunner, S., Jayalekshmi, A. C., Fasoli, A., and and, G. M. (2019). Effects of collisionality and  $t_e/t_i$  on fluctuations in positive and negative  $\delta$  tokamak plasmas. *Nuclear Fusion*, 60(1):016006.
- [66] Freidberg, J. P. (2007). *Plasma Physics and Fusion Energy*. Cambridge University Press, Cambridge.
- [67] Furno, I., Angioni, C., Porcelli, F., Weisen, H., Behn, R., Goodman, T., Henderson, M., Pietrzyk, Z., Pochelon, A., Reimerdes, H., and Rossi, E. (2001). Understanding sawtooth activity during intense electron cyclotron heating experiments on TCV. *Nuclear Fusion*, 41(4):403–420.
- [68] Gao, C., Rice, J., Sun, H., Reinke, M., Howard, N., Mikkelsen, D., Hubbard, A., Chilenski, M., Walk, J., Hughes, J., Ennever, P., Porkolab, M., White, A., Sung, C., Delgado-Aparicio, L., Baek, S., Rowan, W., Brookman, M., Greenwald, M., Granetz, R., Wolfe, S., and and, E. M. (2014). Non-local heat transport in alcator c-mod ohmic l-mode plasmas. *Nuclear Fusion*, 54(8):083025.
- [69] Garbet, X., Payan, J., Laviron, C., Devynck, P., Saha, S., Capes, H., Chen, X., Coulon, J., Gil, C., Harris, G., Hutter, T., Pecquet, A.-L., Truc, A., Hennequin, P., Gervais, F., and Quemeneur, A. (1992). Turbulence and energy confinement in TORE SUPRA ohmic discharges. *Nuclear Fusion*, 32(12):2147–2155.
- [70] Garcia, J. et al. (2022). New h-mode regimes with small elms and high thermal confinement in the joint european torus. *Physics of Plasmas*, 29(3):032505.
- [71] Girardo, J.-B., Sharapov, S., Boom, J., Dumont, R., Eriksson, J., Fitzgerald, M., Garbet, X., Hawkes, N., Kiptily, V., Lupelli, I., Mantsinen, M., Sarazin, Y., and Schneider, M. (2016). Stabilization of sawteeth with third harmonic deuterium icrf-accelerated beam in jet plasmas. *Physics of Plasmas*, 23(1):012505.

- 
- [72] Gohil, P., Burrell, K., Doyle, E., Groebner, R., Kim, J., and Seraydarian, R. (1994). The phenomenology of the l-h transition in the DIII-d tokamak. *Nuclear Fusion*, 34(8):1057–1068.
- [73] Goldston, R. and Rutherford, P. (1995). *Introduction to Plasma Physics*. Taylor & Francis.
- [74] Goodman, T. P., Felici, F., Sauter, O., and Graves, J. P. (2011). Sawtooth pacing by real-time auxiliary power control in a tokamak plasma. *Phys. Rev. Lett.*, 106:245002.
- [75] Hahm, T., Wang, L., Wang, W., Yoon, E., and Duthoit, F. (2013). Isotopic dependence of residual zonal flows. *Nuclear Fusion*, 53(7):072002.
- [76] Hahm, T. S. (1994). Rotation shear induced fluctuation decorrelation in a toroidal plasma. *Physics of Plasmas*, 1(9):2940–2944.
- [77] Haskey, S. R., Grierson, B. A., Chrystal, C., Ashourvan, A., Burrell, K. H., Groebner, R. J., Belli, E. A., Stagner, L., Battaglia, D. J., Stoltzfus-Dueck, T., and Bortolon, A. (2018). Main ion and impurity edge profile evolution across the l- to h-mode transition on DIII-d. *Plasma Physics and Controlled Fusion*, 60(10):105001.
- [78] Hastie, R. J. (1997). Sawtooth Instability in Tokamak Plasmas. *Astrophys. Space Sci.*, 256(1/2):177–204.
- [79] Hazeltine, R. D. (1974). Rotation of a toroidally confined, collisional plasma. *The Physics of Fluids*, 17:961.
- [80] Hazeltine, R. D. and Prager, S. C. (2002). New physics in fusion plasma confinement. *Physics Today*, 55(7):30–36.
- [81] Heidbrink, W., Fredrickson, E., Mau, T., Petty, C., Pinsker, R., Porkolab, M., and Rice, B. (1999). High harmonic ion cyclotron heating in DIII-d: Beam ion absorption and sawtooth stabilization. *Nuclear Fusion*, 39(10):1369–1389.
- [82] Helander, P. and Sigmar, D. J. (2002). *Collisional transport in magnetized plasmas*. Cambridge University Press, New York.
- [83] Herfindal, J. L., Maurer, D. A., Hartwell, G. J., Ennis, D. A., Hanson, J. D., Knowlton, S. F., Ma, X., Pandya, M. D., Roberds, N. A., and Traverso, P. J. (2019). Sawtooth oscillation behavior with varying amounts of applied stellarator rotational transform. *Physics of Plasmas*, 26(3):032502.
- [84] Hinton, F. L. and Hazeltine, R. D. (1976). Theory of plasma transport in toroidal confinement systems. *Rev. Mod. Phys.*, 48:239–308.
- [85] Hinton, F. L. and Wong, S. K. (1985). Neoclassical ion transport in rotating axisymmetric plasmas. *The Physics of Fluids*, 28:3082.

## Bibliography

---

- [86] Hirshman, S. and Sigmar, D. (1981). Neoclassical transport of impurities in tokamak plasmas. *Nuclear Fusion*, 21(9):1079–1201.
- [87] Hirshman, S. P. and Sigmar, D. J. (1977). Neoclassical transport of a multispecies toroidal plasma in various collisionality regimes. *The Physics of Fluids*, 20(3):418–426.
- [88] Hofmann, F., Lister, J. B., Anton, W., Barry, S., Behn, R., Bernel, S., Besson, G., Buhlmann, F., Chavan, R., Corboz, M., Dutch, M. J., Duval, B. P., Fasel, D., Favre, A., Franke, S., Heym, A., Hirt, A., Hollenstein, C., Isoz, P., Joye, B., Llobet, X., Magnin, J. C., Marletaz, B., Marmillod, P., Martin, Y., Mayor, J. M., Moret, J. M., Nieswand, C., Paris, P. J., Perez, A., Pietrzyk, Z. A., Pitts, R. A., Pochelon, A., Rage, R., Sauter, O., Tonetti, G., Tran, M. Q., Troyon, F., Ward, D. J., and Weisen, H. (1994). Creation and control of variably shaped plasmas in TCV. *Plasma Physics and Controlled Fusion*, 36(12B):B277–B287.
- [89] Hornsby, W., Angioni, C., Lu, Z., Fable, E., Erofeev, I., McDermott, R., Medvedeva, A., Lebschy, A., and and, A. P. (2018). Global gyrokinetic simulations of intrinsic rotation in ASDEX upgrade ohmic l-mode plasmas. *Nuclear Fusion*, 58(5):056008.
- [90] HOSHINO, K. (1990). Electron cyclotron heating (ech) of tokamak plasmas. *Journal of Nuclear Science and Technology*, 27(5):391–405.
- [91] Huang, Z. and and, S. C. (2018). Dependence of density fluctuations on shape and collisionality in positive- and negative-triangularity tokamak plasmas. *Plasma Physics and Controlled Fusion*, 61(1):014021.
- [92] Ida, K., Hidekuma, S., Kojima, M., Miura, Y., Tsuji, S., Hoshino, K., Mori, M., Suzuki, N., and Yamauchi, T. (1992). Edge poloidal rotation profiles of h-mode plasmas in the jft-2m tokamak. *Physics of Fluids B: Plasma Physics*, 4(8):2552–2559.
- [93] Ikeda, K. (2007). Progress in the ITER physics basis. *Nuclear Fusion*, 47(6).
- [94] Ishida, S., Shirai, H., Nagashima, K., Nishitani, T., and Fukuda, T. (1988). Sawtooth observations in ohmic discharges compared between hydrogen and helium plasmas on JT-60. *Plasma Physics and Controlled Fusion*, 30(8):1069–1081.
- [95] ITER (2021). Iter website. <https://www.iter.org/mach>. Accessed: 2021-01-28.
- [96] Itoh, S. (1992). Anomalous viscosity due to drift wave turbulence. *Physics of Fluids B: Plasma Physics*, 4(4):796–803.
- [97] Jackson, J. D. (1962, 1975, 1999). *Classical electrodynamics (3rd ed.)*. Wiley, New York.
- [98] JET (2021). Jet website. <https://www.euro-fusion.org/devices/jet/>. Accessed: 2021-01-28.
- [99] Jones, T., Bickley, A., Challis, C., Ciric, D., Cox, S., de Esch, H., Falter, H.-D., Godden, D., Martin, D., Stork, D., Svensson, S., Watson, M., and Young, D. (1999). Tritium operation of the jet neutral beam systems. *Fusion Engineering and Design*, 47(2):205–231.

- [100] Kadomtsev, B. and Pogutse, O. (1966). A comparative study of transport in stellarators and tokamaks. *Zh. Eksp. Teor. Fiz.*, 51(1734).
- [101] Karpushov, A. N., Chavan, R., Coda, S., Davydenko, V. I., Dolizy, F., Dranitchnikov, A. N., Duval, B. P., Ivanov, A. A., Fasel, D., Fasoli, A., Kolmogorov, V. V., Lavanchy, P., Llobet, X., Marlétaz, B., Marmillod, P., Martin, Y., Merle, A., Perez, A., Sauter, O., Siravo, U., Shikhovtsev, I. V., Sorokin, A. V., and Toussaint, M. (2017). Neutral beam heating on the tcv tokamak. *Fusion Engineering and Design*, 123:468–472. Proceedings of the 29th Symposium on Fusion Technology (SOFT-29) Prague, Czech Republic, September 5-9, 2016.
- [102] Keilhacker, M., Gibson, A., Gormezano, C., Lomas, P., Thomas, P., Watkins, M., Andrew, P., Balet, B., Borba, D., Challis, C., Coffey, I., Cottrell, G., Esch, H. D., Deliyanakis, N., Fasoli, A., Gowers, C., Guo, H., Huysmans, G., Jones, T., Kerner, W., König, R., Loughlin, M., Maas, A., Marcus, F., Nave, M., Rimini, F., Sadler, G., Sharapov, S., Sips, G., Smeulders, P., Söldner, F., Taroni, A., Tubbing, B., von Hellermann, M., Ward, D., and Team, J. (1999). High fusion performance from deuterium-tritium plasmas in JET. *Nuclear Fusion*, 39(2):209–234.
- [103] Kikuchi, M., Takizuka, T., Medvedev, S., Ando, T., Chen, D., Li, J., Austin, M., Sauter, O., Villard, L., Merle, A., Fontana, M., Kishimoto, Y., and Imadera, K. (2019). L-mode-edge negative triangularity tokamak reactor. *Nuclear Fusion*, 59(5):056017.
- [104] Lawson, J. D. (1955). Some criteria for a power producing thermonuclear reactor. Technical report, Atomic Energy Research Establishment, Harwell, Berkshire, U. K.
- [105] Lawson, K. D. et al. (1998). Impurity Accumulation in JET ELMy H-mode Discharges. *JET-CP(98)27*.
- [106] Lebschy, A., McDermott, R., Angioni, C., Geiger, B., Prisiazhniuk, D., Cavedon, M., Conway, G., Dux, R., Dunne, M., Kappatou, A., Pütterich, T., Stroth, U., and and, E. V. (2017). Measurement of the complete core plasma flow across the LOC–SOC transition at ASDEX upgrade. *Nuclear Fusion*, 58(2):026013.
- [107] Lister, J. B., Hofmann, F., Moret, J.-M., Bühlmann, F., Dutch, M. J., Fasel, D., Favre, A., Isoz, P.-F., Marletaz, B., Marmillod, P., Martin, Y., Perez, A., and Ward, D. J. (1997). The control of tokamak configuration variable plasmas. *Fusion Technology*, 32(3):321–373.
- [108] Liu, Y., Liu, Z., Liu, A., Zhou, C., Feng, X., Yang, Y., Zhang, T., Xia, T., Liu, H., Wu, M., Zou, X., Kong, D., Li, H., Xie, J., Lan, T., Mao, W., Zhang, S., Ding, W., Zhuang, G., and Liu, W. (2020). Power threshold and confinement of the i-mode in the EAST tokamak. *Nuclear Fusion*, 60(8):082003.
- [109] Ltd, A. T. (2021). User’s guide to: SDK. *andor.com*, 2.102.
- [110] Maggi, C. F., Weisen, H., Hillesheim, J. C., Chankin, A., Delabie, E., Horvath, L., Auriemma, F., Carvalho, I. S., Corrigan, G., Flanagan, J., Garzotti, L., Keeling, D., King, D., Lerche, E., Lorenzini, R., Maslov, M., Menmuir, S., Saarelma, S., Sips, A. C. C., Solano, E. R.,

## Bibliography

---

- Belonohy, E., Casson, F. J., Challis, C., Giroud, C., Parail, V., Silva, C., and and, M. V. (2017). Isotope effects on l-h threshold and confinement in tokamak plasmas. *Plasma Physics and Controlled Fusion*, 60(1):014045.
- [111] Marini, C. (2017). *Poloidal CX visible light plasma rotation diagnostics in TCV*. PhD thesis, EPFL, Lausanne.
- [112] Marinoni, A. (2009). *Plasma fluctuation studies in the TCV tokamak*. PhD thesis, EPFL, Lausanne.
- [113] Marinoni, A., Austin, M. E., Hyatt, A. W., Walker, M. L., Candy, J., Chrystal, C., Lasnier, C. J., McKee, G. R., Odstrčil, T., Petty, C. C., Porkolab, M., Rost, J. C., Sauter, O., Smith, S. P., Staebler, G. M., Sung, C., Thome, K. E., Turnbull, A. D., and Zeng, L. (2019). H-mode grade confinement in l-mode edge plasmas at negative triangularity on diii-d. *Physics of Plasmas*, 26(4):042515.
- [114] Marinoni, A., Brunner, S., Camenen, Y., Coda, S., Graves, J. P., Lapillonne, X., Pochelon, A., Sauter, O., and Villard, L. (2009). The effect of plasma triangularity on turbulent transport: modeling TCV experiments by linear and non-linear gyrokinetic simulations. *Plasma Physics and Controlled Fusion*, 51(5):055016.
- [115] Marinoni, A., Coda, S., Chavan, R., and Pochon, G. (2006). Design of a tangential phase contrast imaging diagnostic for the tcv tokamak. *Review of Scientific Instruments*, 77(10):10E929.
- [116] Martinelli, L. et al. (2021). Spectroscopic studies of TCV divertor plasma with the DSS upgrade. *47th EPS Conference on Plasma Physics*.
- [117] McClements, K. G. and Hole, M. J. (2010). On steady poloidal and toroidal flows in tokamak plasmas. *Physics of Plasmas*, 17(8):082509.
- [118] McCracken, G. and Stott, P. (2012). *Fusion: The Energy of the Universe*. Academic Press.
- [119] McDermott, R., Angioni, C., Conway, G., Dux, R., Fable, E., Fischer, R., Pütterich, T., Rytter, F., and and, E. V. (2014). Core intrinsic rotation behaviour in ASDEX upgrade ohmic l-mode plasmas. *Nuclear Fusion*, 54(4):043009.
- [120] McDermott, R. M., Dux, R., Pütterich, T., Geiger, B., Kappatou, A., Lebschy, A., Bruhn, C., Cavedon, M., Frank, A., den Harder, N., and and, E. V. (2018). Evaluation of impurity densities from charge exchange recombination spectroscopy measurements at ASDEX upgrade. *Plasma Physics and Controlled Fusion*, 60(9):095007.
- [121] McDermott, R. M., Lipschultz, B., Hughes, J. W., Catto, P. J., Hubbard, A. E., Hutchinson, I. H., Granetz, R. S., Greenwald, M., LaBombard, B., Marr, K., Reinke, M. L., Rice, J. E., and Whyte, D. (2009). Edge radial electric field structure and its connections to h-mode confinement in alcator c-mod plasmas. *Physics of Plasmas*, 16(5):056103.



- 
- [122] Merle, A., Sauter, O., and Medvedev, S. Y. (2017). Pedestal properties of h-modes with negative triangularity using the EPED-CH model. *Plasma Physics and Controlled Fusion*, 59(10):104001.
  - [123] Merlo, G. (2016). *Flux-tube and global grid-based gyrokinetic simulations of plasma microturbulence and comparisons with experimental TCV measurements*. PhD thesis, EPFL, Lausanne.
  - [124] Merlo, G., Brunner, S., Sauter, O., Camenen, Y., Görler, T., Jenko, F., Marinoni, A., Told, D., and Villard, L. (2015). Investigating profile stiffness and critical gradients in shaped TCV discharges using local gyrokinetic simulations of turbulent transport. *Plasma Physics and Controlled Fusion*, 57(5):054010.
  - [125] Merlo, G., Fontana, M., Coda, S., Hatch, D., Janhunen, S., Porte, L., and Jenko, F. (2019). Turbulent transport in tcv plasmas with positive and negative triangularity. *Physics of Plasmas*, 26(10):102302.
  - [126] Meyer, H., Bunting, C., Carolan, P. G., Conway, N. J., Dunstan, M. R., Kirk, A., Scannell, R., Temple, D., Walsh, M., the MAST, and Teams, N. (2008). The structure, evolution and role of the radial edge electric field in h-mode and l-mode on MAST. *Journal of Physics: Conference Series*, 123:012005.
  - [127] Moret, J.-M., Buhlmann, F., Fasel, D., Hofmann, F., and Tonetti, G. (1998). Magnetic measurements on the tcv tokamak. *Review of Scientific Instruments*, 69(6):2333–2348.
  - [128] Moret, J.-M., Franke, S., Weisen, H., Anton, M., Behn, R., Duval, B. P., Hofmann, F., Joye, B., Martin, Y., Nieswand, C., Pietrzyk, Z. A., and van Toledo, W. (1997). Influence of plasma shape on transport in the tcv tokamak. *Phys. Rev. Lett.*, 79:2057–2060.
  - [129] Muck, A. M. (2003). *Study of the Sawtooth Instability and its Control in the ASDEX Upgrade Tokamak*. PhD thesis, Max-Planck-Institut für Plasmaphysik (IPP), Munich.
  - [130] Murakami, M., Neilson, G. H., Howe, H. C., Jernigan, T. C., Bates, S. C., Bush, C. E., Colchin, R. J., Dunlap, J. L., Edmonds, P. H., Hill, K. W., Isler, R. C., Ketterer, H. E., King, P. W., McNeill, D. W., Mihalcz, J. T., Neidigh, R. V., Pare, V. K., Saltmarsh, M. J., Wilgen, J. B., and Zurro, B. (1979). Plasma confinement studies in the isx-a tokamak. *Phys. Rev. Lett.*, 42:655–658.
  - [131] Nakata, M., Nunami, M., Sugama, H., and Watanabe, T.-H. (2017). Isotope effects on trapped-electron-mode driven turbulence and zonal flows in helical and tokamak plasmas. *Phys. Rev. Lett.*, 118:165002.
  - [132] Nave, F. (2022a). 28th itpa meeting, 2022. 03-2022.
  - [133] Nave, F. (2022b). 48th eps meeting, 2022. 27-06-2022.
  - [134] Nelson, A. O., Paz-Soldan, C., and Saarelma, S. (2022). H-mode inhibition in negative triangularity tokamak reactor plasmas.

## Bibliography

---

- [135] Nicolas, T. et al. (2013). Role of the sawtooth crash in the electron and impurity transport in the Tore Supra and JET tokamaks. *40th EPS Conference on Plasma Physics*.
- [136] NIF (2021). Nif website. <https://lasers.llnl.gov/about/what-is-nif>. Accessed: 2021-01-28.
- [137] Parra, F. I. and Barnes, M. (2015). Intrinsic rotation in tokamaks: theory. *Plasma Physics and Controlled Fusion*, 57(4):045002.
- [138] Peeters, A. G. and Angioni, C. (2005). Linear gyrokinetic calculations of toroidal momentum transport in a tokamak due to the ion temperature gradient mode. *Physics of Plasmas*, 12(7):072515.
- [139] Peeters, A. G., Angioni, C., and Strintzi, D. (2007). Toroidal momentum pinch velocity due to the coriolis drift effect on small scale instabilities in a toroidal plasma. *Phys. Rev. Lett.*, 98:265003.
- [140] Peeters, A. G., Strintzi, D., Camenen, Y., Angioni, C., Casson, F. J., Hornsby, W. A., and Snodin, A. P. (2009). Influence of the centrifugal force and parallel dynamics on the toroidal momentum transport due to small scale turbulence in a tokamak. *Physics of Plasmas*, 16(4):042310.
- [141] Phillips, J., Hodapp, T., Holtrop, K., Jackson, G. L., Moyer, R., Watkins, J., and Winter, J. (1992). Initial boronization of the diii-d tokamak. *Journal of Vacuum Science & Technology A*, 10(4):1252–1255.
- [142] POCHELON, A., ANGELINO, P., BEHN, R., BRUNNER, S., CODA, S., KIRNEVA, N., MEDVEDEV, S. Y., REIMERDES, H., ROSSEL, J., SAUTER, O., VILLARD, L., WÁGNER, D., BOTTINO, A., CAMENEN, Y., CANAL, G. P., CHATTOPADHYAY, P. K., DUVAL, B. P., FASOLI, A., GOODMAN, T. P., JOLLIET, S., KARPUSHOV, A., LABIT, B., MARINONI, A., MORET, J.-M., PITZSCHKE, A., PORTE, L., RANCIC, M., UDINTSEV, V. S., and the TCV Team (2012). Recent tcv results - innovative plasma shaping to improve plasma properties and insight. *Plasma and Fusion Research*, 7:2502148–2502148.
- [143] Pusztai, I., Candy, J., and Gohil, P. (2011). Isotope mass and charge effects in tokamak plasmas. *Physics of Plasmas*, 18(12):122501.
- [144] Ramisch, M., Mahdizadeh, N., Stroth, U., Greiner, F., Lechte, C., and Rahbarnia, K. (2005).  $\rho$  s scaling of characteristic turbulent structures in the torsatron tj-k. *Physics of Plasmas*, 12(3):032504.
- [145] Rebut, P.-H. (1992). The JET preliminary tritium experiment. *Plasma Physics and Controlled Fusion*, 34(13):1749–1758.
- [146] Reimerdes, H., Duval, B., Elaian, H., Fasoli, A., Février, O., Theiler, C., Bagnato, F., Baquero-Ruiz, M., Blanchard, P., Brida, D., Colandrea, C., Oliveira, H. D., Galassi, D., Gorno, S., Henderson, S., Komm, M., Linehan, B., Martinelli, L., Maurizio, R., Moret, J.-M., Perek, A., Raj, H., Sheikh, U., Testa, D., Toussaint, M., Tsui, C., Wensing, M., the TCV team, and

- the EUROfusion MST1 team (2021). Initial TCV operation with a baffled divertor. *Nuclear Fusion*, 61(2):024002.
- [147] Reimerdes, H., Pochelon, A., Sauter, O., Goodman, T. P., Henderson, M. A., and Martynov, A. (2000). Effect of triangular and elongated plasma shape on the sawtooth stability. *Plasma Physics and Controlled Fusion*, 42(6):629–639.
- [148] Rice, J. (2022a). private communication. 14-07-2022.
- [149] Rice, J., Citrin, J., Cao, N., Diamond, P., Greenwald, M., and Grierson, B. (2020). Understanding LOC/SOC phenomenology in tokamaks. *Nuclear Fusion*, 60(10):105001.
- [150] Rice, J., Duval, B., Reinke, M., Podpaly, Y., Bortolon, A., Churchill, R., Cziegler, I., Diamond, P., Dominguez, A., Ennever, P., Fiore, C., Granetz, R., Greenwald, M., Hubbard, A., Hughes, J., Irby, J., Ma, Y., Marmar, E., McDermott, R., Porkolab, M., Tsujii, N., and Wolfe, S. (2011a). Observations of core toroidal rotation reversals in alcator c-mod ohmic l-mode plasmas. *Nuclear Fusion*, 51(8):083005.
- [151] Rice, J., Gao, C., Reinke, M., Diamond, P., Howard, N., Sun, H., Cziegler, I., Hubbard, A., Podpaly, Y., Rowan, W., Terry, J., Chilenski, M., Delgado-Aparicio, L., Ennever, P., Ernst, D., Greenwald, M., Hughes, J., Ma, Y., Marmar, E., Porkolab, M., White, A., and Wolfe, S. (2013). Non-local heat transport, rotation reversals and up/down impurity density asymmetries in alcator c-mod ohmic l-mode plasmas. *Nuclear Fusion*, 53(3):033004.
- [152] Rice, J., Ince-Cushman, A., deGrassie, J., Eriksson, L.-G., Sakamoto, Y., Scarabosio, A., Bortolon, A., Burrell, K., Duval, B., Fenzi-Bonizet, C., Greenwald, M., Groebner, R., Hoang, G., Koide, Y., Marmar, E., Pochelon, A., and Podpaly, Y. (2007). Inter-machine comparison of intrinsic toroidal rotation in tokamaks. *Nuclear Fusion*, 47(11):1618–1624.
- [153] Rice, J. D. (2022b). *Driven Rotation, Self-Generated Flow, and Momentum Transport in Tokamak Plasmas*. Springer Series on Atomic, Optical, and Plasma Physics.
- [154] Rice, J. E. (2008). Spontaneous rotation and momentum transport in tokamak plasmas. *Journal of Physics: Conference Series*, 123:012003.
- [155] Rice, J. E., Cziegler, I., Diamond, P. H., Duval, B. P., Podpaly, Y. A., Reinke, M. L., Ennever, P. C., Greenwald, M. J., Hughes, J. W., Ma, Y., Marmar, E. S., Porkolab, M., Tsujii, N., and Wolfe, S. M. (2011b). Rotation reversal bifurcation and energy confinement saturation in tokamak ohmic l-mode plasmas. *Phys. Rev. Lett.*, 107:265001.
- [156] Rice, J. E., Ince-Cushman, A. C., Reinke, M. L., Podpaly, Y., Greenwald, M. J., LaBombard, B., and Marmar, E. S. (2008). Spontaneous core toroidal rotation in alcator c-mod l-mode, h-mode and ITB plasmas. *Plasma Physics and Controlled Fusion*, 50(12):124042.
- [157] Romanelli, F., Tang, W., and White, R. (1986). Anomalous thermal confinement in ohmically heated tokamaks. *Nuclear Fusion*, 26(11):1515–1528.

## Bibliography

---

- [158] Rutherford, P. H. (1974). Impurity transport in the pfirsch-schlüter regime. *The Physics of Fluids*, 17(9):1782–1784.
- [159] Ryter, F., Angioni, C., Peeters, A. G., Leuterer, F., Fahrbach, H.-U., and Suttrop, W. (2005). Experimental study of trapped-electron-mode properties in tokamaks: Threshold and stabilization by collisions. *Phys. Rev. Lett.*, 95:085001.
- [160] Saarelma, S., Austin, M. E., Knolker, M., Marinoni, A., Paz-Soldan, C., Schmitz, L., and Snyder, P. B. (2021). Ballooning instability preventing the h-mode access in plasmas with negative triangularity shape on the DIII-d tokamak. *Plasma Physics and Controlled Fusion*, 63(10):105006.
- [161] Schlatter, C. (2009). *Turbulent ion heating in TCV tokamak plasmas*. PhD thesis, EPFL, Lausanne.
- [162] Schneider, P., Bustos, A., Hennequin, P., Ryter, F., Bernert, M., Cavedon, M., Dunne, M., Fischer, R., Görler, T., Happel, T., Igochine, V., Kurzan, B., Lebschy, A., McDermott, R., Morel, P., and Willensdorfer, M. (2017). Explaining the isotope effect on heat transport in l-mode with the collisional electron-ion energy exchange. *Nuclear Fusion*, 57(6):066003.
- [163] Shen, Y., Dong, J. Q., Sun, A. P., Qu, H. P., Lu, G. M., He, Z. X., He, H. D., and Wang, L. F. (2016). Isotope effects of trapped electron modes in the presence of impurities in tokamak plasmas. *Plasma Physics and Controlled Fusion*, 58(4):045028.
- [164] Söldner, F. X., McCormick, K., Eckhardt, D., Kornherr, M., Leuterer, F., Bartiromo, R., Becker, G., Bosch, H. S., Brocken, H., Derfler, H., Eberhagen, A., Fussmann, G., Gehre, O., Gernhardt, J., Gierke, G. v., Giuliana, A., Glock, E., Gruber, O., Haas, G., Hesse, M., Hofmann, J., Izvozchikov, A., Janeschitz, G., Karger, F., Keilhacker, M., Klüber, O., Lackner, K., Lenoci, M., Lisitano, G., Mast, F., Mayer, H. M., Meisel, D., Mertens, V., Müller, E. R., München, M., Murmann, H., Niedermeyer, H., Pietrzyk, A., Poschenrieder, W., Rapp, H., Riedler, H., Röhr, H., Ryter, F., Schmitter, K. H., Schneider, F., Setzensack, C., Siller, G., Smeulders, P., Speth, E., Steuer, K. H., Vien, T., Vollmer, O., Wagner, F., Woyna, F. v., and Zasche, D. (1986). Suppression of sawtooth oscillations by lower-hybrid current drive in the asdex tokamak. *Phys. Rev. Lett.*, 57:1137–1140.
- [165] Solomon, W. M., Burrell, K. H., Andre, R., Baylor, L. R., Budny, R., Gohil, P., Groebner, R. J., Holcomb, C. T., Houlberg, W. A., and Wade, M. R. (2006). Experimental test of the neo-classical theory of impurity poloidal rotation in tokamaks. *Physics of Plasmas*, 13(5):056116.
- [166] Soltwisch, H. and Koslowski, H. R. (1995). Sawtooth modulation of the poloidal field in TEXTOR under ohmic heating conditions. *Plasma Physics and Controlled Fusion*, 37(6):667–678.
- [167] STEP (2022). Step website. <https://ccfe.ukaea.uk/research/step/>. Accessed: 14-07-2022.
- [168] Stix, T. H. (1973). Decay of poloidal rotation in a tokamak plasma. *The Physics of Fluids*, 16(8):1260–1267.

- 
- [169] Stroth, U. (1998). A comparative study of transport in stellarators and tokamaks. *Plasma Physics and Controlled Fusion*, 40(1):9–74.
  - [170] Stroth, U., Manz, P., and Ramisch, M. (2011). On the interaction of turbulence and flows in toroidal plasmas. *Plasma Physics and Controlled Fusion*, 53(2):024006.
  - [171] Sugama, H. and Horton, W. (1997). Neoclassical electron and ion transport in toroidally rotating plasmas. *Physics of Plasmas*, 4(6):2215–2228.
  - [172] Sung, C., White, A., Howard, N., Oi, C., Rice, J., Gao, C., Ennever, P., Porkolab, M., Parra, F., Mikkelsen, D., Ernst, D., Walk, J., Hughes, J., Irby, J., Kasten, C., Hubbard, A., and and, M. G. (2013). Changes in core electron temperature fluctuations across the ohmic energy confinement transition in alcator c-mod plasmas. *Nuclear Fusion*, 53(8):083010.
  - [173] Suttrop, W., Maraschek, M., Conway, G. D., Fahrbach, H.-U., Haas, G., Horton, L. D., Kurki-Suonio, T., Lasnier, C. J., Leonard, A. W., Maggi, C. F., Meister, H., ck, A. M., Neu, R., Nunes, I., tterich, T. P., Reich, M., Sips, A. C. C., and the ASDEX Upgrade Team (2003). ELM-free stationary h-mode plasmas in the ASDEX upgrade tokamak. *Plasma Physics and Controlled Fusion*, 45(8):1399–1416.
  - [174] T. Happel, T. Putterich, J. H., Zohm, H., and the ASDEX Upgrade Team (2020). . *Bull. Am. Phys. Soc.*
  - [175] Tanaka, K., Ohtani, Y., Nakata, M., Warmer, F., Tsujimura, T., Takemura, Y., Kinoshita, T., Takahashi, H., Yokoyama, M., Seki, R., Igami, H., Yoshimura, Y., Kubo, S., Shimozuma, T., Tokuzawa, T., Akiyama, T., Yamada, I., Yasuhara, R., Funaba, H., Yoshinuma, M., Ida, K., Goto, M., Motojima, G., Shoji, M., Masuzaki, S., Michael, C., Vacheslavov, L., Osakabe, M., and Morisaki, T. (2019). Isotope effects on energy, particle transport and turbulence in electron cyclotron resonant heating plasma of the large helical device. *Nuclear Fusion*, 59(12):126040.
  - [176] Tardini, G., Hobirk, J., Igochine, V., Maggi, C., Martin, P., McCune, D., Peeters, A., Sips, A., Stäbler, A., Stober, J., and the ASDEX Upgrade Team (2007). Thermal ions dilution and ITG suppression in ASDEX upgrade ion ITBs. *Nuclear Fusion*, 47(4):280–287.
  - [177] Terry, P. W. (2000). Suppression of turbulence and transport by sheared flow. *Rev. Mod. Phys.*, 72:109–165.
  - [178] Theiler, C. (2011). *Basic Investigation of Turbulent Structures and Blobs of Relevance for Magnetic Fusion Plasmas*. PhD thesis, EPFL, Lausanne.
  - [179] Valovič, M., Lang, P., Kirk, A., Suttrop, W., Bock, A., McCarthy, P., Faitsch, M., Plöckl, B., and and (2020). Compatibility of pellet fuelling with ELM suppression by RMPs in the ASDEX upgrade tokamak. *Nuclear Fusion*, 60(5):054006.
  - [180] Verhaegh, K., Lipschultz, B., Duval, B., Harrison, J., Reimerdes, H., Theiler, C., Labit, B., Maurizio, R., Marini, C., Nespoli, F., Sheikh, U., Tsui, C., Vianello, N., and Vijvers, W.

## Bibliography

---

- (2017). Spectroscopic investigations of divertor detachment in tcv. *Nuclear Materials and Energy*, 12:1112–1117. Proceedings of the 22nd International Conference on Plasma Surface Interactions 2016, 22nd PSI.
- [181] Victor, B. S., Odstrcil, T., Paz-Soldan, C. A., Grierson, B. A., Hinson, E., Jarvinen, A., Hollmann, E. M., Chrystal, C., Collins, C. S., Thome, K. E., and Allen, S. L. (2020). Impurity transport in the pedestal of h-mode plasmas with resonant magnetic perturbations. *Plasma Physics and Controlled Fusion*, 62(9):095021.
- [182] Viezzer, E. (2012). *Radial electric field studies in the plasma edge of ASDEX Upgrade*. PhD thesis, Ludwig Maximilians Universitat Munchen, Munchen.
- [183] Viezzer, E. (2018). Access and sustainment of naturally ELM-free and small-ELM regimes. *Nuclear Fusion*, 58(11):115002.
- [184] Viezzer, E., Pütterich, T., Angioni, C., Bergmann, A., Dux, R., Fable, E., McDermott, R., Stroth, U., and and, E. W. (2013). Evidence for the neoclassical nature of the radial electric field in the edge transport barrier of ASDEX upgrade. *Nuclear Fusion*, 54(1):012003.
- [185] Wang, X., Mordijck, S., Zeng, L., Schmitz, L., Rhodes, T. L., Doyle, E. J., Groebner, R., Meneghini, O., Staebler, G. M., and Smith, S. P. (2016). Turbulent particle transport as a function of toroidal rotation in DIII-d h-mode plasmas. *Plasma Physics and Controlled Fusion*, 58(4):045026.
- [186] Weisen, H., Maggi, C. F., Oberparleiter, M., Casson, F. J., Camenen, Y., Menmuir, S., Horvath, L., Auriemma, F., Bache, T. W., Bonanomi, N., and et al. (2020). Isotope dependence of energy, momentum and particle confinement in tokamaks. *Journal of Plasma Physics*, 86(5):905860501.
- [187] Wesson, J. (2011). *Tokamaks*. Oxford, 4th edition.
- [188] Whyte, D., Hubbard, A., Hughes, J., Lipschultz, B., Rice, J., Marmar, E., Greenwald, M., Cziegler, I., Dominguez, A., Golfinopoulos, T., Howard, N., Lin, L., McDermott, R., Porkolab, M., Reinke, M., Terry, J., Tsujii, N., Wolfe, S., Wukitch, S., and and, Y. L. (2010). I-mode: an h-mode energy confinement regime with l-mode particle transport in alcator c-mod. *Nuclear Fusion*, 50(10):105005.
- [189] Wilson, H., Chapman, I., Denton, T., Morris, W., Patel, B., Voss, G., Waldon, C., and the STEP Team (2020). *STEP—on the pathway to fusion commercialization*. 2053-2563. IOP Publishing.
- [190] Xu, Y., Hidalgo, C., Shesterikov, I., Krämer-Flecken, A., Zoletnik, S., Van Schoor, M., Vergote, M., and the TEXTOR Team (2013). Isotope effect and multiscale physics in fusion plasmas. *Phys. Rev. Lett.*, 110:265005.
- [191] Zabolotsky, A. et al. (2006). Carbon transport in TCV. *Proceedings of the 33rd EPS conference on plasma physics*, 33.

- [192] Zimmermann, C. F. B., McDermott, R. M., Fable, E., Angioni, C., Duval, B. P., Dux, R., Salmi, A., Stroth, U., Tala, T., Tardini, G., and Pütterich, T. (2022). Analysis and modelling of momentum transport based on NBI modulation experiments at ASDEX upgrade. *Plasma Physics and Controlled Fusion*, 64(5):055020.

# Filippo Bagnato

55 Route Cantonale  
St Sulpice, CH 1025,  
Switzerland

Phone: +41786249377  
Email 1: [filippo.bagnato92@gmail.com](mailto:filippo.bagnato92@gmail.com)  
Email 2: [filippo.bagnato@epfl.ch](mailto:filippo.bagnato@epfl.ch)  
Born: 12/11/1992  
Nationality: Italian

## Curriculum Vitae

### Education

---

01/2018 – 07/2022: **PhD** in Plasma Physics at the Swiss Plasma Center (EPFL, Lausanne), supervised by Dr MER Basil P. Duval, “ Study of impurity ions transport through the CX diagnostic in TCV”.

11/2017: **Master degree** in Physics at Sapienza University in Rome, Italy. Curriculum Nuclear and Subnuclear Physics, 120 ECTS degree course. Experimental thesis about the calibration and operation of a Cherenkov probe for runaway electrons detection in the FTU tokamak. Supervised by Dr. Paolo Montani, Dr. Lori Gabellieri, MSc Afra Romano. Final grade: 110/110 cum laude.

01/2015: **Bachelor degree** in Physics at Sapienza University in Rome, Italy. Curriculum Nuclear and Subnuclear Physics, 180 ECTS degree course. Experimental thesis about the development of a trigger for a GPS tracking system applied to a particle detector. Supervised by Prof. Franco Meddi.

### Research collaborations

---

04/2017 – 10/2017: Internship at ENEA Frascati research center. Co-responsible for a Cherenkov detector data acquisition and analysis during FTU tokamak experimental operations.

### Publications

---

#### Papers in international journals

- F. Bagnato *et al*, Triple Cherenkov probe measurements on FTU: calibration and runaway energy spectra, 2018 *Plasma Phys. Control. Fusion* **60** 115010, DOI: <https://doi.org/10.1088/1361-6587/aae0b3>

- H. Reimerdes *et al* (including F. Bagnato), Initial TCV operation with a baffled divertor, 2021 *Nucl. Fusion* **61** 024002 , DOI: <https://doi.org/10.1088/1741-4326/abd196>

- M. Wensing *et al* (including F. Bagnato), SOLPS-ITER validation with TCV L-mode discharges, *Physics of Plasmas* **28**, 082508 (2021), DOI: <https://doi.org/10.1063/5.0056216>

- S. Coda *et al* (including F. Bagnato), Enhanced confinement in diverted negative-triangularity L-mode plasmas in TCV, 2022 *Plasma Phys. Control. Fusion* **64** 014004, DOI: <https://doi.org/10.1088/1361-6587/ac3fec>

- B. Labit *et al* (including F. Bagnato), Dependence on plasma shape and plasma fueling for small edge-localized mode regimes in TCV and ASDEX Upgrade, 2019 *Nucl. Fusion* **59** 086020 , DOI: <https://doi.org/10.1088/1741-4326/ab2211>

- D. Carnevale *et al* (including F. Bagnato), Runaway electron beam control, 2019 *Plasma Phys. Control. Fusion* **61** 014036, DOI: <https://doi.org/10.1088/1361-6587/aaef53>



- G. Pucella *et al* (including F. Bagnato), Overview of the FTU results, 2019 *Nucl. Fusion* **59** 112015, DOI: <https://doi.org/10.1088/1741-4326/ab19ef>
- B. Geiger *et al* (including F. Bagnato), Observation of Alfvén Eigenmodes driven by off-axis neutral beam injection in the TCV tokamak, 2020 *Plasma Phys. Control. Fusion* **62** 09501, DOI: <https://doi.org/10.1088/1361-6587/aba19e>
- S. Coda *et al* (including F. Bagnato), Physics research on the TCV tokamak facility: from conventional to alternative scenarios and beyond, 2019 *Nucl. Fusion* **59** 112023, DOI: <https://doi.org/10.1088/1741-4326/ab25cb>

### **Posters (selection)**

- F. Bagnato *et al*, Study of impurity ions transport through the CX diagnostic in TCV, 2021 47th EPS virtual conference
- A. N. Karpushov *et al* (including F. Bagnato), Instabilities and fast ion confinement on the TCV tokamak, 2019 46th EPS conference, Milan
- R. M. McDermott *et al* (including F. Bagnato), Development of NBI modulation experiments in the TCV tokamak, 2018 23rd Joint EU-US Transport Task Force Meeting (TTF), Seville
- A. Romano *et al* (including F. Bagnato), Effects of pellets and impurity injection on runaway control experiments on FTU , 2018 45th EPS conference, Prague
- G. Ferrò *et al* (including F. Bagnato), Adaptive control design and energy distribution estimation via nonlinear observer for runaway electron in FTU, 2017 44th EPS conference, Belfast

### **Seminars**

F. Bagnato *et al*, Isotope effect on plasma confinement and rotation in TCV, ITPA T&C spring meeting (virtual), 2022

### **Languages**

---

Italian: Native  
 English: Advanced C1  
 French: Intermediate B2  
 Arabic (standard): Elementary A2

### **Relevant activities and skills**

---

#### **Teaching assistant**

2018 spring semester: Assisting during exercise sessions for EPFL MAN Algebra classes.

2018 winter semester – 2022 winter semester: Lab assistant for the TPIII (Travaux pratiques) Plasma I & II experiments. Assisting multiple groups of students, guiding them through experiments on plasma physics and correcting final reports.

## **Guide for visitors**

Guide for groups visiting the Swiss Plasma Center, introducing concepts on plasma physics and nuclear fusion, tour of TCV and TORPEX facilities. Presentations given in English, Italian and French.

## **Computer skills**

Matlab, Python, LATEX, Linux.

## **Technical skills**

Expert in spectroscopy: design, installation and calibration of optical devices integrated in complex systems. Data analysis and interpretation.

Experienced in working with Langmuir probes for electron temperature and density measurements in basic plasma devices.

Experienced in working with photomultipliers.

## **Extra-curricular activities**

---

### **Sports**

Advanced level rock climber with multiple 7c (sport), 7B/V8 (boulder) and ED- (alpine trad) ascents realised in Italy, France, Spain, Switzerland and Greece.